

## Vortex sound in confined flows

**Citation for published version (APA):**

Hofmans, G. C. J. (1998). *Vortex sound in confined flows*. [Phd Thesis 1 (Research TU/e / Graduation TU/e), Applied Physics and Science Education]. Technische Universiteit Eindhoven. <https://doi.org/10.6100/IR514917>

**DOI:**

[10.6100/IR514917](https://doi.org/10.6100/IR514917)

**Document status and date:**

Published: 01/01/1998

**Document Version:**

Publisher's PDF, also known as Version of Record (includes final page, issue and volume numbers)

**Please check the document version of this publication:**

- A submitted manuscript is the version of the article upon submission and before peer-review. There can be important differences between the submitted version and the official published version of record. People interested in the research are advised to contact the author for the final version of the publication, or visit the DOI to the publisher's website.
- The final author version and the galley proof are versions of the publication after peer review.
- The final published version features the final layout of the paper including the volume, issue and page numbers.

[Link to publication](#)

**General rights**

Copyright and moral rights for the publications made accessible in the public portal are retained by the authors and/or other copyright owners and it is a condition of accessing publications that users recognise and abide by the legal requirements associated with these rights.

- Users may download and print one copy of any publication from the public portal for the purpose of private study or research.
- You may not further distribute the material or use it for any profit-making activity or commercial gain
- You may freely distribute the URL identifying the publication in the public portal.

If the publication is distributed under the terms of Article 25fa of the Dutch Copyright Act, indicated by the "Taverne" license above, please follow below link for the End User Agreement:

[www.tue.nl/taverne](http://www.tue.nl/taverne)

**Take down policy**

If you believe that this document breaches copyright please contact us at:

[openaccess@tue.nl](mailto:openaccess@tue.nl)

providing details and we will investigate your claim.

Vortex  
Sound in Confined Flows



G.C.J. Hofmans

# VORTEX SOUND IN CONFINED FLOWS

Copyright ©1998, G.C.J. Hofmans  
Omslagontwerp: Ben Mobach, TUE  
Druk: Universiteitsdrukkerij, TUE

CIP-DATA LIBRARY TECHNISCHE UNIVERSITEIT EINDHOVEN

Hofmans, Gerardus Carolus Johannes

Vortex sound in confined flows / by Gerardus Carolus Johannes Hofmans. -  
Eindhoven: Technische Universiteit Eindhoven, 1998. -  
Proefschrift. - ISBN 90-386-0697-4  
NUGI 812

Trefw.: aero-akoestiek / geluidsinteractie / geluidsleer / stromingsleer.  
Subject headings: aerodynamics / vortices / flow separation.

# VORTEX SOUND IN CONFINED FLOWS

PROEFSCHRIFT

ter verkrijging van de graad van doctor aan de Technische  
Universiteit Eindhoven, op gezag van de Rector Magnificus,  
prof.dr. M. Rem, voor een commissie aangewezen door het  
College voor Promoties in het openbaar te verdedigen op  
maandag 28 september 1998 om 16.00 uur

door

GERARDUS CAROLUS JOHANNUS HOFMANS

geboren te Horst

Dit proefschrift is goedgekeurd door de promotoren:

prof.dr.ir. H.W.M. Hoeijmakers

en

prof.dr.ir. G.J.F. van Heijst

Copromotor:

dr.ir. A. Hirschberg

This research was financed by the Technology Foundation STW,  
grant ETN33.2952



# Contents

1	Introduction	1
2	Theoretical background	8
2.1	Introduction	8
2.2	Acoustics	8
2.2.1	Fundamentals	8
2.2.2	Lighthill's analogy applied to a diaphragm in a pipe	11
2.2.3	Howe's energy formulation	15
2.3	Integral representation for the pressure	17
2.3.1	Introduction	17
2.3.2	The pressure field for a two-dimensional incompressible flow	18
2.4	Numerical methods	22
2.4.1	Vorticity-transport equation	22
2.4.2	Vortex-blob method for inviscid flow	23
2.4.3	Vortex-blob method for viscous flow	28
2.5	Boundary-layer theory	30
2.5.1	Introduction	30
2.5.2	Boundary-layer equations	31
2.5.3	The von Kármán equation	33
2.5.4	Flow separation	35
2.5.5	Approximate boundary-layer descriptions	36
2.6	Concluding remarks	39
3	Flow through a square-edge nozzle at low Mach number	44
3.1	Introduction	44
3.2	Experiments	46
3.2.1	Experimental set-up	46
3.2.2	Experimental results	49
3.3	Numerical simulations	55
3.3.1	Numerical methods and input	55
3.3.2	Numerical results	59
3.4	Results of the unsteady boundary-layer model	72
3.5	Concluding remarks	74

4	Flow through in vitro models of the vocal folds	77
4.1	Introduction	77
4.2	Experiments	80
4.2.1	Experimental set-up	80
4.2.2	Results for the lip-like round model	81
4.2.3	Results for the 20°-diverging model	87
4.2.4	Results for the 10°-diverging model	93
4.2.5	Results for the asymmetric diffuser model	97
4.3	Numerical simulation	101
4.3.1	Input for the simulations	101
4.3.2	Results	103
4.4	Concluding remarks	111
5	Aeroacoustic behaviour of a diaphragm in a pipe	114
5.1	Introduction	114
5.2	Quasi-steady modelling	116
5.2.1	Defining the approximations	116
5.2.2	Incompressible-flow model	118
5.2.3	Compressible-flow model	121
5.3	Vena contracta	124
5.4	Experimental results for low-frequencies	127
5.4.1	Experimental set-up and procedure	127
5.4.2	Results	130
5.5	Application of vortex-blob method	134
5.6	Acoustic source power	136
5.7	Acoustic response	139
5.8	Results for low-Mach-number unsteady flows	140
5.9	Concluding remarks	144
6	Numerical study of the acoustic interaction in a T-joint	148
6.1	Introduction	148
6.2	T-joint configurations	149
6.3	Acoustic-velocity field	150
6.4	Quasi-steady modelling	151
6.4.1	Introduction	151
6.4.2	Acoustic outflow	153
6.4.3	Acoustic inflow	158
6.5	Acoustic power versus Strouhal number	163
6.5.1	Introduction	163
6.5.2	Configurations with flow separation at one edge	164
6.5.3	Influence of second separation	175
6.5.4	Period doubling	177
6.5.5	Remarks on rounding the upstream edge	178



---

6.6	Acoustic power versus acoustic amplitude . . . . .	179
6.7	Comparison of numerical simulation to experiments . . . . .	183
6.7.1	Low- to moderate-amplitude oscillations . . . . .	183
6.7.2	High-amplitude oscillations . . . . .	186
6.8	Concluding remarks . . . . .	196
7	General discussion, conclusions and recommendations . . . . .	199
A	Lighthill's analogy . . . . .	203
B	Pressure measurements . . . . .	206
C	Aspects of the inviscid vortex-blob method . . . . .	213
D	Scattering matrix for the compressible-flow model . . . . .	216
E	The vena contracta in the Borda mouthpiece . . . . .	219
F	Correction for visco-thermal dissipation in a turbulent main flow . . . . .	224
	Summary . . . . .	227
	Samenvatting . . . . .	229
	Dankwoord . . . . .	231
	Curriculum vitae . . . . .	233



## Chapter 1

---

# Introduction

In this introduction the scope of this thesis is discussed. The definition of “vortex sound” is given and the “confined flows” that are studied are specified.

Sound has been (historically) defined as the pressure fluctuations  $p'$  which can be detected by the human ear. Such fluctuations are small compared to the atmospheric pressure:  $p'/p_{atm} = \mathcal{O}(10^{-4})$  which justifies the use of linear theory. As the human ear is sensitive to fluctuations in the limited frequency range  $20 \text{ Hz} < f < 20 \text{ kHz}$  sound is an essentially unsteady phenomenon. In many applications the propagation of sound is considered in a uniform stagnant fluid over such length scales that thermal and viscous dissipation are negligible. In that case propagation of sound in a fluid at rest otherwise is described by the scalar wave equation for density fluctuations  $\rho'$ :

$$\frac{\partial^2 \rho'}{\partial t^2} - c_0^2 \nabla^2 \rho' = 0, \quad (1.1)$$

where  $c_0$  is the mean value of the speed of sound and the density fluctuations are related to the pressure fluctuations by:

$$p' = c_0^2 \rho'. \quad (1.2)$$

Sound generation is at such circumstances due to boundary conditions.

When the study of sound is extended to its generation in flows one is considering aeroacoustics and sound suddenly becomes hard to define. Lighthill (1952, 1954) proposes to define the acoustic field as the extension into the non-linear flow region of the linear acoustic field around a listener who is assumed to be immersed into a uniform and stagnant fluid. He assumes that the perturbations  $\rho'$  reaching the listener satisfy locally the wave equation (1.1). Departures from this ideal behaviour are not neglected but are acting as sources of sound  $Q_\rho$ :

$$\frac{\partial^2 \rho'}{\partial t^2} - c_0^2 \nabla^2 \rho' = Q_\rho.$$

Using the mass and momentum conservation laws, Lighthill obtained an exact expression for  $Q_\rho$ . The resulting non-homogeneous wave equation is within an exact approach

useless because it does not provide any new information compared to the original mass and momentum conservation laws. The procedure proposed by Lighthill, which is called an “analogy”, is only a convenient framework to introduce approximations. Such approximations can be inspired by the structure of the source  $Q_\rho$ . At this point it is important to realise that while in acoustics all variables such as  $p'$  and  $\rho'$  are equivalent, i.e. satisfy the same wave equation, this is not the case in aeroacoustics. For example the source term  $Q_\rho$  found when using  $\rho'$  as the basic aeroacoustic variable is<sup>1</sup>:

$$Q_\rho = \frac{\partial^2}{\partial x_i \partial x_j} [\rho u_i u_j - \tau_{ij} + (p' - c_0^2 \rho') \delta_{ij}] - \frac{\partial f_i}{\partial x_i},$$

where  $u_i$  is the flow velocity,  $\tau_{ij}$  the viscous shear stress and  $f_i$  an external force density. When we use  $p'$  as the basic aeroacoustic variable the source term becomes:

$$Q_p = \frac{\partial^2}{\partial x_i \partial x_j} [\rho u_i u_j - \tau_{ij}] - \frac{\partial f_i}{\partial x_i} - \frac{\partial^2 \rho_e}{\partial t^2},$$

where  $\rho_e$  is the so-called excess density defined as:

$$\rho_e = \rho' - \frac{p'}{c_0^2}.$$

The first expression for the source term  $Q_\rho$  is best suited for understanding sound production due to non-uniformity in the entropy of the flow. The term  $\frac{\partial^2}{\partial x_i \partial x_j} (p' - c_0^2 \rho')$  can be seen as the effect of the force due to the difference in the acceleration of particles due to differences in density (Morfey 1973, Powell 1990). The analogy in terms of  $p'$  provides a source  $Q_p$  in which unsteadiness in entropy is almost explicit. This makes it most suitable to describe sound production due to unsteady combustion (Dowling 1992).

In the original approach of Lighthill a next key step is the use of a formal solution of the inhomogeneous wave equation in terms of a convolution of the source with the free field Green's function. After some formal manipulation a most suitable environment is found to obtain scaling rules for the sound production based on first order of magnitude estimates of flow parameters. The integral formulation tends to smooth out “random” errors in flow parameter estimates. The success of Lighthill's approach applied to free turbulent jets (Fisher & Morfey 1982) has promoted aeroacoustics to an independent chapter of acoustics and fluid dynamics. It is worthwhile noting that this success was based on some very intuitive assumptions. For example the effect of viscous dissipation on the free jet sound production is still subject of discussion (Morfey 1976, Obermeier 1985, Iafrati & Riccardi 1996).

The approach of Lighthill has been generalised for the presence of walls by Curle (1955) and Ffowcs Williams & Hawkins (1969). Ffowcs Williams (1969) has replaced the free field Green's function by a low-frequency one-dimensional Green's function for application in a

<sup>1</sup>The summation convention is used. An index that appears twice means that the sum over this index is taken: e.g.  $\frac{\partial u_i}{\partial x_i}$  means  $\sum_i \frac{\partial u_i}{\partial x_i} = \frac{\partial u_1}{\partial x_1} + \frac{\partial u_2}{\partial x_2} + \frac{\partial u_3}{\partial x_3}$ .

pipe. We will present in chapter 2 an application of Curle's formalism to confined flows based on the use of the same one-dimensional Green's function.

Lighthill's analogy allows for an extraction of a maximum amount of information on sound production from a given amount of data on a flow field. For example Bastin *et al.* (1997) and Colonius *et al.* (1997) use an acoustic analogy to extract information on mixing noise from their numerical calculations of the flow field. In such a procedure one often neglects the feedback of the acoustic field on the flow. As we are interested in such feedback effects we have to carry out numerical calculations of the unsteady flow field. We limit ourselves to homentropic subsonic two-dimensional flows at high Reynolds numbers. Furthermore, we consider only low frequencies so that wave propagation in the source region is negligible. Under such conditions the main source of sound is the pressure force exerted by walls on the flow. This force is directly related to the dynamics of vortices generated by flow separation at the walls. A description of a two-dimensional incompressible flow is very convenient in terms of vorticity  $\vec{\omega} = \vec{\nabla} \times \vec{u}$  because this quantity is conserved when we move with a fluid particle ( $D\omega_z/Dt = 0$ ). Point-vortex methods based on this property have the advantage that they provide a concentration of point vortices in the region where vorticity is significant, which is equivalent to a local mesh refinement. Furthermore, the calculation domain can be unbounded which avoids the problem of "numerical sound" generated by the interaction of vorticity and the numerical boundaries. We will use such numerical methods. It is therefore most convenient to have an aeroacoustic analogy in which the relationship between vorticity dynamics and sound production is more explicit.

While such a relationship between vortices and sound production was already obvious at the beginning of this century (Bouasse 1929) a formal theory was established when Powell (1964) demonstrated that for a subsonic compact flow in free space Lighthill's sound source was:

$$Q_\rho = -\vec{\nabla} \cdot \vec{f}_c$$

in which

$$\vec{f}_c = -\rho_0(\vec{\omega} \times \vec{u}).$$

This is the Coriolis force experienced when moving with the fluid velocity  $\vec{u}$ . Howe (1975, 1984) assumed that such an elegant result should be much more general than supposed by Powell. He searched for another aeroacoustic variable which would allow a more general application of the result of Powell. He found that the vortex sound theory could be generalised to confined flows provided the source of sound is not defined relative to a uniform stagnant fluid, as proposed by Lighthill, but with respect to a potential flow. The fluctuation in the total enthalpy  $B'$  appears in such a case as a natural variable, see Howe (1984), Doak (1995, 1998), Musafir (1997), and Auregan (1998). The last two authors recently proposed a modification of Howe's analogy. We will restrict ourselves to conditions for which the vortex sound theory of Howe is most appropriate (i.e. subsonic homentropic flows).

The present research is concerned with three main subjects: physical modelling of speech production, damping of acoustic waves in pipes by the use of diaphragms, and self-sustained pulsations in gas-transport systems. In all three cases flow separation results in

vortex shedding which is the mechanism by which sound is either produced or absorbed. In all three cases we seek for simplified models which can be used for engineering type of applications. Furthermore, we try to determine the range of validity of these models. We present a study of some aspects of these problems which may allow a more systematic approach to engineering models of vortex sound interaction in such confined flows.

The speech research was initiated by the previous work on physical modelling of human voiced sound production (Pelorson *et al.* 1994). We consider both the numerical generation of speech by physical models and the design of vocal-fold prosthesis. A simplified model for the flow through the glottis is available in the form of the laminar quasi-steady boundary-layer model of Pohlhausen (Pelorson *et al.* 1994). Two-dimensional incompressible numerical simulations of the flow through fixed rigid vocal-fold models and starting-flow experiments on similar models have resulted in an increased understanding of the dominant flow phenomena occurring in the flow through the glottis. This work has accumulated in the proposal of a new vocal-fold model (Lous *et al.* 1998) and a study of the generation of plosive sounds (Pelorson *et al.* 1997).

Previous experimental work on the acoustic effect of sudden changes in pipe diameter by Ronneberger (1967, 1987) and open pipes by Peters (1993) has inspired our work on a diaphragm in a pipe. This research has applications in the design of anechoic pipe terminations or silencers (e.g. car mufflers). A quasi-steady model based on the previous models of Bechert (1980) and Ronneberger (1967) is proposed. Numerical simulations of the flow through a two-dimensional (slit-shaped) diaphragm in a channel have extended results to essentially unsteady flow conditions. The work on quasi-steady modelling of the flow through a diaphragm in a pipe has resulted in the design of an anechoic pipe termination (Boot 1995).

Previous work by Bruggeman (1987), Peters (1993) and Kriesels *et al.* (1995) initiated the present research on self-sustained pulsations in gas-transport systems. We look for either verbal design rules which reduce the chance of pulsations or a sound source which can be implemented into a low-frequency acoustic model of a complex pipe manifold. A simplified theory is in this case available in the form of Nelson's single vortex model (Nelson *et al.* 1983, Hirschberg 1995). The focus in the present research is on the T-joint configuration with sharp edges which is studied by means of numerical simulations for two-dimensional flow. Several of the most relevant flow configurations in a T-joint are investigated. This work has resulted in a simple procedure to predict pulsations in pipe systems with closed side branches (Hirschberg 1997).

We start our discussion in chapter 2 with a summary of the theoretical background. We consider the basic equations of fluid dynamics, both Lighthill's and Howe's analogies, and simplified boundary-layer models. Furthermore, the background to the numerical methods used in the present research is provided. The flow through a square-edge nozzle at low Mach number is discussed in chapter 3, laying the groundwork for the flow through models of the vocal folds considered in chapter 4. Both chapters rely heavily on the combination of experimental and numerical work, while chapter 4 additionally considers the quasi-steady boundary-layer model of Pohlhausen applied to the prediction of flow separation. A low-frequency model of the flow through a diaphragm in a pipe is proposed in chapter 5.

This model may include compressibility effects and can therefore be applied up to a Mach number equal to one in the jet formed at the diaphragm. In particular we consider the effect of the Mach-number dependence of the *vena contracta* factor of the jet flow. The importance of this effect became clear after experiments by Parchen & Bruggeman (1995). Also numerical results of the unsteady flow through a slit-like diaphragm at low Mach number are presented, which upon implementation into an acoustic model are compared to measurements of the transmission matrix of such a diaphragm carried out by Ajello (1997a, 1997b). In chapter 6 nine different flow configurations in a T-joint are considered. We focus on the case of side-branch diameters equal to the main pipe diameter and on T-joints with sharp edges. A simplified quasi-steady model of these flows is proposed for engineering applications. An overview of the acoustic properties of the different flow configurations is given. The configuration with a mean (steady) flow through the main pipe and an oscillatory flow between side branch and downstream main pipe segment is considered in more detail. Using an energy balance numerical results for this configuration are compared to measured pulsation levels in the side branch. Finally in chapter 7 we present final remarks and the main conclusions of the present work.

## References

- AJELLO, G. (1997a) Mesures acoustiques dans les guides d'ondes en présence d'écoulement: mise au point d'un banc de mesure applications à des discontinuités *PhD thesis Université du Maine*
- AJELLO, G. (1997b) *Private communication*
- AUREGAN, Y. (1998) *Private communication*
- BASTIN, F., LAFON, P., & CANDEL, S. (1997) Computation of jet mixing noise due to coherent structures: the plane jet case. *J. Fluid Mech.* **335**, 261–304
- BECHERT, D.W. (1980) Sound absorption caused by vorticity shedding, demonstrated with a jet flow. *J. Sound & Vibr.* **70**, 389–405
- BOOT, R.J.J. (1995) Het aeroakoestisch gedrag van diafragma's. *Report R-1370-A, Eindhoven University of Technology*
- BOUASSE, H. (1929) Instrument à vent, volumes I & II. *Libraries Delagrave, Paris*
- BRUGGEMAN, J.C. (1987) Flow induced pulsations in pipe systems. *PhD thesis Eindhoven University of Technology*
- COLONIUS T., LELE, S.K., & MOIN, P. (1997) Sound generation in a mixing layer. *J. Fluid Mech.* **330**, 375–409

- CURLE, N. (1955) The influence of solid boundaries upon aerodynamical sound. *Proc. Roy. Soc. A* **231**, 505–514
- DOAK, P.E. (1995) Fluctuating total enthalpy as a generalized field. *Acoust. Phys.* **44**, 677–685
- DOAK, P.E. (1998) Fluctuating total enthalpy as the basic generalized acoustic field. *Theoret. Comput. Fluid Dynamics* **10**, 115–133
- DOWLING, A.P. (1992) Thermoacoustic sources and instabilities. Appeared in “Modern methods in analytical acoustics.” CRIGHTON, D.G., DOWLING, A.P., FLOWCS WILLIAMS, J.E., HECKL, M., & LEPPINTON, F.G. *Springer Verlag, London*, 378–403
- FLOWCS WILLIAMS, J.E. (1969) Hydrodynamic noise. *Ann. Rev. Fluid Mech.* **1**, 197–222
- FLOWCS WILLIAMS, J.E. & HAWKINS, D.L. (1969) Sound generation by turbulence and surfaces in arbitrary motion. *Proc. Roy. Soc. A* **264**, 321–342
- FISHER, M.J. & MORFEY, C.L. (1982) Jet noise. Appeared in “Noise and vibration” *Ellis Horwood, Chichester*, 308–335
- HIRSCHBERG, A (1995) Aeroacoustics of wind instruments. Appeared in “Mechanics of musical instruments”, A. Hirschberg, J. Kergomard and G. Weinreich editors *CISM courses and lectures No. 355, Springer Verlag, Wien*, 291–369
- HIRSCHBERG, A (1997) Self-sustained aeroacoustical oscillations in gas transport systems: a prediction method for pulsations induced by closed pipe segments. *Report TUE NT R-1428-D, Laboratory for Fluid Dynamics and Heat Transfer, Department of Physics, Eindhoven University of Technology*
- HOWE, M.S. (1975) Contribution to the theory of aerodynamic sound, with application to excess jet noise and the theory of the flute. *J. Fluid Mech.* **71**, 625–673
- HOWE, M.S. (1985) On the absorption of sound by turbulence and other hydrodynamic flows. *IMA, J. Appl. Math.* **32**, 187–209
- IAFRATI, A. & RICCARDI, G. (1996) A numerical evaluation of viscous effects on vortex induced noise. *J. Sound & Vibr.* **196**, 129–146
- KRIESELS, P.C, PETERS, M.C.A.M., HIRSCHBERG, A. & WIJNANDS, A.P.J. (1995) High amplitude vortex-induced pulsations in a gas transport system. *J. Sound & Vibr.* **184**, 343–368
- LIGHTHILL, M.J. (1952) On sound generated aerodynamically I. *Proc. Roy. Soc. A* **211**, 564–587



- LIGHTHILL, M.J. (1954) On sound generated aerodynamically II. *Proc. Roy. Soc. A* **222**, 1–32
- LOUS, N.J.C., HOFMANS, G.C.J., VELDHUIS, R.N.J., & HIRSCHBERG, A. (1998) A symmetrical two-mass vocal-fold model coupled to vocal tract and trachea, with application to prosthesis design. *accepted for publication in Acta Acoustica*
- MORFEY, G.L. (1973) Amplification of aerodynamic noise by convected flow inhomogeneities. *J. Sound & Vibr.* **31**, 391–397
- MORFEY, G.L. (1976) Sound radiation due to unsteady dissipation in turbulent flows. *J. Sound & Vibr.* **48**, 95–111
- MUSAFIR, R.E. (1997) A discussion on the structure of aeroacoustic wave equations. Proceedings of the 4<sup>th</sup> Congress on Acoustics, Marseilles *Teknea, Toulouse*, 923–926
- NELSON, P.A., HALLIWELL, N.A. & DOAK, P.E. (1983) Fluid dynamics of flow excited resonance, part 2: theory. *J. Sound & Vibr.* **91**, 375–402
- OBERMEIER, F. (1985) Aerodynamic sound generation caused by viscous processes. *J. Sound & Vibr.* **99**, 111–120
- PARCHEN, R.R. & BRUGGEMAN, J.C. (1995) *Private communication*
- PELORSON, X., HIRSCHBERG A., VAN HASSEL, R.R., WIJNANDS, A.P.J., & AUREGAN Y. (1994) Theoretical and experimental study of quasi-steady flow separation within the glottis during phonation. Application to a modified two-mass model. *J. Acoust. Soc. Am.* **96**, 3416–3431
- PELORSON, X., HOFMANS, G.C.J., RANUCCI, M., & BOSCH R.C.M. (1997) On the fluid mechanics of bilabial plosives. *Speech Comm.* **22**, 155–172
- PETERS, M.C.A.M. (1993) Aeroacoustical sources in internal flows. *PhD thesis Eindhoven University of Technology*
- POWELL A. (1964) Vortex sound theory. *J. Acoust. Soc. Am.* **36**, 177–195
- POWELL A. (1990) Some aspects of aeroacoustics: from Rayleigh until today. *Trans. ASME J. Vibr. & Acoust.* **112**, 145–159
- RONNEBERGER, D. (1967) Experimentelle Untersuchungen zum akustischen Reflexionsfaktor von un stetigen Querschnittsänderungen in einem luftdurchströmten Rohr. *Acustica* **19**, 222–235
- RONNEBERGER, D. (1987) Theoretische und experimentelle Untersuchung der Schallausbreitung durch Querschnittsprünge und Lochplatten in Strömungskanälen. *Report Ro 369/11, 12, 14, "Drittes Physikalisches Institut", University of Göttingen*

# Theoretical background

## 2.1 Introduction

In the preceding chapter we already discussed some aspects of aeroacoustics with respect to the use of an analogy. In this chapter we present the mathematical background to what was discussed by applying Lighthill's analogy to the flow through a diaphragm in a pipe. Furthermore, Howe's analogy is derived for an incompressible source region. Next we derive an integral formulation for the total-pressure, which is implemented in the two vortex-blob methods as an alternative to Howe's formulation. Both methods for inviscid and viscous flow are explained in the subsequent section. We then proceed to provide some background information on the boundary-layer theory and we discuss flow separation. To conclude we discuss a few simplified boundary-layer models.

The treatment of aeroacoustics in this chapter is very basic and is not intended as a comprehensive introduction to aeroacoustics. For further reading one is referred to one of the following textbooks: Goldstein (1976), Crighton *et al.* (1992).

Background information on vortex dynamics and vortex methods can be found in Lewis (1991) and Saffman (1992) while interesting reviews on the subject are presented in Anderson & Greengard (1985) and Sarpkaya (1989).

For further reading on boundary-layer theory the following textbooks are suggested: Schlichting (1979) and Cousteix (1988). More information on how to solve the boundary-layer equations numerically can be found in Fletcher (1988) and Sherman (1990).

## 2.2 Acoustics

### 2.2.1 Fundamentals

A fluid with density  $\rho$  moving at a velocity  $\vec{u}$  obeys the fundamental physical laws of conservation: conservation of mass, momentum, and energy. When no external sources of

mass and energy are present the conservation equations have the following form:

$$\frac{\partial \rho}{\partial t} + \vec{\nabla} \cdot \rho \vec{u} = 0, \quad (2.1a)$$

$$\frac{\partial \rho \vec{u}}{\partial t} + \vec{\nabla} \cdot \rho \vec{u} \vec{u} = -\vec{\nabla} p + \vec{\nabla} \cdot \vec{\tau} + \vec{f}, \quad (2.1b)$$

$$\frac{\partial \rho E}{\partial t} + \vec{\nabla} \cdot \rho \vec{u} E = -\vec{\nabla} \cdot (p \vec{u}) + \vec{\nabla} \cdot (\vec{\tau} \cdot \vec{u}) + \vec{f} \cdot \vec{u} - \vec{\nabla} \cdot \vec{q}, \quad (2.1c)$$

in which  $p$  is the pressure,  $\vec{\tau}$  is the viscous stress tensor,  $\vec{f}$  is an external body force density,  $E = e + \frac{1}{2}|\vec{u}|^2$  is the total energy per unit mass,  $e$  is the internal energy per unit mass, and  $\vec{q}$  is the heat flux vector which is related to the gradient of the temperature  $T$  by Fourier's law:  $\vec{q} = -\kappa \vec{\nabla} T$ , where  $\kappa$  is the coefficient of thermal conductivity. Considering a so-called Newtonian fluid the viscous stress tensor can be written as:

$$\vec{\tau} = 2\eta \vec{D} + \eta'(\vec{\nabla} \cdot \vec{u}) \vec{I} \quad (2.2)$$

in which  $\eta$  is the dynamic viscosity,  $\vec{D}$  is the deformation tensor,  $\vec{I}$  is the identity tensor, and  $\eta'$  is the second viscosity coefficient. The elements of the deformation tensor are defined by:  $D_{ij} = \frac{1}{2}(\frac{\partial u_i}{\partial x_j} + \frac{\partial u_j}{\partial x_i})$ .

For the problems that we study the total enthalpy  $B = e + \frac{p}{\rho} + \frac{1}{2}|\vec{u}|^2$  is an important quantity. The energy equation (2.1c) can be rewritten as an equation for the total enthalpy  $B$ :

$$\frac{\partial \rho B}{\partial t} + \vec{\nabla} \cdot \rho \vec{u} B = \frac{\partial p}{\partial t} + \vec{\nabla} \cdot (\vec{\tau} \cdot \vec{u}) + \vec{f} \cdot \vec{u} - \vec{\nabla} \cdot \vec{q}. \quad (2.3)$$

Even if all coefficients are assumed to be known functions of the unknown variables, no matter which set of equations is chosen - (2.1a), (2.1b) and (2.1c) or (2.3) - there are still only 5 equations for 7 unknowns:  $\rho$ ,  $\vec{u}$ ,  $p$ ,  $E$ , and  $T$ . To complete the set of equations additional assumptions are necessary. The assumption of local thermodynamic equilibrium states that for a fluid of fixed chemical composition there are only two independent thermodynamic variables, so that choosing for example  $\rho$  and  $T$  as the independent thermodynamic variables we have:

$$p = p(\rho, T), \quad e = e(\rho, T)$$

We use the equations of state for a calorically perfect gas, which are the ideal gas law:

$$\frac{p}{\rho} = RT, \quad (2.4)$$

and the equation for the internal energy:

$$e = C_v T, \quad (2.5)$$

in which  $R$  is the specific gas constant and  $C_v$  is the specific heat at constant volume which for a calorically perfect gas is constant. The quantities  $R$  and  $C_v$  are related by another

important quantity the specific heat at constant pressure  $C_p = C_v + R$ . However, the ratio of specific heats  $\gamma$  is a more commonly used parameter:  $\gamma = \frac{C_p}{C_v}$ .

In acoustics one usually considers only small perturbations in a uniform stagnant ( $\vec{u}_0 = 0$ ) mean flow with properties  $p_0$ ,  $\rho_0$ , etc. So that the equations (2.1a) to (2.1c) may be linearised to yield an inhomogeneous wave equation for the pressure perturbations ( $p' = p - p_0$ ):

$$\frac{1}{c_0^2} \frac{\partial^2 p'}{\partial t^2} - \nabla^2 p' = Q'_p. \quad (2.6)$$

The right-hand side represents all acoustic pressure sources and when it is equal to zero the homogeneous wave equation for  $p'$  is obtained. In that case the pressure perturbations travel unperturbed with the speed of sound  $c_0$ . The speed of sound is defined as the derivative of the pressure with respect to the density at constant entropy  $S$ :

$$c^2 = \left( \frac{\partial p}{\partial \rho} \right)_S.$$

For an ideal gas the speed of sound in the unperturbed medium is  $c_0 = \sqrt{\gamma RT_0}$ . In aeroacoustic experiments an accurate value for the speed of sound can be vital for an accurate interpretation of the results. Corrections on the speed of sound in air due to for instance humidity can be found in references (Wong & Embleton 1985, Cramer 1993).

A similar wave equation can be derived for the density perturbation  $\rho'$ , however, the structure of the source term on the right-hand side will be different. The inhomogeneous wave equation for  $\rho'$ , neglecting external mass sources and external forces, is known as Lighthill's wave equation. Depending on the problem being studied different wave equations are proposed in the literature. For instance Doak (1998) proposes the perturbations in the total enthalpy  $B'$  as the basic acoustic field.

Equation (2.6) suggests an approach to acoustic problems that is commonly used. The flow domain is divided into a source region where  $Q'_p \neq 0$  and a wave propagation region where  $Q'_p = 0$ . This approach has several advantages. First of all, in the wave propagation region far away from the source region the details of the source region are not important, only the global sound produced is important. A second advantage is found by non-dimensionalising the wave equation:

$$He^2 \frac{\partial^2 \hat{p}}{\partial \hat{t}^2} - \hat{\nabla}^2 \hat{p} = \hat{Q}_{\hat{p}} \quad (2.7)$$

in which  $\hat{\cdot}$  represents the non-dimensionalised quantity and  $He$  is the Helmholtz number. It is defined as  $He = \frac{L}{\lambda}$  with  $L$  a reference length scale and  $\lambda$  the wave length of the acoustic perturbation. When  $He \ll 1$  with  $L$  the typical size of the source region the effects of wave propagation in the source region can be ignored: the source region is considered compact.

An important approximation in fluid dynamics is the incompressible-flow approximation: density variations can be ignored in the flow domain ( $\rho = \rho_0$ ). Introducing the Mach number  $M$  as the ratio of the velocity  $u_0$  and the speed of sound  $c$  it can be shown that a necessary condition for this approximation is that in the whole flow domain the Mach

number is small enough:  $M^2 \ll 1$ . Then mass conservation in a compact region reduces to the simple equation:

$$\vec{\nabla} \cdot \vec{u} = 0, \quad (2.8)$$

and the non-dimensionalised incompressible momentum equation has the following form:

$$Sr \frac{\partial \vec{u}}{\partial t} + (\vec{u} \cdot \vec{\nabla}) \vec{u} = - \vec{\nabla} p + \frac{1}{Re} \nabla^2 \vec{u}. \quad (2.9)$$

In this equation we see two important non-dimensional numbers: the Strouhal number  $Sr = \frac{fL}{u_0}$  and the Reynolds number  $Re = \frac{u_0 L}{\nu}$ , where  $f$  is the frequency of the typical time-variation,  $L$  is the typical length scale,  $u_0$  is the typical velocity, and  $\nu = \frac{\eta}{\rho}$  is the kinematic viscosity. When an appropriate choice of reference quantities is made, the Strouhal number represents the importance of the unsteady inertial force relative to the convection term, and the Reynolds number represents the importance of the convection term relative to the viscous forces. When  $Sr \ll 1$  the flow may be considered quasi-steady and when  $Re \gg 1$  the flow may be considered inviscid.

Considering the definition of the Strouhal number and the Mach number we find that the Helmholtz number, introduced in equation (2.7), is related to these non-dimensional numbers by:  $He = Sr M$ . So we can identify two possible requirements for the compactness of the source region: (1), the flow in the source region is quasi-steady ( $Sr \ll 1$  and  $M = \mathcal{O}(1)$ ) or (2), the flow in the source region can be considered incompressible ( $M \ll 1$  and  $Sr = \mathcal{O}(1)$ ).

### 2.2.2 Lighthill's analogy applied to a diaphragm in a pipe

In order to understand the relation between the flow around an object in a pipe and the acoustic response we will treat the case of a diaphragm in a pipe. By rewriting the conservation equations into Lighthill's wave equation it is possible to find a formal solution of the problem in terms of the so-called Green's function. Similar to the approach used by Curle (1955), based on the free-space Green's function, we use the one-dimensional low-frequency Green's function for an infinite pipe (not the tailored Green's function) to find an equation for the acoustic response of a diaphragm in a pipe. This choice for the Green's function implies that only plane acoustic waves are assumed outside the source region. Please note that the mean flow velocity at the position of the observer is negligible.

In order to obtain Lighthill's wave equation first the time derivative of the mass conservation equation:<sup>1</sup>

$$\frac{\partial}{\partial t} \left\{ \frac{\partial \rho}{\partial t} + \frac{\partial \rho u_i}{\partial x_i} = 0 \right\}, \quad (2.10)$$

and next the divergence of the momentum equation is taken:

$$\frac{\partial}{\partial x_i} \left\{ \frac{\partial \rho u_i}{\partial t} + \frac{\partial \rho u_i u_j}{\partial x_j} = - \frac{\partial P_{ij}}{\partial x_j} \right\}, \quad (2.11)$$

<sup>1</sup>The summation convention is used. An index that appears twice means that the sum over this index is taken: e.g.  $\frac{\partial u_i}{\partial x_i}$  means  $\sum_i \frac{\partial u_i}{\partial x_i} = \frac{\partial u_1}{\partial x_1} + \frac{\partial u_2}{\partial x_2} + \frac{\partial u_3}{\partial x_3}$ .

in which  $P_{ij}$  is the pressure tensor. Then subtracting these two equations and adding on both sides the term  $-c_0^2 \frac{\partial^2 \rho'}{\partial x_i^2}$  yields the inhomogeneous wave equation for the time-dependent density perturbation  $\rho'$ :

$$\frac{\partial^2 \rho'}{\partial t^2} - c_0^2 \frac{\partial^2 \rho'}{\partial x_i^2} = \frac{\partial^2 T_{ij}}{\partial x_i \partial x_j}, \quad (2.12)$$

in which  $T_{ij} = \rho u_i u_j + P_{ij} - c_0^2 \rho' \delta_{ij}$ . This is Lighthill's wave equation and  $T_{ij}$  is the so-called Lighthill stress tensor. A formal solution of this equation can be found by using the Green's function  $G(\vec{x}, t | \vec{y}, \tau)$  or in short notation just  $G$  defined by:

$$\frac{1}{c_0^2} \frac{\partial^2 G}{\partial t^2} - \frac{\partial^2 G}{\partial y_i^2} = \delta(\vec{x} - \vec{y}) \delta(t - \tau), \quad (2.13)$$

where the pulse  $\delta(\vec{x} - \vec{y}) \delta(t - \tau)$  is released at the location  $\vec{y}$  of the source point at time  $\tau$  and  $G$  is measured at the observation point  $\vec{x}$  at time  $t$ .

Now subtracting

$$G \times \left\{ \frac{\partial^2 \rho'}{\partial y_i^2} - \frac{1}{c_0^2} \frac{\partial^2 \rho'}{\partial \tau^2} = -\frac{1}{c_0^2} \frac{\partial^2 T_{ij}}{\partial y_i \partial y_j} \right\} \quad (2.14)$$

from

$$\rho' \times \left\{ \frac{\partial^2 G}{\partial y_i^2} - \frac{1}{c_0^2} \frac{\partial^2 G}{\partial \tau^2} = -\delta(\vec{x} - \vec{y}) \delta(t - \tau) \right\} \quad (2.15)$$

and integrating over the volume  $V(\vec{y})$  enclosing all contributions to the source terms leads to the following equation for  $p'$  ( $= c_0^2 \rho'$ ):

$$\begin{aligned} p'(\vec{x}, t) &= \int_{-\infty}^t \iiint_V G(\vec{x}, t | \vec{y}, \tau) \frac{\partial^2 T_{ij}}{\partial y_i \partial y_j} dV(\vec{y}) d\tau \\ &+ \int_{-\infty}^t \iiint_V \left[ \rho'(\vec{y}, \tau) \frac{\partial^2 G}{\partial \tau^2} - G \frac{\partial^2 \rho'(\vec{y}, \tau)}{\partial \tau^2} \right] dV(\vec{y}) d\tau \\ &+ \int_{-\infty}^t \iiint_V \left[ G \frac{\partial^2 c_0^2 \rho'(\vec{y}, \tau)}{\partial y_i^2} - c_0^2 \rho'(\vec{y}, \tau) \frac{\partial^2 G}{\partial y_i^2} \right] dV(\vec{y}) d\tau, \end{aligned} \quad (2.16)$$

where  $\vec{x}$  is a point within  $V$ . The second integral is equal to zero due to the initial condition and due to causality (more information on the properties of Green's functions can be found in Morse & Feshbach (1953)). The first and the third integral are rewritten using partial integration. This results in:

$$\begin{aligned} p'(\vec{x}, t) &= \int_{-\infty}^t \iiint_V \frac{\partial^2 G(\vec{x}, t | \vec{y}, \tau)}{\partial y_i \partial y_j} T_{ij} dV(\vec{y}) d\tau \\ &- \int_{-\infty}^t \iint_{\partial V} \frac{\partial G(\vec{x}, t | \vec{y}, \tau)}{\partial y_i} [P_{ij} + \rho u_i u_j] n_j dS(\vec{y}) d\tau \end{aligned}$$

$$- \int_{-\infty}^t \iint_{\partial V} G(\vec{x}, t | \vec{y}, \tau) \frac{\partial \rho u_i}{\partial \tau} n_i dS(\vec{y}) d\tau, \quad (2.17)$$

where  $\partial V$  is the surface enclosing the volume  $V(\vec{y})$ ,  $dS$  represents the integration along the surface, and  $\vec{n}$  is the unit vector normal to  $\partial V$  directed outwards of  $V$ . In the last integral the momentum equation was used in order to arrive at this result.

Since we are interested in the acoustics in a straight pipe at low frequencies the one-dimensional low-frequency Green's function  $g(x_1, t | y_1, \tau)$  is introduced:

$$g(x_1, t | y_1, \tau) = \frac{c_0}{2} \text{H} \left( t - \tau - \frac{|x_1 - y_1|}{c_0} \right),$$

where H is the so-called Heaviside function. Inserting  $g(x_1, t | y_1, \tau)$  into equation (2.17) and using the properties<sup>2</sup> of  $g(x_1, t | y_1, \tau)$  yields:

$$\begin{aligned} S_p p'(\vec{x}, t) &= \int_{-\infty}^t \left( -\frac{\partial}{\partial x_1} \right) \iiint_V \frac{\partial g(x_1, t | y_1, \tau)}{\partial y_1} T_{11} dV(\vec{y}) d\tau \\ &- \int_{-\infty}^t \iint_{\partial V} \frac{\partial g(x_1, t | y_1, \tau)}{\partial y_1} [P_{1j} + \rho u_1 u_j] n_j dS(\vec{y}) d\tau \\ &- \int_{-\infty}^t \iint_{\partial V} g(x_1, t | y_1, \tau) \frac{\partial \rho u_i}{\partial \tau} n_i dS(\vec{y}) d\tau, \end{aligned} \quad (2.18)$$

where  $S_p$  is the cross-sectional area of the pipe which appears due to the definition of  $g(x_1, t | y_1, \tau)$ . The third integral is rewritten by partial integration relative to  $\tau$  so:

$$- \int_{-\infty}^t \iint_{\partial V} g(x_1, t | y_1, \tau) \frac{\partial \rho u_i}{\partial \tau} n_i dS(\vec{y}) d\tau = I_1 + I_2,$$

where

$$I_1 = - \left[ \iint_{\partial V} g(x_1, t | y_1, \tau) \rho u_i n_i dS(\vec{y}) \right]_{-\infty}^{\tau=t} = 0$$

due to causality, and

$$\begin{aligned} I_2 &= \int_{-\infty}^t \iint_{\partial V} \rho u_i \frac{\partial g(x_1, t | y_1, \tau)}{\partial \tau} n_i dS(\vec{y}) d\tau \\ &= -\frac{c_0}{2} \iint_{\partial V} [\rho u_i]_{t^*} n_i dS(\vec{y}) \end{aligned}$$

<sup>2</sup> $g(x_1, t | y_1, \tau)$  has the following properties:  $\frac{\partial g}{\partial x_1} = -\frac{\partial g}{\partial y_1}$ , and  $\frac{\partial g}{\partial t} = -\frac{\partial g}{\partial \tau}$ . The derivatives of  $g(x_1, t | y_1, \tau)$  are defined by  $\frac{\partial g}{\partial y_1} = \frac{1}{2} \text{sign}(x_1 - y_1) \delta(t^* - \tau)$  and  $\frac{\partial g}{\partial \tau} = -\frac{c_0}{2} \delta(t^* - \tau)$  using the retarded time  $t^* = t - \frac{|x_1 - y_1|}{c_0}$ .

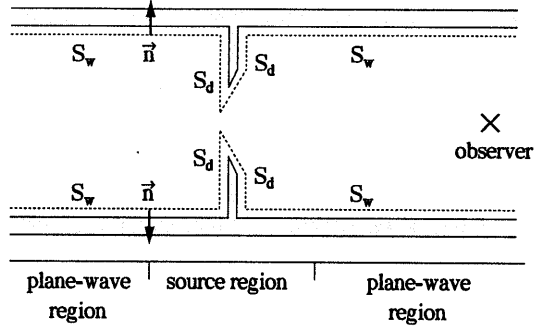


Figure 2.1: Definition of surface integral in the case of a diaphragm in a straight pipe. The integration surface consist of two parts: the top and bottom wall  $S_w$  and the diaphragm  $S_d$ .

in which  $t^*$  is the retarded time:  $t^* = t - \frac{|x_1 - y_1|}{c_0}$ . Upon inserting Green's function into equation (2.18) we finally obtain the following expression for the pressure fluctuation:

$$\begin{aligned}
 S_p p'(\vec{x}, t) &= -\frac{1}{2} \frac{\partial}{\partial x_1} \iiint_V [T_{11}]_{t^*} \text{sign}(x_1 - y_1) dV(\vec{y}) \\
 &- \frac{1}{2} \iint_{\partial V} [P_{1j} + \rho u_1 u_j]_{t^*} \text{sign}(x_1 - y_1) n_j dS(\vec{y}) \\
 &- \frac{c_0}{2} \iint_{\partial V} [\rho u_i]_{t^*} n_i dS(\vec{y}). \tag{2.19}
 \end{aligned}$$

In the application to the case of the diaphragm in a pipe the control volume is defined as shown in figure 2.1. It is important to note that the control volume consists of the whole pipe of infinite length, that the normal vector at the walls is directed outwards, and that the observer is inside the control volume. The volume is divided into three regions: one region far left and one region far right of the diaphragm, where only planar waves are assumed, and the source region around the diaphragm. The observer is inside one of the plane-wave regions so that the following applies:  $\frac{\partial}{\partial x_1} = -\frac{1}{c_0} \text{sign}(x_1 - y_1) \frac{\partial}{\partial t}$ . Since at the walls the normal component of the velocity is equal to zero, equation (2.19) reduces to:

$$\begin{aligned}
 p'(\vec{x}, t) &= \frac{1}{2c_0 S_p} \frac{\partial}{\partial t} \iiint_V [\rho u_1^2 + p - c_0^2 \rho']_{t^*} dV(\vec{y}) \\
 &- \frac{1}{2S_p} \iint_{\partial V} [P_{1j}]_{t^*} \text{sign}(x_1 - y_1) n_j dS(\vec{y}). \tag{2.20}
 \end{aligned}$$

When viscous forces are neglected (inviscid-flow description) the pressure tensor is equal to  $p\delta_{ij}$  so that  $P_{1j}n_j = pn_1$  and the contributions to the surface integral due to the top



and bottom wall vanish (because  $n_1 = 0$ ). Finally this leads to the following equation for the pressure fluctuation:

$$p'(\vec{x}, t) = \frac{1}{2c_0 S_p} \frac{\partial}{\partial t} \iiint_V [\rho u_1^2 + p - c_0^2 \rho']_{t^*} dV(\vec{y}) - \frac{1}{2S_p} \iint_{S_d} [p]_{t^*} \text{sign}(x_1 - y_1) n_1 dS(\vec{y}), \quad (2.21)$$

where  $S_d$  is the surface area of the walls of the diaphragm. Note that in case of a purely acoustic flow the volume integral vanishes while the contribution to the surface integral is induced by the particular choice of a stagnant fluid in a pipe of constant cross-sectional area as reference state for the analogy. The volume integral is estimated to be of order  $He$  relative to the surface integral, and is therefore negligible for low Helmholtz numbers. In that case the acoustic pressure perturbation is due to the pressure difference across the diaphragm. Note that this result applies only to flows where the convective effects are neglected ( $M \ll 1$ ) outside the source region. In that case the contribution to this integral in the plane-wave regions is of second order in the perturbations and therefore neglected in the linear acoustic approximation. When convective effects in the main pipe are to be taken into account the following changes have to be made: the wave equation has to be converted to the convected-wave equation and consequently the source term changes, and also the Green's function has to be converted to a form that takes convective effects into account. Another possible approach to take into account convective effects is suggested by the treatment of Ffowcs Williams and Hawkings for moving rigid bodies (Ffowcs-Williams & Hawkings 1969, Goldstein 1976). In Crighton *et al.* (1992), this approach and several methods to solve the convected wave equation are discussed.

### 2.2.3 Howe's energy formulation

In the preceding paragraph we used Lighthill's analogy to determine the acoustic source due to the flow through a diaphragm in a pipe. We found that the time-dependent pressure drop across the diaphragm is radiated as an acoustic pressure perturbation. For some problems it is however more convenient to reformulate the acoustic source. In this thesis we will use a numerical method based on vortex dynamics (vortex-blob method). In that case it is convenient to express the sound production in terms of the evolution of the vorticity field. Howe (1975, 1980, 1984) derived an analogy that relates the vorticity distribution  $\vec{\omega} = \vec{\nabla} \times \vec{u}$  in a compact source region to the acoustic energy production. The rate of production of acoustic energy, according to Howe's analogy, is given by:

$$\mathcal{P}(t) = - \iiint_V \rho_0 (\vec{\omega} \times \vec{u}) \cdot \vec{u}' dV, \quad (2.22)$$

in which  $\rho_0$  is the constant density and  $\vec{u}'$  is the acoustic velocity field defined as the time-dependent irrotational part of the total velocity field:  $\vec{u}' = \vec{\nabla} \phi'$ . In order to understand

the range of validity of this analogy and to show that  $\mathcal{P}(t)$  is indeed the rate of acoustic energy production we will derive Howe's formulation.

For an inviscid flow without external forces acting on the flow Crocco's equation reads:

$$\frac{\partial \vec{u}}{\partial t} + \vec{\nabla} B = -(\vec{\omega} \times \vec{u}) + T \vec{\nabla} S. \quad (2.23)$$

Upon introducing the total enthalpy perturbation  $B' = B - B_0$ , in which the subscript 0 indicates the solution of the potential flow without vorticity, i.e.:

$$\frac{\partial \vec{u}_0}{\partial t} + \vec{\nabla} B_0 = 0. \quad (2.24)$$

The two equations (2.23) and (2.24) are subtracted, thus yielding the following equation for the perturbation  $B'$ :

$$\frac{\partial}{\partial t}(\vec{u} - \vec{u}_0) + \vec{\nabla} B' = -(\vec{\omega} \times \vec{u}) + T \vec{\nabla} S. \quad (2.25)$$

In order to find the acoustic power that is generated the inner product of this equation is taken with the acoustic velocity field  $\vec{u}'$  and subsequently the equation is integrated over the control volume  $V$ , thus yielding:

$$\iiint_V \frac{\partial}{\partial t}(\vec{u} - \vec{u}_0) \cdot \vec{u}' dV + \iiint_V \vec{\nabla} B' \cdot \vec{u}' dV = - \iiint_V (\vec{\omega} \times \vec{u}) \cdot \vec{u}' dV + \iiint_V T \vec{\nabla} S \cdot \vec{u}' dV. \quad (2.26)$$

Using the vector identity  $(\vec{\nabla} f) \cdot \vec{g} = \vec{\nabla} \cdot (f\vec{g}) - f \vec{\nabla} \cdot \vec{g}$  and the definition of the acoustic field as being the gradient of a scalar potential:  $\vec{u}' = \vec{\nabla} \phi'$ , the first term on the left-hand side of equation (2.26) upon partial integration results in:

$$\begin{aligned} \iiint_V \frac{\partial}{\partial t}(\vec{u} - \vec{u}_0) \cdot \vec{\nabla} \phi' dV &= \iint_{\partial V} \phi' \frac{\partial}{\partial t}(\vec{u} - \vec{u}_0) \cdot \vec{n} dS \\ &- \iiint_V \phi' \vec{\nabla} \cdot \left( \frac{\partial}{\partial t}(\vec{u} - \vec{u}_0) \right) dV, \end{aligned} \quad (2.27)$$

where  $\vec{n}$  is the outward pointing normal on the boundary  $\partial V$  of the control volume  $V$ . Similarly the second term on the left-hand side of equation (2.26) is rewritten as:

$$\iiint_V \vec{\nabla} B' \cdot \vec{u}' dV = \iint_{\partial V} B' \vec{u}' \cdot \vec{n} dS - \iiint_V B' \vec{\nabla} \cdot \vec{u}' dV. \quad (2.28)$$

In some special cases additional assumptions about these integrals can be made. We choose the boundaries of the integration domain such that  $(\vec{u} - \vec{u}_0) \cdot \vec{n} = 0$  on the boundary. In that case the first term on the right-hand side of (2.27) is equal to zero. When only compact source regions are considered we have  $\vec{\nabla} \cdot \vec{u}' = 0$  which makes the second term

on the right-hand side of equation (2.28) equal to zero. Neglecting either unsteady effects or compressibility in the source region results in  $\vec{\nabla} \cdot (\vec{u} - \vec{u}_0) = 0$ . Interchanging the differentiation with respect to time and space, also makes the second term on the right-hand side of equation (2.27) equal to zero. Finally, only considering homentropic flows ( $\vec{\nabla} S = 0$ ) we find the following identity:

$$\iint_{\partial V} B' \vec{u}' \cdot \vec{n} dS = - \iiint_V (\vec{\omega} \times \vec{u}) \cdot \vec{u}' dV. \quad (2.29)$$

The left-hand side of the equation is related to the net outflow out of  $V$  of acoustic energy per unit time if the acoustic power flux is identified as  $\rho_0 B' \vec{u}'$ . Such a definition is reasonable for a compact flow region at low Mach numbers. Therefore the right-hand side represents a source of acoustic energy. For low-Mach-number flows this can be further approximated by:

$$\iint_{\partial V} p' \vec{u}' \cdot \vec{n} dS = -\rho_0 \iiint_V (\vec{\omega} \times \vec{u}) \cdot \vec{u}' dV. \quad (2.30)$$

Note that in Howe's analogy the reference state is the potential-flow solution of the flow as opposed to the uniform stagnant fluid used as a reference state in Lighthill's analogy. Conform Howe's analogy it is plausible to define an acoustic source pressure  $\Delta p_{source}$  in terms of the difference  $p - p_{pot}$  of the actual pressure and the pressure  $p_{pot}$  of the potential flow solution between the acoustic outflow boundary and the acoustic inflow boundary:  $\Delta p_{source} = \Delta p - \Delta p_{pot}$ . The acoustic source pressure is defined as the jump in the acoustic pressure  $p'$  from the inflow to the outflow boundary:

$$\iint_{\partial V} p' \vec{u}' \cdot \vec{n} dS = \iint_{\partial V} \Delta p_{source} \vec{u}' \cdot \vec{n} dS. \quad (2.31)$$

We will show that equations (2.30) and (2.31) implemented in a numerical method yield results that are in agreement.

## 2.3 Integral representation for the pressure

### 2.3.1 Introduction

Up to this point we discussed the problem of sound generation in a general way. In the next sections we focus on the source region of the flow domain, specifically we focus on source regions that can be considered two-dimensional and incompressible.

We present a natural way of computing the pressure field for an incompressible flow starting from a known vorticity distribution and boundary conditions. The adoption of an integral representation leads to a more accurate evaluation of the solution than a direct numerical integration along the boundary of the tangential projection of the momentum equation (Navier-Stokes or Euler, according to the nature of the flow). Moreover, the

deduction we will present can suggest a quite straightforward application to acoustic problems. In appendix A Lighthill's analogy is formulated in such a way that the result of the next paragraph can be compared to Lighthill's analogy and the range of validity of our approach can be judged.

In the framework of vortex methods for incompressible flows (either viscous or not) it is common to ignore the pressure field for two main reasons. Firstly, to solve the momentum equations written in terms of vorticity, knowledge of the pressure distribution is not needed, since  $p$  and  $\omega$  are decoupled variables. The vorticity does not depend directly on the pressure, meanwhile  $p$  is explicitly determined by the dynamics of  $\omega$ . Secondly, the total load acting on a surface (both for internal or external flow problems) can easily be obtained in terms of the time variation of the vortex impulse (Saffman 1992).

An accurate solution of the momentum equations may provide the tool for a deeper analysis of the physical phenomena that determine the evolution of the flow. However, we can claim the validity of the solution obtained by a numerical computation only by a close comparison with experimental results. In our opinion a 'close' comparison cannot be obtained by only looking at the 'topology' of the flow or at global averaged quantities as, for instance, the loading or the total acoustic power produced by the unsteadiness of the flow. The flow visualisations in experiments are usually obtained by following suspended particle paths and are not able to give a clear answer to the possibly significant differences between the physics and the results of the numerical method. On the other hand the knowledge of the pressure field can easily lead to a quantitative comparison with experimental results and permits the comprehension of the validity of the model adopted (laminar, two-dimensional flow). This is partially due to the fact that quantitative wall-pressure measurements are easier to obtain than quantitative flow velocity data.

In the following we will report in detail on the analytical derivation of the pressure field for an incompressible two-dimensional flow, together with some physical consideration related to the final form obtained.

### 2.3.2 The pressure field for a two-dimensional incompressible flow

The dynamics of incompressible flows are governed by the conservation of mass and the conservation of momentum. Sometimes it is convenient to scale these equations. In the following we do so by choosing a reference length  $L_{ref}$  and a reference velocity  $U_{ref}$ . Then in primitive variables, the non-dimensionalised equations are in two dimensions:

$$\begin{aligned} \vec{\nabla} \cdot \vec{u} &= 0, \\ \vec{\nabla} \left( p + \frac{|\vec{u}|^2}{2} \right) &= -\frac{\partial \vec{u}}{\partial t} - \omega \vec{u}^\perp + \frac{1}{Re} \vec{\nabla}^\perp \omega, \end{aligned} \quad (2.32)$$

in which  $\omega$  is the vorticity,  $\vec{u}^\perp = (-u_2, u_1)$  is the velocity vector rotated over  $90^\circ$ , and  $\vec{\nabla}^\perp = \left( -\frac{\partial}{\partial x_2}, \frac{\partial}{\partial x_1} \right)$  is the gradient operator rotated over  $90^\circ$ . In a two-dimensional flow the only non-zero component of the vorticity is directed along the third dimension hence  $\vec{\omega} = (0, 0, \omega)$ .

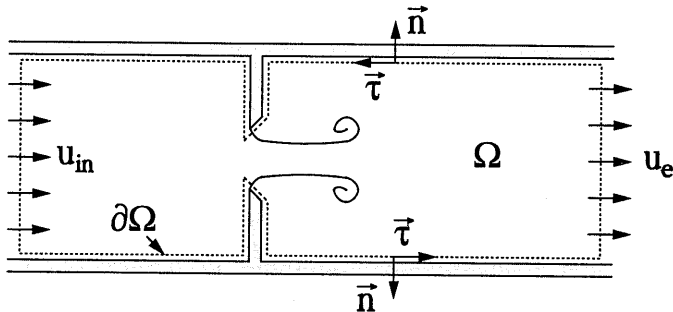


Figure 2.2: Definition of the integration domain and the unit vectors in the case of a diaphragm in a straight pipe.

Note that the density  $\rho$  drops out due to the scaling of the equation, nevertheless it is present in the scaling of the pressure with  $\rho U_{ref}^2$ .

The boundary conditions are the no-slip velocity on solid walls and an imposed uniform inlet velocity profile. Therefore

$$\vec{u} = (0, 0)$$

on solid walls and

$$u_n = -u_{in}(t), u_\tau = 0$$

at the inlet section. Here  $u_n$  and  $u_\tau$  represent the normal projection and the tangential projection of the velocity vector with respect to the wall, respectively. Note that the unit normal vector  $\vec{n}$  is directed outwards and because  $u_{in}$  is the inflow velocity, the minus sign on the right-hand side appears. Moreover, the computational domain consists also of a far outlet section for which

$$u_n = u_e(t), u_\tau = 0,$$

where  $u_e(t)$  is the uniform exit velocity that is evaluated applying the conservation of mass. This is strictly only true if the outlet section is really at infinity. Nevertheless the asymptotic behaviour of the perturbation velocity is a dipole-like one, hence the dependency of the solution on this approximation may be easily relaxed choosing a boundary sufficiently far downstream. The unit tangential vector  $\vec{\tau}$  along the boundary is defined in an anti-clockwise direction (leaving the fluid domain on the left), while the normal one is directed outwards of the domain, so that:  $\vec{n}^\perp = \vec{\tau}$  as is shown in figure 2.2.

If we apply the divergence operator to the equation (2.32) we obtain a Poisson differential equation for the non-dimensionalised total pressure  $P = p + |u|^2/2$ :

$$\nabla^2 P = -\vec{\nabla} \cdot (\omega \vec{u}^\perp). \quad (2.33)$$

The boundary conditions for  $P$  have to be chosen according to those for the velocity field. This means that the dynamic boundary condition for  $P$  is provided by the normal

projection of the Navier-Stokes equations:

$$\vec{n} \cdot \vec{\nabla} P = -\frac{\partial u_n}{\partial t} - \omega u_\tau + \frac{1}{Re} \vec{\tau} \cdot \vec{\nabla} \omega.$$

Therefore  $P$  appears to be the solution of an inner Neumann problem, which admits a non-unique solution. This is consistent with the physical definition of the pressure and so  $P$  will be correctly found subtracting a particular solution independent of the boundary conditions ( $P = \text{constant}$ ).

A straightforward application of Green's second identity provides an integral representation for the total pressure:

$$\begin{aligned} c(\vec{x})P(\vec{x}) &= -\iint_{\Omega} \vec{\nabla}_y \cdot (\omega \vec{u}^\perp) G(\vec{x} - \vec{y}) d\Omega(\vec{y}) + \\ &\quad - \int_{\partial\Omega} P(\vec{y}) \vec{\tau} \cdot \vec{K}(\vec{x} - \vec{y}) ds(\vec{y}) \\ &\quad - \int_{\partial\Omega} \frac{\partial P(\vec{y})}{\partial n} G(\vec{x} - \vec{y}) ds(\vec{y}), \end{aligned}$$

where  $\vec{y}$  is the integration variable,  $\Omega$  is the two-dimensional control area,  $\partial\Omega$  is the closed curve enclosing the control area, and  $ds$  denotes integrating along the curve  $\partial\Omega$ . The coefficient  $c(\vec{x})$  is equal to 1/2 or 1 as the point  $\vec{x}$  is on the fluid side of the boundary or in the fluid domain, respectively;  $G(\vec{x} - \vec{y})$  is the free space Green's function for the Laplace problem, given by:

$$G(\vec{x}) = \frac{1}{2\pi} \log |\vec{x}|, \quad \vec{x} \in R^2,$$

and  $\vec{K}(\vec{x} - \vec{y}) = -\vec{\nabla}_y^\perp G(\vec{x} - \vec{y})$  is the Biot-Savart kernel:

$$\vec{K}(\vec{x}) = \frac{1}{2\pi} \frac{\vec{x}^\perp}{|\vec{x}|^2}, \quad \vec{x}^\perp = (-x_2, x_1).$$

Integrating the previous expression by parts and taking into account the boundary condition we find:

$$\begin{aligned} c(\vec{x})P(\vec{x}) &= \iint_{\Omega} \omega \vec{u} \cdot \vec{K}(\vec{x} - \vec{y}) d\Omega(\vec{y}) + \int_{\partial\Omega} \omega u_\tau G(\vec{x} - \vec{y}) ds(\vec{y}) \\ &\quad - \int_{\partial\Omega} P(\vec{y}) \vec{\tau} \cdot \vec{K}(\vec{x} - \vec{y}) ds(\vec{y}) + \int_{\partial\Omega} \frac{\partial u_n}{\partial t} G(\vec{x} - \vec{y}) ds(\vec{y}) \\ &\quad - \int_{\partial\Omega} \omega u_\tau G(\vec{x} - \vec{y}) ds(\vec{y}) + \int_{\partial\Omega} \frac{1}{Re} \frac{\partial \omega}{\partial s} G(\vec{x} - \vec{y}) ds(\vec{y}). \end{aligned}$$

Moreover, we can consider, for  $\vec{y} \in \partial\Omega$ , the following identity :

$$G(\vec{x} - \vec{y}) \frac{\partial \omega}{\partial s} = \frac{\partial}{\partial s} [G(\vec{x} - \vec{y})\omega] - \omega \vec{n} \cdot \vec{K}(\vec{x} - \vec{y}).$$

The contour  $\partial\Omega$  is a closed curve and the functions  $G(\vec{x} - \vec{y})$  and  $\omega$  are single-valued on it, hence the integral of the first term on the right-hand side will drop out. The solution of the problem (2.33) is then expressed in terms of an integral representation, valid for  $\vec{x} \in \partial\Omega$  or  $\vec{x} \in \Omega$ :

$$\begin{aligned}
c(\vec{x})P(\vec{x}) &= \iint_{\Omega} \omega \vec{u} \cdot \vec{K}(\vec{x} - \vec{y}) d\Omega(\vec{y}) \\
&- \int_{\partial\Omega} P(\vec{y}) \vec{\tau} \cdot \vec{K}(\vec{x} - \vec{y}) ds(\vec{y}) \\
&+ \int_{\partial\Omega} \frac{\partial u_n}{\partial t} G(\vec{x} - \vec{y}) ds(\vec{y}) \\
&- \int_{\partial\Omega} \frac{1}{Re} \omega \vec{n} \cdot \vec{K}(\vec{x} - \vec{y}) ds(\vec{y}). \tag{2.34}
\end{aligned}$$

As mentioned before, for  $\vec{x} \in \partial\Omega$  the constant  $c(\vec{x})$  is equal to 1/2 and the relation (2.34) gives rise to the following boundary-integral equation of the second kind:

$$\begin{aligned}
\frac{1}{2}P(\vec{x}) + \int_{\partial\Omega} P(\vec{y}) \vec{\tau} \cdot \vec{K}(\vec{x} - \vec{y}) ds(\vec{y}) &= \iint_{\Omega} \omega \vec{u} \cdot \vec{K}(\vec{x} - \vec{y}) d\Omega(\vec{y}) \\
&+ \int_{\partial\Omega} \frac{\partial u_n}{\partial t} G(\vec{x} - \vec{y}) ds(\vec{y}) \\
&- \int_{\partial\Omega} \frac{1}{Re} \omega \vec{n} \cdot \vec{K}(\vec{x} - \vec{y}) ds(\vec{y}). \tag{2.35}
\end{aligned}$$

As a result of the adoption of a Neumann boundary condition, only the pressure distribution is unknown, which is obtained by imposing in a discretised fashion the integral equation at a number of collocation points. The boundary of the geometry  $\partial\Omega$  is approximated by straight elements (panels) carrying a panel-wise uniform distribution of  $P$  (for a first-order scheme).

We want to point out that the discretised form of (2.35) leads to an algebraic system of linear equations. The square matrix of coefficients is singular, with one eigenvalue equal to zero (i.e. its rank is equal to  $N - 1$ ). Therefore the solution of (2.35) should be obtained by applying a Singular-Value-Decomposition (SVD) technique for the inversion of the matrix, and then selecting the solution by subtracting the reference far-field value of the total pressure  $P_{\infty}$ : the numerical technique needed for solving (2.35) reflects exactly the non-uniqueness property of the pressure field. However, we found that the problem can be transformed to a non-singular one simply by replacing the equation at one of the collocation points with the condition  $P = P_{ref}$  at some point on the boundary. This technique leads to a solution consistent and equal to that obtained with an SVD procedure, with the main advantage of a simpler and faster algorithm based on an LU decomposition of the coefficients matrix.

Looking at the right-hand side of the equation (2.35) we can observe the interaction of some physical mechanisms in determining the actual value of the total-pressure field  $P$ . Firstly we have to recall that in the case of a Navier-Stokes solution for a fixed geometry the total pressure is equal to the pressure for  $\vec{x}$  belonging to the solid walls  $\partial\Omega$ . Moreover, by using the definition of the stress at the boundary:

$$\vec{t}_b(\vec{x}) = -p(\vec{x}) \vec{n} + \frac{1}{Re} \omega(\vec{x}) \vec{\tau},$$

we can rewrite the equation (2.35):

$$\begin{aligned} \frac{1}{2}P(\vec{x}) &= \iint_{\Omega} \omega \vec{u} \cdot \vec{K}(\vec{x} - \vec{y}) d\Omega(\vec{y}) + \int_{\partial\Omega} \frac{\partial u_n}{\partial t} G(\vec{x} - \vec{y}) ds(\vec{y}) \\ &+ \int_{\partial\Omega} \vec{t}_b^{\perp}(\vec{y}) \cdot \vec{K}(\vec{x} - \vec{y}) ds(\vec{y}) - \int_{\partial\Omega} \frac{1}{2} |\vec{u}|^2 \vec{\tau} \cdot \vec{K}(\vec{x} - \vec{y}) ds(\vec{y}). \end{aligned}$$

Note that the last integral only has contributions due to the inflow and outflow domain of the boundary because the velocity is zero at the walls. We make three remarks on this last relation:

(1), the inner product  $\vec{t}_b^{\perp}(\vec{y}) \cdot \vec{K}(\vec{x} - \vec{y})$  is also equal to  $-\vec{t}_b(\vec{y}) \cdot \vec{K}^{\perp}(\vec{x} - \vec{y})$ , hence the stress at the boundary  $\vec{t}_b(\vec{y})$  at the point  $\vec{y} \in \partial\Omega$  affects the pressure field at another point  $\vec{x}$  on the wall only by its components parallel to the direction of  $\vec{x} - \vec{y}$ .

(2), since  $\vec{u} \cdot \vec{K}(\vec{x} - \vec{y}) = \vec{u}^{\perp} \cdot \vec{K}^{\perp}(\vec{x} - \vec{y})$  we see that the Coriolis force  $\rho_0(-\vec{u}^{\perp}\omega)$  influences  $p(\vec{x})$  by its component parallel to the direction of  $\vec{x} - \vec{y}$ .

(3), the inertial effects due to the unsteadiness of the inflow velocity are taken into account by the source-like term, the strength of which is given by the time derivative of the inflow and/or outflow velocity.

## 2.4 Numerical methods

### 2.4.1 Vorticity-transport equation

In the previous sections we have assumed that for some aeroacoustic problems it is possible to separate the flow domain into a region of wave propagation and an acoustic source region. When the source region is small in size relative to the wavelength of the acoustic perturbation ( $He \ll 1$ ) the source region is considered compact. There are two reasons for the source region to be compact, i.e. (1) the local flow in the source region can be considered quasi-steady or (2) the local flow in the source region can be considered incompressible. In the first case the acoustic source can be described by a quasi-steady model even taking compressibility effects into account. In the second case the unsteady incompressible-flow equations have to be solved. It is usually necessary to solve these equations numerically.

For low-Mach-number isentropic flows unsteady vorticity is the main source of sound. Therefore we restrict ourselves to solving the flow in the source region accurately describing



the development of the vorticity field in the incompressible-flow limit. Furthermore, we only consider source regions for which a two-dimensional description is reasonable.

We chose to solve the vorticity-transport equation numerically, as opposed to solving the Navier-Stokes equations for the primitive variable  $\vec{u}$ . The velocity field is then obtained from the distribution of vorticity and also the pressure field is then available through the integral formulation of the previous paragraph. By solving the vorticity-transport equation the computational effort can be focused on the regions of the domain where vorticity is present. At high Reynolds numbers vorticity is restricted to boundary layers next to the walls and thin shear layers as a result of flow separation.

The dynamics of incompressible two-dimensional flows are governed by the conservation of mass and momentum, i.e. in non-dimensional form:

$$\begin{aligned} \vec{\nabla} \cdot \vec{u} &= 0, \\ \frac{\partial \vec{u}}{\partial t} - \omega \vec{u}^\perp &= -\vec{\nabla} \left( p + \frac{|u|^2}{2} \right) + \frac{1}{Re} \vec{\nabla}^\perp \omega. \end{aligned} \quad (2.36)$$

In a similar way as the pressure equation (2.33) was derived the vorticity-transport equation is derived by taking the curl of the momentum equation (2.36):

$$\frac{\partial \omega}{\partial t} + \vec{u} \cdot \vec{\nabla} \omega = \frac{1}{Re} \nabla^2 \omega. \quad (2.37)$$

In this equation we recognise the two processes that change the vorticity distribution. The first process is the inviscid advection of vorticity described by the advection equation:

$$\frac{D\omega}{Dt} = 0, \quad (2.38)$$

in which  $\frac{D}{Dt}$  is the material derivative defined as:  $\frac{D}{Dt} = \frac{\partial}{\partial t} + \vec{u} \cdot \vec{\nabla}$ . The second process is the diffusion of vorticity described by the heat-transfer equation:

$$\frac{\partial \omega}{\partial t} = \frac{1}{Re} \nabla^2 \omega. \quad (2.39)$$

That these processes can occur on very different time scales suggests an approach for solving these equations with the appropriate boundary conditions. In the next section we will first treat a numerical method to solve the inviscid-flow equation (2.38): the inviscid vortex-blob method. This is the limit of very large Reynolds number ( $Re \rightarrow \infty$ ). Subsequently, a numerical method is described to solve the complete equation (2.37): the viscous vortex-blob method.

#### 2.4.2 Vortex-blob method for inviscid flow

At high Reynolds number the process of diffusion has only a small effect on the evolution of distributed vorticity. In that case the transport of vorticity is governed by the advection

equation (2.38). In this section we present a numerical method to solve the vorticity-transport equation while neglecting diffusion (see also Peters (1993)). In the subsequent part of this thesis the method is referred to as “the inviscid vortex-blob” method (or sometimes simply “the vortex-blob method”).

When considering the transport of vorticity in a fixed two-dimensional domain  $\Omega$  enclosed by a contour  $\partial\Omega$  the velocity field is given by:

$$\vec{u}(\vec{x}, t) = \int_{\partial\Omega} u_n \vec{K}^\perp(\vec{x} - \vec{y}) ds(\vec{y}) - \int_{\partial\Omega} u_\tau \vec{K}(\vec{x} - \vec{y}) ds(\vec{y}) + \iint_{\Omega} \omega \vec{K}(\vec{x} - \vec{y}) d\Omega(\vec{y}), \quad (2.40)$$

where  $\vec{K}(\vec{x})$  is the Biot-Savart kernel:

$$\vec{K}(\vec{x}) = \frac{1}{2\pi} \frac{\vec{x}^\perp}{|\vec{x}|^2}, \quad \vec{x}^\perp = (-x_2, x_1).$$

The unit tangential vector  $\vec{\tau}$  along the boundary is defined in an anti-clockwise direction (with the fluid domain on the left) orthogonal to the unit normal vector that is directed outwards:  $\vec{\tau} = \vec{n}^\perp$  (see figure 2.2). The velocity field has to satisfy only one boundary condition on the solid walls in the domain:  $u_n = 0$ . On the inflow section of the domain the uniform inflow velocity  $u_{in}$  is prescribed:  $u_n = -u_{in}(t)$ . On the outflow section of the domain the uniform outflow velocity  $u_n$  follows through mass conservation from the inflow velocity.

The vorticity field  $\omega$  is approximated as a set of point vortices:

$$\omega(\vec{x}, t) = \sum_{j=1}^N \Gamma_j \delta(\vec{x} - \vec{x}_j),$$

in which  $\Gamma_j$  is the constant circulation of the  $j^{\text{th}}$  point vortex at position  $\vec{x}_j$  and  $\delta(\vec{x} - \vec{x}_j)$  is the Dirac delta function. The positions of the individual vortices change in time according to

$$\frac{d\vec{x}_j}{dt} = \vec{u}(\vec{x}_j, t). \quad (2.41)$$

In the absence of solid walls in the flow domain the velocity is completely determined by the vorticity distribution. This leads to the following result for the velocity field:

$$\vec{u}(\vec{x}, t) = \sum_{j=1}^N \vec{K}(\vec{x} - \vec{x}_j) \Gamma_j. \quad (2.42)$$

When  $\vec{x} = \vec{x}_j$  the above relation gives a singular value for the velocity at the  $j^{\text{th}}$  vortex: It has been shown that ignoring this contribution leads to a correct approximation of the continuous velocity field, see (Anderson & Greengard 1985), i.e. each vortex has to move as if convected by the net velocity field of all the other vortices. Moreover, the numerical evaluation of the convolution (2.42) can be affected by large inaccuracies as  $\vec{x} \rightarrow \vec{x}_j$ . Two vortices can be so close that their mutual interaction is diverging as  $1/r$ . This causes the

development of a singularity in the solution at finite time, the effect of which can only be removed by solving the system (2.41) with an arbitrarily small time step.

In the literature several approaches have been made to regularise the solution. Chorin & Bernard (1973) suggested the adoption of a regular vorticity field, with finite-core vortices (blobs) instead of the Dirac delta function. The convolution with the singular Biot-Savart kernel produces a new modified kernel for the velocity representation (2.42). A better approximation of the solution is obtained even if the dynamics of these vortices is only approximately a solution of the original equations. In fact the vorticity distribution of each blob, and therefore its shape, is fixed in time ignoring the action of the local strain field on the vorticity field.

Beale & Majda (1985) proved the accuracy, the linear stability and the convergence of this model for the solution of the original equations. They proposed the following desingularised kernel:

$$\vec{K}_\delta(\vec{x}) = \vec{K}(\vec{x}) \left(1 - \exp(-|\vec{x}|^2/\delta^2)\right). \quad (2.43)$$

In this equation  $\delta$  is the so-called desingularisation parameter. The contribution to the vorticity distribution of the  $j^{\text{th}}$  vortex associated with this vortex blob is

$$\omega_j(\vec{x}) = \frac{\Gamma_j}{2\pi} \frac{2}{\delta^2} \exp(-|\vec{x} - \vec{x}_j|^2/\delta^2), \quad (2.44)$$

which is a Gaussian distribution. An alternative kernel was proposed by Krasny (1986a, 1986b, 1987):

$$\vec{K}_\delta(\vec{x}) = \vec{K}(\vec{x}) \cdot \frac{|\vec{x}|^2}{|\vec{x}|^2 + \delta^2}. \quad (2.45)$$

The vorticity distribution associated with this kernel is

$$\omega_j(\vec{x}) = \frac{\Gamma_j}{2\pi} \cdot \frac{2\delta^2}{(|\vec{x} - \vec{x}_j|^2 + \delta^2)^2}. \quad (2.46)$$

The value of  $\delta$  in equations (2.43) and (2.45) determines the level of desingularisation. Although these desingularisation kernels are significantly different, it has been shown that the influence of the exact form of the kernels on the numerical result is much less important than the value of  $\delta$ : comparable values of  $\delta$  with different forms of the desingularisation kernel lead to very similar results for the kind of problems we are interested in, as shown by Hofmans *et al.* (1995). However, note that both equations (2.44) and (2.46) indicate that the vorticity distribution is not localised to the immediate neighbourhood of  $\vec{x} = \vec{x}_j$  but rather spreads out to infinity.

In the presence of solid boundaries the tangential velocity along the boundaries of the domain is obtained from the projection of equation (2.40) along the local tangent, i.e. for a point  $\vec{x}$  on  $\partial\Omega$ :

$$\begin{aligned} \frac{1}{2} u_\tau(\vec{x}) + \int_{\partial\Omega} u_\tau(\vec{y}) \vec{K}(\vec{x} - \vec{y}) \cdot \vec{\tau}(\vec{x}) ds(\vec{y}) &= \int_{\partial\Omega} u_n(\vec{x}) \vec{K}^\perp(\vec{x} - \vec{y}) \cdot \vec{\tau}(\vec{x}) ds(\vec{y}) \\ &+ \iint_{\Omega} \omega(\vec{y}) \vec{K}(\vec{x} - \vec{y}) \cdot \vec{\tau}(\vec{x}) d\Omega(\vec{y}). \end{aligned} \quad (2.47)$$

Associated with the tangential velocity at the boundary is a circulation density  $\gamma$  on the boundary. It is given by the jump of the tangential velocity from the value given by (2.47) to a prescribed value just outside the computational domain.

The closed boundary of the computational domain is discretised by a set of  $N_p$  straight panels, each having a uniform source density  $q$  and circulation density  $\gamma$ . Across such a panel the normal and the tangential component of the velocity jump by an amount of  $q$  and  $\gamma$ , respectively. In case we choose the velocity outside the fluid domain to be zero, the boundary condition of zero normal velocity at solid walls requires a zero source strength, while at the parts of the boundary where there is an in- or outflow the source strength is specified equal to the in- or outflow. The Dirichlet condition (velocity potential is specified) is used on the boundary to determine the circulation density on each panel. It is implemented by imposing a zero tangential velocity on the non-fluid side of the boundary, i.e. in discretised form at each panel midpoint. The discretised equation representing the Dirichlet boundary condition has the following form:

$$\frac{1}{2}\gamma_j + \sum_{k=1, k \neq j}^{N_p} \gamma_k K_\gamma(j, k) + \sum_{k=1, k \neq j}^{N_p} q_k K_q(j, k) + \sum_{k=1}^N \Gamma_k K_\Gamma(j, k) = 0, \quad \text{for } j = 1..N_p, \quad (2.48)$$

where  $K(j, k)$  are the aerodynamic influence coefficients which determine the influence of the source ( $K_q$ ) or the surface vortex distribution ( $K_\gamma$ ) of the  $k^{\text{th}}$  panel (or the influence of the  $k^{\text{th}}$  point vortex ( $K_\Gamma$ ) exercised at the midpoint of the  $j^{\text{th}}$  panel. For non-moving solid boundaries  $K_q(j, k)$  and  $K_\gamma(j, k)$  only depend on the fixed geometry of the computational domain and are independent of time.  $K_\Gamma(j, k)$ , however, is time-dependent since the vortex blobs are advected with the flow. In the case of straight panels with uniform source and surface vortex distributions the aerodynamic influence coefficients can be written as

$$\begin{aligned} K_\gamma(j, k) &= \int_{s_k} \vec{K}(\vec{x}_j - \vec{x}_k) \cdot \vec{\tau}_j ds, \\ K_q(j, k) &= - \int_{s_k} \vec{K}^\perp(\vec{x}_j - \vec{x}_k) \cdot \vec{\tau}_j ds, \\ K_\Gamma(j, k) &= \vec{K}(\vec{x}_j - \vec{x}_k) \cdot \vec{\tau}_j. \end{aligned} \quad (2.49)$$

In these equations  $s$  denotes the arc length along a panel and  $s_k$  is the part of the boundary belonging to the  $k^{\text{th}}$  panel. Note that for the implementation of the boundary condition the singular kernel for the vortex blobs is used. For every time step the surface vortex distribution on the boundary can be solved using an algorithm based on an LU-decomposition. When the circulation density is known the vortex blobs can be advanced in time by integrating equation (2.41). This equation is integrated in time using a fourth-order Runge-Kutta scheme.

The method we have described in this paragraph solves the vorticity-transport equation for inviscid flow but does not include any means to generate vorticity. If this method is to be applied to separating flows a mechanism for generating vorticity is needed. For flow separation from sharp edges, as shown in figure 2.3, simplified models are available.

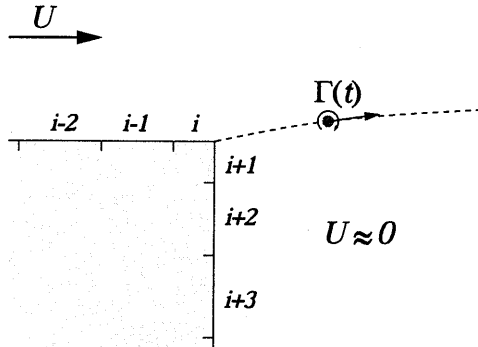


Figure 2.3: Close-up of the numerical model of the flow separation over a downward facing step, specifically the generation of a new vortex.

These models have in common that they can be considered as an implementation of an approximate Kutta-condition at the sharp edge. The method we used is described below.

When a two-dimensional flow is separating from a wall vorticity that was previously in the boundary layer is transported with a certain transport velocity into the main flow domain. In our model the vorticity of the boundary layer is concentrated in the circulation density on the solid walls, which is equal to the tangential (slip) velocity at the walls. The total amount of vorticity that is released into the domain per unit time is then the product of the transport velocity and the vorticity in the boundary layer. In our method at a sharp corner this process can be modelled as shown in figure 2.3.

A new vortex blob is generated at an initial position determined by the velocity at the midpoints of the two corner panels:

$$\vec{x}_{init} = \vec{x}_{corner} + \frac{1}{2}(\vec{u}_i + \vec{u}_{i+1})\Delta t,$$

where  $\Delta t$  is the time step. The constant  $\frac{1}{2}$  in this equation is rather arbitrary. Results are fortunately not sensitive to this choice (Peters 1993). From this initial position onwards the nascent vortex blob is transported with the local flow velocity. The circulation of the nascent vortex blob is growing until a new vortex is generated. The change of the shear-layer circulation is determined by:

$$\frac{d\Gamma}{dt} = -\frac{1}{2}|\vec{u}_i + \vec{u}_{i+1}|(\vec{u}_i \cdot \vec{\tau}_i + \vec{u}_{i+1} \cdot \vec{\tau}_{i+1}).$$

In this equation the transport velocity is represented by the term  $\frac{1}{2}(\vec{u}_i + \vec{u}_{i+1})$ , which is the average of the velocities at the midpoints of the two corner panels. The amount of vorticity that is transported into the flow domain is the average of the circulation density on the two corner panels. Although this is a very simple approximation of a complex process it is very robust, leading to a very reasonable description of flow separation at sharp edges as our results will confirm.

### 2.4.3 Vortex-blob method for viscous flow

In this section we present a numerical approach to solve the Navier-Stokes equations for incompressible two-dimensional flow by solving the vorticity-transport equation (2.37). It is solved via a vortex-blob method (Ranucci 1995, Graziani *et al.* 1995), the main features of which are outlined in the following. The method is an extension of the method discussed in the previous section. The method is labelled “the viscous vortex-blob” method as opposed to the “inviscid vortex-blob” method discussed in the previous section.

For an appropriate treatment of both the convective and the diffusive time scale as well as for the accurate approximation of the non-linear term, the equation has been split into an “Euler step” and a “Stokes” step according to the Chorin–Marsden product formula (Chorin *et al.* 1978). The former step is governed by the inviscid-flow equation stating that the material identity of the vortical particles is advected by the velocity field:

$$\frac{D\omega}{Dt} = 0. \quad (2.50)$$

In the second step, Stokes’ equation in vorticity form becomes, in two dimensions, completely equivalent to the heat-transfer equation:

$$\frac{\partial\omega}{\partial t} = \frac{1}{Re}\nabla^2\omega, \quad (2.51)$$

with suitable boundary conditions on  $\omega$ , to be discussed later. The fractional-step scheme provides the most appropriate and convenient solution for each sub-step. The vorticity field is approximated, defined on the computational body-fitted grid with mesh size  $h$  as

$$\omega(\vec{x}, t^n) = \sum_{j=1}^N \Gamma(\vec{x}_j, t^n) \delta(\vec{x} - \vec{x}_j), \quad (2.52)$$

where  $\Gamma(\vec{x}_j, t^n) = \omega(\vec{x}_j, t^n)h^2$  is the circulation at the grid point  $\vec{x}_j$  and time  $t^n$  and  $\delta(\vec{x} - \vec{x}_j)$  is the Dirac delta function.

In the Euler step only the position of the vortices changes in time according to

$$\frac{d\vec{x}_\Gamma}{dt} = \vec{u}(\vec{x}_\Gamma, t), \quad (2.53)$$

where the velocity at each time step is computed from the Poincaré representation, which is an integral and explicit equivalent to the Helmholtz decomposition (Bassanini *et al.* 1991a,b) and reduces to the Biot-Savart formula in free space.

Equation (2.40) provides the velocity field:

$$\vec{u}(\vec{x}, t) = \int_{\partial\Omega} u_n \vec{K}^\perp(\vec{x} - \vec{y}) ds(\vec{y}) - \int_{\partial\Omega} u_\tau \vec{K}(\vec{x} - \vec{y}) ds(\vec{y}) + \iint_{\Omega} \omega \vec{K}(\vec{x} - \vec{y}) d\Omega(\vec{y})$$

where the terms with the normal and tangential velocity components on the boundaries,  $u_n$  and  $u_\tau$ , account for the contribution of in- and outflow and the slip velocity on the

body, respectively, while the volume integral evaluates the contribution from the vorticity within the flow field. The function  $\vec{K}$  is the Biot-Savart kernel. In discretised form the volume integral is desingularised by the higher-order kernel of Lucquin-Descreux (1987):

$$\vec{K}_\delta(\vec{x}) = \frac{\vec{x}^\perp}{2\pi} \left[ \frac{r^4 + 3\delta^2 r^2 + 4\delta^4}{(\delta^2 + r^2)^3} \right],$$

where  $r = |\vec{x}|$  and  $\delta$  is the desingularisation parameter.

The domain integral is evaluated through an algorithm based on a multi-pole expansion of the velocity field induced by the vortices, this in order to reduce the computational effort (Greengard & Rokhlin 1987, Van Dommelen & Rundensteiner 1989). An alternative acceleration method for particle-particle is presented by Draghicescu & Draghicescu (1995). Their method is based on local Taylor expansions of the particle-particle interactions. The tangential wall velocity  $u_\tau$  is evaluated by solving the integral equation obtained from the projection of (2.40) along the local tangent, i.e. for a point  $\xi$  on the fluid side of  $\partial\Omega_b$ :

$$\begin{aligned} \frac{1}{2}u_\tau(\vec{x}) + \int_{\partial\Omega} u_\tau(\vec{y}) \vec{K}(\vec{x} - \vec{y}) \cdot \vec{\tau}(\vec{x}) ds(\vec{y}) &= \int_{\partial\Omega} u_n(\vec{x}) \vec{K}^\perp(\vec{x} - \vec{y}) \cdot \vec{\tau}(\vec{x}) ds(\vec{y}) \\ &+ \iint_{\Omega} \omega(\vec{y}) \vec{K}(\vec{x} - \vec{y}) \cdot \vec{\tau}(\vec{x}) d\Omega(\vec{y}). \end{aligned} \quad (2.54)$$

The numerical solution of the integral equation of the second kind provides the surface vortex distribution  $\gamma$  of the vortex sheet, which is given by the jump in the tangential velocity across the boundary  $\partial\Omega$  of the domain, from the value given by (2.54) to the prescribed wall value  $u_\tau^0 \vec{\tau}$ , which is zero for a non-moving rigid wall. A good approximation of the physical boundary conditions  $\vec{u} = u_\tau^0 \vec{\tau}$  at the end of a global step needs the adoption of an appropriate set of boundary conditions on  $\omega$  for each sub-step. We generate, by equation (2.54), a vortex sheet on the body which implies a discontinuity in the tangential velocity, not physically consistent with the presence of viscosity. Hence, as suggested by Chorin (Chorin & Bernard 1973, Chorin 1978), during the subsequent diffusive step the surface of the body may be considered as a continuous distribution of sources of positive or negative vorticity, with an intensity that is directly related to the value of  $\gamma$  computed according to (2.54). After the convective transport we have a new vorticity field given by:

$$\tilde{\omega}(\vec{x}) = \sum_{j=1}^N \Gamma(\vec{x}_j) \delta(\vec{x} - \vec{x}_j) + \sum_{j=1}^M \Gamma(\vec{s}_j) \delta(\vec{x} - \vec{s}_j), \quad (2.55)$$

where  $\vec{x}_j$  defines the current positions of the initial set of point vortices and the vortex sheet is discretised into a collection of  $M$  point vortices at positions  $\vec{s}_j$  on the boundary. In our numerical model the diffusion is evaluated by the integral representation for the solution of equation (2.51), together with the reflection boundary condition  $\frac{\partial\omega}{\partial n} = 0$  on  $\partial\Omega$ . The convergence proof discussed by Benfatto and Pulvirenti (1986) for a flat plate confirms the consistency of the splitting procedure also in the presence of a solid wall. With this

assumption the vorticity after one time step  $\Delta t = t^{n+1} - t^n$  is expressed as

$$\begin{aligned}\omega(\vec{x}, t^{n+1}) &= \int_{\Omega} \tilde{\omega}(\vec{y}, t^n) F(\vec{y} - \vec{x}, \Delta t) dV(\vec{y}) \\ &= \sum_{j=1}^N \Gamma(\vec{x}_j, t^n) F(\vec{x}_j - \vec{x}, \Delta t) + \sum_{j=1}^M \Gamma(\vec{s}_j, t^n) F(\vec{s}_j - \vec{x}, \Delta t),\end{aligned}\quad (2.56)$$

where  $F$  is the Green's function of the heat-transfer equation, which satisfies a Neumann condition of zero normal velocity on  $\partial\Omega_b$ . The operator splitting allows for the assumption of two different values of the time increment: one for convection and one for diffusion. In particular, a smaller  $\Delta t$  is chosen for the accurate treatment of convection in the Lagrangian scheme, while a larger value is allowed for the diffusion process to act on the predefined mesh.

The present numerical approach shows some interesting features in comparison with other, more traditional, computational techniques. In particular, when compared with finite-difference methods, only the vortical region of the computational domain needs to be discretised without any approximation due to fictitious far-field boundary conditions. Moreover, the Lagrangian approach, the most appropriate to treat convection, is here further improved by an algorithm for the velocity evaluation involving a multi-pole expansion of the Biot-Savart kernel, which avoids the interpolations required by other mixed Eulerian-Lagrangian computational schemes (e.g. Vortex-in-Cell). In fact, the interpolation from grid nodes to vortex positions and vice versa for the vorticity and the velocity, respectively, induces a numerical diffusion which is absent in the present computational method.

## 2.5 Boundary-layer theory

### 2.5.1 Introduction

The flows that we study are all characterised by a high Reynolds number, defined by:  $Re = \frac{U_0 L}{\nu}$ . In this definition of the Reynolds number  $U_0$  is the cross-sectional average of the mean flow velocity,  $L$  is the length of the flow channel or the diameter of the pipe, and  $\nu$  is the kinematic viscosity of air ( $\nu_{air} = 1.5 \cdot 10^{-5} \text{ m}^2/\text{s}$  at room temperature and standard atmospheric pressure). For the problems that we considered this results in a Reynolds number in the range of  $10^3$  to  $10^6$ . From equation (2.9) it would then follow that the effects of viscosity are negligible. There are, however, always regions in the flow where the effect of viscosity is dominant. This is near the walls of the flow domain, as we will show. The viscosity of the flow causes the fluid to "stick" to the walls, resulting in the no-slip boundary condition at the walls ( $\vec{u} = 0$  at a wall).

In high-Reynolds-number flows the region near the wall in which viscous flow effects are important is very thin. It is called the boundary layer. The bulk flow outside this region is considered inviscid. In figure 2.4 a schematic drawing of such a situation is shown. Near the walls of the pipe the velocity changes rapidly from the main flow velocity at the edge



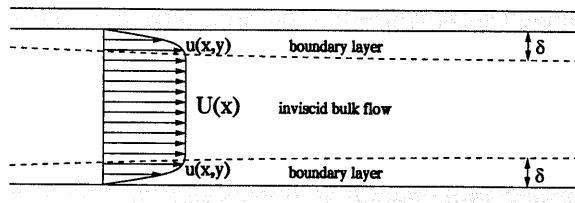


Figure 2.4: Boundary layer in a channel of constant cross section.

of the boundary layer to zero at the wall. All viscous effects are confined to the boundary layers and the main pipe flow can be considered inviscid. For many flow problems the effect of this thin boundary layer on the main flow is not important and the whole flow domain is considered to be inviscid. This implies that at the walls of the domain the no-slip condition cannot be imposed and is replaced by the less restricting condition of zero velocity normal to the wall ( $\vec{u} \cdot \vec{n} = 0$  with  $\vec{n}$  the normal vector to the wall). In these cases either the Euler equations or the potential-flow equation are solved. Although these equations can form a valid approximation in (almost) the complete flow domain, there is one important viscous-flow phenomenon that is not captured by these equations: flow separation.

Flow separation is an inherent viscous-flow effect and the full Navier-Stokes equations are necessary to describe this phenomenon. In some cases, however, it is possible to use an inviscid description while taking flow separation into account. It is possible to combine an inviscid bulk flow model with a boundary-layer model. The boundary layer and the bulk flow can often be solved sequentially, but in case of flow separation they have to be solved simultaneously. For external flows this is discussed extensively by Lock & Williams (1987). Applications of this approach can be found in references (Fiddes 1980, Drela *et al.* 1985, Wolles & Hoeijmakers 1996). In this approach the boundary-layer model would lead to a description of flow separation. In the case of flow separation at a sharp edge the separation point is known. In that case a simple model such as a Kutta condition can be applied to incorporate the effect of flow separation, as is the case in the vortex-blob method.

### 2.5.2 Boundary-layer equations

In order to describe the (incompressible) flow next to a wall the full Navier-Stokes equations are to be used:

$$\begin{aligned}\vec{\nabla} \cdot \vec{u} &= 0, \\ \frac{\partial \vec{u}}{\partial t} + (\vec{u} \cdot \vec{\nabla}) \vec{u} &= -\frac{1}{\rho} \vec{\nabla} p + \nu \nabla^2 \vec{u}.\end{aligned}$$

We assume that the  $x$ -direction is along the wall and the  $y$ -direction is perpendicular to the wall and  $\vec{u} = (u, v)$ , then an estimate of the relative importance of the different terms

can be made using the following characteristic parameters:  $U$  is the characteristic velocity in the  $x$ -direction;  $L$  is the characteristic length scale in the  $x$ -direction; and the boundary-layer thickness  $\delta$  is the characteristic length scale in the  $y$ -direction. Here we implicitly assume that in high-Reynolds-number flows  $\delta$  is much smaller than  $L$ . Using these scales in the mass conservation equation we find that in order to balance the term  $\partial u/\partial x$ , which is of order  $\mathcal{O}(U/L)$ , the vertical velocity  $v$  has to be of order  $\mathcal{O}(U\delta/L)$ , since  $\partial v/\partial y$  is of order  $\mathcal{O}(v/\delta)$ . So we find that the vertical component of the velocity is much smaller than the velocity along the wall, but it is not equal to zero. Using these findings in the  $x$ -momentum equation and assuming a balance of the viscous forces and the inertial forces in the boundary layer we find that:  $\frac{\delta}{L} = \mathcal{O}(\frac{\nu}{UL})^{\frac{1}{2}} = \mathcal{O}(Re^{-\frac{1}{2}})$ . So the boundary-layer thickness scales with the inverse of the square root of the Reynolds number. In the  $y$ -momentum equation the term with  $\partial p/\partial y$  is the only leading term, so that the pressure across the boundary layer can be assumed constant.

The complete set of the unsteady boundary-layer equations is then:

$$\frac{\partial u}{\partial x} + \frac{\partial v}{\partial y} = 0, \quad (2.57a)$$

$$\frac{\partial u}{\partial t} + u \frac{\partial u}{\partial x} + v \frac{\partial u}{\partial y} = -\frac{1}{\rho} \frac{\partial p}{\partial x} + \nu \frac{\partial^2 u}{\partial y^2}, \quad (2.57b)$$

$$0 = -\frac{1}{\rho} \frac{\partial p}{\partial y}. \quad (2.57c)$$

Since the pressure in the boundary layer is only a function of the  $x$ -coordinate along the wall, the pressure at the edge of the boundary layer is equal to the pressure in the main inviscid flow. The pressure gradient in the main flow is provided by the  $x$ -momentum equation for inviscid flow. In the steady-flow case this yields:

$$\frac{dp(x)}{dx} = -\rho U(x) \frac{dU(x)}{dx}. \quad (2.58)$$

In the unsteady-flow case this changes to:

$$\frac{\partial p(x, t)}{\partial x} = -\rho \frac{\partial U(x, t)}{\partial t} - \rho U(x, t) \frac{\partial U(x, t)}{\partial x}. \quad (2.59)$$

This equation for the pressure gradient introduces the coupling of the main inviscid flow to the boundary-layer flow.

For most flow problems there is no exact solution of the boundary-layer equations, so either a numerical solution of these equations is necessary or some further simplifying assumptions have to be made. Further information on numerically solving the boundary-layer equations can be found in Fletcher (1988) and Sherman (1990). In the next section the von Kármán equation is introduced. This is an integrated form of the momentum equation that allows for a global modelling of the boundary layer in terms of integrated properties. This equation will be shown to be very useful for modelling the boundary-layer flow.

### 2.5.3 The von Kármán equation

Before deriving the von Kármán equation a number of quantities related to the boundary-layer thickness need to be introduced. The boundary-layer equations are asymptotic equations valid near the walls of a flow domain, this at high Reynolds number only. There is, however, no exact limit to the region where the boundary layer ends and where the inviscid main flow region starts. Therefore the boundary-layer thickness  $\delta$  is an ambiguous quantity. The displacement thickness  $\delta^*$  on the other hand is a well-defined quantity, in steady incompressible flow:

$$\delta^*(x) = \int_0^{\infty} \left(1 - \frac{u(y)}{U}\right) dy. \quad (2.60)$$

The integration is asymptotically extended to infinity by scaling with the boundary-layer thickness  $\delta$ . For internal flows the displacement thickness is related to the loss of flux due to the presence of the boundary layer relative to an equivalent inviscid flow. For a uniform main flow with velocity  $U$  through a straight channel of height  $H$  the flux is equal to  $U(H - 2\delta^*)$  in which the factor 2 is due to the presence of a boundary layer along the bottom wall and the top wall, as shown in figure 2.4. The integral (2.60) is taken across the whole boundary layer. Outside of the boundary layer there is no contribution to the integral, thus the integral can be taken to infinity.

A second well-defined quantity is the momentum thickness  $\theta$ , in incompressible flow:

$$\theta(x) = \int_0^{\infty} \frac{u(y)}{U} \left(1 - \frac{u(y)}{U}\right) dy. \quad (2.61)$$

Due to the presence of the boundary layer the main flow loses momentum. The momentum thickness is defined in such a way that the additional momentum loss relative to the equivalent situation without boundary layers but including the displacement thickness is equal to  $\rho U^2 \theta$ . For a uniform main flow with velocity  $U$  through a straight channel of height  $H$  the total momentum flux is equal to:  $\rho U^2 (H - 2\delta^* - 2\theta)$ .

The effect of the boundary layer on the main flow is to a large extent described by the integrated quantities  $\delta^*$  and  $\theta$ . It is therefore convenient to rewrite the boundary-layer equations in terms of these quantities so that further simplifications are possible. This is possible by integrating the  $x$ -momentum equation across the boundary layer. A steady flow is assumed and in the main flow the velocity is only a function of  $x$  so that we can use equation (2.58). Taking the steady version of equation (2.57b), while adding and subtracting a term  $u \frac{dU}{dx}$  and using that  $\frac{dU}{dy} = 0$ , the following equation is obtained:

$$(U - u) \frac{dU}{dx} + u \frac{\partial(U - u)}{\partial x} + v \frac{\partial(U - u)}{\partial y} = -\nu \frac{\partial^2 u}{\partial y^2}. \quad (2.62)$$

Integrating this equation across the boundary layer using the various boundary conditions and the equation of mass conservation yields:

$$\frac{d}{dx} (U^2 \theta) + \delta^* U \frac{dU}{dx} = \frac{\tau_0}{\rho}, \quad (2.63)$$

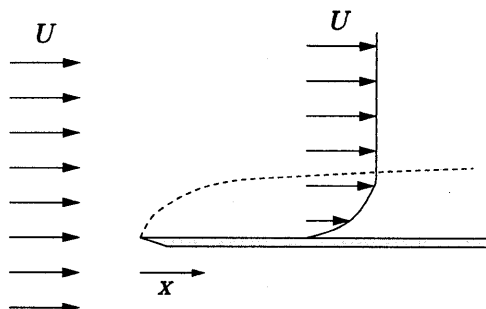


Figure 2.5: Boundary layer over a flat plate in a uniform flow.

in which  $\tau_0$  is the wall shear stress defined as:  $\tau_0 = \eta \partial u / \partial y|_{y=0}$  and  $\eta$  the dynamic viscosity coefficient:  $\eta = \rho \nu$ . This equation is known as the von Kármán momentum integral equation.

In a similar way the unsteady version of the von Kármán equation can be derived using the unsteady boundary-layer equation (2.57b) and the unsteady equation for the pressure gradient in the main flow (2.59), yielding:

$$\frac{\partial}{\partial t} (U \delta^*) + \frac{\partial}{\partial x} (U^2 \theta) + \delta^* U \frac{\partial U}{\partial x} = \frac{\tau_0}{\rho}. \quad (2.64)$$

The von Kármán equation (steady or unsteady) is useful because it allows a parametric description of the velocity profile in the boundary layer that satisfies as many conditions as possible. Then equation (2.63) or (2.64) predicts the boundary-layer thickness and other parameters such as the wall shear stress.

As an example we consider the development of the boundary layer along a semi-infinite flat plate due to an impulsively started flow. This problem has been solved by Blasius in the steady-flow case. Another associated problem is the problem of an impulsively started plate of infinite extent, the so-called Rayleigh problem. At  $t = 0$  the flow is impulsively accelerated from rest to  $U$ . So that at  $t > 0$  the situation is as sketched in figure 2.5. We will use the unsteady von Kármán equation (2.64) to solve this problem using the simplest possible boundary-layer description: a linear velocity profile within the boundary layer. This velocity profile  $u(x, y, t)$  can satisfy two boundary conditions:  $u(x, 0, t) = 0$  and  $u(x, \delta, t) = U$ . So we have  $u(x, y, t) = \frac{y}{\delta(x, t)} U$  for  $y < \delta$  and  $u(x, y, t) = U$  elsewhere. The displacement thickness and the momentum thickness are related to the boundary-layer thickness  $\delta$  by the simple relations:  $\delta^* = \frac{1}{2} \delta$  and  $\theta = \frac{1}{6} \delta$ . Inserting this in equation (2.64) yields an equation for  $\delta^*$ :

$$\left( \frac{\partial}{\partial t} + \frac{1}{3} U \frac{\partial}{\partial x} \right) (\delta^*)^2 = \nu.$$

The solution of this problem is split in two parts: one part near the leading edge of the plate, where the solution is steady like Blasius' result, and one part further downstream,

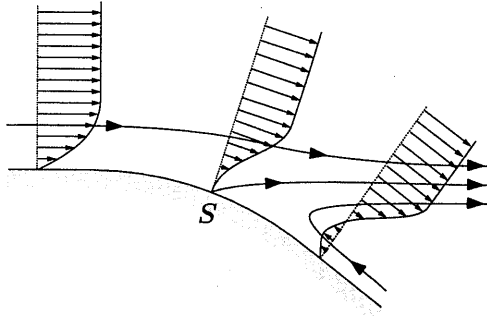


Figure 2.6: Separating boundary layer over a curved wall.  $S$  indicates the position of the separation point.

where the solution is completely unsteady as in Rayleigh's problem:

$$(\delta^*)^2 = 3 \frac{\nu x}{U}, \quad 0 < x < \frac{1}{3}Ut,$$

$$(\delta^*)^2 = \nu t, \quad x \geq \frac{1}{3}Ut.$$

The transition between the two solutions takes place at the line  $x = \frac{1}{3}Ut$ . This implies that in the boundary layer information typically travels at a speed of one third of the main flow velocity. The exact results in both regions far from the transition region are:

$$(\delta^*)^2 = 2.96 \frac{\nu x}{U}, \quad x \ll \frac{1}{3}Ut,$$

$$(\delta^*)^2 = \frac{4}{\pi} \nu t, \quad x \gg \frac{1}{3}Ut.$$

So this simple boundary-layer model already provides surprisingly accurate results for the boundary-layer parameters. This example also illustrates that the effect of the unsteadiness of the main flow on the boundary layer is related to the horizontal length scale and a velocity that is typically one third of the main flow velocity.

#### 2.5.4 Flow separation

Boundary layers at high Reynolds numbers are usually very thin and the effect on the main inviscid flow can be neglected. In that case either the Euler equations or the potential flow equations are solved and no viscous effects are taken into account. There is however a viscous effect that is always important no matter the value of the Reynolds number: flow separation.

Flow separation occurs when the flow can no longer follow the contour of the wall and reversed flow occurs near the wall. In figure 2.6 the flow near the separation point  $S$  is

shown. The separation point is defined as the point along the wall at which the reversed flow starts. At the wall the velocity is equal to zero so that reversed flow near the wall ( $u(y) < 0$ ) requires that  $\frac{\partial u}{\partial y} < 0$  at the wall. So for a steady flow the onset of separation is defined by:

$$\left. \frac{\partial u}{\partial y} \right|_{y=0} = 0 \quad (\text{separation point}). \quad (2.65)$$

and we find that at this point the shear stress  $\tau_0$  is equal to zero. In a steady flow this behaviour is driven by the pressure gradient in the main flow only since near the wall the momentum equation reduces to a balance of the pressure gradient and the viscous term:

$$\nu \left. \frac{\partial^2 u}{\partial y^2} \right|_{y=0} = \left. \frac{1}{\rho} \frac{\partial p}{\partial x} \right|_{y=0}.$$

In order to have a solution  $u(y)$  that can satisfy the conditions in a separated flow, a necessary condition is that  $\left. \frac{\partial^2 u}{\partial y^2} \right|_{y=0} > 0$  at the wall. This is only the case when  $\left. \frac{\partial p}{\partial x} \right|_{y=0} > 0$  in the main flow. Therefore flow separation only occurs under influence of an adverse pressure gradient in the main flow, which implies a decelerating main flow. When a steady inflow is provided to a channel with a variable height the acceleration and deceleration of the main flow is due to the changing height of the channel. When the height of the channel increases strongly in the stream-wise direction the flow decelerates and flow separation can occur.

Near the separation point the boundary layer rapidly increases in thickness. This implies that the assumption of quasi-tangential flow in the boundary-layer equations is no longer valid. In the case of strong flow separation this is certainly true at some distance beyond the separation point. It is therefore not always possible to describe the flow far beyond the separation point using the boundary-layer equations. However, up to the separation point the boundary-layer description applies and it is possible to predict flow separation using the boundary-layer equations as long as the inner flow and the outer flow are solved simultaneously.

### 2.5.5 Approximate boundary-layer descriptions

The von Kármán equation is well-suited for the use with a parametric description of the velocity profile within the boundary layer. We already treated the case of a linear velocity profile in the boundary layer. This profile is obviously not useful for describing a separating flow. Also the number of boundary conditions that can be satisfied by the linear model is restricted to only two. Pohlhausen (1921) used a fourth-order polynomial to describe the velocity profile. Pelorson *et al.* (1994) claim that a third-order polynomial provides a more accurate result than the fourth-order description. Our experience confirmed this claim, and therefore we restrict ourselves to a third-order polynomial description of the velocity profile in the boundary layer:

$$u(x, y) = U \sum_{i=0}^3 a_i \left( \frac{y}{\delta} \right)^i, \quad (2.66)$$

in which the coefficients  $a_i$  are a function of the coordinate  $x$  along the wall. The third-order polynomial approximation is sufficient to describe the velocity profile for a steady separating flow around the separation point.

A third-order polynomial has to satisfy four boundary conditions to be fully determined, these are:

$$\begin{aligned} u(x, 0) &= 0, \\ u(x, \delta) &= U, \\ \frac{\partial u}{\partial y} \Big|_{y=\delta} &= 0, \\ \nu \frac{\partial^2 u}{\partial y^2} \Big|_{y=0} &= -U \frac{dU}{dx}. \end{aligned} \quad (2.67)$$

The first three boundary conditions ensure a smooth transition of the velocity profile from zero at the wall to the main flow value  $U$  at the edge of the boundary layer. The last boundary condition is obtained by applying the boundary-layer equation at the wall and replacing the pressure gradient by the main flow pressure gradient, which is related to the main flow velocity gradient.

Upon substitution of the polynomial in the boundary conditions the coefficients  $a_i$  are determined. Introducing the parameter  $\Lambda = \frac{\delta^2}{\nu} \frac{dU}{dx}$  the coefficients are:

$$\begin{aligned} a_0 &= 0, \\ a_1 &= \frac{\Lambda}{4} + \frac{3}{2}, \\ a_2 &= -\frac{\Lambda}{2}, \\ a_3 &= \frac{\Lambda}{4} - \frac{1}{2}. \end{aligned} \quad (2.68)$$

Using the parameters  $a_i$  the displacement thickness  $\delta^*$  and the momentum thickness  $\theta$  can also be expressed in terms of the boundary layer thickness  $\delta$  and the parameter  $\Lambda$ :

$$\delta^* = \delta \left( \frac{3}{8} - \frac{1}{48} \Lambda \right), \quad (2.69)$$

$$\theta = \delta \left( \frac{39}{280} - \frac{1}{560} \Lambda - \frac{1}{1680} \Lambda^2 \right). \quad (2.70)$$

In figure 2.7 the velocity profiles obtained for the third-order polynomial fit are shown for four values of  $\Lambda$ . Three of the profiles can be considered to be special cases. The velocity profile for  $\Lambda = 6$  represents the boundary layer associated with the upper limit on  $\Lambda$ . For  $\Lambda > 6$  the velocity profile will have a maximum value for  $u$  that exceeds the main flow value  $U$ . This does not represent a boundary-layer solution that we are interested in. The velocity profile for  $\Lambda = 0$  represents the solution for a boundary layer over a flat plate in a uniform flow (solved exactly by Blasius). This solution is valid when the pressure gradient in stream-wise direction is equal to zero. The velocity profile for  $\Lambda = -6$  represents the boundary layer at the separation point (see (2.65) for the definition). The wall shear stress is equal to zero for this profile. The fourth velocity profile for  $\Lambda = -10$  represents a separated boundary layer. Values of  $\Lambda$  much smaller than  $-6$  will result in velocity profiles with very strong reversed flow, which are solutions for which the boundary-layer approximation is questionable.

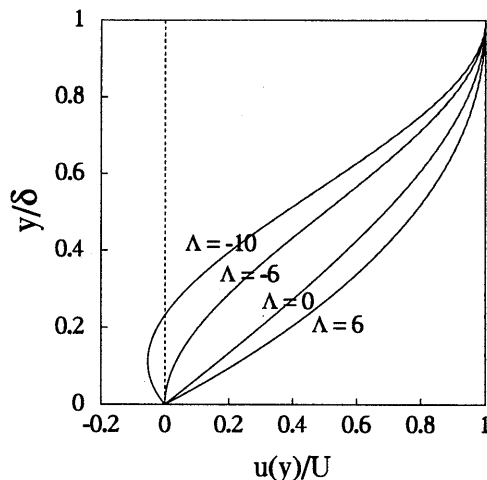


Figure 2.7: Velocity profiles in the boundary layer as a function of the parameter  $\Lambda = \frac{\delta^2}{\nu} \frac{dU}{dx}$  for the third-order polynomial description:  $-6 < \Lambda < 6$  attached flow;  $\Lambda < -6$  separated flow.

In order to solve the von Kármán momentum equation it is useful to introduce two so-called shape parameters that are only functions of the shape of the velocity profile:  $H = \frac{\delta^*}{\theta}$  and  $T = \frac{\theta}{\nu U} \frac{\tau_w}{\rho}$ . The von Kármán equation (2.63) can then be rewritten in terms of one unknown variable  $\theta$ :

$$\frac{d}{dx} \left( \frac{\theta^2}{\nu} \right) + \frac{2}{U} \left[ (H + 2) \frac{dU}{dx} \left( \frac{\theta^2}{\nu} \right) - T \right] = 0. \quad (2.71)$$

In Cousteix (1988) several approaches to solve this equation are discussed. However, several people noticed that values of  $H$  and  $T$  are almost completely determined by  $\lambda = \frac{dU}{dx} \frac{\theta^2}{\nu}$ . Note the difference between  $\Lambda$  and  $\lambda$ . Thwaites (1949) noticed that to good approximation the following relation can be used in equation (2.71):

$$2(H + 2)\lambda - 2T = 6.0\lambda - 0.45. \quad (2.72)$$

Using this relation equation (2.71) can be integrated, resulting in:

$$\theta^2 U^6 \Big|_x - \theta^2 U^6 \Big|_{x_0} = 0.45 \nu \int_{x_0}^x U(x')^5 dx'. \quad (2.73)$$

In order to calculate the skin friction and displacement thickness this equation can be combined with the fitted formula for  $T(\lambda)$  provided by White (1986):

$$T \approx (\lambda + 0.09)^{0.62}. \quad (2.74)$$



Flow separation occurs for  $T = 0$ , so for  $\lambda = -0.09$ . This method provides a very fast way to calculate the steady laminar boundary layer for several applications. In Sherman (Sherman 1990) some applications of Thwaites' method are presented.

In order to show the performance of some of the approximations, we calculated the development of  $\delta^*$  and  $\theta$  along a flat plate in a uniform steady flow (see figure 2.5). This problem was solved exactly in terms of the boundary-layer equations by Blasius. The pressure gradient along the plate is equal to zero so that the profile for  $\Lambda = 0$  applies. In table 2.1 the results are presented. The linear approximation yields a surprisingly almost exact prediction for  $\delta^*$  but not for  $\theta$ . The higher-order polynomials yield a similar result for  $\delta^*$  but a much improved prediction for  $\theta$ . That Thwaites' method gives such good predictions is not so surprising since the Blasius results were used for his correlation. Note that the 4<sup>th</sup>-order polynomial does not automatically yield a better prediction than the third order polynomial.

	exact	1 <sup>st</sup> -order	3 <sup>rd</sup> -order	4 <sup>th</sup> -order	Thwaites
$\delta^* \frac{\sqrt{Re_x}}{x}$	1.72	1.73	1.74	1.75	1.71
$\theta \frac{\sqrt{Re_x}}{x}$	0.664	0.577	0.647	0.685	0.671

Table 2.1: Comparison of results for  $\delta^*$  and  $\theta$  obtained with three different polynomial descriptions of the velocity profile in the boundary layer and Thwaites' method over a flat plate in a uniform flow. The leading edge of the plate is at  $x = 0$ . The exact solution is the Blasius solution.

Schlichting (1979) reported that a calculation based on Pohlhausen's method using the 4<sup>th</sup>-order polynomial did not accurately predict flow separation, i.e. flow separation occurred too late. Our experience confirms the claim by Pelorson *et al.* (1994) that a 3<sup>rd</sup>-order polynomial provides much better results. A problem with the 3<sup>rd</sup>-order-polynomial approach is, however, that it shows singular behaviour near a stagnation point. That the 3<sup>rd</sup>-order-polynomial description provides a better prediction for the separation point is perhaps already indicated by the value of  $\lambda$  at the separation point. It is generally accepted that Thwaites's value of  $\lambda = -0.092$  at the separation point gives a reasonable indication of the separation point. The 3<sup>rd</sup>-order-polynomial description yields a value for  $\lambda = -0.0992$  at the separation point. The 4<sup>th</sup>-order-polynomial description on the other hand yields a value that is much higher, namely  $\lambda = -0.1557$ , which might explain the late separation predicted by this approach.

## 2.6 Concluding remarks

In this chapter we have provided the mathematical background to the remaining part of this thesis. We have introduced Howe's analogy and derived an integral formulation for the total pressure. In the following chapters we show that the results of the two formulations are in agreement.

Two vortex-blob methods have been introduced. Although the viscous-vortex blob method is a more complete model of the flow, it is restricted to a Reynolds number less than  $10^4$  because of the limitations of present-day computers. The alternative method, the inviscid vortex-blob method, is therefore very useful for high Reynolds number flows ( $Re > 10^4$ ). But we will show that also at lower Reynolds number (of the order  $10^3$ ) this method can give reasonable results.

We have introduced the concept of the momentum integral equation, the so-called von Kármán equation, and suggested some approaches to solving this equation. Solving the unsteady version of this equation is problematic when using the simplified boundary-layer models. In Matsushita *et al.* (1984) an integral method is used for solving unsteady flow separation. The problems that one encounters when using the unsteady boundary-layer equations to describe unsteady flow separation are discussed in Henkes & Veldman (1987).

## References

- ANDERSON, C.R. & GREENGARD, C. (1985) On vortex methods. *SIAM J. Stat. Comp.* **22**, 413–440
- BASSANINI, P., CASCIOLA, C.M., LANCIA, M.R., & PIVA, R. (1991) A boundary integral formulation for the kinetic field in aerodynamics. Part I, *European J. Mech. B/Fluids* **10**, 605–627
- BASSANINI, P., CASCIOLA, C.M., LANCIA, M.R., & PIVA, R. (1991) A boundary integral formulation for the kinetic field in aerodynamics. Part II, *European J. Mech. B/Fluids* **11**, 69–92
- BEALE, J.T. & MAJDA, A. (1985) High order accurate vortex methods with explicit velocity kernels. *J. Comp. Phys.* **58**, 188–208
- BENFATTO, G. & PULVIRENTI, M. (1986) Convergence of Chorin-Marsden product formula in the half-plane. *Commun. Math. Phys.* **106**, 427–458
- CHORIN, A.L. & BERNARD, P.S. (1973) Discretization of a vortex sheet, with an example of roll-up. *J. Comp. Phys.* **13**, 423–429
- CHORIN, A.J. (1978) Vortex sheet approximation of boundary layers. *J. Comp. Phys.* **27**, 428–442 of slightly viscous flow. *J. Fluid Mech.* **57**, 785–796
- CHORIN, A.J., HUGHES, T.J.R., MCCracken, M.F., & MARSDEN, J.E. (1978) Product formulas and numerical algorithms. *Comm. Pure Appl. Math.* **31**, 205–256
- COUSTEIX, J. (1988) Aérodynamique: Couche limite laminaire. *CEPAD, Toulouse*
- CRAMER, O. (1993) The variation of the specific heat ratio and the speed of sound in air with temperature, pressure, humidity, and CO<sub>2</sub> concentration. *J. Acoust. Soc. Am.* **93**, 2510–2516

- CRIGHTON, D.G., DOWLING, A.P., FLOWCS WILLIAMS, J.E., HECKL, M., & LEPPINTON, F.G. (1992) Modern methods in analytical acoustics. *Springer Verlag, London*
- CURLE, N. (1955) The influence of solid boundaries upon aerodynamic sound. *Proc. Roy. Soc. A* **231**, 505–514
- DOAK, P.E. (1998) Fluctuating total enthalpy as the basic generalized acoustic field. *Theoret. Comput. Fluid Dynamics* **10**, 115–133
- DRAGHICESCU, C.I. & DRAGHICESCU, M. (1995) A fast algorithm for vortex blob interactions. *J. Comp. Phys.* **116**, 69–78
- DRELA, M., GILES, M., & THOMPSON, W.T. (1985) Newton solution of coupled Euler and boundary layer equations. *Third Symposium on Numerical and Physical Aspects of Aerodynamical flows, Longbeach*
- FFOWCS WILLIAMS, J.E. & HAWKINGS, D.L. (1969) Sound generation by turbulence and surfaces in arbitrary motion. *Phil. Trans. R. Soc. Lond. A* **264**, 321–342
- FIDDES, S.P. (1980) A theory of the separated flow past a slender elliptic cone at incidence *AGARD CP 291*, (30-1)–(30-14)
- FLETCHER, C.A.J. (1988) Computational techniques for fluid dynamics. Volume II. Chapter 15: Boundary layer flow. *Springer, Berlin*, 204–251
- GOLDSTEIN, M.E. (1976) Aeroacoustics. *McGraw-Hill, New York*
- GRAZIANI, G., RANUCCI, M., & PIVA, R. (1995) From a boundary integral formulation to a vortex method for viscous flows. *Comp. Mech.* **15**, 301–314
- GREENGARD, L. & ROKHLIN, V. (1987) A fast algorithm for particle simulations. *J. Comp. Phys.* **73**, 325–348
- HENKES, R.A. & VELDMAN, A.E.P. (1987) On the breakdown of the steady and unsteady interacting boundary-layer description. *J. Fluid Mech.* **179**, 513–529
- HOFMANS, G.C.J., VAN DE VEN, E.A.I., DEN DOELDER, C.F.J., HIRSCHBERG, A., & WIJNANDS, A.P.J. (1995) Unsteady flow through 2D channels with a constriction. *Forum on Vortex Methods for Engineering Applications, Albuquerque*
- HOWE, M.S. (1975) Contributions to the theory of aerodynamic sound, with applications to excess jet noise and the theory of the flute. *J. Fluid Mech.* **71**, 625–673
- HOWE, M.S. (1980) The dissipation of sound at an edge. *J. Sound & Vibr.* **70**, 407–411
- HOWE, M.S. (1984) On the absorption of sound by turbulence and other hydrodynamic flows. *I.M.A. J. of Appl. Math.* **32**, 187–209

- KRASNY, R. (1986) Desingularization of periodic vortex sheet roll-up. *J. Comp. Phys.* **65**, 292–313
- KRASNY, R. (1986) A study of singularity formation in a vortex sheet by the point-vortex approximation. *J. Fluid Mech.* **167**, 65–93
- KRASNY, R. (1987) Computation of vortex sheet roll-up in the Trefftz plane. *J. Fluid Mech.* **184**, 123–155
- LEWIS, R.I. (1991) Vortex element methods for fluid dynamic analysis of engineering systems. *Cambridge University Press, New York*
- LOCK, R.C. & WILLIAMS, B.R. (1987) Viscous-inviscid interactions in external aerodynamics. *Prog. Aerospace. Sci.* **24**, 51–171
- LUCQUIN-DESCREUX, B. (1987) Particle approximation of the two-dimensional Navier-Stokes equations. *La Recherche Aéronautique* **4**, 1–12
- MATSUSHITA, M., MURATA, S., & AKAMATSU, T. (1984) Studies on boundary-layer separation in unsteady flows using an integral method. *J. Fluid Mech.* **149**, 477–501
- MORSE, P.M. & FESHBACH, H. (1953) *Methods of Theoretical Physics, Part I* McGraw-Hill, New York
- PELORSON, X., HIRSCHBERG, A., VAN HASSEL, R.R., & WIJNANDS, A.P.J. (1994) Theoretical and experimental study of quasisteady-flow separation within the glottis during phonation. Application to a modified two-mass model. *J. Acoust. Soc. Am.* **96**, 3416–3431
- PETERS, M.C.A.M. (1993) Aeroacoustical sources in internal flows. *PhD thesis Eindhoven University of Technology*
- POHLHAUSEN, K. (1921) Zur Näherungsweise Integration der Differentialgleichung der laminaren Reibungsschicht. *Zeitschrift für angew. Math. und Mech.* **1**, 252–268
- RANUCCI, M. (1995) Effetti del rilascio di vorticità nell'interazione corpo-fluido. *PhD Thesis University of Rome "La Sapienza"*
- SAFFMAN, P.G. (1992) Vortex dynamics. Chapter 3: Vortex momentum Cambridge University Press, New York
- SARPKAYA, T. (1989) Computational methods with vortices – The 1988 Freeman scholar lecture. *ASME J. Fluids Eng.* **111**, 5–52
- SCHLICHTING, H. (1979) Boundary-layer theory. seventh edition McGraw-Hill, New York
- SHERMAN, F.S. (1990) Viscous flow. Chapter 12: Laminar boundary layers. McGraw-Hill, New York, 310–437

- 
- THWAITES, B. (1949) Approximate calculation of the laminar boundary layer. *Aeronautical Quarterly I*, 245–280
- VAN DOMMELEN, L. & RUNDENSTEINER, E.A. (1989) Fast adaptive summation of point forces in two-dimensional Poisson equation. *J. Comp. Phys.* **83**, 126–147
- WHITE, F.M. (1986) *Fluid Mechanics*. McGraw-Hill, New York, 408
- Wolles, B.A., & Hoeijmakers, H.W.M. (1996) Mathematical modelling of viscid-inviscid interaction problems. '96 *ECCOMAS Conference on Numerical Methods in Fluid Dynamics*, John Wiley & Sons, New York
- WONG, G.S.K. & EMBLETON, T.F.W. (1985) Variation of the speed of sound in air with humidity and temperature. *J. Acoust. Soc. Am.* **77**, 1710–1712

# Flow through a square-edge nozzle at low Mach number

### 3.1 Introduction

Flow separation is encountered in many practical engineering applications, which include internal flow systems such as channels with sudden expansions. When the expansion ratio is very large, so the channel height  $H$  after the expansion is much larger than the height of the channel  $h$  before the expansion, then the resulting jet flow will resemble a free jet flow into a semi-infinite space. This type of flow can also result in case of a very strong constriction in a channel. An example of such a constriction is the diaphragm that is treated in chapter 5.

Similar flows are also encountered in biomechanics such as the flow through the vocal folds: under certain conditions the vocal folds are tightened and thus form a strong constriction in the trachea (wind pipe) with a small slit-like aperture. The constriction formed by the vocal folds is a rapidly but smoothly converging-diverging channel that due to its high aspect ratio of width  $W$  across the trachea (typically 15 mm) over height  $h$  (typically 1 mm) usually is approximated by a two-dimensional description. Typical velocities  $u_0$  through the glottis (the aperture between the vocal folds) are in the range of 10 m/s to 30 m/s which implies a low Mach number. Furthermore, the typical frequencies associated with the movement of the vocal folds are in the range of 100 Hz to 200 Hz, so the Strouhal number as well as the Helmholtz number are quite low. This implies that the region around the glottis can be considered compact, and an incompressible description of the flow through the glottis is a reasonable approximation. By defining the Reynolds number as  $Re = hu_0/\nu$  and considering the typical geometry of the vocal folds an assumption of laminar (boundary) layer flow inside the glottis is also justified. The kinematic viscosity  $\nu$  of air at atmospheric pressure and room temperature is  $\nu = 1.5 \cdot 10^{-5} \text{ m}^2/\text{s}$ . The Reynolds number has a value in the order of  $10^3$  based on the height of the glottis. The jet flow resulting from flow separation in the glottis on the other hand becomes turbulent.

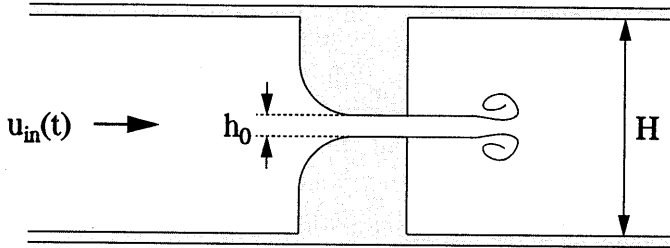


Figure 3.1: Configuration of a square-edge nozzle in a two-dimensional channel. The inflow velocity  $U_{in}$  is a function of time resulting in vortex shedding from the square edge.

The actual problem of the flow through the vocal folds is very complex due to the interaction of the flow and the movement of the vocal folds. Furthermore, flow separation occurring in the diverging part of the constriction is influenced by the jet structure, unsteadiness of the flow and movement of the vocal folds. Our interest in this type of flow lies in the fluid-dynamical description of the flow through the vocal folds and not in the interaction of flow and movement of the vocal folds. Therefore we study the flow through fixed rigid models shaped like a typical vocal-fold configuration. The problem that we study is a free jet flow into a large channel (or semi-infinite space). The jet flow is a result of flow separation in the diverging part of the constriction. Because our aim is to provide a simplified description of the flow through the vocal folds we start by studying the flow through a square-edge nozzle configuration as shown in figure 3.1. This configuration is used as a reference configuration for both the experimental as well as the numerical investigation. Then, in the next chapter, we treat the flow through vocal-fold like constrictions. Here we focus on the behaviour of the jet and are interested in the sound generation in this jet. In order to understand the importance of the different physical aspects such as viscous diffusion and compressibility we will use three different numerical methods to describe the flow through a square-edge nozzle and compare the results.

The configuration of a sudden expansion in a channel has received attention from several authors who have numerically investigated this type of flow. In most cases the focus is on quite low expansion ratios. Le *et al.* (1997) investigated the three-dimensional turbulent flow over a backward facing step with an expansion ratio of  $H/h = 1.2$ . They focus on the re-attachment of the flow. Kaiktsis *et al.* (1996) investigated the shear-layer instabilities for a two-dimensional flow over a backward facing step with an expansion ratio of  $H/h = 2$ . A similar investigation was carried out by Allenborn *et al.* (1997) studying the influence of the expansion ratio up to  $H/h = 10$ . In all these investigations the numerical model was based on the incompressible flow equations. Grinstein *et al.* (1991) calculated the evolving mixing layer while focusing on the role of feedback in vortex roll-up using a two-dimensional inviscid compressible flow model. Other authors who investigated the sound generation in a two-dimensional shear layer by means of a numerical method also used a compressible flow description (Bastin *et al.* 1997, Colonius *et al.* 1997) and also discuss the

problems of describing the acoustic source using an acoustic analogy.

This chapter is set up as follows. First an experimental investigation of the steady flow through the square-edge nozzle is presented. Results are compared to boundary-layer-theory predictions. These results will support the validity of the various assumptions that are made about the flow. Next, unsteady pressure measurements are presented and it is shown that it is possible to compute the velocity in the constriction from measured pressures. Then numerical results of three different methods are compared to each other and to experimental flow visualisations. The results of the viscous vortex-blob method are also compared to results of a boundary-layer description.

## 3.2 Experiments

### 3.2.1 Experimental set-up

The set-up used for the experiments consists of a channel containing a constriction. The shape of the constriction that is studied in this chapter is the square-edge nozzle configuration as presented in figure 3.1. The constriction is formed by two brass blocks placed opposite to each other in the channel. The channel is placed in between two large pressure reservoirs: one reservoir is the laboratory (volume approximately  $3.5 \cdot 10^3 \text{ m}^3$ ) and the other reservoir is the smaller experiment room (volume approximately  $75 \text{ m}^3$ ). Using the ventilation system of the building the room can be brought to a pressure lower than ambient while the laboratory remains at atmospheric pressure. In this way pressure differences up to 800 Pa can be attained across the set-up. The size of the reservoirs provides the stability of the pressure drop across the set-up (typically within 1 % during one experimental run). A valve operated by a spring blade is used to block the flow. By opening the valve an unsteady flow through the constriction is created. With this valve we can create two types of flow: one is a starting flow and the other is a single pulse of flow as shown in figure 3.2. By changing the characteristics of the spring blade the time-constant of the unsteady flow

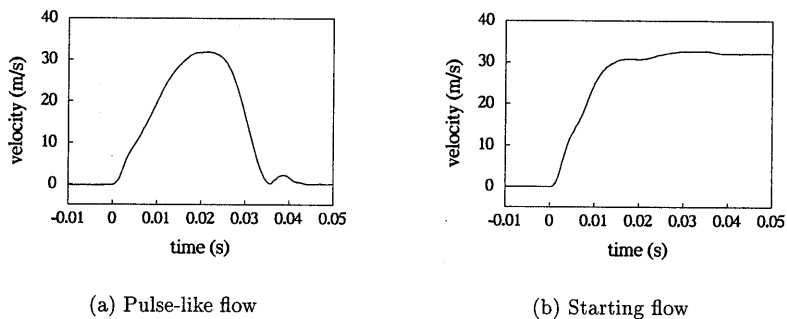


Figure 3.2: Velocity in the nozzle as a function of time.



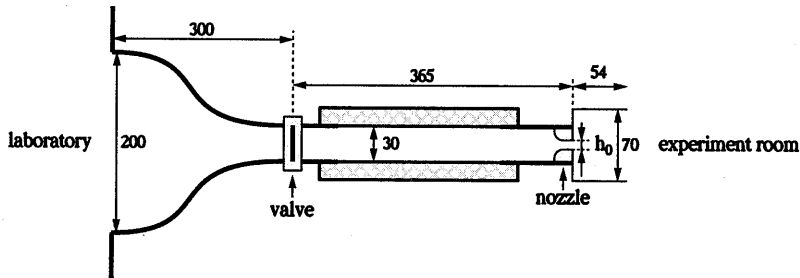


Figure 3.3: Schematic representation of the experimental set-up. Measures are in millimetres.  $h_0$  is the height of the aperture (typically 1 or 3 mm).

is controlled in the range of 5 ms to 40 ms.

In figure 3.3 a schematic representation of the set-up is shown. Using a smoothly converging inlet the air flows from the laboratory into a cylindrical pipe (diameter 30 mm). This pipe connects the inlet section to the square-edge nozzle configuration. This is followed by a short channel with a rectangular cross section (70 × 30mm). Usually glass plates are used for the side walls of this channel, however in some experiments the side walls extend no further than the end of the constriction. A detailed drawing of this region is shown in figure 3.4. At the end of the square channel the air exits the set-up and enters the experiment room. The valve is positioned just downstream of the inlet section. The pipe connecting the inlet section and the nozzle configuration has the interior walls

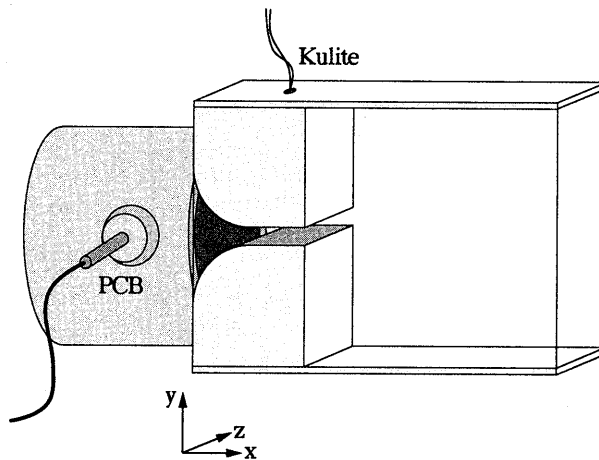


Figure 3.4: Close-up of the constriction showing the transition from the cylindrical pipe to the square constriction and channel with definition of the coordinate axes.

covered by a layer of 2 cm acoustic foam (illustrated in figure 3.3 by the shaded area) in order to dampen acoustic perturbations that result from the opening and closing of the valve. The nozzle configuration is also mechanically disconnected from the inlet section to avoid transmission of vibrations. In the set-up the geometry of the constriction and the height of the aperture  $h_0$  can be varied independently by changing the brass blocks that form the constriction. In this chapter we only present results for the square-edge nozzle configuration. In the next chapter we present results for three differently shaped (smooth) constrictions.

Using a laser detector system the opening of the valve is detected and the measurement is triggered by this signal. During an experimental run pressures are measured and sometimes the velocity is measured simultaneously using a hot-wire anemometer. The signals are fed into a data acquisition system that is connected to a personal computer by means of a 4-channel 12-bit ADC card (Keithley DAS-50). A typical experimental run lasts 500 ms while data are sampled at a frequency of 20 kHz.

The hot-wire probe consists of a 4  $\mu\text{m}$  thick wire with a length of 5 mm stretched between two prongs of the probe that is connected to a constant temperature anemometer. The hot-wire anemometer is calibrated using a separate larger free-jet set-up in which the air flow is slowly (quasi-steadily) reduced from a maximum value to zero. This allows for an independent calibration in the whole velocity range that we are interested in. The output of the anemometer as a function of the velocity is fitted using a fifth-order polynomial. This results in a typical accuracy of 2% at high velocities (in the range 10 m/s to 40 m/s). The accuracy is less in the range below 10 m/s because of difficulties in determining the velocity and due to the complex behaviour of the anemometer at low velocities.

The velocity can be measured at different positions by traversing the probe. Some measurements were carried out with the probe within the constriction of our model. For small values of the height of the aperture ( $h_0 \approx 1$  mm) we found that the probe significantly disturbed the air flow while for  $h_0 \approx 3$  mm this effect is negligible when the hot-wire probe is positioned not too deep into the constriction. Therefore the hot-wire velocity measurements are only carried out in the configuration that has  $h_0 \geq 3$  mm.

The pressure is measured at two positions in the set-up. The first position is in the pipe just upstream of the constriction (see figure 3.4). A piezo-electric transducer (PCB type 116A) with a diameter of 10.4 mm is mounted flush in the side wall of the cylindrical pipe 8 mm upstream of the start of the constriction. The signal of this pressure transducer is amplified using a charge amplifier (Kistler type 5011). Opposite the pressure transducer is a steady pressure tab (diameter 1 mm) to measure the steady pressure drop across the set-up. The second position where the pressure is measured is inside the straight nozzle channel 5 mm upstream of the square edge. Because of the size of the set-up a small pressure transducer is necessary. We used a small piezo-resistive pressure transducer (Kulite XCS 062) with a diameter of 1.6 mm. In figure 3.5 a detailed drawing of the mounting of the Kulite pressure transducer is shown. Since the diameter of the pressure tab is only 0.4 mm a very good seal is necessary to prevent any leakage. By fastening the seal control screw the Teflon seal is made to fit tightly around the pressure transducer ensuring a good seal. The pressure transducer is positioned approximately 0.5 mm lower than the pressure

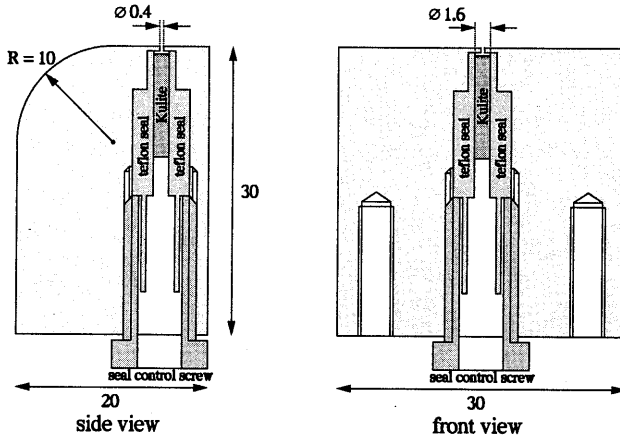


Figure 3.5: Mounting of the Kulite pressure transducer in one of the brass blocks that form the constriction. A seal made of Teflon controlled by a screw is used to ensure a tight fit.

tab thus creating a small cavity that is 0.5 mm high. This enables a fast response of the pressure transducer to pressure changes. The block containing the piezo-resistive pressure transducer can be replaced by a block with a steady pressure tab (diameter 0.3 mm) which is used for the steady pressure measurements.

In order to make a qualitative comparison between the development of the jet flow during an experiment and a numerically computed jet flow, flow visualisations have been done using a standard Schlieren method. The cylindrical pipe of the set-up is filled with a buoyancy neutral mixture of 50 % argon and 50 % neon. When the valve is opened the mixture is forced through the constriction resulting in a variation of the refractive index across the shear layers. A photo camera is focussed on the region downstream of the constriction and a single pulse of light (duration 10 ns) is generated by a Nanolite spark discharge to expose the photographic film. The Nanolite is triggered by a delay unit, which in its turn is triggered by the opening of the valve. In this way during one experimental run one picture is obtained. By repeating the experiment several times, while changing the delay time, a series of photographs is obtained that shows the development of the jet flow. By simultaneously recording the signal send to the Nanolite and the pressure signal, the time with respect to the start of the experiment associated with each picture can be determined. The time-accuracy that is achieved in this way is 0.3 ms. The reproducibility of the time history of the pressure signal during such a time series is approximately 2 %.

### 3.2.2 Experimental results

In order to confirm our assumption of laminar flow inside the nozzle in the range of pressure differences (0 to 800 Pa) and nozzle heights  $h_0$  (1 to 3 mm) we did various pressure and

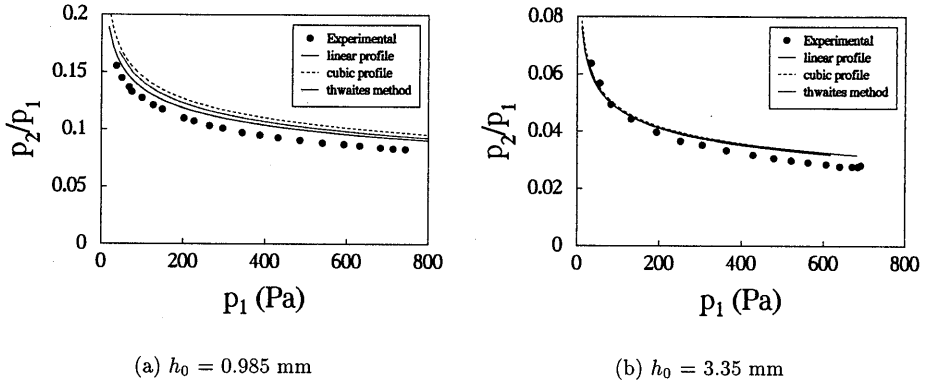


Figure 3.6: Comparing boundary-layer predictions with the steady pressure measurements obtained with the small round pressure tab.  $p_1$  is measured in the pipe and  $p_2$  is measured 5 mm upstream of the square edge in the straight nozzle channel.

velocity measurements for a steady nozzle flow. Since any pressure loss inside the straight nozzle channel is due to viscous losses (boundary-layer growth) these measurements can be compared to a pressure loss calculated by means of a boundary-layer description of the flow through the channel; a turbulent boundary layer will grow much faster than a laminar one and thus the resulting pressure loss will be much larger.

In figure 3.6 the ratio  $p_2/p_1$  of the pressure loss inside the nozzle channel is presented as a function of the pressure loss across the whole nozzle configuration for two values of  $h_0$ . Pressure  $p_1$  measured inside the cylindrical pipe 8 mm upstream of the start of the nozzle is the whole pressure loss across the nozzle. Pressure  $p_2$  is the pressure loss over the last 5 mm of the nozzle channel. By measuring  $p_2$  as a function of  $p_1$  the typical relationship between viscous losses and Reynolds number is recovered. The markers in figure 3.6 are the experimental results. Also shown by means of the lines are the results of three different boundary-layer descriptions that were treated in chapter 2. A good agreement between experiment and theory is found for both values of  $h_0$  confirming the validity of the assumption of laminar flow inside the nozzle. This is also confirmed by the hot-wire measurements of the velocity profile inside the nozzle and just outside the nozzle, as illustrated by figure 3.7.

The assumption of two-dimensional flow inside the nozzle is supported by the velocity profile measured across the width of the channel. This velocity profile is presented in figure 3.8. This profile is measured just outside the nozzle and it shows that the flow is uniform across a large part of the width of the channel. Also shown is the ideal uniform profile inside the channel. As one can observe the flow is uniform except for a small region near the side walls of the channel. Attempts to measure the pressure  $p_2$  using a pressure tab in the side walls of the channel indicated significant deviations from the measurements at the

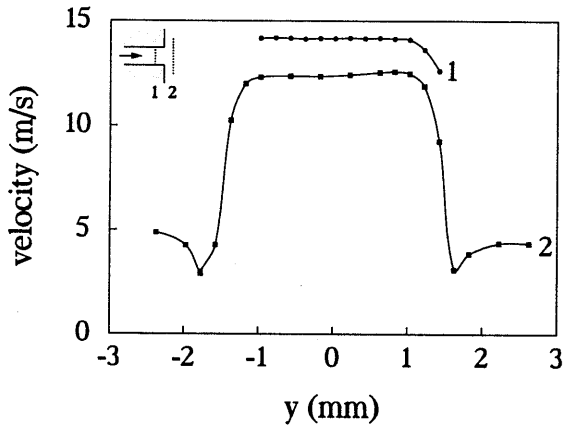


Figure 3.7: Velocity profile just inside the nozzle channel(1) and just outside the exit (2). This demonstrates the uniform bulk flow and the thin (laminar) boundary layers near the top and bottom wall.

centre of the channel described above. This suggests that three-dimensionality of the flow does play a role (see appendix B). However, these velocity measurements confirm that the influence is small when we focus on the flow in the middle of the set-up. Indeed the large “boundary-layer” thickness of approximately 3 mm, which can be observed at the sides of

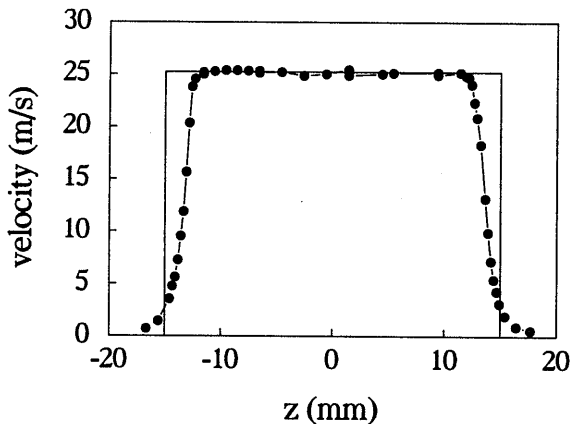


Figure 3.8: Velocity profile across the width of the slit on the centre line of the nozzle just outside the exit. The velocity profile is uniform except near the side walls of the nozzle. The solid line represents the ideal two-dimensional profile.

the channel in the  $z$ -direction in figure 3.8, are expected to be due to three-dimensional flow in the sharp corners of the channel.

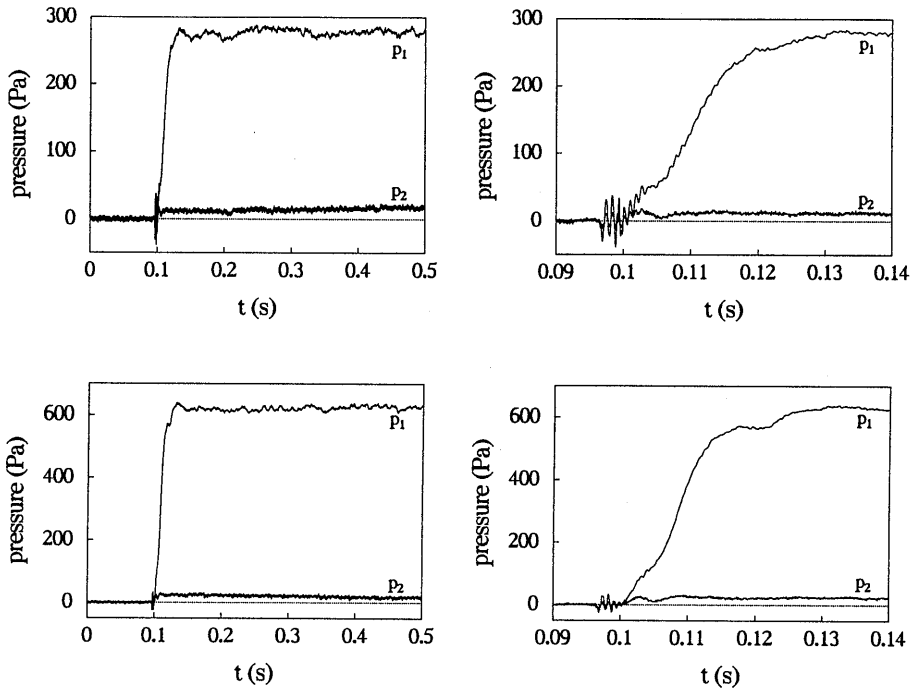


Figure 3.9: Pressure measured in the pipe  $p_1$  and in the constriction  $p_2$  of the square-edge nozzle geometry:  $h_0 = 3.35$  mm, top graphs  $\Delta p = 270$  Pa, bottom graphs  $\Delta p = 622$  Pa. The right graphs are a close-up of the left graph, showing the transient behaviour.

In figure 3.9 unsteady pressure measurements in the square-edge nozzle are shown. Pressure  $p_1$  is measured in the cylindrical pipe 8 mm upstream of the start of the constriction and pressure  $p_2$  is measured inside the channel of the nozzle 5 mm upstream of the square edge. The experiment lasted 0.5 s as is shown in the left graphs. The right graphs show a close-up of the transient behaviour in a time range of 50 ms. The origin of the time axis is determined by the trigger for the measurement. In these graphs the trigger signal was generated at  $t = 0.1$  s: by using the pre-trigger capability of the ADC-card the measurement has already been recorded 0.1 s before the trigger is generated. The actual start of the experiment is not well determined since the laser detector set-up is triggered by the valve after it starts moving but it is reasonable to assume this to be close to the trigger point. Using the trigger point as a reference point in time for each experiment results in reproducible measurements. A high-frequency oscillation precursor is starting

approximately 3 ms earlier. This precursor is expected to be due to acoustic waves generated by transversal movement of the valve just before it has opened. Using the steady pressure drop  $\Delta p = \lim_{t \rightarrow \infty} p_1(t)$  the reference velocity  $u_0$  is evaluated by means of the steady Bernoulli equation:  $u_0 = \sqrt{2\Delta p/\rho}$  in which  $\rho$  is the density of air ( $\rho = 1.204 \text{ kg/m}^3$  for dry air at 20 °C and 1 atmosphere). So the Mach number in the nozzle is less than 0.1 and the Reynolds number varies from 4700 for  $\Delta p = 270 \text{ Pa}$  up to 7200 for  $\Delta p = 622 \text{ Pa}$ . The Strouhal number based on the length of the nozzle (20 mm) and the rise time of the pressure (approximately 20 ms) is 0.05 and 0.03, respectively.

Some typical behaviour can be observed in both signals ( $p_1$  and  $p_2$ ). Initially pressure  $p_1$  rises very rapidly but after 5 ms there is a small hesitation. This is expected to be related to the acoustic response of the pipe upstream of the nozzle. Similarly the pressure  $p_2$  rises very rapidly the first few milliseconds but then decreases again to a minimum value after 5 ms. This is explained by the fact that during the initial phase of the experiment boundary layers are still negligible and the flow behaves like a potential flow. In that case the only time-dependent contribution to the pressure  $p_2$  results from inertial effects. The acceleration of the flow is time dependent and apparently decreases after a few milliseconds. When the flow is no longer accelerating at a high rate the pressure in the channel of the nozzle is close to the pressure at the exit. But the boundary layer is growing in time and consequently the pressure increases again. At the same time a jet structure is developing which also can contribute to the pressure measured inside the nozzle channel. After approximately 30 ms steady values are reached. These steady values for  $p_1$  and  $p_2$  agree with the steady data that are presented in figure 3.6.

Because in the bulk flow (outside the boundary layer) viscous effects are negligible the unsteady Bernoulli equation can be applied to determine the velocity in the nozzle channel from the pressure measurements:

$$\rho \frac{\partial \phi_1}{\partial t} + \frac{1}{2} \rho u_1^2 + p_1 = \rho \frac{\partial \phi_2}{\partial t} + \frac{1}{2} \rho u_2^2 + p_2 \quad (3.1)$$

in which  $\phi$  is the velocity potential. Neglecting displacement effects of the boundary layer on the velocity and assuming a uniform velocity profile across the height of the channel (assumption of one-dimensional bulk flow) the inertial contribution can be written as an effective length  $L_{eff}$  times the time derivative of the velocity. This yields:

$$L_{eff} \frac{\partial u_2}{\partial t} = \frac{1}{2} (u_1^2 - u_2^2) + \frac{p_1 - p_2}{\rho} \quad (3.2)$$

in which  $L_{eff}$  is determined by the geometry of the channel and is defined as:

$$L_{eff} = \int_{x_1}^{x_2} \frac{u(x)}{u_2} dx = \int_{x_1}^{x_2} \frac{h_0}{h(x)} dx \quad (3.3)$$

where we used the one-dimensional continuity equation  $h(x)u(x) = \text{constant}$ . In our case ( $h_0 = 3.35 \text{ mm}$ )  $L_{eff} = 2.48h_0$ .

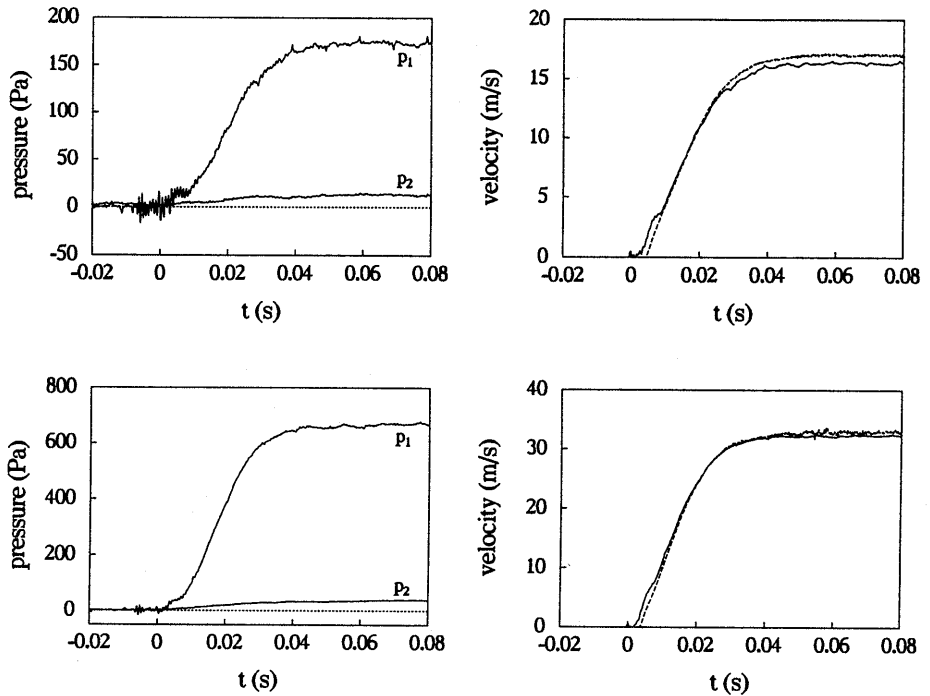


Figure 3.10: In the right graphs the velocity measured (dashed line) in the constriction 5 mm upstream of the square edge is compared with the velocity calculated (solid line) by integration of the unsteady Bernoulli equation using the measured pressures  $p_1$  and  $p_2$  shown in the left graphs.  $h_0 = 3.35$  mm, top graphs  $\Delta p = 178$  Pa, bottom graphs  $\Delta p = 677$  Pa.

In figure 3.10 the velocity measured at the level of the pressure transducer (5 mm upstream of the square edge) inside the nozzle channel is presented, together with the velocity calculated by equation (3.2) using the pressure signals shown in the left graphs. One low pressure-difference result ( $\Delta p = 178$  Pa) and one high pressure-difference result ( $\Delta p = 677$  Pa) is shown. These results confirm that the velocity calculated from the pressure measurements is accurate. This is most useful because, as mentioned earlier, for narrower channels we cannot use the hot wire to measure the flow velocity. The general agreement between calculation and measurement is quite good, although at the start of the experiment at low velocities there is a distinct systematic deviation. The hot-wire measurement produces systematically lower values of the velocity during the first milliseconds of each experiment. Typically this velocity is 2 m/s too low, which is very significant since this happens when velocities are still small. But also compared to the difference at the steady-flow conditions



(usually less than 0.5 m/s) this difference is very high. An explanation could be that due to the noise on the pressure signals the integration does not yield accurate results. Since the time-integration is non-linear, this could result in a systematic deviation. Using a smoothing technique we were able to reduce the noise on the pressure signals. The velocity calculated from these signals, however, did not change significantly. It is therefore unlikely that this is the explanation for the systematic difference. Another possibility is that the response of the hot-wire anemometer is too slow. It is well known that an ordinary hot-wire set-up is not very reliable for rapidly changing low velocities. Special care has to be taken to ensure accurate measurements under these conditions. Apparently the diameter of the hot wire ( $4\ \mu\text{m}$ ) is too large for the rapid response that is needed in the initial phase of our experiments. This still remains to be investigated.

### 3.3 Numerical simulations

#### 3.3.1 Numerical methods and input

In the remaining part of this chapter we focus on comparing the results of three different numerical methods representing three different descriptions of the flow. The viscous vortex-blob method (see chapter 2) is a numerical method that solves the two-dimensional incompressible Navier-Stokes equations in the vorticity formulation. This method therefore includes viscous diffusion and is Reynolds-number dependent. Flow separation is a natural result of the simulation. The method does however not include wave propagation so that an acoustic analogy is necessary to determine the aeroacoustic response. A simplification of this method is the inviscid vortex-blob method (see chapter 2). This method is similar to the viscous vortex-blob method minus viscous diffusion. It solves the two-dimensional potential flow equations including singularities such as point vortices. In this method flow separation has to be modelled by either a Kutta condition (in the case of a sharp edge) or by a boundary-layer model coupled to the inviscid bulk flow. The method is intended for high-Reynolds-number flows in which viscous diffusion is negligible. Also in this method an acoustic analogy is necessary to determine the aeroacoustic response. The third method is an Euler method. It solves the inviscid compressible flow equations (Euler equations) in either a two- or three-dimensional domain. Although the Euler method does not include viscous effects, flow separation from sharp edges is an unavoidable result of the numerical scheme; the presence of only a tiny amount of numerical diffusion is sufficient to cause the flow to separate from a sharp edge, resulting in a non-singular flow around the edge. Similar to the inviscid vortex-blob method, this method does not depend on the Reynolds number and should be used as an approximation for high-Reynolds-number flows. In contrast to the two incompressible vortex methods the aeroacoustic response can be a natural result of this method. It appears that also in this case the aeroacoustic response is easier to extract from the calculated flow field by means of an acoustic analogy than directly by means of local flow "measurements".

In order to compare the results of the simulations to experimental flow visualisations

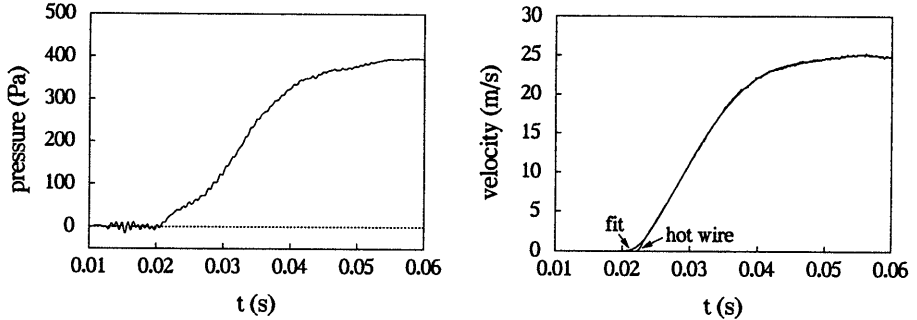


Figure 3.11: Experimental pressure and hot-wire velocity measurement used as input for the numerical simulations. In the right graph also the polynomial fit to the velocity profile is shown. The height of the nozzle channel  $h_0$  is 3.25 mm.

and velocity measurements, the time-dependent inflow velocity is obtained from an experimental measurement. In figure 3.11 the pressure  $p_1$  measured 8 mm upstream of the start of the nozzle and the velocity measured on the centre line of the nozzle channel 3.4 mm (approximately  $1 \times h_0$ ) upstream of the square edge of the nozzle exit. The height  $h_0$  of the channel is 3.25 mm. The trigger is generated at  $t = 0.0194$  s. The time evolution of the velocity is fitted with two polynomials of order 6; one is fitted to the velocity as a function of time in the first 5 ms and the other is fitted to the velocity in the range of 5 to 30 ms. They are also shown in figure 3.11. At low velocities the fit to the velocity signal deviates from the measured velocity signal. This is due to the imposed condition that at the start of the experiment the time derivative of the velocity has to be zero in order to prevent a jump in pressure.

The fitted time dependence of the velocity  $u_{in}(t)$  is used to determine the two-dimensional inflow of air  $\Phi(t)$  that is prescribed in the numerical simulations by using a simple estimate of the displacement thickness based on Blasius's boundary-layer for a flat plate ( $\delta^* = 0.018h_0$ ):  $\Phi(t) = u_{in}(t)/(h_0 - 2\delta^*)$ . The Reynolds number is based on the two-dimensional volume flux and is evaluated to be 5270. The Strouhal number based on the rise time of the pressure signal and the nozzle length (0.02 m) is estimated to be 0.04. Because the three numerical methods require different input parameters we now briefly discuss the methods and the input that was used in each case.

The computational domain used in the numerical simulations with the viscous vortex-blob method is shown in figure 3.12. The inflow-velocity determined by  $\Phi(t)$  is uniformly imposed on the left inflow boundary. The height of the inflow channel is related to the radius of curvature  $r$  of the nozzle inlet and the throat height  $h_0$ . It is defined as the reference length  $l_{ref}$  in the simulation:  $l_{ref} = 2r + h_0$ . On the right the outflow boundary is a far-field semi-circular domain (at a distance of  $27 l_{ref}$ ) On this boundary a radial outflow is assumed and the outflow velocity is determined from the inflow velocity by the

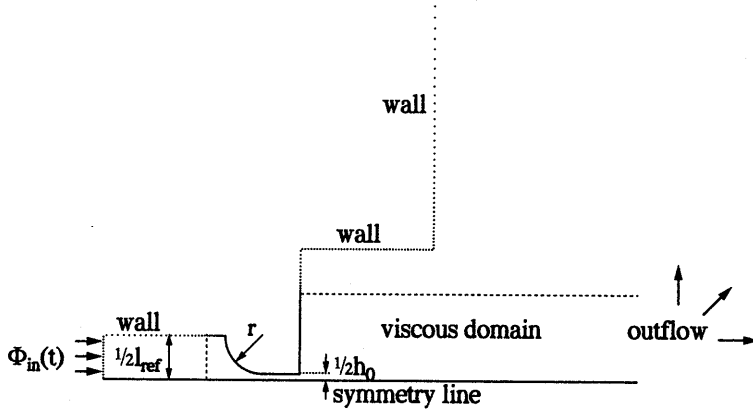


Figure 3.12: Two-dimensional domain used in the numerical simulations with the viscous and inviscid vortex-blob method. Nozzle height  $h_0$  is an input parameter. The inflow channel has a total height of  $2r + h_0$ .

continuity equation. Since the geometry that we are interested in is symmetric with respect to its centre line, the computation is restricted to the upper half of the domain, hence the use of a symmetry line as a lower boundary and only half a model as the upper boundary. This reduces the computational time and memory requirements by approximately a factor of two, but imposes a symmetry to the flow.

The boundary is discretised by a set of panels. A densification of panels is applied in the region of the square-edge nozzle model and on the symmetry line. The viscous vortex-blob method requires a dense distribution of panels along the whole section of the wall where viscous diffusion is acting which is the whole nozzle geometry. The numerical simulation required 1700 panels to represent the geometry and used 156,000 point vortices to discretise the vorticity field. Using a fourth-order Runge Kutta time integration, 640 equal time steps are needed to compute the flow for a period of time of 22 ms. The run-time of the calculation was less than one week on a DEC-Alpha 266 MHz workstation.

The region in which the full (viscous) Navier-Stokes equations are solved is restricted to the viscous-flow domain. Outside this domain only the inviscid incompressible-flow equations are solved. The viscous-flow domain includes the whole jet-region and the region of flow separation (the whole nozzle area). The nozzle area is covered by a fine mesh (approximately 100 points per channel height) based on the diffusive length scale and time step. Here viscous diffusion is applied at each time step. The jet region is covered by a twice courser mesh and diffusion is applied every four time steps. In the inflow domain and in the upper region of the outflow channel viscous diffusion is neglected completely since these regions are expected to have negligible influence on the results.

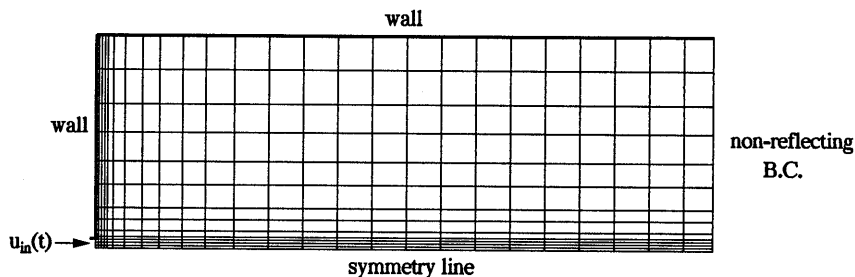


Figure 3.13: Two-dimensional domain used in the Euler simulation. The mesh is only an indication of the actual mesh used in the simulation in order to show the regions in which refinement was applied.

The computational domain used in the numerical simulations with the inviscid vortex-blob method is the same as shown in figure 3.12. In this case the outflow boundary is at a distance of  $18 l_{ref}$ . Similarly the outflow is assumed to be radial and is determined from the inflow velocity by the continuity equation.

The distribution of panels along the boundary of the computational domain is different from that used in the viscous-flow method, since the requirements are different. The distribution of panels is very dense near the square edge at the exit of the nozzle ( $0.0015 h_0$  at the edge) in order to maintain an accurate description of the local flow and to ensure the accuracy of the approximate Kutta condition. The distribution on the symmetry line is however very similar to the one for the viscous-flow method. The numerical simulation required 1900 panels to represent the geometry and used 7000 point vortices to discretise the shear layer. Using a fourth-order Runge Kutta time-integration 7000 time steps are used to simulate 21 ms of the flow. The first 1000 time steps are distributed non-uniformly over the first 1.3 ms. The run-time of the total calculation was approximately one week on a DEC-Alpha 266 MHz workstation.

As we will show later in this chapter an important parameter for the development of the details in the jet flow is the shear-layer thickness. The vortex-blob method is however intended as an approximation for a flow with an infinitesimal shear-layer thickness ( $Re \rightarrow \infty$ ). This means that in its purest form the vortex-blob method cannot be applied to this problem. As we have demonstrated in an earlier paper (Hofmans *et al.* 1995) a solution to this problem is provided by relating the desingularisation parameter  $\delta$  to the shear-layer thickness. We are aware of the fact that this is not a physically correct solution and that this is not an alternative to diffusion, as was pointed out by Greengard (1985). The results obtained in this way, however, are very convincing. In this numerical simulation the desingularisation parameter  $\delta$  is equal to the time-dependent displacement thickness at the exit of the nozzle channel as obtained by the simplified unsteady boundary-layer model as discussed in chapter 2 using a linear velocity profile in the boundary layer.  $\delta(t)$  is therefore used as an additional input parameter in the simulation.

The Euler solution of the square-edge nozzle problem was computed using a second-order accurate finite-volume method, coupled with a scalar non-linear artificial viscosity model. Time integration was performed using an explicit Runge-Kutta technique, see (Hulshoff *et al.* 1996). The inflow and outflow boundary conditions were applied using the compatibility relations as described by Thompson (1987, 1990). The inflow condition was applied directly at the exit plane of the channel (i.e. the channel was not included in the simulation) by specifying a velocity profile as a function of time. Although this prohibits the flow at the exit plane of the nozzle from responding to the developing flow inside the domain, it was found to be the most convenient solution in order to impose a boundary condition similar to the ones used in the two vortex-blob methods. The outflow condition was applied by specifying zero incoming wave strengths.

Flow separation in the Euler method is a result of the numerical viscosity of the scheme. This also implies that the thickness of the resulting shear layer is determined by the numerical viscosity. In order to avoid a mesh-dependence of the solution a boundary-layer profile is prescribed at the exit plane of the nozzle channel. The inflow velocity was applied as a uniform profile, except for a linear region of thickness  $2\delta^*$  close to the wall. The displacement thickness  $\delta^*$  is a function of time and is equal to the one used in the inviscid vortex-blob simulation. The calculation was performed on a rectangular half-domain shown in figure 3.13 with a discretisation (and size) of 320 cells (0.107 m) in the stream-wise direction and 160 cells (0.037 m) in the normal direction. The cells were concentrated at the inflow region and along the shear layer, as is illustrated by the mesh shown in figure 3.13. Approximately 400,000 time steps are used to compute 18 ms of the flow. The run-time of this calculation was approximately four weeks on a workstation equivalent to a DEC-Alpha 266 MHz workstation.

### 3.3.2 Numerical results

Figure 3.14 shows the development of the jet structure in time for a Reynolds number of 5270. The pressure signal as a function of time associated with these results is given in figure 3.11. The flow visualisations have been done by a standard Schlieren technique. The Schlieren effect is obtained by a spatially changing refractive index due to the use of a mixture of 50 % argon and 50 % neon inside the flow channel. Since this mixture is convected with the local flow and diffusion of this mixture into the surrounding air is similar to the diffusion of vorticity by viscous effects, the visualisations showing the contact line between this mixture and air provide qualitative information about the distribution of vorticity. Vorticity that is shed from the square edge satisfies equivalent equations of convection and diffusion. We therefore compare the flow visualisations to a numerically calculated spatial distribution of vorticity. Since the time accuracy of the photographs is only 0.3 ms and the output of the numerical methods is only available at certain points in time this only provides us with a qualitative comparison of the results of the three numerical methods and the results of the experiment.

Results of the viscous vortex-blob method are presented in figure 3.15 by means of the spatial distribution of vorticity. The lower half of each picture is obtained by flipping the

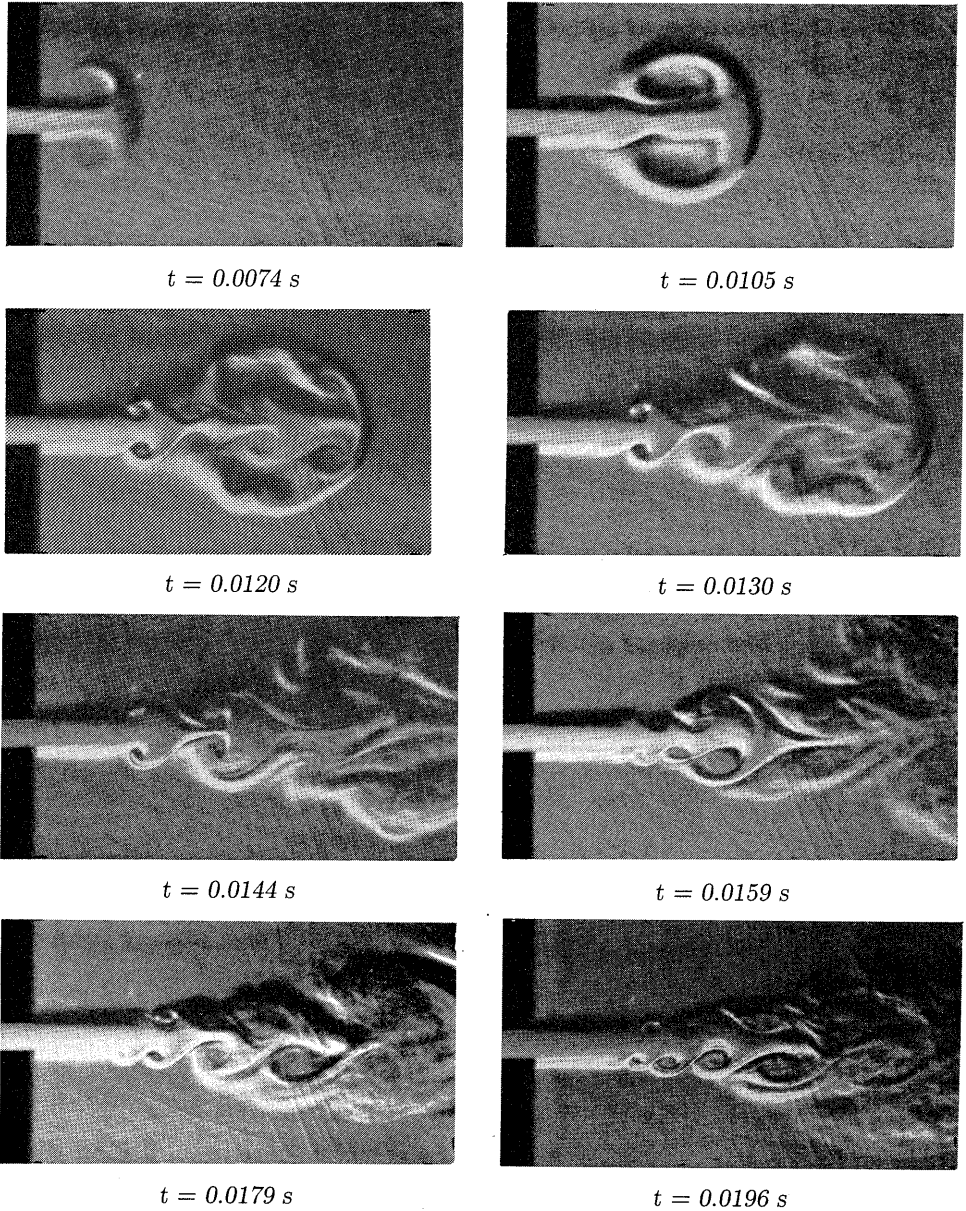


Figure 3.14: Flow visualisations by means of Schlieren photography in the square-edge-nozzle set-up.  $\Delta p = 394 \text{ Pa}$ ,  $Re = 5270$  and  $h_0 = 3.25 \text{ mm}$ .

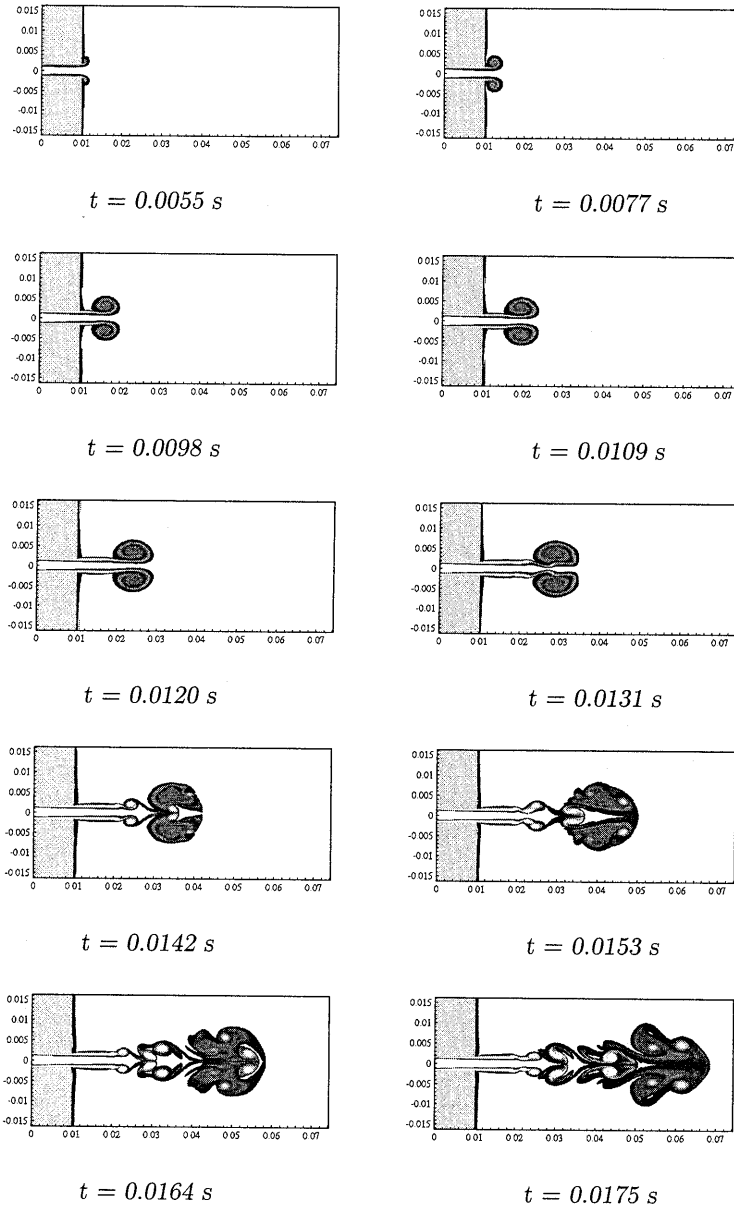


Figure 3.15: Contours of constant vorticity at different moments in time. Results obtained with the viscous vortex-blob method for  $Re = 5270$  and  $h_0 = 3.25 \text{ mm}$ .

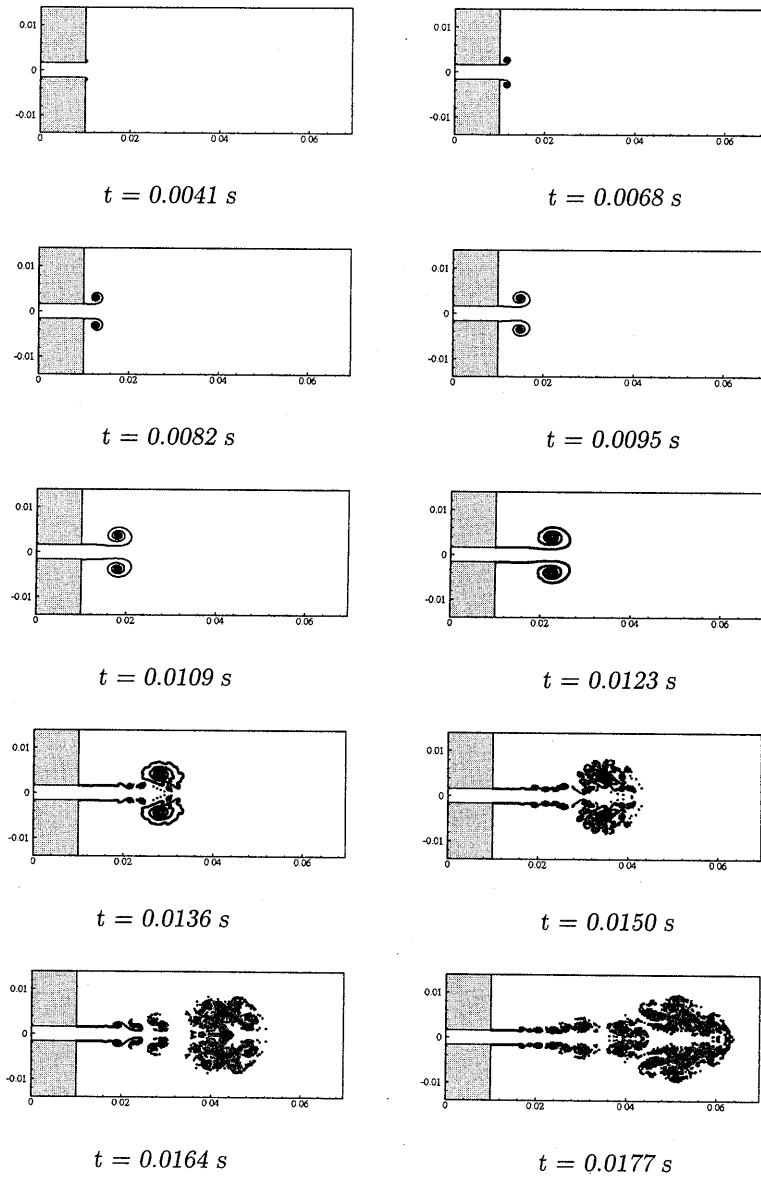


Figure 3.16: Vortex-blob positions as a function of time showing developing shear layer and the resulting jet structure. Results obtained with inviscid vortex-blob method for  $\Delta p = 394 \text{ Pa}$  and  $h_0 = 3.25 \text{ mm}$ .



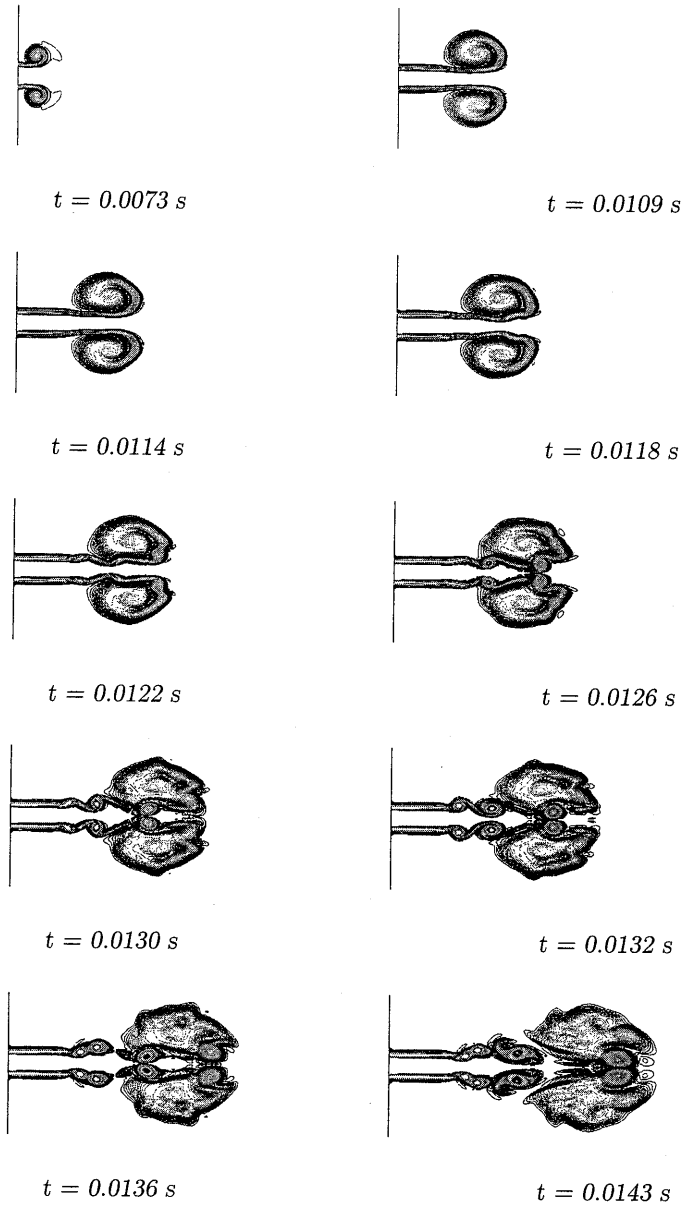


Figure 3.17: Contours of constant vorticity at different moments in time. Results obtained with the Euler method for  $\Delta p = 394 \text{ Pa}$  and  $h_0 = 3.25 \text{ mm}$ .

upper half. The sign of the vorticity has not been changed for visualisation purposes. In figure 3.16 the vortex positions obtained by the inviscid vortex-blob method are shown as a function of time thus visualising the resulting jet structure. Finally, in figure 3.17 results of the Euler method are plotted by means of contours of constant vorticity.

The experimental flow visualisations show the following time history of the jet structure. Initially a large-scale dipolar vortex structure is formed that results in the jet flow in its wake. After 10 ms an instability is observed in the stem of the large-scale vortex structure. This is apparently the onset of instabilities in the shear layer that is trailing the initial vortex structure. It appears that these instabilities are convected along the shear layer and are subsequently taken up by the large-scale vortex structure. After 11 ms multiple secondary vortices are observed, also inside the large-scale vortex structure. The recognisable structure of one large-scale vortex is lost after 13 ms and after 14 ms the coherence of the secondary vortices inside the large-scale structure is lost due to the development of (three-dimensional) turbulent flow. The jet structure has become asymmetric after 15 ms. During the last 5 ms the jet flow still contains a region in which two-dimensional coherent vortex structures are dominant, although the leading part has become fully turbulent. These results confirm that the assumptions of two-dimensionality and symmetry are reasonable up to 14 or 15 ms after the start of the experiment. They also illustrate that, even after the jet structure has become turbulent and asymmetric, two-dimensional structures still play a role in the time-dependent jet flow.

Apart from the transition to turbulent flow and the asymmetric jet structure the results of the numerical simulation show similar global behaviour. The exact moment at which the jet instabilities appear in the shear layer are different for each simulation. For instance, the viscous blob method shows these instabilities only after 13 ms. The different characteristics of the methods can also be recognised from the results. The viscous-flow method can maintain the structure of the secondary vortices very well, even in the large-scale vortex structure individual vortices can still be recognised. It also shows a lot of details of the interactions taking place between the secondary vortices in the form of pairing and merging. On the other hand, the Euler method has problems maintaining the structure of individual vortices, since the numerical dissipation is acting strongly on the regions of concentrated vorticity. The predicted onset of instabilities is quite reasonably in agreement with experiments. In the inviscid vortex-blob calculations the vortex structures lose their well defined structure after 14 ms due to stretching of the shear layer and interactions of a large number of individual vortex blobs. The global jet structure is however still recognisable.

A more quantitative comparison between experiment and numerical simulations is shown in figure 3.18. The velocity measured as a function of time at six positions along the centre line is compared to the numerical results. The velocity was measured inside the nozzle channel at  $x = -1h_0$ , at the nozzle exit  $x = 0h_0$  and outside the nozzle at  $x = 1h_0$ ,  $x = 2h_0$ ,  $x = 3h_0$ ,  $x = 4h_0$ . Because the three numerical methods yield results that are very similar, the three velocity profiles are separately plotted in each graph. The velocity gives an indication of the arrival of the jet structure at each position (note the sudden strong increase). This property is well predicted by each method and is very insensitive to details. However, the results of the inviscid vortex-blob method are clearly lagging behind.

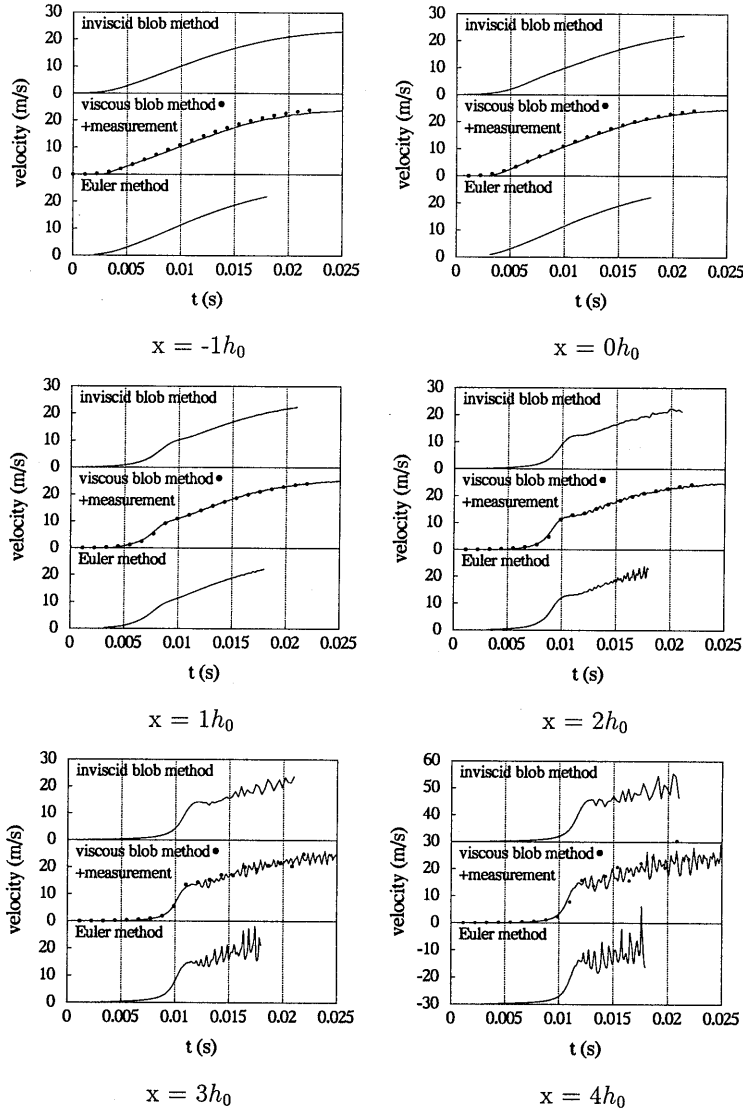


Figure 3.18: Velocity measured on the centre line and the numerical results. The velocity is measured at 6 positions: inside the nozzle channel at  $x = -1h_0$ , at the nozzle exit  $x = 0h_0$  and outside the nozzle at  $x = 1h_0$ ,  $x = 2h_0$ ,  $x = 3h_0$ ,  $x = 4h_0$ . The top line in each graph is the result of the inviscid vortex-blob method. The middle line is the experimentally measured velocity while the markers  $\bullet$  are results of the viscous blob method. The bottom line is the result of the Euler method.

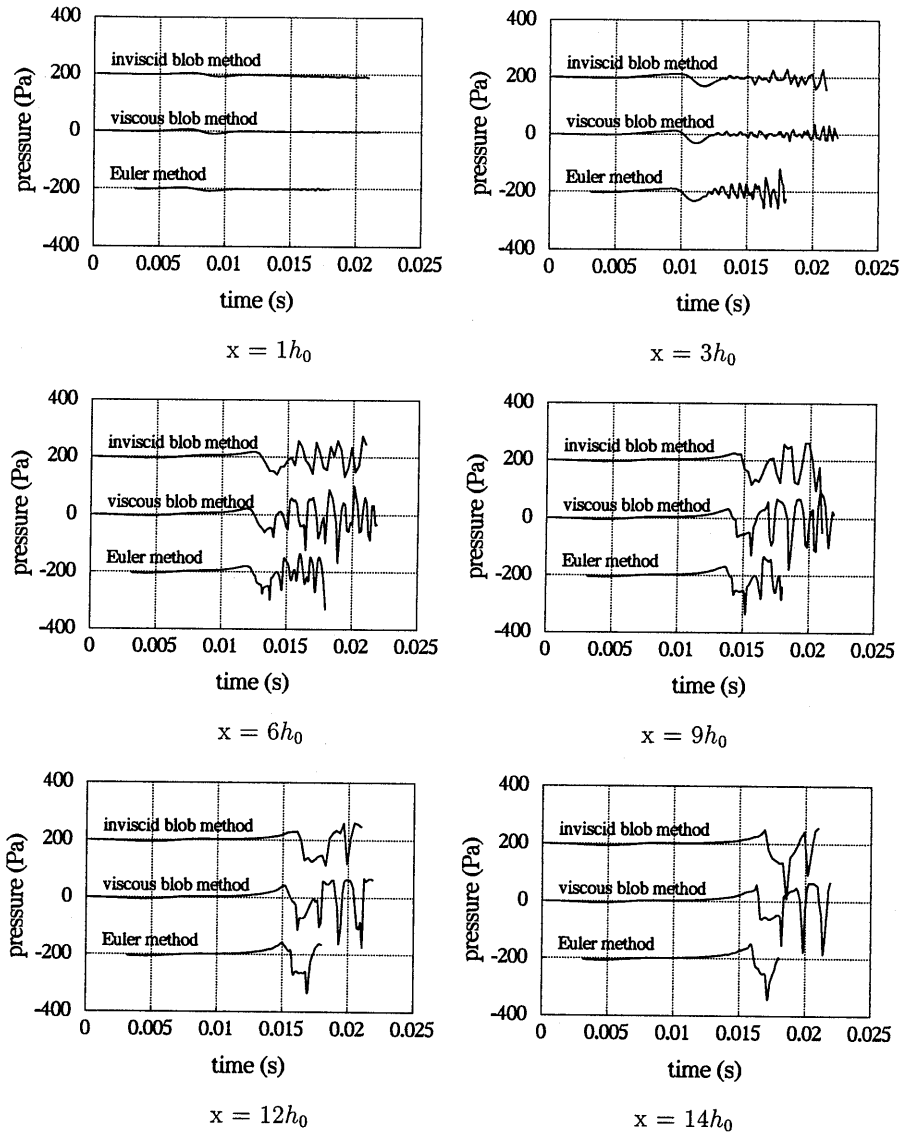


Figure 3.19: Pressure relative to the pressure at the exit plane of the nozzle on the symmetry line as a function of time at 6 positions:  $x = 1h_0$ ,  $x = 3h_0$ ,  $x = 6h_0$ ,  $x = 9h_0$ ,  $x = 12h_0$ , and  $x = 14h_0$ . Results of the three numerical methods are compared: top lines are inviscid vortex-blob results; middle lines are viscous vortex-blob results; and bottom lines are Euler results.

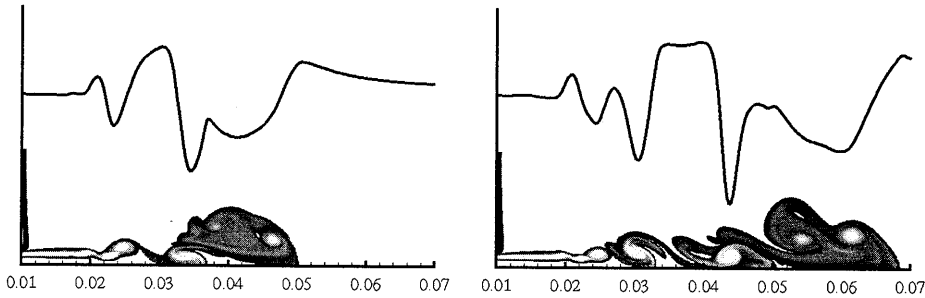


Figure 3.20: Relating the pressure on the symmetry line to the vortex structures in the jet.

This might be related to the treatment of the vortex blobs when the boundary condition is imposed. The treatment results in a lower convection velocity of the vorticity because the vortex blobs represent a shear layer of zero thickness.

The appearance of secondary vortices can be detected by means of high-frequency oscillations. Also this is quite well predicted by the Euler method and the inviscid vortex blob method. The amplitude of these oscillations seem to be exaggerated by the Euler method. The data for the viscous blob-method are not sufficient to draw a definite conclusion about this.

Comparing pressure signals obtained by the three numerical methods on the symmetry line as a function of time shows similar results. These results are shown in figure 3.19. Figure 3.19 illustrates that the frequencies of the pressure fluctuations are very similar in all three methods and that the frequency changes spatially as we will show in more detail further on.

Pressure fluctuations recorded on the symmetry line are related to the instabilities and secondary vortices as is shown in figure 3.20. A pattern of vortex structures results in a distinctive pressure signal on the symmetry line of the jet structure. Associated with each vortex core is a spatial pressure minimum, while the region between two vortex structures is characterised by a spatial maximum in the pressure. This implies that by recording the pressure along the symmetry line as a function of time a concise history of the developing jet flow is obtained. The result is shown in figure 3.21 for the three numerical methods. The pressure is presented as a function of space and time. The spatial range is 0 to  $14h_0$  from the nozzle exit and the time range is 3 to 18 ms. In these figures a complex pattern of local pressure minima and maxima can be observed. As we can relate these pressure extremes to passing vortex structures, one can recognise a complex pattern of interacting vortex structures.

Clearly recognisable is the large-scale vortex structure. It manifests itself by the large curved area of low pressure. One can see that the vortex structure is accelerating while moving downstream and absorbing a lot of smaller vortices (the dark lines). One can also

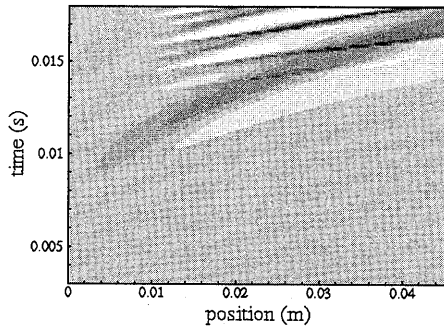
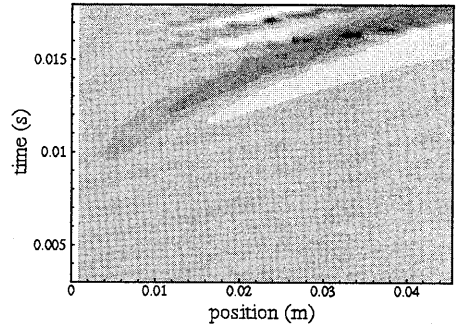
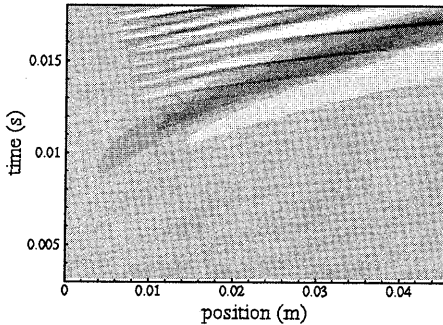
*Viscous vortex-blob method**Inviscid vortex-blob method**Euler method*

Figure 3.21: Plot of pressure on the symmetry line as a function of time and space. Darker shades represent low pressures while lighter shades represent high pressures.

see that these smaller scale vortices sometimes are the result of two still smaller vortices pairing and merging into one structure. Another distinct feature is the pressure maximum just in front of the large-scale vortex structure. This is associated with the pressure of a kind of stagnation point just in front of this structure. Fluid in the jet above the symmetry line is moving rapidly upwards while the fluid in the jet below the symmetry line is moving rapidly downwards. On the symmetry line these conflicting effects result in a very low velocity, and hence a high pressure.

Pairing and merging of vortices is a very important phenomenon in the developing jet flow. We will show that frequencies associated with this behaviour are in the audible range and might therefore be important as sources of sound in human speech production. It is a well-known phenomenon in the study of free-shear-layer flows and free-jet flows that

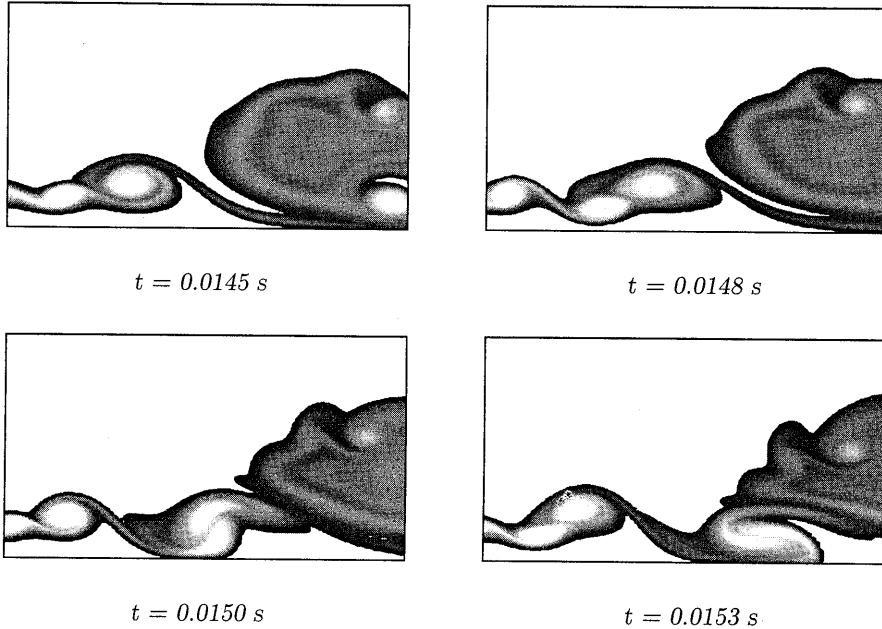


Figure 3.22: Close-up of the merging/pairing taking place in the shear layer. Result obtained by means of the viscous vortex-blob method. The horizontal range is 0.02 m.

pairing and merging of vortices is very important for the spatial development of these types of flow (Ho & Huerre 1984, Huerre & Monkewitz 1990). Grinstein *et al.* (1995) present a figure that illustrates vortex ring histories by visually tracking the centres of vortex cores. This results in a graph very similar to the graphs presented in figure 3.21.

Figure 3.22 shows a close-up of the pairing and subsequent merging of two secondary vortices. The figure again shows the vorticity distribution in a small part of the flow domain (0.02 m). The pictures displayed in figure 3.22 are the result of the viscous vortex-blob simulation and are a close-up of the results presented in figure 3.15. This figure illustrates that the pairing/merging process is a very rapid process. Within one millisecond two vortices approach each other, start co-rotating and subsequently merge into an effectively single vortex structure. The last picture shows even a new pairing starting at the same position as where the previous pairing started.

Due to the time scale and time-dependence of the inflow in the previous simulations it is not possible to get any accurate results for the frequency associated with the above presented phenomenon. Therefore an additional numerical simulation was carried out with the viscous vortex-blob method for the purpose of obtaining this kind of information. The simulation has been performed in the square-edge nozzle geometry but at a lower Reynolds

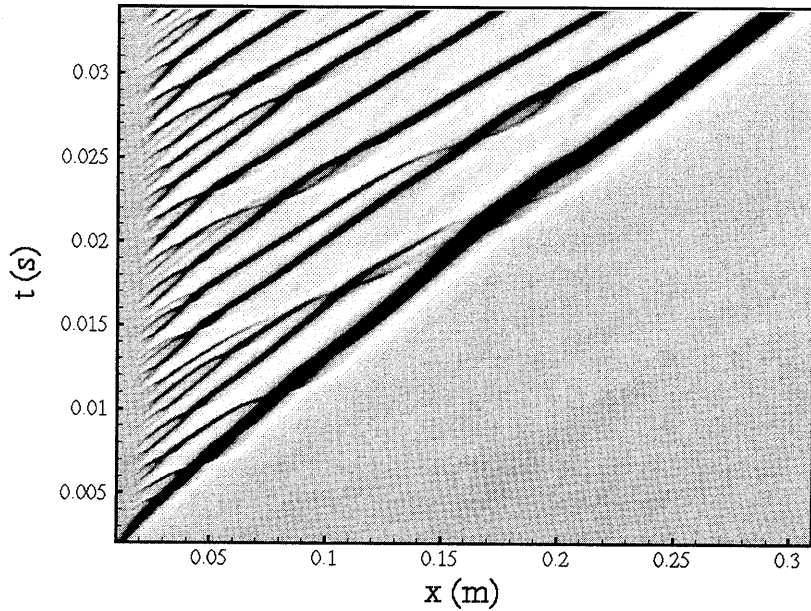


Figure 3.23: Pressure along the symmetry axis as a function of time. The flow is impulsively accelerated to a reference velocity of 15.8 m/s and the nozzle height is 3.25 mm, resulting in  $Re = 3410$ . Results obtained with the viscous vortex-blob method.

number ( $Re = 3410$ ). In this way a longer time history could be obtained at the same computational cost. Similarly the time-history of the inflow was changed so that a steady state was approached within the simulation time. To this purpose the flow was linearly accelerated from rest to its steady value within 1.43 ms. Figure 3.23 shows the pressure plot as a function of time and space, thus providing the concise history of the developing jet flow. This picture shows that previous results only showed a small part of what is taking place in this kind of two-dimensional jet flow.

A complex pattern of pairing/merging vortices can be recognised and even co-rotating vortices can be distinguished. Clearly visible is the fact that after one merging has taken place, further downstream another merging will happen. In this way vortex structures undergo multiple mergings. These processes result in quasi-periodic pressure signals. In fact this figure shows that the positions of first, second, and subsequent mergings are not randomly placed in space but are limited to certain regions.

Another feature that is evident is that (on average) the distance between subsequent mergings is growing. This is a well known phenomenon in free shear-layer instabilities, which, by forcing the flow at the right frequency, can exhibit this feature very distinctly. It was found that the distance between subsequent mergings is doubling with each merging taking place. This kind of behaviour is also found in the present results, although the



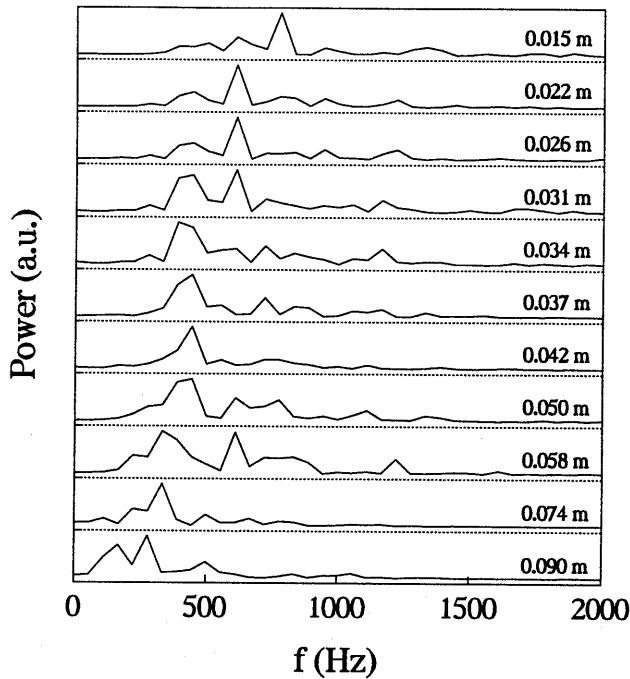


Figure 3.24: Power spectra of the pressure signal at different positions along the symmetry line for the impulsively started jet flow. Note the shift towards lower frequencies in the downstream direction. Results obtained with the viscous blob method. Experimentally found onset of turbulence takes place at 0.03 m.

periodicity is not so exact because we do not impose a basic frequency by forcing the flow. The power spectra show that these periodic features are still present.

The power spectra shown in figure 3.24 were obtained by applying a fast Fourier transform to the pressure signals as a function of time at various spatial positions. The distance with respect to the nozzle exit is increasing in the downstream direction from top to bottom in the figure. The preferred frequency of the jet flow is clearly a function of this distance. The frequency decreases in the downstream direction from 800 to 300 Hz. The frequency of 800 Hz near the nozzle exit compares quite well to data presented in Ho & Huerre for the preferred mode of two-dimensional jets.

As is clear from figure 3.14 the two-dimensionality of the jet flow is restricted to a area of approximately 10 times the nozzle height  $h_0$ . This implies that only the top four power spectra are relevant. The frequencies encountered in this region are in the range of 500 to 800 Hz. Since our model is a three to one scale model of the vocal folds, the frequencies encountered in the flow through the actual (square-edge) vocal folds would be three times

higher. So these frequencies are in the physiological range of 1.5 to 2.5 kHz which is an important frequency range since the human ear is most sensitive in the range of 2 to 4 kHz. This indicates that a significant part of broad-band noise in voiced speech could be due to quasi-periodic two-dimensional flow instabilities rather than to three-dimensional turbulence. However, how much of those pressure fluctuations are radiated as sound and how it would be transmitted to actual speech is unknown.

### 3.4 Results of the unsteady boundary-layer model

Results obtained from a simplified unsteady boundary-layer model were used as input to the inviscid-vortex blob method and the Euler method. In this section we will show by comparison with the Navier-Stokes solution (viscous vortex-blob method) that this simple model predicts the boundary-layer growth inside the nozzle geometry quite well.

In the square-edge nozzle geometry flow separation is a very local effect as opposed to flow separation in a smooth diverging channel which we will discuss in the next chapter. Therefore it is possible to use a boundary layer description up to the edge without taking the possibility of flow separation into account. In order to confirm the accuracy of the numerical results and to demonstrate the applicability of a very simple boundary-layer model in such a converging flow we compare the solution of the Navier-Stokes equations as obtained by the viscous blob method to results obtained by solving the unsteady von Kármán equation (see chapter 2 equation (2.64)) by approximating the velocity profile in the boundary layer with a linear profile.

In figure 3.25 the spatial development of the displacement thickness inside the nozzle is presented. The solid lines represent the results from the the simplified boundary-layer model while the dashed lines represent results from the viscous blob method. The region shown contains a small part of the converging part of the nozzle and the whole straight part of the nozzle (the edge is at  $x/h_0 = 3.077$ ). The horizontal and vertical scales are not taken the same because of the large difference in the scale of the boundary-layer thickness and the scale of the nozzle. The numerical displacement thickness has been determined from the imposed flux and the velocity on the symmetry line using an assumption of uniform bulk flow:  $\Phi = (h_0 - 2\delta^*)u$ . Although this is not the exact displacement thickness the assumption is equivalent to the assumption of uniform bulk flow in the simplified boundary-layer model. The general agreement is quite satisfactory (especially considering the difference in computational time, which is 2 minutes for the simplified model and 1 week for the viscous blob method). Furthermore, the numerical results confirm that information in the boundary layer travels at an approximate speed of one third of the main flow velocity (as discussed in chapter 2). In the top left picture a transition can be seen from a spatially growing boundary layer to a spatially uniform boundary layer inside the straight channel. In the other pictures this transition has disappeared and only a spatially growing boundary layer is left. In these cases a quasi-steady description is quite reasonable. The decrease in the displacement thickness near the square edge at  $t = 5.41$  ms is due the lack of a fully developed jet structure at this time. The two-dimensionality of the flow is still important

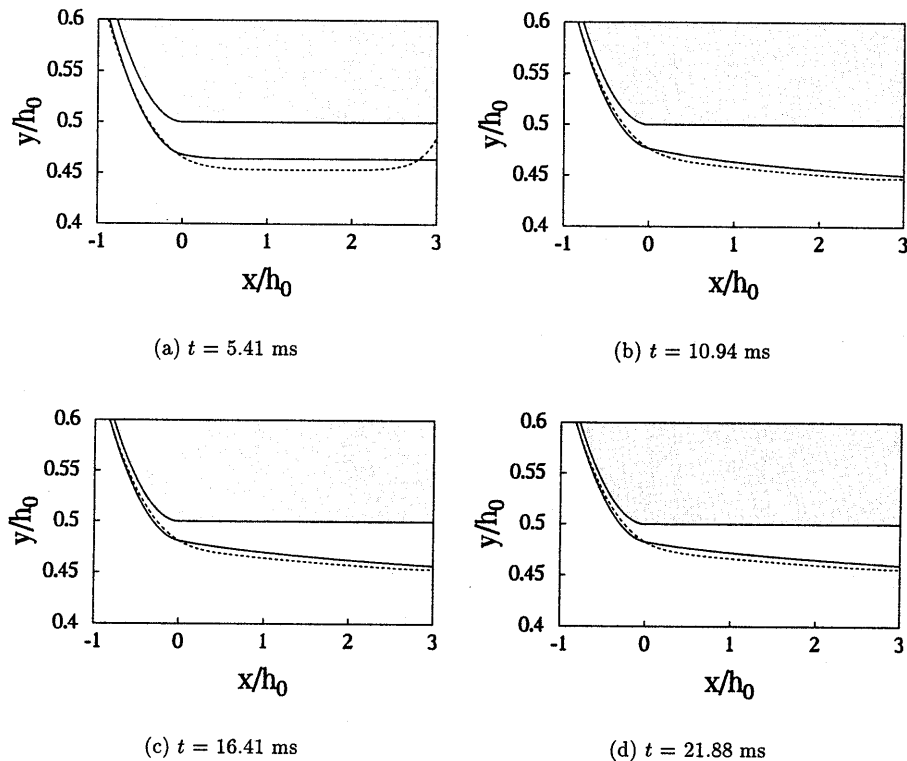


Figure 3.25: Comparing boundary-layer calculations (dashed lines) of the displacement thickness to results obtained with the viscous vortex-blob method (solid lines).

near the edge. There is an acceleration of the flow near the edges as one expects in a potential flow. When the jet is fully developed the assumption of a quasi one-dimensional flow is also valid near the edge.

Since our interest lies in modelling the acoustic source due to movement of the vocal folds a more relevant quantity to be compared is the pressure. In figure 3.26 the pressure as a function of time is shown. The pressure is determined at the two points in the geometry discussed in our description of the experimental set-up. The pressure  $p_1$  is measured 8 mm upstream of the start of the nozzle, while  $p_2$  is measured inside the straight nozzle channel 5 mm upstream of the edge. In the boundary-layer theory a quasi-steady jet is assumed which is a jet without a pressure drop, so with the pressure equal to the ambient pressure at the end of the flow channel. In order to compare the numerically obtained pressure to this theoretical model the pressure is determined with respect to the pressure at the end of the channel  $p_e$ , which is not equal to zero. Figure 3.26 therefore shows  $(p_1 - p_e)$  and

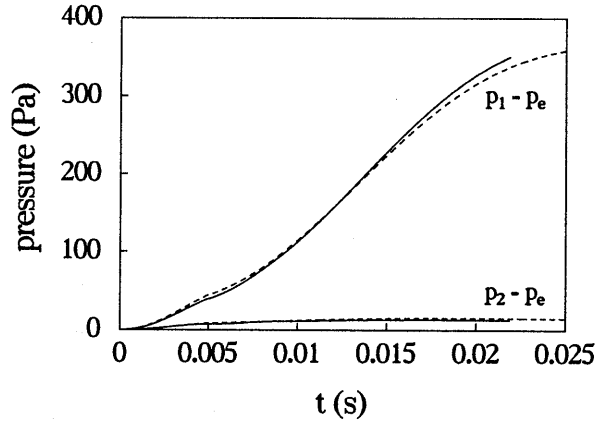


Figure 3.26: Comparing boundary-layer calculations of the pressure differences across the nozzle (dashed lines) to results obtained with the viscous vortex-blob method (solid lines).

( $p_2 - p_e$ ). The agreement between the two results is excellent. Typically they differ no more than 10 % and at most a difference of 20 % is encountered during a short period of time. This shows that the simplified boundary-layer model is capable of capturing the essentials of the flow through the square-edge nozzle. The influence of the jet structure is not taken into account, however, and - considering the phenomena encountered in the simulations of the jet flow - it might be an additional important source of sound (noise).

### 3.5 Concluding remarks

Steady measurements of the pressure drop inside the nozzle channel together with velocity measurements of the spatial velocity profile confirmed our assumptions about laminar quasi two-dimensional flow. Unsteady pressure measurements combined with simultaneous velocity measurements inside the nozzle channel on the centre line showed that the velocity measurement does not provide us with additional information, so that subsequent experiments can be performed without a hot-wire probe inside the nozzle channel.

The results obtained experimentally and with the three numerical methods were very similar in the global features of the flow, thus demonstrating their capability. The details of the flow concerning the instabilities obtained with these methods were quite different, however. Although this might just reflect the physical nature of the unstable shear layer, details of the channel or the environment can cause a very different time history of the growth of an instability. Global features of the instabilities like frequency and amplitude were very similar in the results of the three numerical methods and compared quite well to those obtained by velocity measurements. In order to control this phenomenon one should repeat experiment and numerical simulation under conditions that the flow is forced. In

that way a reproducible instability can be achieved.

The two-dimensional developing jet flow exhibits a very complex behaviour of interacting vortices that are the result of flow instabilities. A very important process observed is the pairing/merging of vortices. Frequencies of pressure perturbations associated with this phenomenon are in the audible range and might therefore be important in human speech production.

Experimental flow visualisations showed that two-dimensional vortex structures are an important feature of the jet flow out of a slit, even after the main part of the jet has become turbulent (i.e. three-dimensional). Although the above mentioned phenomena are typical for two-dimensional flows there are even indications that three-dimensional turbulence still exhibits features that can be related to two-dimensional phenomena.

The flow inside the nozzle can be accurately described by a simplified boundary-layer model inserted into the unsteady momentum integral equation using a linear velocity profile (von Kármán equation). It is important, however, to recall that the most interesting phenomena take place in the jet and this is of course not captured by the boundary-layer model.

Which type of simulation is best suited for this type of flow is still undecided. The least complex method (the inviscid vortex-blob method) yields results that are not significantly different from the other two methods. It requires an input parameter (the desingularisation parameter  $\delta$ ), however, that has its value based on physical phenomena, for which this parameter is not intended to be used. On the other hand, this method can be by far the fastest of the three methods. By reducing the number of point vortices representing the shear layer the run-time can be considerably reduced without too much loss of accuracy. The run-time is also independent of the Reynolds number, which is not the case for the viscous vortex-blob method. For this type of flow the run-time of the viscous vortex-blob method increases dramatically with Reynolds number. It can neither be accelerated by adjusting numerical parameters such as geometry discretisation and number of point vortices used. However, the viscous vortex-blob method can be used to simulate flow separation from smooth surfaces which is something the other methods are not capable of. The Euler computation has by far the longest run-time and in that respect is less attractive than the other two methods. The formulation of the boundary conditions was however conservative in order to prevent non-physical reflections of acoustic waves that are generated. By relaxing this stringent boundary condition the method might be accelerated by a factor 100, but the consequences need to be investigated in detail. On the other hand, it is the only method that can be extended to three-dimensional flows. One should keep in mind that all the models lose their significance when turbulence appears in the jet.

## References

- ALLENBORN, N., NANDAKUMAR, K., RASZILLIER, H., & DURST, F. (1997) Further contributions on the two-dimensional flow in a sudden expansion. *J. Fluid Mech.* **330**, 169–188

- BASTIN, F., LAFON, P., & CANDEL, S. (1997) Computation of jet mixing noise due to coherent structures: the plane jet case. *J. Fluid Mech.* **335**, 261–304
- COLONIUS T., LELE, S.K., & MOIN, P. (1997) Sound generation in a mixing layer. *J. Fluid Mech.* **330**, 375–409
- GREENGARD, C. (1985) Note: the core spreading vortex method approximates the wrong equation. *J. Comp. Phys.* **61**, 345–348
- GRINSTEIN, F.F., ORAN, E.S., & BORIS, J.P. (1991) Pressure field, feedback, and global instabilities of subsonic spatially developing mixing layers. *Phys. Fluids A* **3**, 2401–2409
- GRINSTEIN, F.F., GLAUSER, M.N., & GEORGE, W.K. (1995) Vorticity in jets. Appeared in “Fluid Vortices” S.I. Green editor. *Kluwer Academic Publishers*, 95–153
- HO, C.-M. & HUERRE, P. (1984) Perturbed free shear layers. *Ann. Rev. Fluid Mech.* **16**, 365–424
- HOFMANS, G.C.J., VAN DE VEN, E.A.I., DEN DOELDER, C.F.J., HIRSCHBERG, A., & WIJNANDS, A.P.J. (1995) Unsteady flow through 2D channels with a constriction. *Forum on Vortex Methods for Engineering Applications, Albuquerque*
- HUERRE, P. & MONKEWITZ, P.A. (1990) Local and global instabilities in spatially developing flows. *Ann. Rev. Fluid Mech.* **22**, 473–537
- HULSHOFF, S.J., HOEIJMAKERS, H.W.M., & MULDER, J.A. (1996) Prediction of aircraft longitudinal response using time-accurate Euler computations. *AIAA Paper 96-2485*
- KAIKTSIS, L., KARNIADAKIS, G.E., & ORSZAG, S.A. (1996) Unsteadiness and convective instabilities in two-dimensional flow over a backward-facing step. *J. Fluid Mech.* **321**, 157–187
- LE, H., MOIN, P., & KIM, J. (1997) Direct numerical simulation of turbulent flow over a backward-facing step. *J. Fluid Mech.* **330**, 349–374
- THOMPSON, K.W. (1987) Time-dependent boundary conditions for hyperbolic systems. *J. Comp. Phys.* **68**, 1–24
- THOMPSON, K.W. (1990) Time-dependent boundary conditions for hyperbolic systems II. *J. Comp. Phys.* **89**, 439–461

# Flow through in vitro models of the vocal folds

## 4.1 Introduction

Researchers in the field of biomechanics have been using numerical simulations as a useful tool for their studies. Topics that are related to the flow of blood through arteries received a lot of attention in recent years (Rosenfeld 1995, Luo & Pedley 1996, Pedrizzetti 1996) but also the flow of air through the vocal folds has been the subject of numerical studies. Interest in the last topic is motivated by two research aims: one is the development of prosthetic vocal folds and the other is the development of artificial speech models. Recently some attempts at numerically simulating the flow through the vocal folds including forced vocal-fold movement have been done by Alipour and Titze (1996) and Alipour *et al.* (1996). Although a complete simulation of the vocal-fold movement and air flow through the glottis (the opening formed by the vocal folds) can yield some interesting results it is not a solution to the problem of artificial (real-time) speech modelling in the near future.

One approach in speech modelling is to model the interaction of the air flow through the glottis and the movement of the vocal folds using simplified models. The problems that are encountered are numerous since the flow through the vocal folds is a result of the coupling between complex fluid dynamics and complex elastic structure (vocal-fold) behaviour. Usually both aspects are simplified until such a level is reached that artificial real-time speech production is possible. This leads to oversimplifying both aspects of vocal-fold movement but especially the fluid dynamical description has been reduced to a caricature of the actual flow. An important parameter in these flow models is the point at which the airflow separates from the vocal folds. This parameter determines not only the volume flow through the glottis but also the hydrodynamical forces exerted on the vocal folds.

In most models of the flow through the glottis *ad hoc* assumptions are made about the separation point in the glottis. Pelorson *et al.* (1994) made an attempt to improve the description of flow separation within the glottis by using a quasi-steady model based on

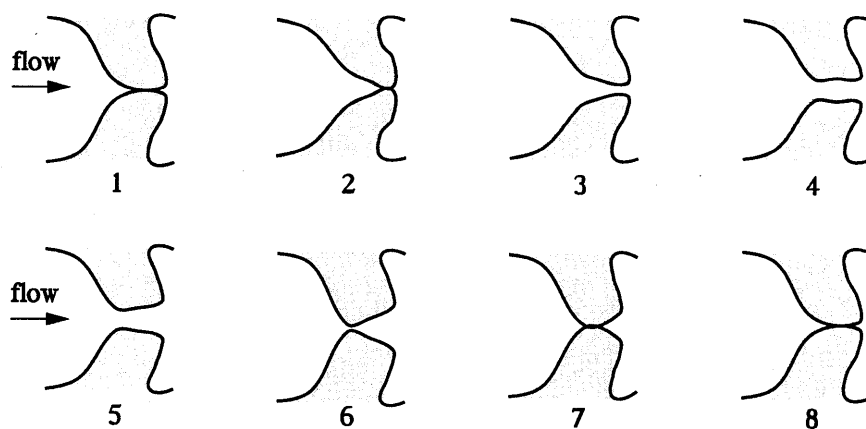


Figure 4.1: Typical vocal-fold movement during one oscillation. Note the changing shape of the glottis.

the boundary-layer theory. They showed that this improved the results obtained from a simplified mechanical model in which the vocal folds are each represented by two coupled oscillators. Lous *et al.* (1998) present a new model based on these results and they discuss the consequences of the various simplifying assumptions that are made in most models for the vocal-fold movement. Hirschberg *et al.* (1996) discuss the flow phenomena that might be important for a model of the flow through the glottis, while Pelorson *et al.* (1997) focus on the fluid dynamics of so-called bilabial plosives. Related work that is concerned with similar flows from an engineering point of view is the work by Roozen *et al.* (1998) on flow separation in a bass-reflex port of loudspeakers, the numerical study of the flow in a two-dimensional diverging channel by Dennis *et al.* (1997), and the combined experimental and theoretical analysis of unsteady flow in diffusers by Kwong & Dowling (1994).

In figure 4.1 a typical cycle of the vocal-fold movement is presented. Note the changing shape of the glottis due to the typical way in which the vocal folds open and close. Because pressure is applied upstream of the vocal folds they first start to open at the upstream side. This results in a converging glottis shape during the opening phase of the vocal folds. The closing of the vocal folds also starts at the upstream side, resulting in a diverging glottis shape during the closing phase. Apparently the movement of the vocal-fold tissue at the downstream side is always lagging the movement at the upstream side. A typical glottal pulse that is the result of such a vocal-fold movement is shown in figure 4.2. The glottal flux presented in this figure represents the sound /a/ at 110 Hz and has been reproduced from (Rothenberg 1981). Note the slight asymmetry in time; the closing occurs more rapidly than the opening.

In this chapter we present an experimental, theoretical and numerical study of the flow through *in vitro* models of the vocal folds. In order to focus on the fluid dynamical aspects



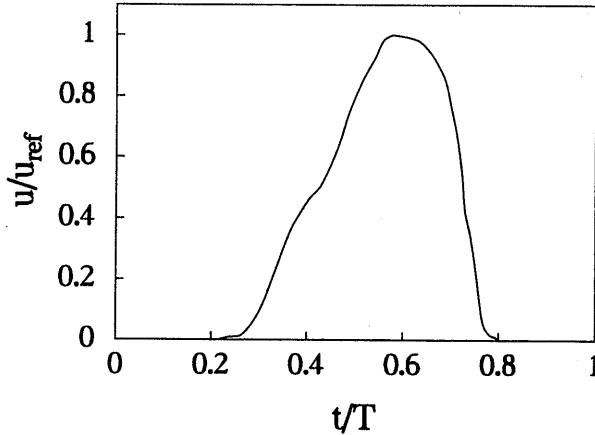


Figure 4.2: Normalised glottal flux  $\phi_g$  for the sound /a/ at 110 Hz according to Rothenberg (1981).

of the flow we used rigid fixed (scale) models of the vocal folds. The size is approximately three times the size of the real vocal folds and the shape of these scale models is inspired by the typical shape of the glottis during the closing phase. In the actual flow through the glottis a steady pressure difference is imposed across the vocal folds, while the opening and closing of the vocal folds result in an unsteady flow. In order to maintain a similarity to the actual flow through the glottis, an unsteady pressure drop is imposed across the vocal folds. Care is taken that the relevant parameters describing the flow through the glottis have the correct values. In the glottis these parameters are the Strouhal number and the Reynolds number. The Strouhal number is defined as:  $Sr = l/u_0T$  in which  $l$  is stream-wise length scale of the glottis (5 - 10 mm),  $u_0$  is a typical velocity in the glottis (10 - 30 m/s) and  $T$  is a typical time scale of the vocal-fold movement. For men the typical frequency of oscillation is 100 Hz, while for women it is twice as large at approximately 200 Hz. A better time scale is, however, the opening time of the vocal folds (2 - 4 ms). The Reynolds number is defined as:  $Re = h_0u_0/\nu$ , in which  $h_0$  is the typical height of the glottis (1 - 2 mm) and  $\nu$  is kinematic viscosity of air ( $\nu = 1.5 \cdot 10^{-5} \text{ m}^2/\text{s}$  at atmospheric pressure and room temperature). The Strouhal number (typically of order  $10^{-2}$ ) is a measure of the influence of unsteady effects on the flow, while the Reynolds number (typically of order  $10^3$ ) reflects the importance of viscous effects on the flow.

In speech modelling the important quantity that has to be modelled accurately is the acoustic pressure source that is the result of the vocal fold movement. This source is the unsteady volume flux through the vocal folds. In particular the time dependence of this flux during the closing phase of the vocal-fold movement is important. This movement is driven by the pressure at the throat of the glottis. So to evaluate the validity and accuracy of the simplified quasi-steady boundary-layer model we compare the numerically

determined pressure at the throat to the theoretical prediction.

This chapter is set up as follows. We start by presenting some steady pressure measurements in a lip-like model and compare them to a simplified boundary-layer model. Next unsteady pressure measurements in both a lip-like model and two diverging vocal-fold models are presented. Attention is paid to the various flow phenomena that are observed. Finally some numerical simulations of the flow through these models are presented using the viscous vortex-blob method. Both numerical and experimental results are compared to a quasi-steady boundary-layer model in order to study the applicability and accuracy of such a model in a description of the flow through the vocal folds.

## 4.2 Experiments

### 4.2.1 Experimental set-up

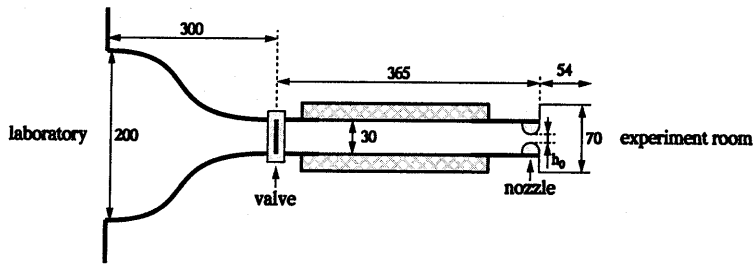


Figure 4.3: Schematic representation of the experimental set-up. Measures are in millimetres.  $h_0$  is the (throat) height of the aperture (typically 1 or 3 mm). The shaded area represents the rubber foam padding.

The experimental results that are presented in this chapter have been obtained in the set-up shown in figure 4.3. This set-up is equivalent to the set-up that is described in the previous chapter. A valve operated by a spring blade separates two large pressure reservoirs: laboratory and experiment room. A cylindrical pipe connects the inlet section to the glottis section. In order to damp mechanical and acoustic vibrations the inner walls of this pipe are covered by a rubber foam (the shaded area in figure 4.3). The sharp edge nozzle geometry has been replaced by a smooth constriction that is built out of either lip-like models or diffuser models that form a glottis-like channel. The brass blocks that form the geometry of the constriction are shown in figure 4.4. All these blocks can be combined to form different geometries of the constriction but we will focus on the combinations that are presented in the figure. The height  $h_0$  representing the smallest aperture in the channel (the throat of the glottis) can be varied from 0.1 mm to 5 mm. As in the sharp edge nozzle set-up, pressures are measured at two positions: the first position is 8 mm upstream of the start of the constriction in the side wall of the cylindrical pipe (the same as before) and

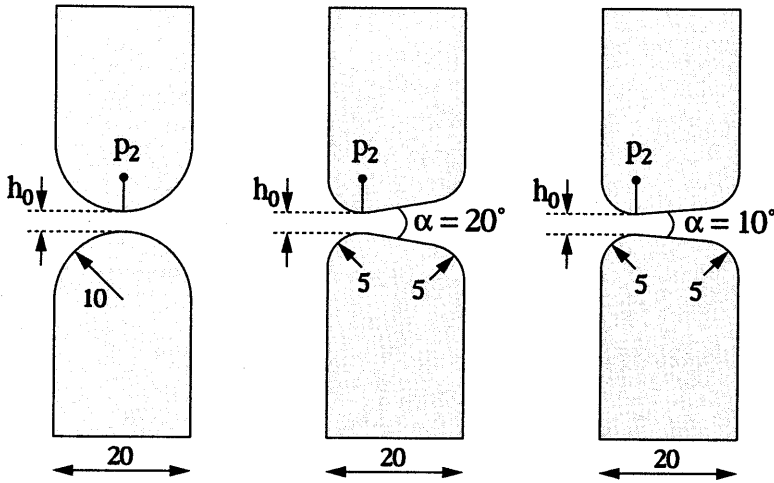


Figure 4.4: Models that are studied: the model on the left is a lip-like model and the models on the right are diverging vocal-fold models. Measures are in millimetres.

the second position is in the throat of the constriction at the smallest aperture. The Kulite pressure transducer is mounted in the new blocks in the same way as is shown in figure 3.5, using a pressure tap with a diameter of 0.4 mm. The lip-like model is built with two semi-cylinders with a radius of 10 mm. The pressure tap is exactly in the middle of the block. The vocal-fold models consist of a cylindrical part, followed by a linearly diverging part and another cylindrical part. The angle of divergence  $\alpha$  is either  $20^\circ$  or  $10^\circ$ , as is shown in figure 4.4. These models are the ones used by Pelorson *et al.* (1994) and are based on typical vocal-fold movement discussed in the introduction. The diffuser angles are chosen in such a way that when  $h_0 \approx 3$  mm with  $\alpha = 10^\circ$  the flow would be in the stable-diffuser-flow region and with  $\alpha = 20^\circ$  the flow would be outside the stable-diffuser-flow region, according to data on diffuser performance at high Reynolds numbers ( $Re$  of the order  $10^5$ ) presented in Blevins (1984).

#### 4.2.2 Results for the lip-like round model

The lip-like round model is studied for two reasons. First of all the model can be considered a reference model for studying flow separation from a curved wall: because of the constant radius of curvature the separation point is usually not sensitive to external influences. The second reason is that this model is considered relevant for the study of the flow through the lips (which is important when considering plosives (Pelorson *et al.* 1997)).

The experiments with the lip-like models are similar to the experiments performed on the sharp edge nozzle configuration and consist of pressure and velocity measurements. The pressure  $p_1$  is measured in the pipe 8 mm upstream of the start of the constriction while

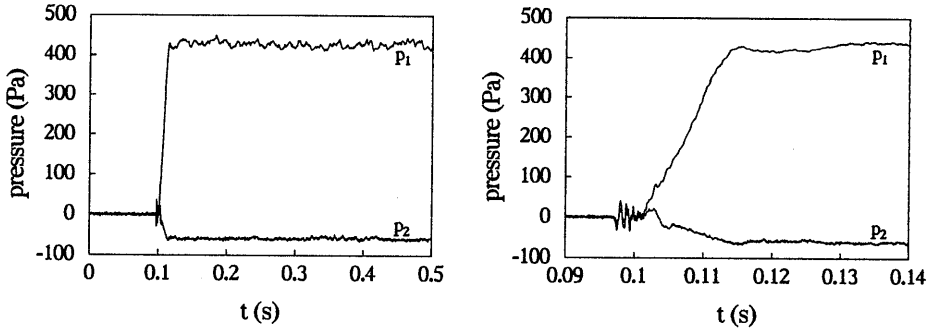


Figure 4.5: Pressure measured in the pipe  $p_1$  and in the throat  $p_2$  for the lip-like geometry:  $\Delta p = 430$  Pa and  $h_0 = 0.99$  mm. The right graph is a close-up of the left graph, showing the transient behaviour.

the pressure  $p_2$  is measured at the smallest aperture (in the throat) of the constriction. The velocity is measured at various positions on the centre line of the set-up using the hot-wire anemometer. Experiments have been performed for two values of the throat height:  $h_0 = 0.99$  mm and  $h_0 = 3.36$  mm. Since the results found for a throat height  $h_0 = 0.99$  mm are very similar to results for  $h_0 = 3.36$  mm mostly results for the latter case are presented. It was also found that the hot-wire probe disturbed the flow too much in the case of  $h_0 = 0.99$  mm, so no velocity measurements were done in this case.

In figure 4.5 a representative measurement is shown for the lip-like models with a throat height  $h_0 = 0.99$  m. The final steady pressure drop  $\Delta p$  across the constriction is equal to 430 Pa. The opening time is approximately 15 ms, which, together with the length of the glottis model (20 mm) and the typical velocity  $u_0 = \sqrt{2\Delta p/\rho}$ , leads to a Strouhal number of 0.05. The Reynolds number is then approximately 1800. The left graph shows the pressure signals in the pipe  $p_1$  upstream of the constriction and in the throat  $p_2$  for a time range of 0.5 s. The right graph is a close-up of the left graph and shows the transient behaviour in more detail in a time range of 0.05 s. The time axis is determined by the trigger for the measurement. In all subsequent graphs the trigger signal was generated at  $t = 0.1$  s: by using the pre-trigger capability of the ADC-card the measurement has already been recorded 0.1 s before the trigger is generated. The actual start of the flow is not determined since the laser detector set-up is triggered by the valve after it starts moving, but it is reasonable to assume this to be close to the trigger point. In figure 4.6 two similar measurements with a throat height  $h_0 = 3.36$  mm at a pressure drop of 290 Pa and 690 Pa are shown. The Strouhal number is 0.05 and the Reynolds number is 4900 in the low pressure experiment and 0.03 and 7600, respectively, in the high-pressure experiment. Except for a few milliseconds before the trigger point the pressure in the pipe  $p_1$  shows a smooth increase from zero to a steady value  $\Delta p$ . The small but distinct oscillations around the trigger point (at 0.1 s) are caused by the opening of the valve and cannot be avoided.

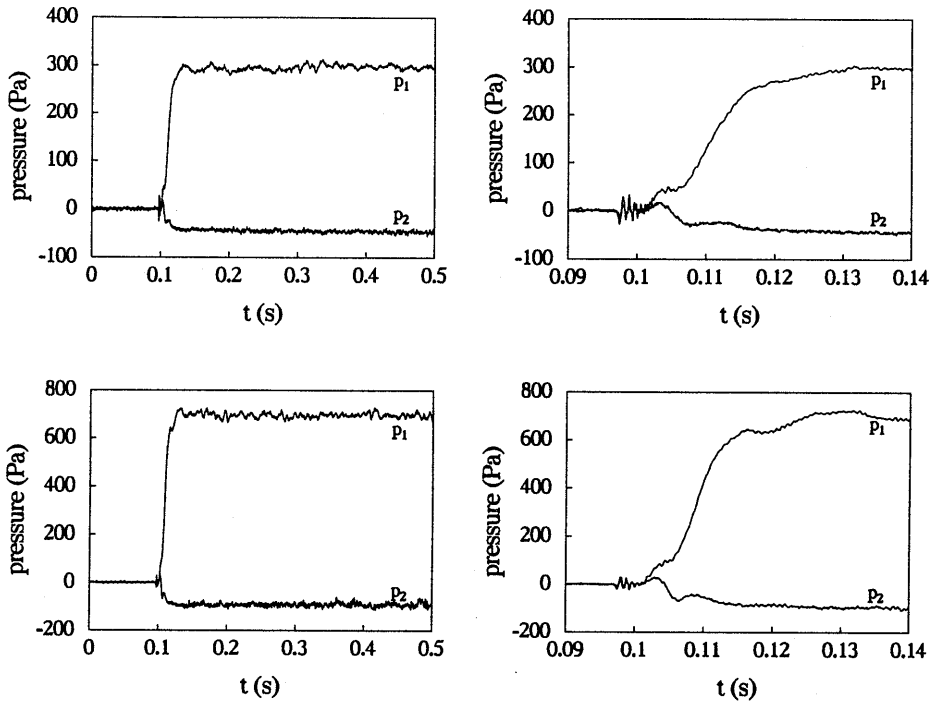


Figure 4.6: Pressure measured in the pipe  $p_1$  and in the throat  $p_2$  for the lip-like geometry: top graphs  $\Delta p = 290$  Pa, bottom graphs  $\Delta p = 690$  Pa,  $h_0 = 3.36$  mm. The right graph is a close-up of the left graph, showing the transient behaviour.

Using the laser detector set-up the speed of the valve during opening is estimated to be in the range of 1.5 to 2 m/s.

In figures 4.5 and 4.6 the pressure  $p_2$  in the throat exhibits a particular behaviour. The first few milliseconds of the experiments the pressure  $p_2$  in the throat is rising proportionally to the pressure  $p_1$ . This is due to the initial flow that is like a potential flow: boundary layers are still very thin and flow separation does not yet occur. The bulk flow is inviscid so velocity and pressure are related by Bernoulli's equation:

$$\rho \frac{\partial \phi_1}{\partial t} + \frac{1}{2} \rho u_1^2 + p_1 = \rho \frac{\partial \phi_2}{\partial t} + \frac{1}{2} \rho u_2^2 + p_2, \quad (4.1)$$

in which  $\rho$  is the density of air,  $u$  the velocity and  $\phi$  the velocity potential. The main contribution to the pressure drop across the constriction is given by the inertial effects (the  $\frac{1}{2} \rho u^2$ -terms are negligible because the velocity is still very small). This implies that the pressure in the throat has a value that is between the pressure in the experiment room

(by definition equal to zero) and the pressure in the pipe  $p_1$ . Typically  $p_2$  is equal to  $0.5p_1$  because the constriction is symmetric with respect to the throat and the main contribution to the inertial terms originates from this region. After the initial stage the flow separates from the walls of the constriction forming a jet. Finally, a steady situation is reached. If we assume the pressure in the jet to be equal to the pressure in the experiment room and if we assume the height of the jet larger than the throat height  $h_0$ , then the pressure in the throat is lower than the pressure in the experiment room, since the velocity in the throat is higher than the velocity in the jet. This can be illustrated by inserting the one-dimensional equation of mass conservation ( $u(x)h(x) = \Phi$ ), thus neglecting boundary-layer effects, into the steady Bernoulli equation. Here  $h(x)$  is the height of the channel and  $\rho\Phi$  is the two-dimensional mass flux. This results in the following equation relating the pressure to the height of the channel:

$$\frac{p(x)}{\rho} + \frac{1}{2} \left( \frac{\Phi}{h(x)} \right)^2 = \frac{1}{2} \left( \frac{\Phi}{h_s} \right)^2, \quad (4.2)$$

in which  $h_s$  is the height of the channel at the separation point. By inserting  $p_1$ , pipe height  $h_p$ ,  $p_2$ , and  $h_0$  the following relationship between the pressure ratio  $p_2/p_1$  and the various channel heights is obtained:

$$\frac{p_2}{p_1} = \frac{1 - \left( \frac{h_s}{h_0} \right)^2}{1 - \left( \frac{h_s}{h_p} \right)^2}, \quad (4.3)$$

which for  $h_p \gg h_s$  reduces to:

$$\frac{h_s}{h_0} = \sqrt{1 - \frac{p_2}{p_1}}. \quad (4.4)$$

Therefore the pressure in the throat is an indication of position of the separation point. So  $p_2$  has to be less than zero in the steady limit, as can be observed in figures 4.5 and 4.6.

Although the experiments for both values of  $h_0$  look very similar, a few small but distinct differences can be observed. The experiment with  $h_0 = 3.36$  mm show an oscillation in the pressures  $p_1$  and  $p_2$  during the first milliseconds after the trigger point. This oscillation is less pronounced in the experiments with  $h_0 = 0.99$  mm and has a lower frequency. Furthermore, the experiments with  $h_0 = 0.99$  mm seem to reach the steady state in a more straightforward way. An explanation for this behaviour has still to be found, but possibly this behaviour is related to the first resonance of the pipe system.

By integrating Bernoulli's equation the velocity in the throat can be computed based on the pressure measurements. For this purpose Bernoulli's equation is rewritten in the following form:

$$\frac{\partial(\phi_2 - \phi_1)}{\partial t} = \frac{1}{2}(u_1^2 - u_2^2) + \frac{p_1 - p_2}{\rho}, \quad (4.5)$$

which, using the definition of  $\phi$ , can be written as:

$$L_{eff} \frac{\partial u_2}{\partial t} = \frac{1}{2}(u_1^2 - u_2^2) + \frac{p_1 - p_2}{\rho}, \quad (4.6)$$

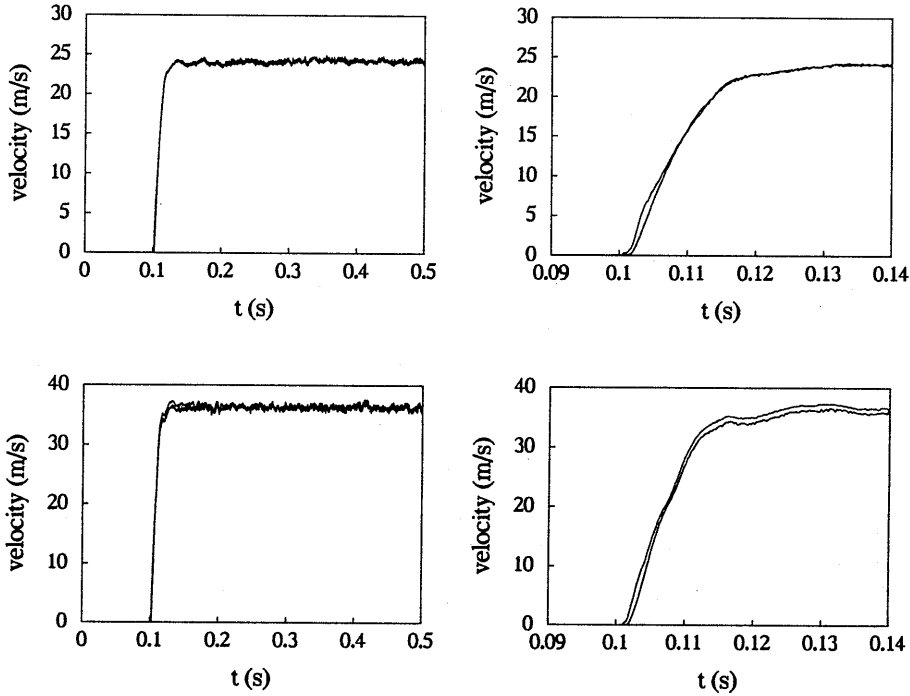


Figure 4.7: Velocity measured in the throat and the velocity calculated in the throat by integration of the unsteady Bernoulli equation using the measured pressures  $p_1$  and  $p_2$ . Experiments performed on the lip-like geometry: top graphs  $\Delta p = 290$  Pa, bottom graphs  $\Delta p = 690$  Pa,  $h_0 = 3.36$  mm. The right graph is a close-up of the left graph, showing the transient behaviour.

in which an effective length  $L_{eff}$  has been introduced. It is defined by:

$$L_{eff} = \int_{x_1}^{x_2} \frac{h_0}{h(x)} dx, \quad (4.7)$$

where in the last step we assumed a uniform flow across the channel. In figure 4.7 the computed velocity is compared to the velocity measured in the throat by means of the hot-wire anemometer. The velocity that is computed is the velocity at the edge of the boundary layer, which does not have to agree with the velocity on the centre line in a curved channel, because of the effect of curved streamlines on the pressure. It has been found, however, that this effect is considerably reduced in the throat because the boundary-layer growth in this region tends to cancel this effect. Furthermore, since flow separation takes place close

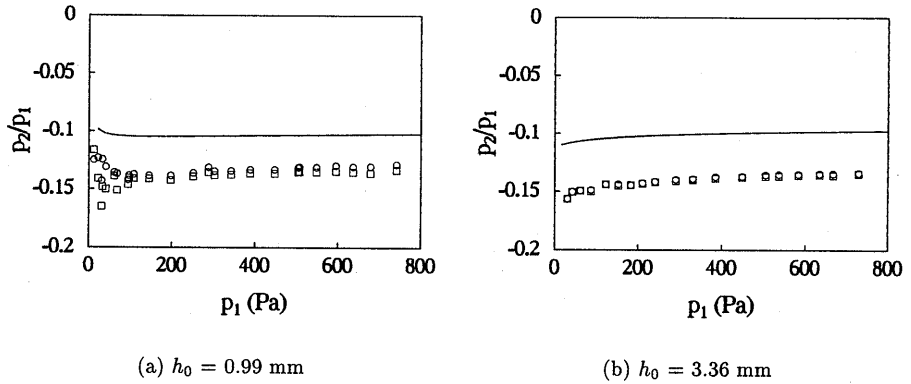


Figure 4.8: Comparing boundary-layer predictions (solid line) with steady pressure measurements at the throat in the top wall ( $\circ$ ) and the bottom wall ( $\square$ ) of the lip-like models.

to the throat, the curvature effect is also reduced (even neglecting boundary-layer growth). For this reason an assumption of uniform flow through the throat is quite reasonable. The pressure measurements of these experiments have been shown in figure 4.6. A good over-all agreement is found between measurement and calculation of the velocity in the throat. However, in the initial stage of the experiments the hot-wire measurements lag behind the computed velocity profile, similar to the results found for the sharp edge nozzle configuration (see chapter 3).

Since one of the aims of this chapter is to determine the validity of simplified models, results of the boundary-layer theory are compared to steady pressure measurements in the lip-like models. The theoretical results are based on Pohlhausen's method using a third order polynomial to describe the velocity profile in the boundary layer and then solving the steady von Kármán equation (see chapter 2, equation (2.63)). The steady pressures are measured by means of Betz water manometers with an accuracy of  $0.05 \text{ mm H}_2\text{O}$  ( $\approx 0.5 \text{ Pa}$ ). Results are shown in figure 4.8. The markers represent measurements in the top and bottom wall of the constriction. The solid line represents the theoretical result.

The boundary-layer theory predicts a too high value of  $p_2/p_1$ . This might be the result of the assumptions that are made. In the theoretical model the boundary layer is calculated up until the separation point. At the separation point the pressure is assumed to be equal to the external pressure (quasi-steady jet model). It is also possible to continue the boundary-layer calculation beyond the separation point. This leads to a lower prediction of  $p_2/p_1$ . However, these calculations do not converge to a constant pressure value and are therefore not reliable; the 3<sup>rd</sup>-order polynomial does not describe the flow accurately (far) beyond the separation point. These results indicate that the assumption of constant pressure in the jet is not valid inside the constriction and that the reference point for the pressure in the model is not correctly chosen. Alternatively this might be due to a poor



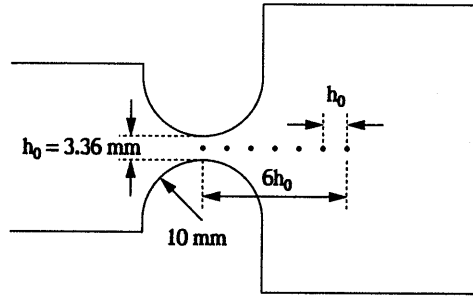


Figure 4.9: Positions at which the velocity in the jet is measured. The round lip-like models are used with an aperture  $h_0$  of 3.36 mm. The velocity is measured on the centre line at distances of  $0h_0$ ,  $1h_0$ ,  $2h_0$ ,  $3h_0$ ,  $4h_0$ ,  $5h_0$ , and  $6h_0$ , respectively, from the centre of the throat.

prediction of the separation point. This last hypothesis will be eliminated by comparison of boundary-layer theory with numerical calculations.

In order to measure the development of the jet as a function of time in the unsteady experiments the hot-wire is traversed along the centre line of the set-up and the velocity is measured at various positions in the lip-like model with  $h_0 = 3.36 \text{ mm}$ . The various positions are illustrated by figure 4.9. The hot-wire is placed at seven positions at distances from the centre of the throat that are a multiple of the throat height  $h_0$  ( $x = 0h_0$ ,  $1h_0$ ,  $2h_0$ ,  $3h_0$ ,  $4h_0$ ,  $5h_0$ , and  $6h_0$ ). Each velocity measurement is one experiment and by repeating the experiment a set of measurements is obtained. The results are presented in figure 4.10. The top left graph shows the seven sets of pressure measurements that belong to the seven velocity measurements shown in the seven other graphs. This illustrates the reproducibility of the experiments, which is typically within a few percent. As a reference for the various velocity signals the velocity measured in the throat is represented in each graph by the dashed line. Note that further downstream a sudden increase in velocity occurs due to the arrival of the jet and that the average steady value, which is reached, decreases due to the expansion of the jet. Also note the increasing level of (random) fluctuations on the signal further downstream: the positions  $x > 3h_0$  are outside the constriction and inside the (turbulent) jet flow where turbulent fluctuations are significant.

### 4.2.3 Results for the $20^\circ$ -diverging model

Models that are more important for the study of the flow through the vocal folds are the two diverging scale models that are shown in figure 4.4. In this section we present results for the diffuser model with a total angle of divergence  $\alpha$  of  $20^\circ$ . The flow through this model is investigated by means of unsteady pressure measurements at two positions: one in the pipe 8 mm upstream of the constriction and the other in the throat of the constriction. Measurements are done with two values for the height of the throat:  $h_0 = 1.12 \text{ mm}$  and

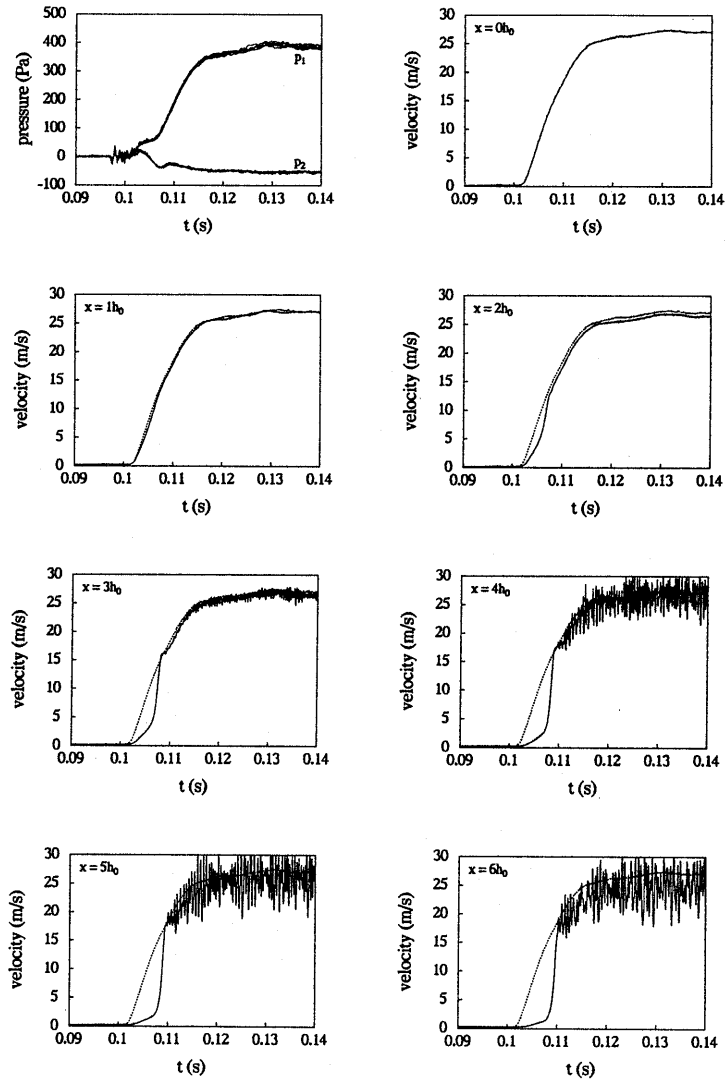


Figure 4.10: Velocity measurements in the jet at  $x = 0h_0, 1h_0, 2h_0, 3h_0, 4h_0, 5h_0,$  and  $6h_0$  (cf. figure 4.9). Pressures measured upstream of the constriction  $p_1$  and in the throat of the constriction  $p_2$  are shown in the top left figure for every velocity measurement. The dashed line is plotted as a reference and represents the velocity in the throat of the constriction. The solid lines represent the velocities measured at the different positions for the round lip-like model,  $h_0 = 3.36$  mm.

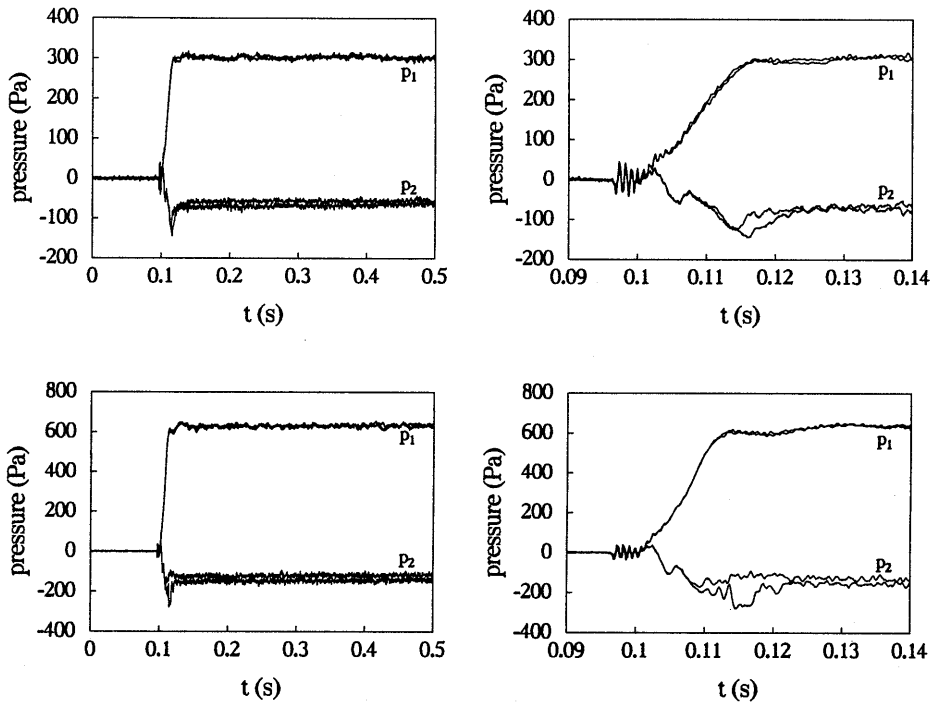


Figure 4.11: Pressure measured in the pipe  $p_1$  and in the throat  $p_2$  for the diffuser geometry with  $\alpha = 20^\circ$ : top graphs  $\Delta p = 301$  Pa, bottom graphs  $\Delta p = 627$  Pa,  $h_0 = 1.12$  mm. The right graph is a close-up of the left graph, showing the transient behaviour.

$h_0 = 3.50$  mm.

In figure 4.11 pressure measurements are presented for  $h_0 = 1.12$  mm and two values of the steady pressure drop:  $\Delta p = 301$  Pa and  $\Delta p = 627$  Pa. The right graphs show a close-up of the left graphs, focusing on the transient behaviour. The pressure signal  $p_1$  is very similar to the signals found in the lip-like model. Also the initial increase in  $p_2$  - corresponding to an unsteady potential flow - can be observed in this case. However, here the similarities with the results of the lip-like model end and a different behaviour of  $p_2$  is observed. Note the rather strong downward peak in  $p_2$  just before the steady limit is reached. In fact each graph consists of two experimental results. Repeating the experiment we found that two distinctly different time histories for the pressure  $p_2$  were obtained. As can be observed in figure 4.11, initially the two time histories collapse to one curve and only after a certain time the two curves start to deviate, leading to two different steady-pressure values for  $p_2$ . This behaviour is explained by an asymmetric flow due to the so-called Coanda effect. The Coanda effect is due to viscous entrainment of the

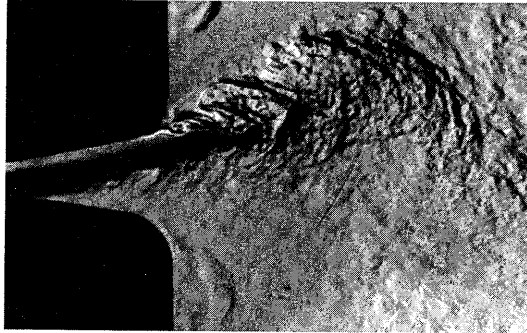


Figure 4.12: The Coanda effect. The flow adheres to one wall until the end of the constriction.

air that is caught between the jet and the walls of the channel. The symmetric jet becomes meta-stable and a small perturbation results in an adherence of the jet to either top or bottom wall of the channel as illustrated by the flow visualisation in figure 4.12. Since this phenomenon can be triggered by a small asymmetry in the flow both states are possible in a symmetric set-up.

In figure 4.13 equivalent pressure measurements are presented for  $h_0 = 3.50$  mm and two values of the steady pressure drop:  $\Delta p = 268$  Pa and  $\Delta p = 528$  Pa. The Coanda effect is also observed in this configuration and the behaviour is very similar to the previous case, except that the bifurcation of the two states is much more prominent. The presence of the Coanda effect is confirmed by flow visualisations (see figure 4.12) and by simultaneous measurements at both sides of the throat using less accurate pressure transducers. Pelorson & Hirschberg (1997) also presented accurate simultaneous pressure measurements that confirm the occurrence of a Coanda effect. Note also the increased level of the fluctuations on the pressure signals which might indicate the onset of turbulent flow. In general it was found that the flow was very unstable in this configuration. Similar results were also reported by Kwong & Dowling (1994) in their study of unsteady flow in a diffuser, although at much higher Reynolds numbers ( $Re$  of the order of  $10^5$ ).

Both figures 4.11 and 4.13 illustrate the fact that the establishment of the Coanda effect takes time. In order to quantify this claim, the time at which the two time histories of  $p_2$  start to deviate is measured as a function of the steady pressure drop. The time is taken with respect to the trigger point, since this is a good indication of the actual start of the flow. The results are presented in figure 4.14. Similar results have been presented by Pelorson & Hirschberg (1997). The results for  $h_0 = 1.12$  mm seem to exhibit a linear relationship with the pressure drop, although data at low pressures ( $p_1 < 300$  Pa) are lacking. On the other hand, the results for  $h_0 = 3.50$  mm do not exhibit this and in fact for a large range of  $p_1$  ( $250 < p_1 < 700$ ) the transition time remains unchanged at approximately 13 ms. Below 250 Pa the transition time increases strongly to 25 ms. These results support the conclusion that the Coanda effect is not important during the

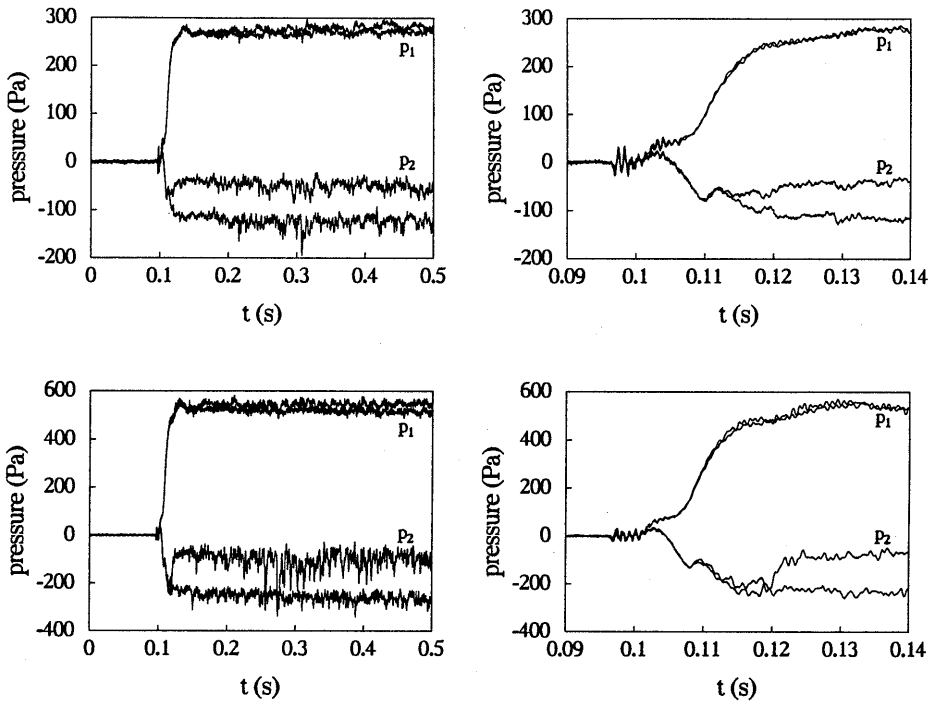


Figure 4.13: Pressure measured in the pipe  $p_1$  and in the throat  $p_2$  for the diffuser geometry with  $\alpha = 20^\circ$ : top graphs  $\Delta p = 268$  Pa, bottom graphs  $\Delta p = 528$  Pa,  $h_0 = 3.50$  mm. The right graph is a close-up of the left graph, showing the transient behaviour.

initial phase of a transient and a sufficiently unsteady flow might delay the onset of the Coanda effect. Considering the scaling of our models by a factor three, the time scale in the glottis is a factor three smaller than in our experiments. The transient in our model lasts approximately 20 ms, hence the closing time of the glottis oscillation is about 7 ms. So the Coanda effect might never have enough time to establish itself during the flow through the vocal folds. On the other hand, in the real glottis the movement of the walls is an important factor and the consequences of this for the Coanda effect are yet to be determined.

In order to compare the experimental results with predictions of the boundary-layer theory the steady pressure ratio  $p_2/p_1$  is determined in the unsteady experiments. The theoretical results are again based on Pohlhausen's method using a third order polynomial to describe the velocity profile in the boundary layer. Results are shown in figure 4.15. For each value of  $p_1$  two values of  $p_2$  are found experimentally. The different solutions are due to the adherence of the flow to either the upper wall of the constriction that contains

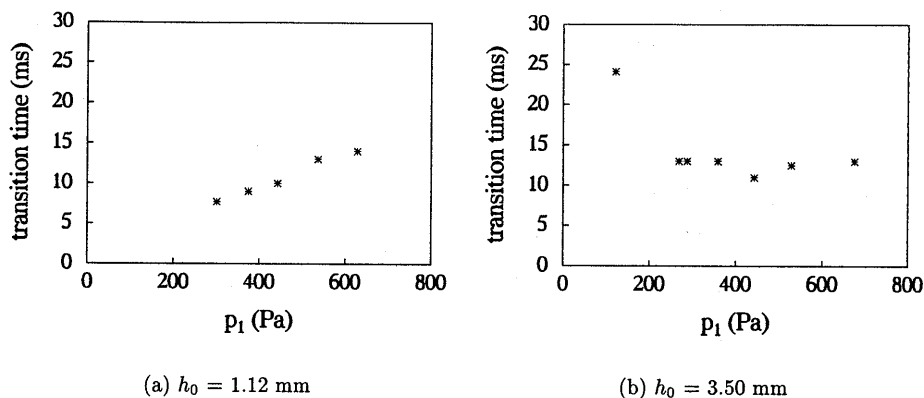


Figure 4.14: The time with respect to the trigger point at 0.1 s at which the flow starts to exhibit two states due to the Coanda effect for the diffuser model with  $\alpha = 20^\circ$ .

the pressure tap (lower results) or to the opposite wall (upper results). For  $h_0 = 1.12$  mm the two solutions are quite close, while for  $h_0 = 3.50$  mm they differ by a factor 2. Again the theoretical prediction results in a too high value of  $p_2$ , although a comparison is not completely justified due to the assumption of a symmetric solution in the theoretical model. Similar to the results found in the lip-like model, an increase in pressure downstream of the separation point is neglected. Because of the asymmetry of the flow, no conclusions on the point of separation can be drawn based on the pressure measurements.

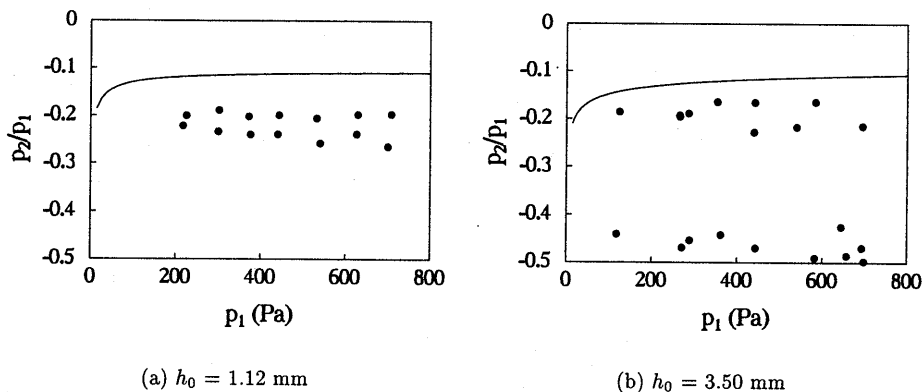


Figure 4.15: Comparing boundary-layer predictions (solid line) with steady limit pressures obtained from the unsteady experiments (markers): vocal-fold model with  $\alpha = 20^\circ$ .

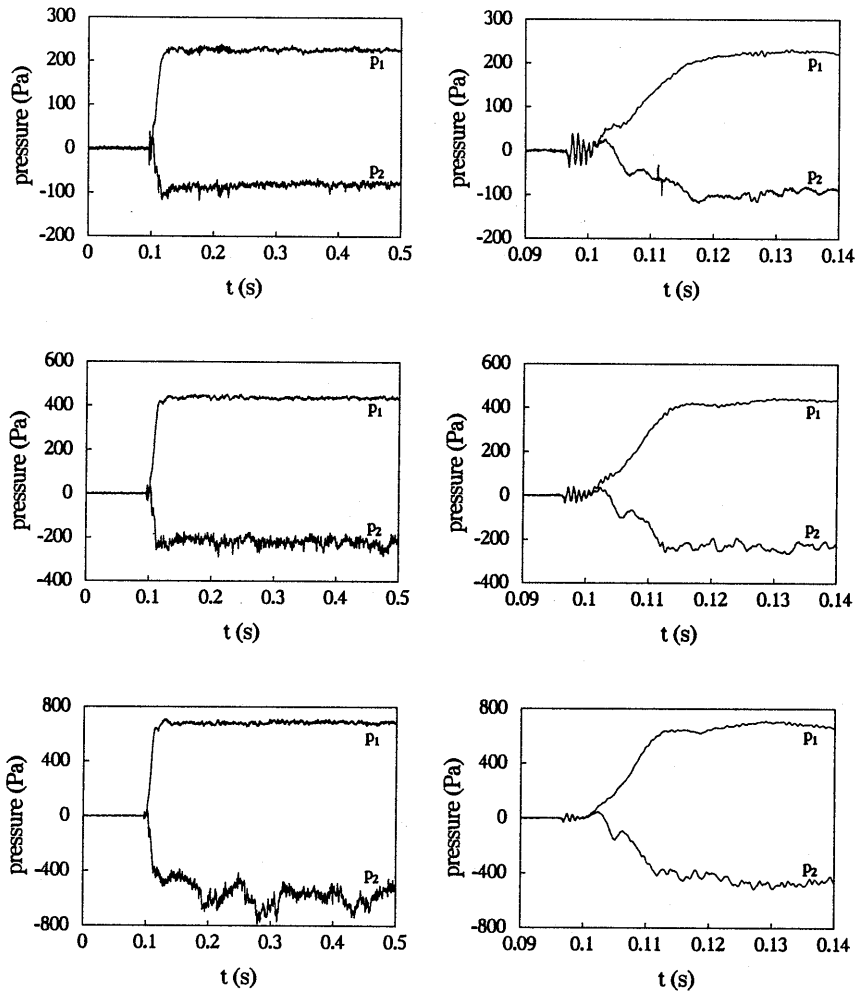


Figure 4.16: Pressure measured in the pipe  $p_1$  and in the throat  $p_2$  for the diffuser geometry with  $\alpha = 10^\circ$ : top graphs  $\Delta p = 224 \text{ Pa}$ , centre graphs  $\Delta p = 432 \text{ Pa}$ , bottom graphs  $\Delta p = 682 \text{ Pa}$ ,  $h_0 = 1.01 \text{ mm}$ . The right graph is a close-up of the left graph, showing the transient behaviour.

#### 4.2.4 Results for the $10^\circ$ -diverging model

In this section we present results for the diffuser model with a total angle of divergence  $\alpha$  of  $10^\circ$ . The flow through this model is investigated by means of unsteady pressure

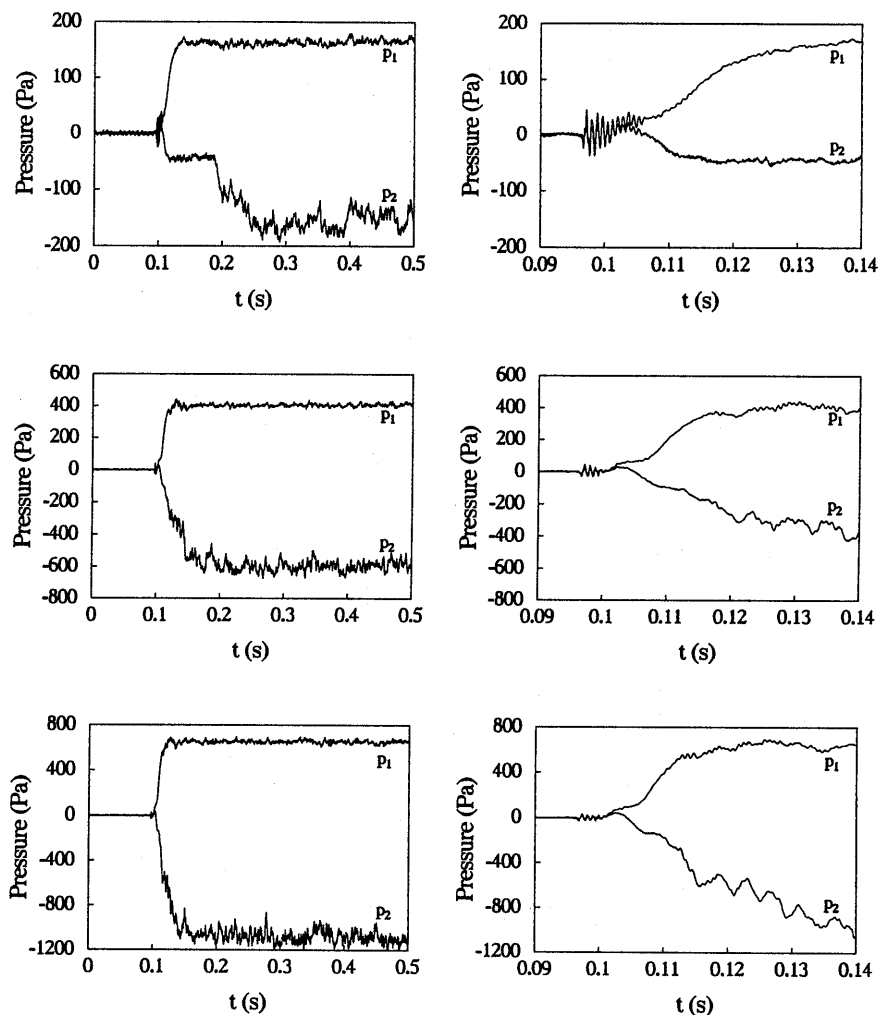


Figure 4.17: As figure 4.16, now with  $\alpha = 10^\circ$ : top graphs  $\Delta p = 161$  Pa, centre graphs  $\Delta p = 407$  Pa, bottom graphs  $\Delta p = 654$  Pa,  $h_0 = 3.39$  mm.

measurements at two positions: one in the pipe 8 mm upstream of the constriction and the other in the throat of the constriction. Measurements are done with two values for the height of the throat:  $h_0 = 1.01$  mm and  $h_0 = 3.39$  mm.

In figure 4.16 pressure measurements are presented for  $h_0 = 1.01$  mm and three values of the steady pressure drop:  $\Delta p = 224$  Pa,  $\Delta p = 432$  Pa and  $\Delta p = 682$  Pa. The right



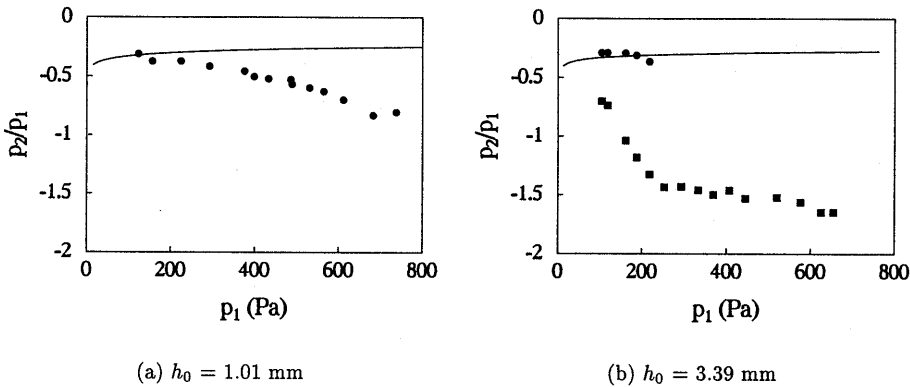


Figure 4.18: Comparing boundary-layer predictions (solid line) with steady limit pressures obtained from the unsteady experiments:  $\bullet$  before transition;  $\blacksquare$  after transition. No transition occurred in the experiments with  $h_0 = 1.01$  mm. Diffuser model with  $\alpha = 10^\circ$ .

graphs show a close-up of the left graphs, focusing on the transient behaviour. The pressure signal  $p_1$  is very similar to the signals found in the previous two scale models. Also the initial increase in  $p_2$  can be observed in this case. However, again here the similarities with previous results end and different behaviour of  $p_2$  is observed. With increasing pressure an increasing level of fluctuations can be observed in  $p_2$ . Especially large fluctuations are observed for  $\Delta p = 682$  Pa. This behaviour is similar to the behaviour observed in the  $20^\circ$ -diverging model with  $h_0 = 3.50$  mm. However,  $p_1$  is much more stable in this case and only one value is found for  $p_2$ . This behaviour is apparently not due to the Coanda effect. A possible explanation is a very unstable separation point due to the transition from laminar flow to turbulent flow.

This effect is even more prominent in the results obtained with  $h_0 = 3.39$  mm as presented in figure 4.17. Three sets of pressure measurements are presented for  $\Delta p = 161$  Pa, 407 Pa, and 654 Pa. The top and centre graphs show a distinctive, abrupt transition from a temporary stable solution to a new stable solution, while in the bottom graph this transition is already occurring during the initial transient. The difference in the level of the fluctuations before and after the transition indicates a transition from a laminar jet flow to a turbulent jet flow. Since a turbulent jet has a strong entrainment while the diffuser angle is small, the net effect is to delay separation until the end of the diffuser. This results in a much smaller value for  $p_2$ . In fact we demonstrate below that the model is acting like a well-designed diffuser for this configuration when turbulence has appeared in the jet flow. This agrees with the data presented in Blevins (1984) at much higher Reynolds numbers ( $Re$  of the order  $10^5$ ).

In figure 4.18 the steady pressure limits are compared to a theoretical prediction based on Pohlhausen's method using a third order polynomial to describe the velocity profile

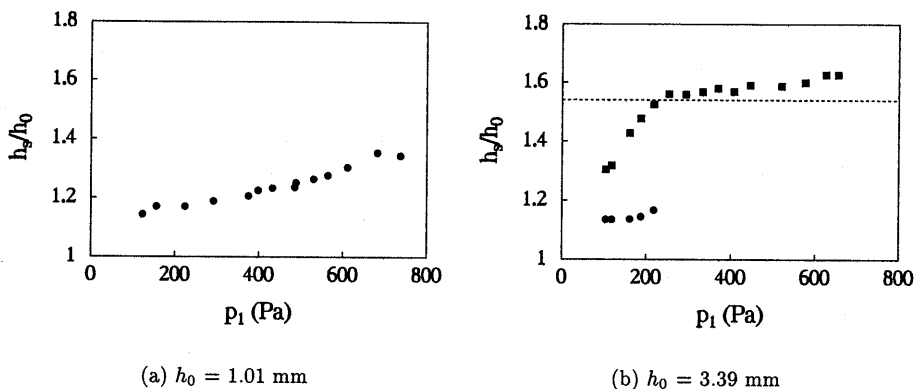


Figure 4.19: The ratio of the channel height at the separation point and the throat height  $h_s/h_0$  as computed from  $p_2/p_1$  using equation (4.4). The dashed line represent the height at the end of the linearly diverging section. Diffuser model with  $\alpha = 10^\circ$ .

in the boundary layer. In the case  $h_0 = 1.01$  mm no abrupt transition is observed and therefore only one set of values is plotted in the left graph of figure 4.18. For low values of  $p_1$  the agreement with the boundary-layer prediction is reasonable. An increasing deviation from the boundary-layer prediction is found with increasing value of  $p_1$ . In the case  $h_0 = 3.39$  mm, a distinctive abrupt transition is found for low values of  $p_1$ . In that case two values for  $p_2$  can be determined. One value before the transition and one value after the transition. For higher values of  $p_1$  the transition occurs too early, so that it is not possible to determine a stable laminar value for  $p_2$  before the transition. The values of  $p_2$  before the transition at low values of  $p_1$  agree quite well with the theoretical prediction. The turbulent results  $p_2$  of course do not agree with the prediction. Using equation (4.4) the height  $h_s$  at the separation point can be calculated from the pressure ratio. In figure 4.19 the results are plotted. Clearly visible is the shift of the separation point in the downstream direction. This means that the flow remains longer attached to the walls of the model as the pressure difference in the experiments increases. For  $h_0 = 3.39$  mm a limit is reached above  $p_1 = 200$  Pa ( $Re = 4500$ ). The limit in the right graph of figure 4.4 coincides with the value of  $h/h_0$  at the end of the linearly diverging part of the constriction. This implies that the model is acting like a well-designed diffuser and only at the end of the diffuser the flow is separating from the walls.

In figure 4.20 the moment at which the transition occurs is plotted as a function of the pressure drop  $p_1$  across the constriction. This figure illustrates that like the Coanda effect, turbulence needs a long time before it is established. So, similar to the Coanda effect, in pulse-like flow with a duration of the order of 10 ms this effect will not be important. Although at high pressures figure 4.17 shows that the pressure in the throat never reaches a steady laminar value before turbulence sets in completely.

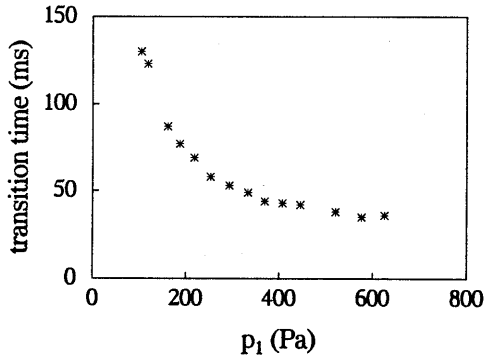


Figure 4.20: The time with respect to the trigger point at 0.1 s at which the flow starts to change significantly due to the onset of turbulence. Diffuser model with  $\alpha = 10^\circ$ .

#### 4.2.5 Results for the asymmetric diffuser model

In order to study the influence of an asymmetry in the geometry on the flow (in particular with respect to the Coanda effect) experiments were done using a combination of two different blocks. The upper has been taken from the  $10^\circ$ -diverging model and the lower block from the  $20^\circ$ -diverging model as illustrated by figure 4.21. The throat height in the experiments is  $h_0 = 3.43$  mm. As opposed to the single side measurements of the previous sections in this set-up pressures in the throat are measured simultaneously in the upper block and in the lower block. Piezo-electric pressure transducers (PCB type 116A) with a diameter of 10.4 mm are mounted in each block. Because of the size of the transducer a

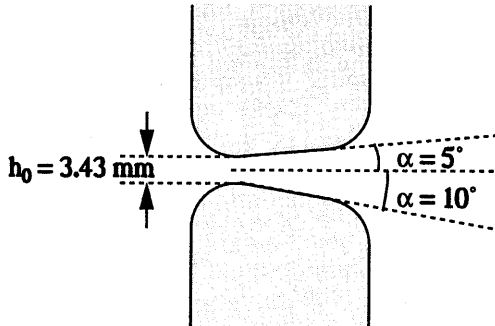


Figure 4.21: Asymmetric model built with two different blocks from the models presented in figure 4.4. Pressures are measured in the throat at both upper wall and lower wall by means of a slit-like pressure tap and two piezo-electric pressure transducers (PCB).

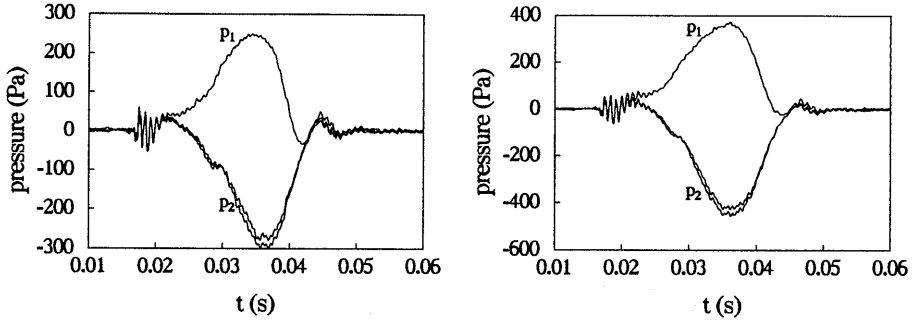


Figure 4.22: Pressure measured in the pipe  $p_1$  and in the throat  $p_2$  for the asymmetric diffuser geometry: top  $\Delta p = 389$  Pa, bottom  $\Delta p = 691$  Pa,  $h_0 = 3.43$  mm. The pressure  $p_2$  is measured simultaneously in the upper block and the lower block. The trigger point is now at 0.02 s.

much larger pressure tap is necessary to ensure a fast response time. A slit of 0.3 mm across the whole width of the block is used. This pressure tap yields unreliable quantitative results as discussed in appendix B but the qualitative results are found to be quite interesting and reproducible. Therefore we will use these results to compare the pressure measurements in upper and lower block.

In figure 4.22 two measurements at medium ( $\Delta p = 389$  Pa) and high ( $\Delta p = 691$  Pa) pressure difference are shown. For these experiments a pulse-like flow is used in order to simulate the pulse-like flow through the vocal folds. Furthermore, the opening time of the valve is decreased by increasing the tension of the spring blade. In these experiments the trigger point is at 0.02 s. A typical opening and subsequent closing takes about 25 ms, corresponding with a glottal pulse with a duration of about 8 ms. The duration is so short that never during the experiments the steady pressure limit is reached, as can be deduced from the value of  $\Delta p$  and the maximum value of  $p_1$  in the experiment. During the opening phase of the experiments a behaviour similar to what was observed in the starting-flow experiments can be observed. The pressures  $p_2$  initially increase proportional to the pressure  $p_1$  and then decreases. During the closing phase an interesting phenomenon is observed: the oscillation of the pressures. The driving pressure  $p_1$  even reaches a small negative value while  $p_2$  again reaches a positive value. However, the pressure difference  $p_1 - p_2$  is very small during these oscillations so that (almost) no flow is associated with this behaviour. These oscillations correspond to acoustic oscillations of the pipe in the fundamental mode when the valve is closed (300 Hz to 500 Hz), which are strongly damped by the porous material covering the inner walls of the pipe.

The most important observation, however, is that the two pressure signals  $p_2$  measured simultaneously at both sides of the throat are very close. Although a small difference around the pressure minimum can be observed, this is not the difference that would be

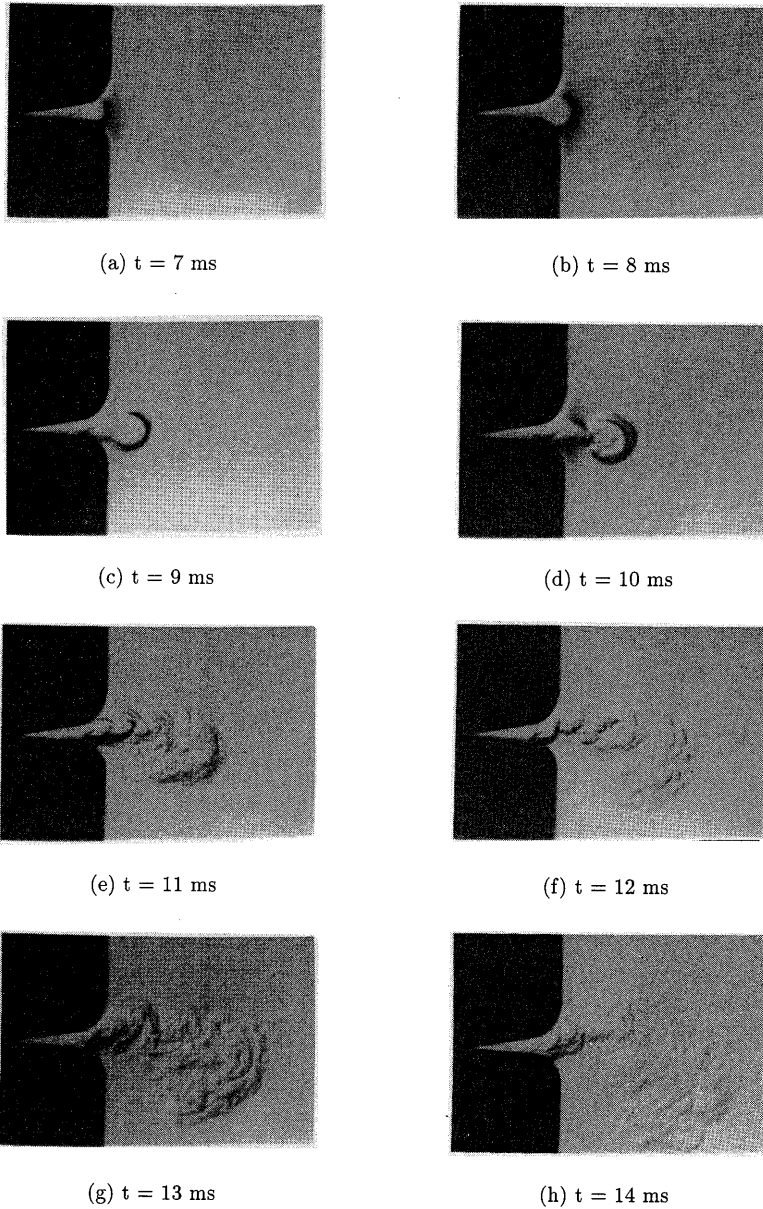


Figure 4.23: Flow visualisations by means of Schlieren photography in the asymmetric set-up. Time is with respect to the trigger point.  $\Delta p = 249$  Pa,  $h_0 = 1.05$  mm.

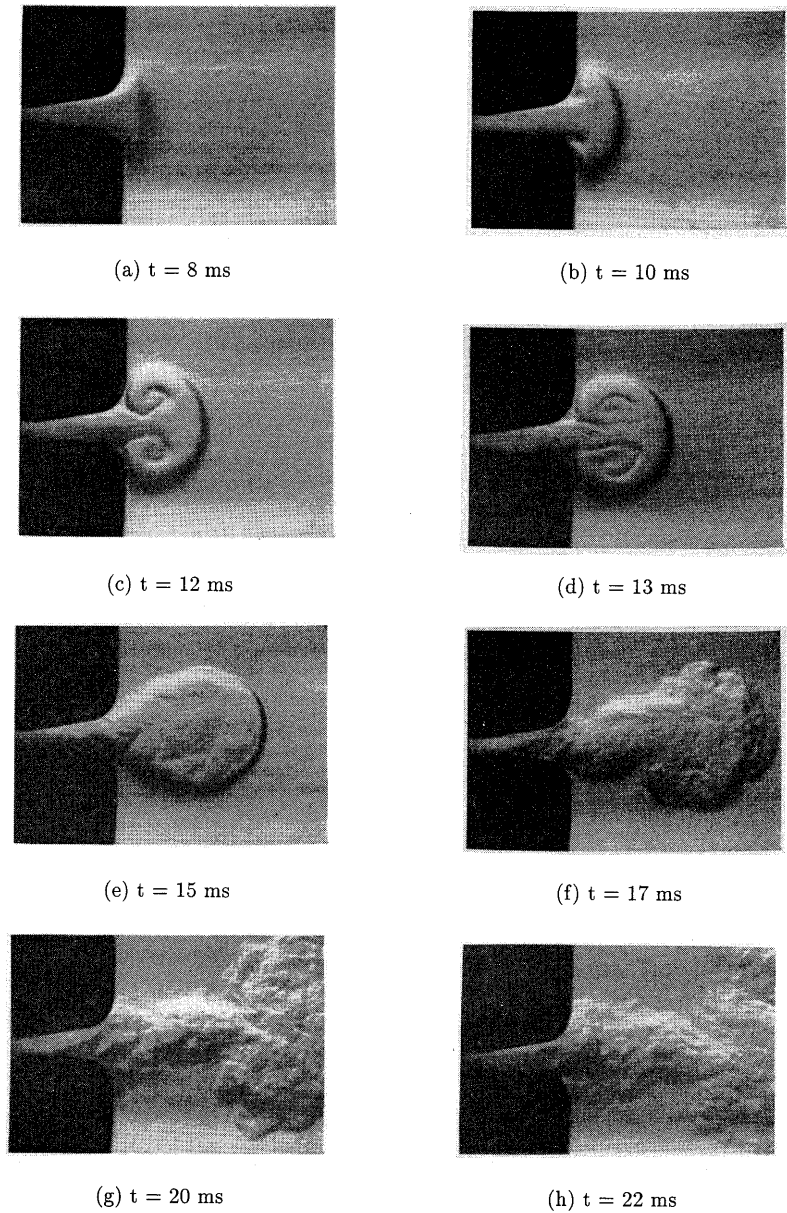


Figure 4.24: Flow visualisations by means of Schlieren photography in the asymmetric set-up. Time is with respect to the trigger point. Note the almost symmetric jet structure.  $\Delta p = 223$  Pa,  $h_0 = 3.43$  mm.

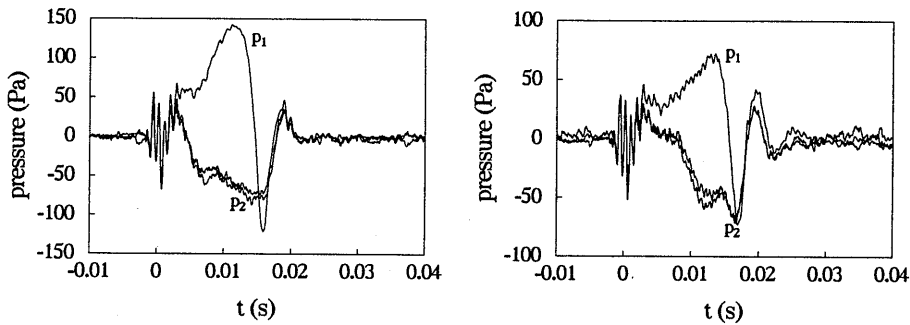


Figure 4.25: Pressure measured in the pipe  $p_1$  and in the throat  $p_2$  for the asymmetric diffuser geometry: in the left graph  $\Delta p = 249$  Pa and  $h_0 = 1.05$  mm, in the right graph  $\Delta p = 223$  Pa and  $h_0 = 3.43$  mm. The pressure  $p_2$  is measured simultaneously in the upper block and the lower block.

associated with a Coanda effect. A small pressure difference is to be expected because of the asymmetry in the geometry. This is further confirmed by the flow visualisations presented in figure 4.23 for  $h_0 = 1.05$  mm at a steady pressure difference of  $\Delta p = 249$  Pa, and in figure 4.24 for  $h_0 = 3.43$  mm at a steady pressure difference of  $\Delta p = 223$  Pa. The pressure signals associated with these experiments are shown in figure 4.25. In the case of  $h_0 = 1.05$  mm the jet structure is initially symmetric and becomes unstable after approximately 10 ms. Immediately thereafter the jet flow becomes turbulent and also asymmetric. Apparently a Coanda effect did occur. The effect on the pressure is small, however, as can be observed in figure 4.25. In the case of  $h_0 = 3.43$  mm an almost symmetric jet structure is observed, which becomes turbulent after approximately 15 ms. In this case the symmetric structure of the jet is more or less maintained during the whole experiment.

## 4.3 Numerical simulation

### 4.3.1 Input for the simulations

Using the viscous vortex-blob method described in chapter 2 four simulations have been done with the diverging vocal-fold models at moderate Reynolds number (in the order of  $10^3$ ):  $\alpha = 20^\circ$ ,  $h_0 = 1.05$  mm and  $h_0 = 3.35$  mm;  $\alpha = 10^\circ$ ,  $h_0 = 1.05$  mm and  $h_0 = 3.35$  mm. This numerical method yields a solution of the two-dimensional incompressible Navier-Stokes equation and needs an imposed inflow as input. This input is obtained from experimental pressure measurements (as presented in the previous paragraphs) by fitting a 9<sup>th</sup>-order polynomial to the pressure difference ( $p_1 - p_2$ ) between pipe and throat as a function of time. Next this smooth fitted pressure profile is integrated in time using

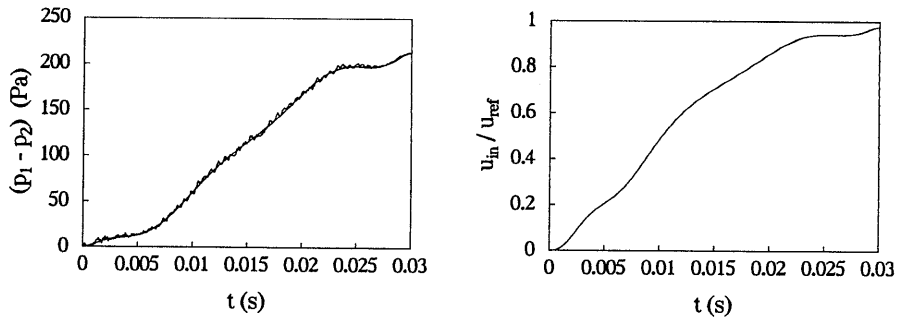


Figure 4.26: Input for a numerical simulation. The scaled inflow  $u_{in}/u_{ref}$  (right graph) for the numerical simulation is obtained from the pressure difference  $(p_1 - p_2)$  (left graph) by fitting a 9<sup>th</sup>-order polynomial (left graph) and integrating the unsteady Bernoulli equation,  $u_{ref} = 2.609$  m/s.

the unsteady Bernoulli equation to find the inflow velocity as a function of time. This method is more practical than a polynomial fit to the velocity profile because this usually requires at least two separate fits. In figure 4.26 an example is shown of the result of this procedure. In the left graph the pressure difference  $(p_1 - p_2)$  is plotted together with the fitted polynomial. In the right graph the resulting scaled inflow velocity is plotted as a function of time. Time equal to 0 is defined to be the start of the simulation.

The computational domain for the diffuser models is shown in figure 4.27. The inflow-velocity is uniformly imposed on the left inflow boundary. The height of the inflow channel is related to the radius of curvature  $r$  and the throat height  $h_0$ . It is defined as the reference length  $l_{ref}$  in the simulation  $l_{ref} = 4r + h_0$ . On the right the outflow boundary is a far-field semi-circular domain (at a distance of  $27 l_{ref}$ ). On this boundary a radial outflow is assumed and the outflow velocity is determined from the inflow velocity by the continuity equation. Since the geometry that we are interested in is symmetric with respect to its centre line the computation is restricted to the upper half of the domain. Hence the use of a symmetry line as a lower boundary and only half a glottis as the upper boundary. This also reduces the computational time and memory requirements by approximately a factor two. The boundary is discretised by a set of panels. A densification of panels is applied in the region around the vocal-fold model and on the symmetry line. A typical run requires 1600 to 1900 panels to build the geometry and uses 50,000 to 100,000 point vortices to discretise the vorticity field. The region in which the full (viscous) Navier-Stokes equations are solved is restricted to the viscous domain. Outside this domain only the inviscid Euler equations are solved. The viscous domain includes the whole jet-region and the region of flow separation (the whole constriction area). In the inflow domain and in the upper region of the outflow channel viscous effects are neglected since they have negligible influence on the results.



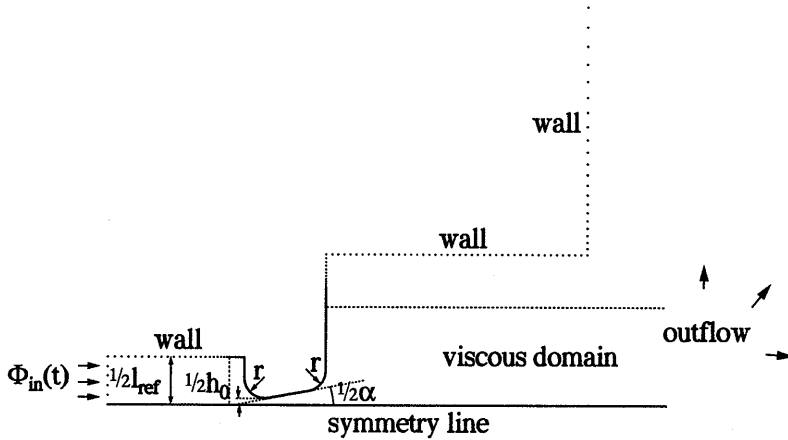


Figure 4.27: Two-dimensional domain used in the numerical simulations. Throat height  $h_0$  and total angle of divergence  $\alpha$  are input parameters. The inflow channel has a total height of  $4r + h_0$ .

#### 4.3.2 Results

In figures 4.28 and 4.29 visualisations of the numerical flow are shown. Since the numerical method we use is based on solving the vorticity transport equations it is most convenient to illustrate the results with the spatial distribution of vorticity. Furthermore, we found that the vorticity distribution exhibits much more features than recognisable when compared to flow visualisations than plots of either streamlines or velocity vectors. The results of two simulations are presented at several moments in time. The results in figure 4.28 are obtained for the geometry defined by  $\alpha = 20^\circ$  and  $h_0 = 3.35$  mm at a Reynolds number of 4061 based on the steady limit velocity ( $Re = u_{ref} l_{ref} / \nu$ ). The results in figure 4.29 are obtained for the geometry with a smaller angle of divergence  $\alpha = 10^\circ$  and a smaller throat height  $h_0 = 1.05$  mm at a Reynolds number of 1256.

Both figures show a global development of the flow. Initially no flow separation occurs and only boundary-layer growth is observed inside the constriction. At a certain moment flow separation occurs and a large vortex structure is formed. This vortex structure travels downstream, leaving the jet structure that is formed in its wake. After a short time one can observe secondary vortices forming in the shear layer that delimits the jet flow. The formation of these vortices is due to the inherent instability of the shear layer. The interaction of the vortices (pairing) leads to complex flow patterns, as is illustrated by the lower pictures. There are, however, also some distinctive differences between the two figures. Firstly, the structures in figure 4.28 are much more complex than the ones in figure 4.29. Secondly in figure 4.28 we observe a lot of interaction of vortex structures within the diffuser while in figure 4.29 this is not the case. These differences are due to the

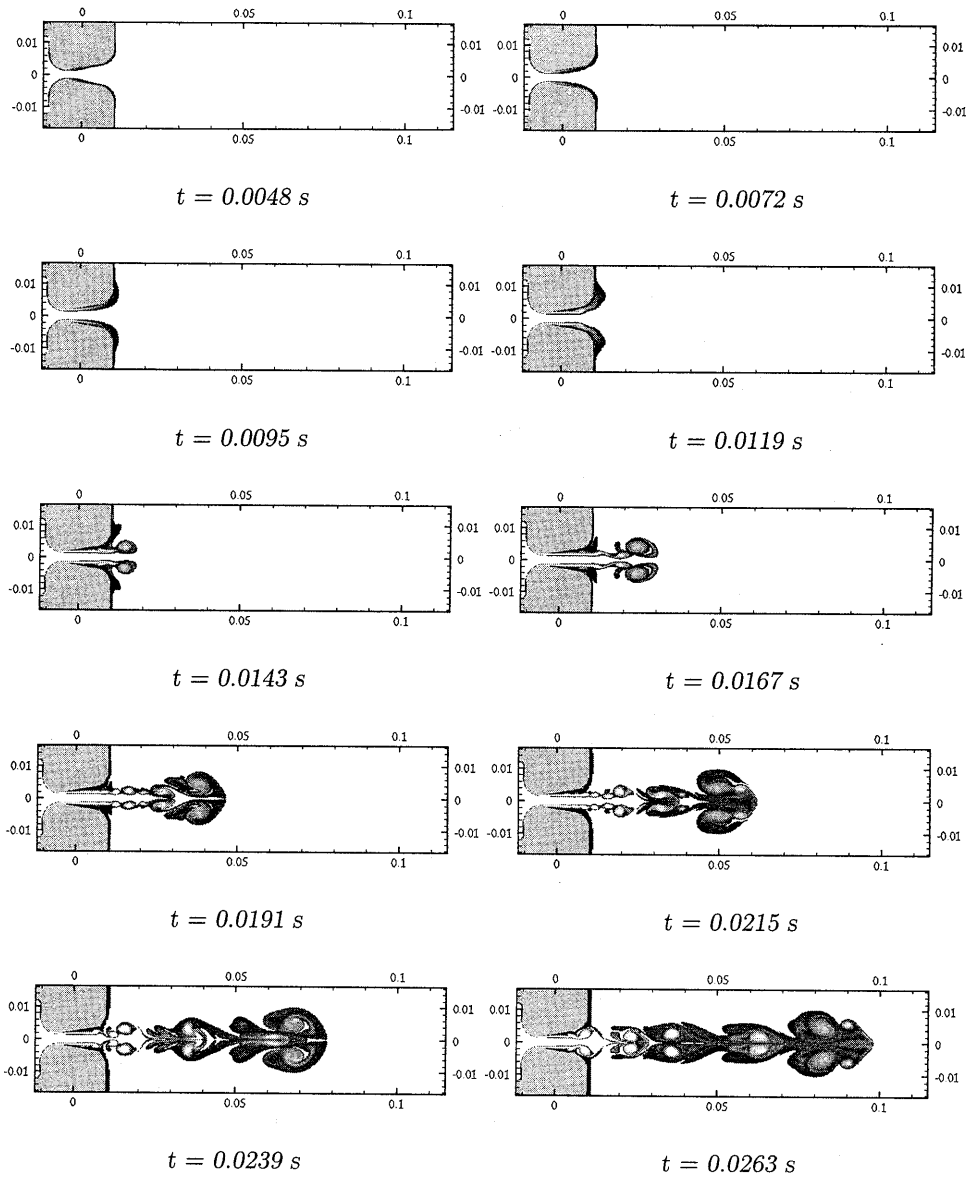


Figure 4.28: Vorticity distribution at several moments in time. The lower half is a mirror image of the top half. Dark implies low (negative) vorticity while light implies high (positive) vorticity.  $\alpha = 20^\circ$ ,  $h_0 = 3.35 \text{ mm}$ , and  $Re = 4061$ .

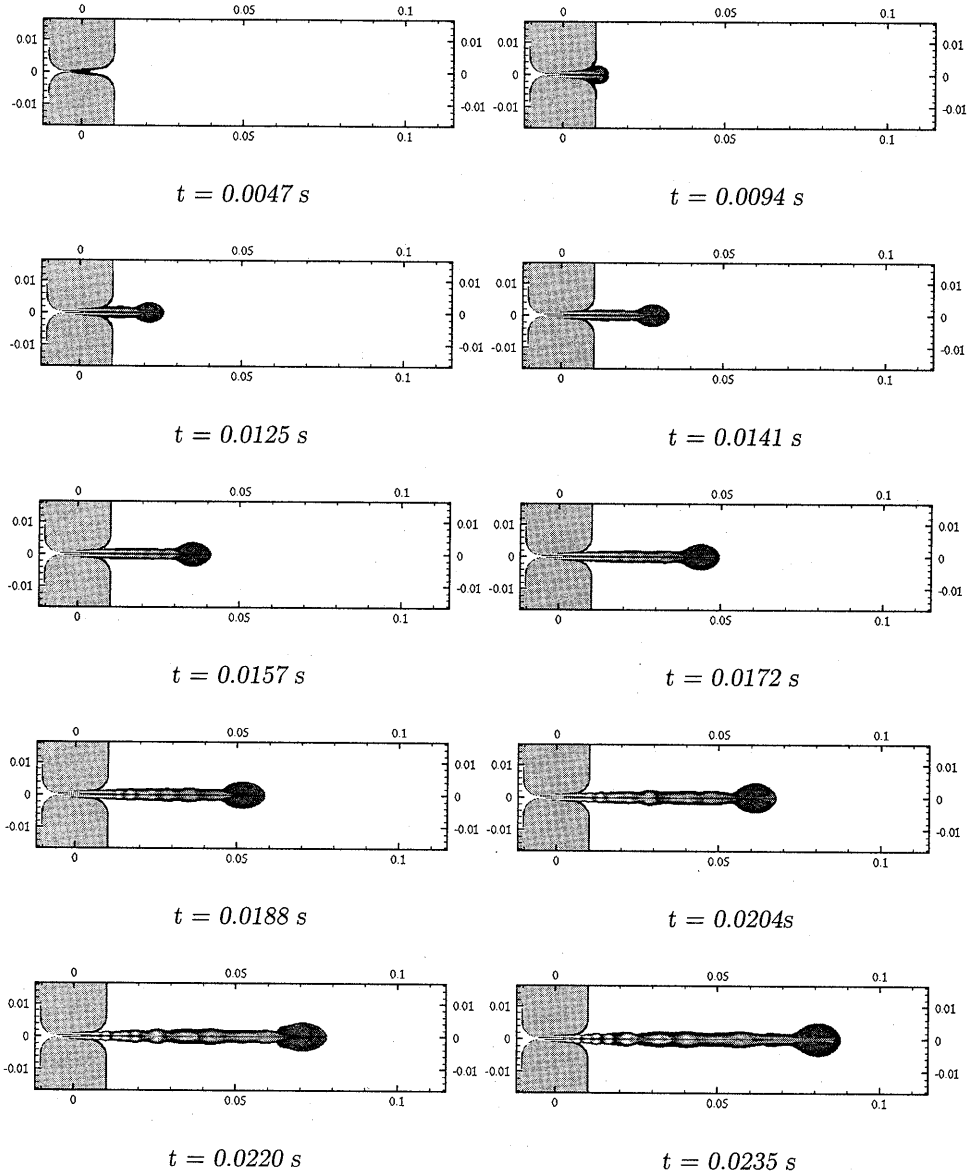


Figure 4.29: Vorticity distribution at several moments in time. The lower half is a mirror image of the top half. Dark implies low (negative) vorticity while light implies high (positive) vorticity.  $\alpha = 10^\circ$ ,  $h_0 = 1.05 \text{ mm}$ , and  $Re = 1256$ .

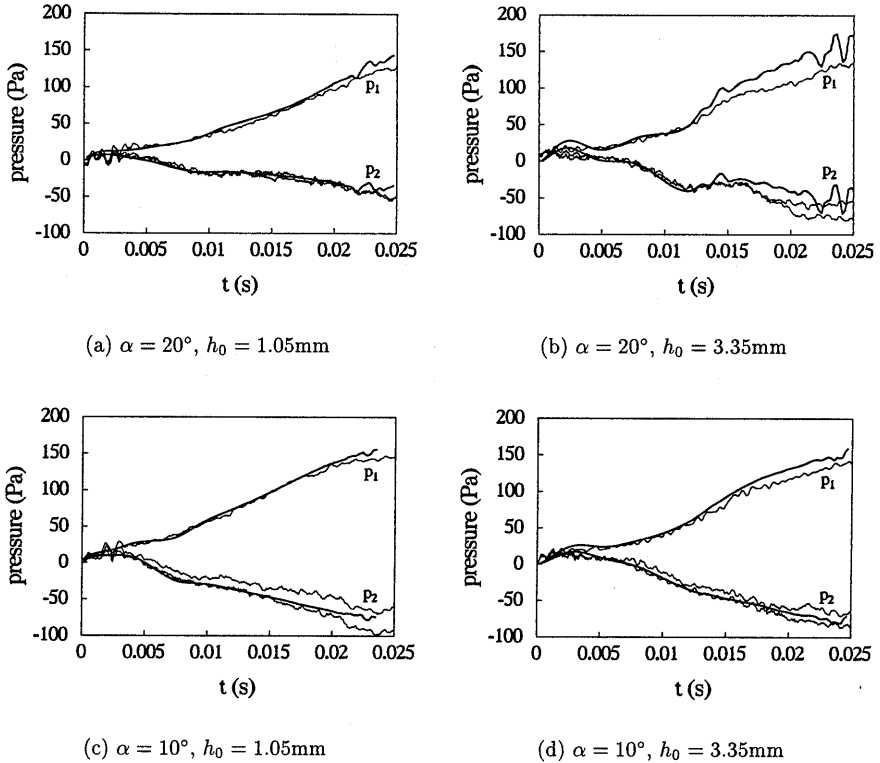


Figure 4.30: Comparing numerical results for the pressures  $p_1$  and  $p_2$  (thick lines) to the experiments (thin lines) from which the respective inflow velocities have been obtained.

geometry and the Reynolds number. In the first case the geometry is relatively more open ( $\alpha = 20^\circ$  and  $h_0 = 3.35\text{ mm}$ ) making it more accessible, while also the Reynolds number is higher, making the shear layer more unstable. We will show that also the separation point behaves differently. Both figures show flows in which coherent vortex structures are the main features. This is not observed in the actual experiments. Due to three-dimensional effects the turbulence will ultimately destroy these structures at some distance from the nozzle exit and thus a turbulent jet flow will follow. However, during an impulsively started experiment these two-dimensional structures are present (see flow visualisations in figures 4.23 and 4.24.)

The inflow boundary condition has been obtained from experimentally measured pressure differences ( $p_1 - p_2$ ) in the four geometries. The experimental pressures are shown in figure 4.30 represented by the thin lines. The pressure  $p_1$  was measured 8 mm upstream of the constriction while the pressure  $p_2$  was measured in the throat of the constriction. Two

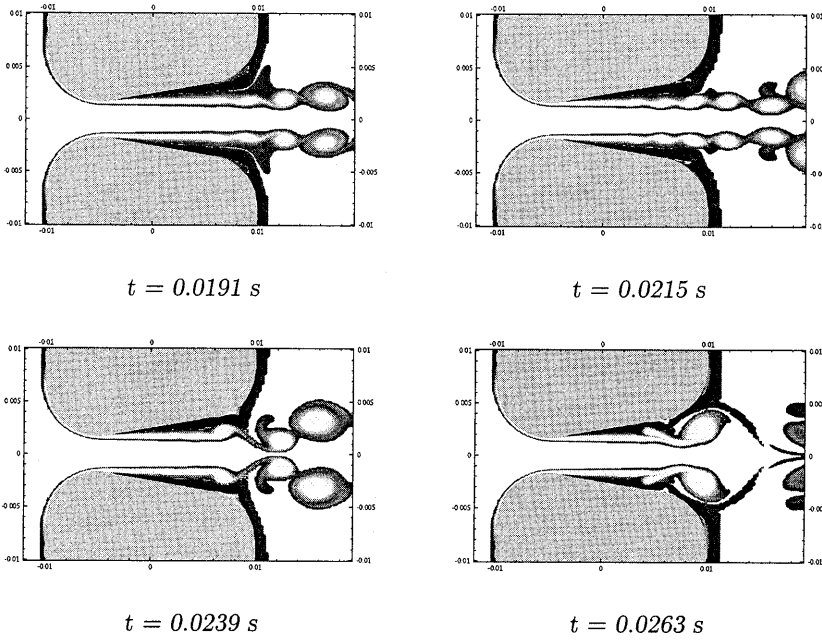


Figure 4.31: Close-up of vorticity distribution in the diffuser region showing a complex interaction of vortices and the diffuser walls. Results obtained for  $\alpha = 20^\circ$  and  $h_0 = 3.35 \text{ mm}$ .

experimental pressure signals  $p_2$  are shown to illustrate whether the experimental flow was symmetric or not. Also shown are the numerical results for  $p_1$  and  $p_2$  by means of the thick lines. Although the experimental pressure difference ( $p_1 - p_2$ ) was used to determine the inflow velocity, this does not impose individual values of either  $p_1$  or  $p_2$ . The results in figure 4.30 demonstrate that the numerical method yields very reasonable results for the pressure. Note that the very unstable behaviour that was found experimentally for the case  $\alpha = 20^\circ$  and  $h_0 = 3.50 \text{ mm}$  (see figure 4.13) seems also to be present in the numerical result for  $\alpha = 20^\circ$  and  $h_0 = 3.35 \text{ mm}$ , shown in the top right graph of figure 4.30. An explanation for this unstable behaviour is suggested by a close-up of the numerical vorticity in the region of the diffuser shown in figure 4.31. As these plots show, the interaction between the jet and the walls of the diffuser is very complex. Burst of vorticity leave the walls at some moments in time. Pressure fluctuations in experiments could well be associated with this behaviour.

In order to study the behaviour of the separation point in these flows the height  $h_s$  of the channel at the separation point is plotted versus time in figure 4.32. As references the heights that are associated with the starting point and the end point of the diffuser

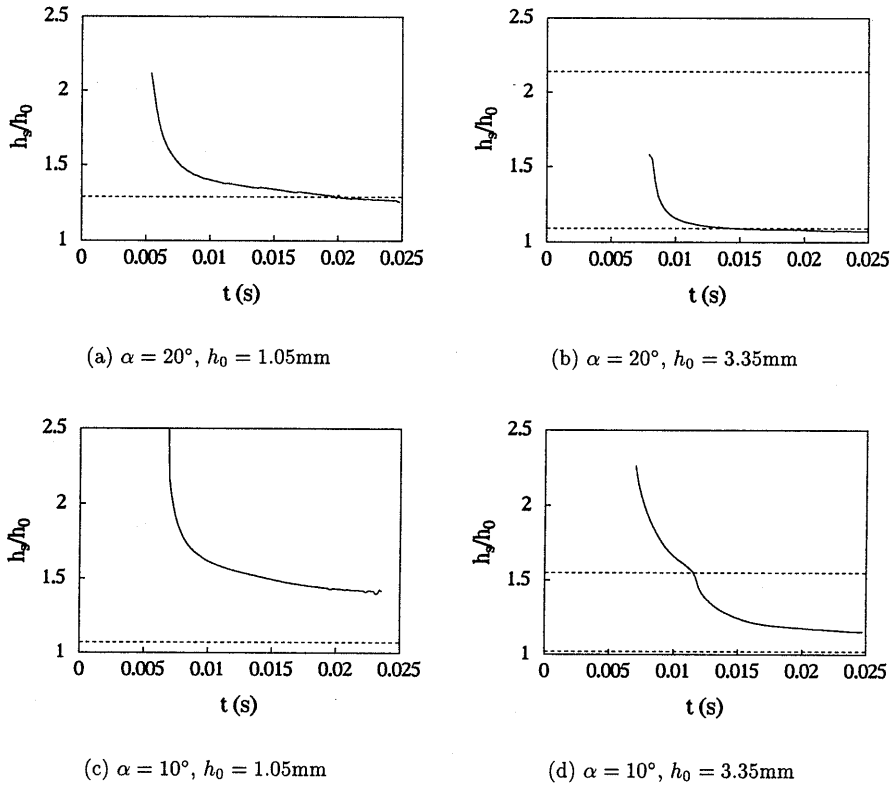


Figure 4.32: Point of zero wall stress (as defined by  $\frac{\partial u}{\partial y} = 0$  on the wall) as a function of time obtained from the numerical simulations. The dashed lines illustrate the starting point (lower line) and the end point (upper line) of the diffuser section.

section are indicated by the dashed horizontal lines. The definition of a separation point is not obvious in an unsteady flow. We used the definition of the separation point for steady flows:  $\frac{\partial u}{\partial y} = 0$  on the wall, which is equivalent to  $\omega_{wall} = 0$ . This choice was made for two reasons: it makes a comparison to a quasi-steady model straightforward and for practical purposes it is the only useful definition. So we define the point of zero wall stress to be the separation point in our results. Furthermore, we expect this to be quite reasonable for our results.

The behaviour visible in the top two graphs for  $\alpha = 20^\circ$  is very different from that in the bottom two graphs for  $\alpha = 10^\circ$ . First of all for  $\alpha = 20^\circ$  flow separation starts somewhere halfway in the constriction and moves very rapidly to the throat of the constriction. A steady value just downstream of the constriction on the cylindrical part is reached after

10 ms. In case  $\alpha = 10^\circ$  flow separation starts at the end of the constriction on the cylindrical part. It then moves rapidly to a stable point somewhere on the diffuser part of the vocal-fold model. The model is acting like a diffuser and a small perturbation can have a significant influence on the separation point. So it is understandable that a transition from a laminar to a turbulent flow results in a sudden change of pressure in the throat as observed in the experiments presented in figure 4.17.

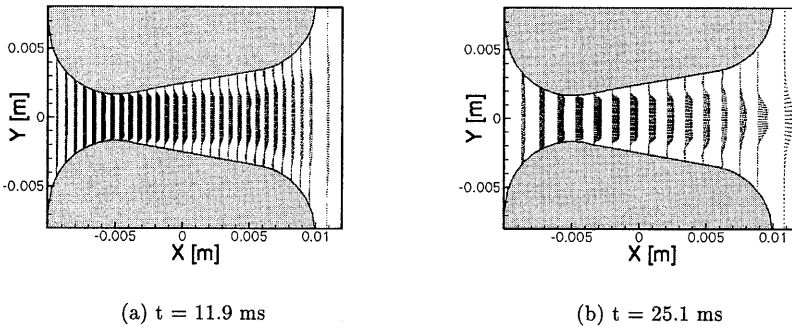


Figure 4.33: Close up of the constriction region showing the velocity vectors.  $\alpha = 20^\circ$  and  $h_0 = 3.35$  mm.

After having demonstrated the complexity of this type of flow we will evaluate a simplified quasi-steady description of the flow. In figure 4.33 a close-up of the flow through the vocal-fold models is presented. The figure shows the velocity profiles in the region of the throat and illustrates the fact that a boundary-layer description is reasonable in the region around the throat. The velocity profiles exhibit a thin boundary layer near the walls and an approximately uniform profile in the bulk of the flow. Only further downstream the first vortical structures can be observed.

Similar to the figures 4.15 and 4.18 we present the pressure ratio  $p_2/p_1$  as a function of  $p_1$ , where both are functions of time, in figure 4.34. Since the theoretical model incorporates the assumption that the pressure at the separation point is equal to zero, we use the pressure at the separation point as the reference pressure for the numerical results and the separation point is determined as explained above (see also figure 4.32). Hence figure 4.34 presents  $(p_2 - p_s)/(p_1 - p_s)$ , where  $p_s$  is the pressure on the symmetry line at the horizontal (stream-wise) position of the separation point.

After an initial stage, in which the flow is essentially unsteady, we see that the agreement between numerical results and theoretical prediction is quite good. This is surprising since the boundary-layer prediction and the steady limit of the experiments did not agree as well (see figures 4.15 and 4.18). An explanation can be found in figure 4.35. In this figure the pressures  $p_1$  and  $p_2$  are plotted together with  $(p_1 - p_s)$  and  $(p_2 - p_s)$  in each graph. The dashed lines represent the pressure with respect to the far field, which agreed

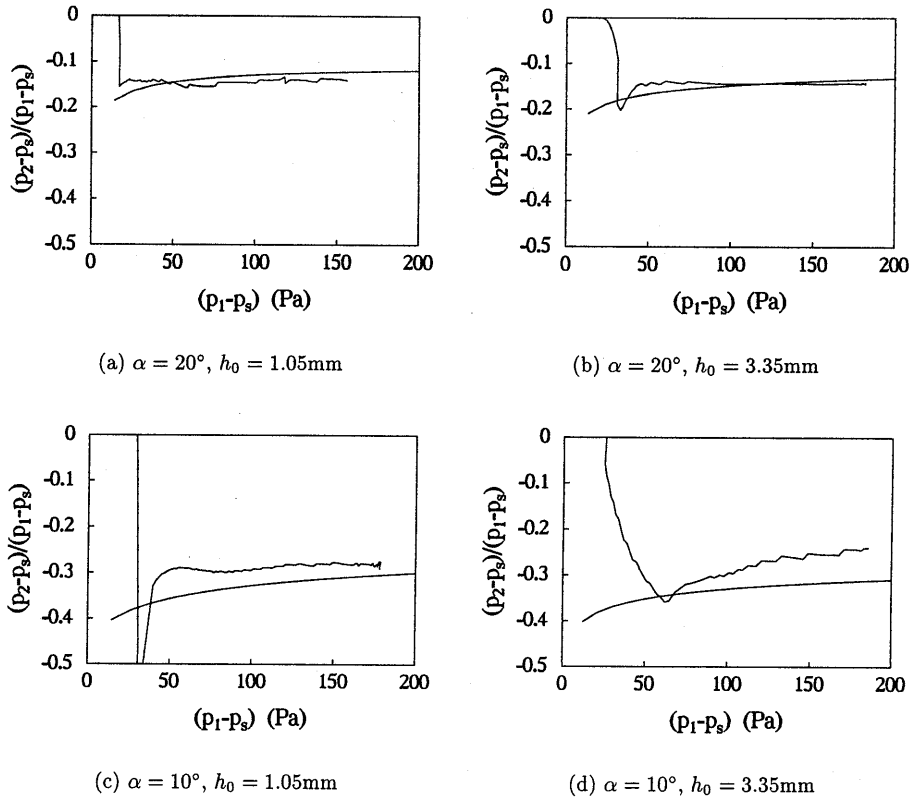


Figure 4.34: Comparing numerical results for the pressure ratio  $p_2/p_1$  to quasi-steady boundary-layer predictions.  $p_1$  and  $p_2$  are determined relative to the pressure at the point of zero wall stress.

with the experimentally measured pressure as illustrated by figure 4.30. The solid smooth lines represent the pressure with respect to the separation point, as used in figure 4.34. The difference between these two lines is the contribution to the pressure due to the flow downstream of the separation point inside the constriction and the jet flow. Note that the pressure drop  $p_2$  from throat to separation point is about equal to the pressure drop from the separation point to the far-field. This explains the large discrepancies found between experiments and boundary-layer theory. Note also that the pressure fluctuations are due to the flow downstream of the separation point. This indicates that the structure of the jet flow might be important to predict the source of sound in speech modelling. In particular the jet instabilities can induce higher frequencies which are experienced in speech as broad-band "noise".



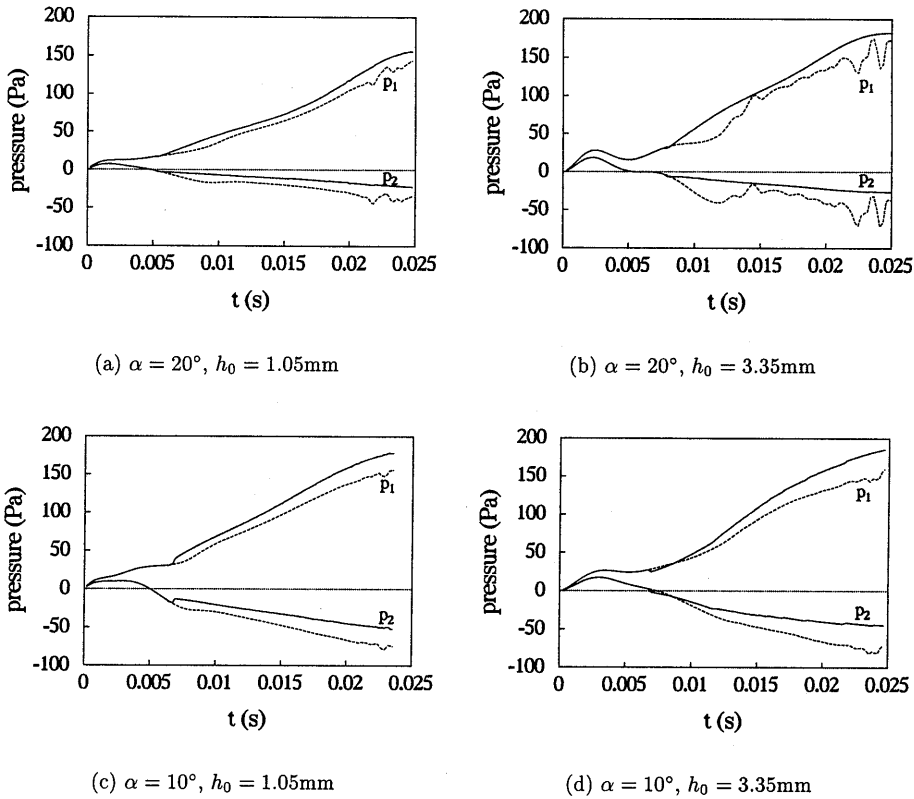


Figure 4.35: Influence of the jet on the pressure signal. Solid lines represent pressures  $(p_1 - p_s)$  and  $(p_2 - p_s)$  with respect to the pressure at point of zero wall stress, while the dashed lines represent pressures  $p_1$  and  $p_2$  with respect to the far-field pressure as used in the experiments.

#### 4.4 Concluding remarks

In this chapter we set out to describe the flow through *in vitro* models of the vocal folds. By means of a combined experimental, numerical and theoretical study we have managed to explain most of what was observed.

First of all the richness of phenomena observed in experiments demonstrates the complexity of this type of flow. However, we have shown results that make it reasonable to ignore some of these phenomena in a model of the flow through the vocal folds; both the Coanda effect as well as the transition to a turbulent flow need time, which in a 100 Hz pulse-like flow as encountered in male speech production, is not available. Female speech

production corresponds to typical frequencies of 200 Hz and will be even less sensitive to these effects. Even an asymmetry in the geometry did not trigger the Coanda effect which would result in a completely asymmetric flow. This conclusion is drawn, however, for rigid models with an unsteady flow. The influence of wall movement on the Coanda effect still has to be determined.

The behaviour of the diffuser-like vocal-fold models at a Reynolds number of the order  $10^3$  seems similar to what has been reported in literature about diffuser performance at much higher Reynolds number of the order  $10^5$ . Similar to results reported by Kwong & Dowling (1994) obtained in a diffuser, we found both experimentally and numerically that the vocal-fold model with a diffuser angle of  $20^\circ$  and an initial height  $h_0 = 3.50$  mm exhibited very unsteady flow behaviour. For the vocal-fold model with a diffuser angle of  $10^\circ$  and an initial height  $h_0 = 3.39$  mm we found experimentally that it acts as a well-designed diffuser. This is conform data presented in Blevins (1984) on diffuser performance.

The comparison between experiment and boundary-layer theory in combination with a quasi-steady free jet indicated that the theoretical model showed typical systematic errors of 30 % in the throat pressure. The numerical study, on the other hand, confirmed that the model was not inadequate but that some of the assumptions had to be adjusted. After an initial period of essentially unsteady flow the quasi-steady boundary-layer model describes the flow up to the separation point with a surprising accuracy. The simplified description of the jet ( $p$  is constant), however, is inadequate to describe the jet. This is confirmed by considering that the difference between the far-field pressure and pressure at the separation point is of the same order as the pressure difference between the pressure at the separation point and the pressure at the throat of the glottis. This implies that the pressure difference due to the jet is significant. Furthermore, all fluctuations on the pressure signals are related to the pressure difference associated with the jet. The assumption of a quasi-steady jet is in fact the main source of inaccuracy in our prediction of the throat pressure. An improvement of the jet model is necessary. Such an improvement, however, is only relevant when the mechanical modelling of the vocal folds has a similar degree of sophistication.

## References

- ALIPOUR, F. & TITZE, I.R. (1996) Combined simulation of two-dimensional airflow and vocal fold vibration. Published in "Vocal fold Physiology: Controlling Complexity and Chaos", P.J. Davis and N.H. Fletcher editors. *Singular Pub. Group, San Diego*, 17-29
- ALIPOUR, F. FAN, C., & SCHERER, R.C. (1996) A numerical simulation of laryngeal flow in a forced-oscillation glottal model. *J. Computer Speech and Language* **10**, 75-93
- BLEVINS, R.D. (1984) Applied fluid dynamics handbook. *Van Nostrand Reinhold Company Inc., New York*

- DENNIS, S.C.R., BANKS, W.H.H., DRAZIN, P.G., & ZATURSKA, M.B. (1997) Flow along a diverging channel. *J. Fluid Mech.* **336**, 183–202
- HIRSCHBERG, A., PELORSON, X., HOFMANS, G.C.J., VAN HASSEL, R.R., & WIJNANDS, A.P.J. (1996) Starting transient of the flow through an in-vitro model of the vocal folds. Published in "Vocal fold Physiology: Controlling Complexity and Chaos", P.J. Davis and N.H. Fletcher editors. *Singular Pub. Group, San Diego*, 31–46
- KWONG, A.H.M. & DOWLING, A.P. (1994) Unsteady flow in diffusers. *ASME J. Fluids Eng.* **116**, 842–847
- LOUS, N.J.C., HOFMANS, G.C.J., VELDHUIS, R.N.J., & HIRSCHBERG, A. (1998) A symmetrical two-mass vocal-fold model coupled to vocal tract and trachea, with application to prosthesis design. *accepted for publication in Acta Acoustica*
- LUO, X.Y. & PEDLEY, T.J. (1996) A numerical simulation of unsteady flow in a two-dimensional collapsible channel. *J. Fluid Mech.* **314** 191–225
- PEDRIZZETTI, G. (1996) Unsteady tube flow over an expansion. *J. Fluid Mech.* **310**, 89–111
- PELORSON, X., HIRSCHBERG A., VAN HASSEL, R.R., WIJNANDS, A.P.J., & AUREGAN Y. (1994) Theoretical and experimental study of quasi-steady flow separation within the glottis during phonation. Application to a modified two-mass model. *J. Acoust. Soc. Am.* **96**, 3416–3431
- PELORSON, X., HOFMANS, G.C.J., RANUCCI, M., & BOSCH R.C.M. (1997) On the fluid mechanics of bilabial plosives. *Speech Comm.* **22**, 155–172
- PELORSON, X. & HIRSCHBERG, A. (1997) In vitro study of the glottal and supra-glottal flow during phonation. Proceedings of the 4<sup>th</sup> Congress on Acoustics, Marseille *Teknea, Toulouse*, 337–340
- ROOZEN, N.B., BOCKHOLTS, M., VAN ECK, P., & HIRSCHBERG A. (1998) Vortex sound in bass-reflex ports of loudspeakers, Part I: Observation of response to harmonic excitation and remedial measures, Part II: A method to estimate the point of separation. *accepted for publication in J. Acoust. Soc. Am.*
- ROSENFELD, M. (1995) A numerical study of pulsating flow behind a constriction. *J. Fluid Mech.* **301**, 203–223
- ROTHENBERG, M. (1981) Acoustic interaction between the glottal source and vocal tract. Proceedings of the Kurume Vocal Fold Physiology Conference, K.N. Stevens and N. Hirano editors. *University of Tokyo Press*, 305–328

# Aeroacoustic behaviour of a diaphragm in a pipe

## 5.1 Introduction

Diaphragms are common elements in pipe systems, either used as a strong constriction of the flow in a pipe or as an aperture to a Helmholtz resonator located in the pipe wall. In figure 5.1 examples of such configurations are shown. Both configurations are commonly used for instance in car mufflers to suppress resonances in the exhaust pipe. Although several experimental investigations into the effects of diaphragms have been carried out previously, a combined experimental, theoretical and numerical study is still lacking. In this chapter we focus on the diaphragm acting as a strong constriction to the main pipe flow and compare experimental, theoretical, and numerical results.

The influence of rapid changes in the pipe cross section on the propagation of acoustic waves was observed already in the nineteenth century (Rayleigh 1896). Ingard (1953) and Ingard & Ising (1967) studied non-linear phenomena associated with the acoustic flow through an orifice. But it was not until 1967 that Ronneberger proposed a simple low-frequency theoretical description for the aeroacoustic effect of a subsonic mean flow

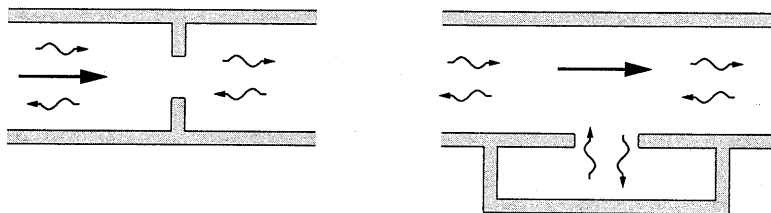


Figure 5.1: Configurations of a diaphragm in a pipe with a mean flow.

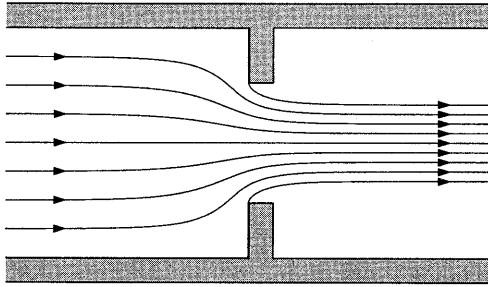


Figure 5.2: The vena contracta of the flow through a diaphragm.

through a stepwise expansion in a pipe taking effects due to compressibility and variations in entropy into account (Ronneberger 1967). Bechert (1980) followed by proposing a similar quasi-steady incompressible-flow description for the effect of a subsonic mean flow through a diaphragm used as a pipe termination. He also provided an overview of the experimental work that was done until 1980. As an important result of his theoretical description Bechert found that for a certain mean flow velocity the pipe termination was completely anechoic. This phenomena has been discussed in terms of vortex-sound theory by Howe (1979) and confirmed experimentally by Cummings and Eversman (1983). Our theoretical work is an extension of the theories of Ronneberger and Bechert. It describes a diaphragm in a pipe (not a diaphragm just as a pipe termination) and it includes compressibility effects which had been neglected by Bechert. Another important phenomenon of the flow that we incorporate in our theoretical model is the so-called *vena contracta* effect. The *vena contracta* effect causes a jet flow through the aperture, which has a cross-sectional area smaller than the aperture itself as sketched in figure 5.2.

First a quasi-steady acoustic model is presented for low-Mach-number flows. The acoustic effect of the diaphragm is studied by considering the acoustic pressure reflection and transmission coefficients. The model is extended by including compressibility effects. It is shown that, depending on the size of the aperture of the diaphragm, compressibility effects are important for an accurate modelling of the acoustic effects even for quite low-Mach-number flows in the main pipe.

The *vena contracta* effect is essential when considering a diaphragm with sharp edges. Therefore this is considered next. The influence of both geometry and Mach number on the *vena contracta* is treated. Then low-frequency experiments on a slit-like diaphragm in a pipe are compared to the quasi-steady acoustic model.

In order to model the high-frequency response of a slit-shaped diaphragm in a pipe the vortex-blob method is used to simulate the flow. It yields a solution of the two-dimensional incompressible-flow equations and it includes flow separation at the edges of the diaphragm. Because the method is an incompressible-flow method the results of the vortex-blob method can only be applied to low-Mach-number flows when the acoustic source region can be considered as compact. Results of the vortex-blob method like the acoustic losses due

to the flow through the diaphragm are presented. A comparison is made between two different formulations of the acoustic source power; results of Howe's energy formulation for the acoustic source power are compared with results of the pressure formulation. The acoustic power is studied as a function of acoustic amplitude and diaphragm opening. Also the influence of details of the geometry of the diaphragm is studied. Another result of the vortex-blob method is the acoustic source pressure that is incorporated in an acoustic model of the diaphragm flow. The acoustic pressures upstream of the diaphragm and the acoustic pressures downstream of the diaphragm are related by the so-called scattering matrix. Predictions of the components of the scattering matrix are compared to low-Mach-number high-frequency experimental results.

## 5.2 Quasi-steady modelling

### 5.2.1 Defining the approximations

In this chapter two different models are presented to determine the acoustic response of a diaphragm in a pipe. The models represent different approximations for the flow through the diaphragm. A set of non-dimensional numbers is introduced in order to define the limits of validity of each model. In this section we discuss the non-dimensional numbers and explain the various limits associated with these numbers. In subsequent sections the following non-dimensional numbers are used:

$$\begin{aligned}
 M_1 &= \frac{u_1}{c_1} && : \text{Mach number} \\
 Sr &= \frac{f h_d}{u_d} && : \text{Strouhal number} \\
 He &= \frac{f h_p}{c_1} && : \text{Helmholtz number} \\
 Re &= \frac{u_1 h_p}{\nu} && : \text{Reynolds number} \\
 u_{ac} &= \frac{u'_1}{u_1} && : \text{Acoustic amplitude} \\
 \Upsilon &= \frac{S_j}{S_d} && : \text{Vena contracta (contraction) ratio} \\
 S &= \frac{S_p}{S_j} = \frac{S_p}{\Upsilon S_d} && : \text{Cross-sectional-area ratio}
 \end{aligned}$$

where  $u_1$  and  $c_1$  are the steady main velocity and the speed of sound in the pipe upstream of the diaphragm, respectively.  $f$  is the frequency of the acoustic waves,  $h_d$  is the height of the aperture of the (two-dimensional) diaphragm,  $u_d = (S_p/S_d)u_1$  is the average velocity across the aperture of the diaphragm,  $h_p$  is the height of two-dimensional channel,  $\nu$  is the kinematic viscosity,  $u'_1$  is the acoustic velocity in the pipe upstream of the diaphragm,

$S_j$  is the cross-sectional area of the jet,  $S_d$  is the cross-sectional area of the aperture of the diaphragm, and  $S_p$  is the cross-sectional area of the pipe. The cross-sectional area is defined as the height times the width  $W$  of the pipe: e.g.  $S_p = W \cdot h_p$ . Some of these quantities are shown in figure 5.3.

The flow through the diaphragm (sketched in figure 5.3) can be separated into three regions: first the uniform flow in the upstream pipe segment, in which plane acoustic waves are travelling in upstream and downstream direction; second the compact flow in the acoustic source region around the diaphragm where acoustic energy is produced or dissipated; and third the uniform flow in the downstream pipe segment, in which again plane acoustic waves are travelling in upstream and downstream direction. The Strouhal number as defined above is a measure for the importance of unsteady flow effects in the source region. A low value indicates that the jet flow can be considered quasi-steady, while a high value indicates an essentially unsteady jet flow. The Helmholtz number is a measure of the size of the source region relative to the wavelength of the acoustic wave. When  $He$  approaches zero the wavelength of the acoustic wave is much larger than the linear dimension of the source region. In that case the phase difference of acoustic quantities across the source region can be neglected and the source region is called compact.  $He = \mathcal{O}(1)$  means that the source region has to be treated as an essentially unsteady flow including effects of acoustic wave propagation. In this chapter we focus on low-frequency acoustic waves only, i.e. the source region can be considered compact although the Strouhal number can be of order unity.

Although we defined seven non-dimensional numbers only five of these numbers can be chosen independently. Therefore when the Strouhal number and the Helmholtz number are chosen as independent numbers the Mach number  $M_1$  is related to  $He$  and  $Sr$  by:  $M_1 = (S_p/S_d)^2(He/Sr)$ .  $M_1$  is a measure of the importance of convection effects on the acoustic wave propagation in the pipe. The limit of  $He \rightarrow 0$  (while keeping  $Sr$  fixed) produces the limit  $M_1 \rightarrow 0$ : consequently an essentially unsteady, but incompressible, description of the source region can be used. The limit of  $Sr \rightarrow \infty$  (while keeping  $He$  constant) also produces the limit  $M_1 \rightarrow 0$ : consequently the convection effects and compressibility effects in the source region are negligible and the description of the source region is essentially unsteady. This last limit corresponds in linear approximation to the classic acoustic behaviour in a stagnant fluid. In that case the potential-flow approximation is actually recovered, because the effect of the convection velocity  $u_1$  on wave propagation and on the flow through the diaphragm is negligible. Although both cases lead to the same limit for the Mach number, they are to be considered as approaching this limit from different directions, and as such both descriptions can be very different. The Mach number in the jet  $M_j$  can be approximated by the product of the cross-sectional-area ratio  $S$  and  $M_1$ . This is measure of the importance of compressibility in the source region: when  $M_j^2 \ll 1$  and  $He \ll 1$  the source region can be considered incompressible and compact.

In this chapter we focus on high-Reynolds-number flows, which means that the effect of viscosity is restricted to thin layers such as boundary layers and shear layers. In that case an inviscid flow description can be used. However, one important viscous effect is taken into account: flow separation at the edge of the diaphragm. Only separation at sharp edges

(meaning fixed separation points even in an unsteady flow) is considered. Furthermore, only a compact source region is considered, so  $He \ll 1$ . The first limit that is treated is  $Sr \ll 1$  such that also  $M_1 \ll 1$ . In that case the quasi-steady incompressible-flow model of subsection 5.2.2 can be used. In case of the limit of  $Sr \ll 1$  such that  $M_1$  is finite, compressibility in the source region is essential, and the quasi-steady compressible-flow model of subsection 5.2.3 is useful. The third limit that is treated is  $Sr$  finite such that  $M_1 \ll 1$ , so that the unsteady incompressible-flow model presented in the second part of this chapter is relevant.

### 5.2.2 Incompressible-flow model

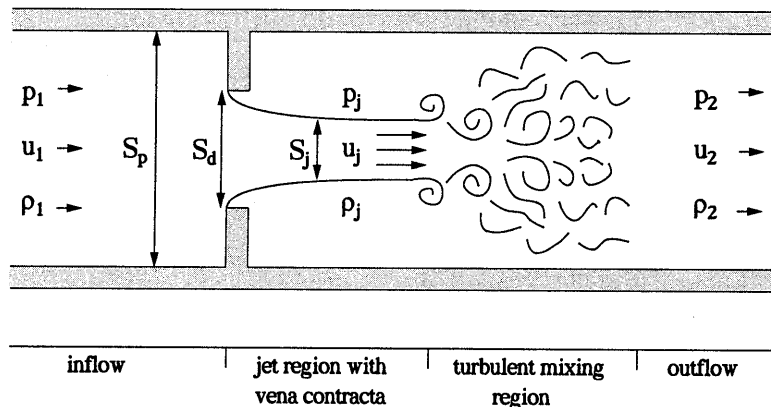


Figure 5.3: Schematic drawing of a steady flow through a diaphragm in a pipe with a mean flow. After a uniform inflow the fluid is accelerated through the diaphragm into the jet. The turbulent jet is followed by the turbulent mixing region which results into the uniform outflow.

An incompressible quasi-steady flow model of the acoustic response of a flow through a diaphragm in a pipe is presented. The effect of the diaphragm on the acoustic flow is reduced to a discontinuity of the acoustic pressure at the position of the diaphragm. If the magnitude of this pressure discontinuity is proportional to the acoustic amplitude, the effect of the diaphragm on the acoustic flow can be described by the scattering matrix: a set of linear equations relating the acoustic pressure downstream of the diaphragm to the acoustic pressure upstream of the diaphragm. Because the assumption of incompressible flow in this model is only valid for low-Mach-number flows with a compact source region. It is important to recall that the jet velocity can be much higher than the velocity in the pipe, but in the present case it has to be much less than the speed of sound.

In figure 5.3 a schematic representation of the flow is shown. A uniform flow is forced through a diaphragm, resulting in the jet flow. Because of the sharp edges of the diaphragm



the jet will exhibit the so-called *vena contracta* effect: the jet will contract further than the aperture of the diaphragm (see section 5.3 for an extensive discussion). Within the jet, the flow is isentropic and irrotational so that Bernoulli's equation can be applied. The velocity outside the jet flow is assumed negligibly small and at the end of the jet the pressure is assumed to be uniform over the cross section. The jet flow becomes turbulent and its structure is destroyed in the turbulent mixing region. This again results in a uniform flow in the pipe downstream of the mixing region. The description of the flow until the jet flow is identical to the description by Bechert (1980) of the flow through a diaphragm as a pipe termination. However, the boundary condition of zero pressure recovery in the turbulent mixing region in free space that is used by Bechert is not valid anymore and is replaced by a model that relates the quantities across the turbulent mixing region. In the turbulent mixing region a pressure recovery takes place. Turbulent dissipation is essential in this region and the flow is assumed to be adiabatic but no longer isentropic. Integral formulations of the steady continuity and momentum equations are applied to this region to describe this behaviour:

$$S_p u_1 = S_j u_j, \quad (5.1)$$

$$S_j u_j = S_p u_2, \quad (5.2)$$

$$p_1 + \frac{1}{2} \rho_0 u_1^2 = p_j + \frac{1}{2} \rho_0 u_j^2, \quad (5.3)$$

$$S_p p_j + S_j \rho_0 u_j^2 = S_p p_2 + S_p \rho_0 u_2^2, \quad (5.4)$$

where in the mixing region friction at the walls is neglected. In these equations the density  $\rho_0$  is constant. It is straightforward to rewrite the equations to a form relating the pressure  $p_1$  at the inflow to the pressure  $p_2$  at the outflow. This results in an equation similar to Bechert's equation for a pipe termination:

$$p_1 - p_2 = \frac{1}{2} \rho_0 u_1^2 \left( \frac{S_p}{S_j} - 1 \right)^2. \quad (5.5)$$

Compared to Bechert's result for a pipe termination the pressure loss ( $p_2 - p_j$ ) is reduced, which is due to the pressure recovery in the turbulent mixing region:

$$p_2 - p_j = \rho_0 u_1^2 \left( \frac{S_p}{S_j} - 1 \right). \quad (5.6)$$

In order to determine the acoustic effect of the diaphragm, small perturbations are introduced:  $p = p_i + p'_i$ ,  $u = u_i + u'_i$  and the equations are linearised. Here  $p_i$  and  $u_i$  are the steady-flow quantities obtained by solving equations (5.1) to (5.4) for the steady flow and  $p'_i$  and  $u'_i$  are the corresponding acoustic perturbations. The acoustic pressure perturbations can be split into downstream travelling waves  $p^+$  and upstream travelling waves  $p^-$ , so that  $p' = p^+ + p^-$ . Then the acoustic velocity perturbations in the pipe are related to the acoustic pressure perturbations by:  $u' = \frac{p^+}{\rho_0 c_0} - \frac{p^-}{\rho_0 c_0}$  with  $c_0$  the speed of sound.

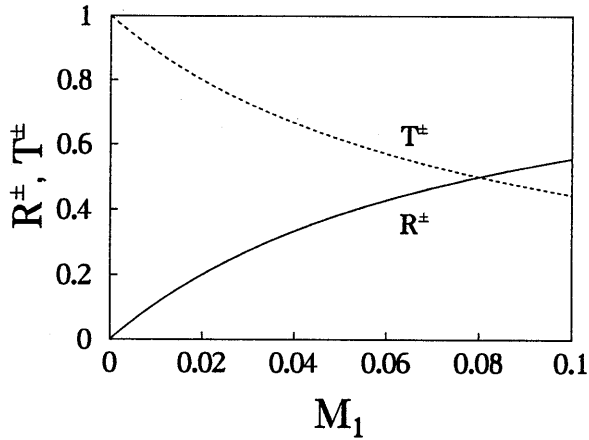


Figure 5.4: Scattering-matrix elements  $R^\pm$  and  $T^\pm$  as defined by equation (5.9) as a function of Mach number  $M_1$ . The value of  $\beta = ((S_p/S_j) - 1)^2$  is 25, so for  $M_1 = 0.1$  compressibility is already important since  $M_j = \frac{u_j}{c_0} = 0.6$ .

The acoustic perturbations satisfy the linearised version of equation (5.5) and of the mass conservation equations (5.1) and (5.2):

$$\begin{aligned} p_1^+ - p_1^- &= p_2^+ - p_2^-, \\ p_1^+ + p_1^- - (p_2^+ + p_2^-) &= M_1 \left( \frac{S_p}{S_j} - 1 \right)^2 (p_1^+ - p_1^-), \end{aligned} \quad (5.7)$$

where  $M_1 = \frac{u_1}{c_0}$  is Mach number of the steady flow in the pipe. These equations can be rewritten in the following form introducing the scattering matrix (Åbom 1991):

$$\begin{pmatrix} p_2^+ \\ p_1^- \end{pmatrix} = \begin{pmatrix} T^+ & R^- \\ R^+ & T^- \end{pmatrix} \begin{pmatrix} p_1^+ \\ p_2^- \end{pmatrix}. \quad (5.8)$$

This notation is very useful because it relates the outgoing waves to the incoming waves by means of reflection and transmission coefficients. In a linear system the outgoing wave  $p_1^-$  is the result of the reflection  $R^+ p_1^+$  of the incoming wave  $p_1^+$  from the left and the transmission  $T^- p_2^-$  of the incoming wave  $p_2^-$  from the right. A similar relationship holds for the outgoing wave  $p_2^+$ . Rewriting equations (5.7) in the form of equation (5.8) yields:

$$\begin{pmatrix} p_2^+ \\ p_1^- \end{pmatrix} = \frac{1}{2 + M_1 \beta} \begin{pmatrix} 2 & M_1 \beta \\ M_1 \beta & 2 \end{pmatrix} \begin{pmatrix} p_1^+ \\ p_2^- \end{pmatrix}, \quad (5.9)$$

where  $\beta = \left( \frac{S_p}{S_j} - 1 \right)^2$  represents the influence of the geometry and the *vena contracta* effect. The matrix is symmetric and the elements satisfy the relationship  $R^+ + T^+ = R^- + T^- = 1$ . This property is a result of the incompressibility of the flow model.

In figure 5.4 the elements of the scattering matrix are presented as a function of the Mach number  $M_1$  in the pipe. The value of  $\beta$  used in this figure is 25 which means that  $\frac{S_p}{S_j} = 6$ . This implies quite a strong constriction in the pipe and already at a Mach number of 0.05 in the main pipe (so a Mach number of 0.3 in the jet) compressibility is becoming significant. When the Mach number is reduced to zero, while keeping  $Sr$  fixed at a small value such that  $Sr \ll 1$ , the influence of the diaphragm in the quasi-steady model disappears, hence  $R^\pm = 0$  and  $T^\pm = 1$ .

Equation (5.9) is valid when convection effects are neglected in the region of acoustic wave propagation. When these effects cannot be neglected, but the source region can still be considered incompressible, then the pressure perturbations should be replaced by total enthalpy perturbations<sup>1</sup>:  $p_i^\pm \rightarrow p_i^\pm(1 \pm M_i)$ . In the next section the compressible-flow model is discussed and it is shown that in that case the total-enthalpy perturbations are a natural choice of variables.

### 5.2.3 Compressible-flow model

When increasing the Mach number of the flow the compressibility has an important effect on the acoustic response of a diaphragm in a pipe. For example, at certain conditions the Mach number in the jet region reaches unity and this restricts the mass flow and cuts off the exchange of acoustic information across the diaphragm from the downstream to the upstream side. In the present study we consider subsonic flows where the jet Mach number is at most equal to unity. Similar to the previous section we can derive a quasi-steady compressible-flow model to describe the acoustic response of a diaphragm in a pipe. A compressible quasi-steady flow model has the same restrictions as the incompressible-flow model, i.e. the source region must be compact (small Helmholtz number) and the Strouhal number low. Our model is based on the compressible low-frequency flow model for the acoustic response of a step-wise expansion in a pipe as presented by Ronneberger (1967). Ronneberger introduced the concept of entropy waves. These are entropy changes that are convected with the main flow velocity. In our model a new scattering matrix in terms of the total enthalpy is introduced that also relates the incoming entropy wave  $\sigma_1$  to the outgoing entropy wave  $\sigma_2$ :

$$\begin{pmatrix} (1 + M_2)p_2^+ \\ (1 - M_1)p_1^- \\ \sigma_2 \end{pmatrix} = \begin{pmatrix} S_{11} & S_{12} & S_{13} \\ S_{21} & S_{22} & S_{23} \\ S_{31} & S_{32} & S_{33} \end{pmatrix} \begin{pmatrix} (1 + M_1)p_1^+ \\ (1 - M_2)p_2^- \\ \sigma_1 \end{pmatrix}. \quad (5.10)$$

In case the incoming entropy wave ( $\sigma_1 = 0$ ) is not present the scattering matrix can be reduced to a form similar to equation (5.8) but now for the total-enthalpy waves:

$$\begin{pmatrix} (1 + M_2)p_2^+ \\ (1 - M_1)p_1^- \end{pmatrix} = \begin{pmatrix} T^+ & R^- \\ R^+ & T^- \end{pmatrix} \begin{pmatrix} (1 + M_1)p_1^+ \\ (1 - M_2)p_2^- \end{pmatrix}. \quad (5.11)$$

<sup>1</sup>Total-enthalpy fluctuations are defined as:  $B_i^\pm = \frac{p_i^\pm}{\rho_i}(1 \pm M_i)$ , neglecting entropy fluctuations

In figure 5.3 a schematic representation of the flow is shown. Because now the density is another variable in the model we need six equations to describe the low-frequency acoustic response of a diaphragm. The four equations of the steady incompressible-flow model are modified and completed by the isentropic gas relation applied to the inflow region up to the jet, and the integral formulation of the energy equation that states that energy is conserved in the flow, because we neglect heat transfer at the walls. Furthermore, we neglect friction at the walls.

$$S_p \rho_1 u_1 = S_j \rho_j u_j, \quad (5.12)$$

$$S_j \rho_j u_j = S_p \rho_2 u_2, \quad (5.13)$$

$$\frac{1}{2} u_1^2 + \frac{\gamma}{\gamma-1} \frac{p_1}{\rho_1} = \frac{1}{2} u_j^2 + \frac{\gamma}{\gamma-1} \frac{p_j}{\rho_j}, \quad (5.14)$$

$$S_p p_j + S_j \rho_j u_j^2 = S_p p_2 + S_p \rho_2 u_2^2, \quad (5.15)$$

$$\frac{p_1}{p_j} = \left( \frac{\rho_1}{\rho_j} \right)^\gamma, \quad (5.16)$$

$$\frac{1}{2} u_1^2 + \frac{\gamma}{\gamma-1} \frac{p_1}{\rho_1} = \frac{1}{2} u_2^2 + \frac{\gamma}{\gamma-1} \frac{p_2}{\rho_2}, \quad (5.17)$$

where we assumed a calorically perfect gas with constant ratio of specific heats  $\gamma$ . The energy equation in that case is equivalent to the conservation of total enthalpy<sup>2</sup>:  $B_1 = B_2$ .

In order to find the elements of the scattering matrix (5.10) the equations are split into a set of non-linear equations for the steady flow and a set of linearised equations for the acoustic perturbations. The elements  $S_{ij}$  of the linearised equations contain only information of the steady flow. So first the non-linear equations for the steady main flow have to be solved. The procedure is as follows. Equations (5.12, 5.14, 5.16) together with  $c^2 = \gamma p / \rho$  yield an equation that relates  $M_1$  to the density ratio  $\varphi_{1j} = \rho_1 / \rho_j$ :

$$M_1 = \sqrt{\frac{2}{\gamma-1}} \sqrt{\frac{1 - \varphi_{1j}^{1-\gamma}}{\mathcal{S}^2 \varphi_{1j}^2 - 1}}, \quad (5.18)$$

where  $\mathcal{S} = S_p / S_j = S_p / (\Upsilon S_d)$  includes the *vena contracta* effect. Given the Mach number in the pipe  $M_1$  this equation yields the density ratio  $\varphi_{1j}$ . Then the jet Mach number is obtained as:

$$M_j = M_1 \mathcal{S} \varphi_{1j}^{\frac{\gamma+1}{2}}. \quad (5.19)$$

The momentum equation (5.15) applied across the turbulent mixing region results in the following equation:

$$p_j (1 + \gamma \mathcal{S}^{-1} M_j^2) = p_2 (1 + \gamma M_2^2).$$

Since  $p_2 / p_j = (p_2 / \rho_2) (\rho_2 / \rho_j) (\rho_j / p_j)$ , and from mass conservation we have (5.13)  $\rho_2 / \rho_j = \mathcal{S}^{-1} u_j / u_2 = \mathcal{S}^{-1} (M_j / M_2) (c_j / c_2)$ , this equation can be rewritten as:

$$\frac{c_2}{c_j} = \frac{\mathcal{S} M_2 (1 + \gamma \mathcal{S}^{-1} M_j^2)}{M_j (1 + \gamma M_2^2)}. \quad (5.20)$$

<sup>2</sup>For a calorically perfect gas the total enthalpy is  $B = C_p T + \frac{1}{2} u^2 = \frac{\gamma}{\gamma-1} \frac{p}{\rho} + \frac{1}{2} u^2$ .

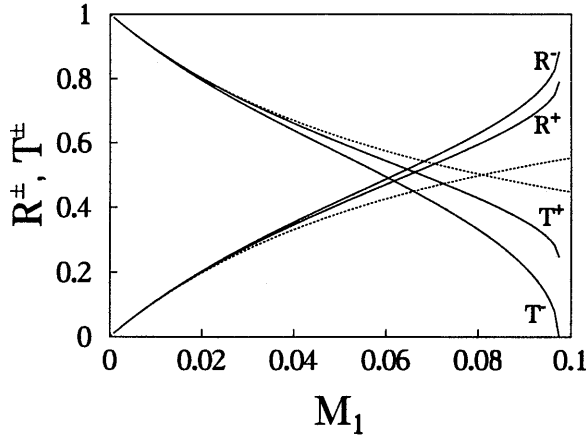


Figure 5.5: Scattering-matrix elements  $R^\pm$  and  $T^\pm$  as defined by equation (5.11) as a function of Mach number  $M_1$  compared to the incompressible flow results for the case where  $S = S_p/S_j = 5.97$ . The incompressible flow results are given by the dashed lines.

Together with the energy equation (5.17) and Bernoulli's equation (5.14):

$$\frac{\gamma - 1}{2} M_j^2 + 1 = \frac{c_2^2}{c_j^2} \left( \frac{\gamma - 1}{2} M_2^2 + 1 \right), \quad (5.21)$$

this results in a quadratic equation for  $M_2^2$ . Now both  $M_2$  and  $\wp_{2j}$  can be obtained as a function of  $M_j$ .

Given  $M_1$  and  $S$  all other parameters  $\wp_{1j}$  (equation (5.18)),  $M_j$  (equation (5.19)),  $M_2$  (equation (5.21)) and  $\wp_{12} = \wp_{1j}/\wp_{2j}$  can be obtained. Since the elements  $S_{ij}$  of the scattering matrix (5.10) can be written as functions of these variables the scattering matrix is hereby known. These elements are functions of these variables, which are too complex to present here. In appendix D the procedure to obtain the value of the elements is described. Also derived in appendix D is the  $2 \times 2$  scattering matrix of equation (5.11) in case of the absence of incoming entropy wave ( $\sigma_1 = 0$ ).

In figure 5.5 the elements of this  $2 \times 2$  matrix (5.11) are compared to the elements of the equivalent matrix in the incompressible case. For low Mach number the incompressible-flow model and the compressible-flow model agree. It can be shown that the matrix elements in the limit of very low Mach number are equal to the elements of the incompressible scattering matrix (5.9). This also indicates that the scattering matrix (even in the incompressible case) should be considered a scattering matrix for total-enthalpy waves. Clearly evident from figure 5.5 is that  $T^+$  diverges from  $T^-$  (as well as  $R^+$  from  $R^-$ ) as the Mach number increases. So the symmetry of the scattering matrix is lost. Another property of the incompressible-flow model is lost:  $T^+$  and  $R^+$  do not add up to one and the same holds for  $T^-$  and  $R^-$ . At a Mach number close to 0.1 the flow in the jet becomes sonic. In that case

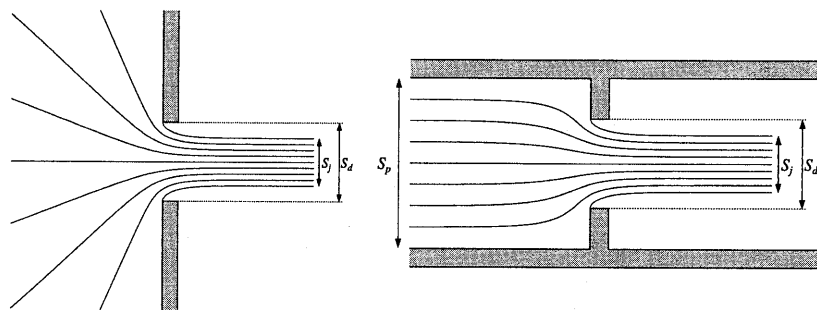


Figure 5.6: Streamlines of the two-dimensional incompressible flow through a diaphragm. Shown on the left is the flow through a hole in a flat plate and on the right the flow through a diaphragm in a pipe.

no information can travel upstream through the diaphragm and therefore  $T^- = 0$ . This restriction does not apply to information that travels downstream through the diaphragm so  $T^+$  is not equal to zero. This already explains the asymmetry between the behaviour of  $T^+$  and that of  $T^-$ . Note that in the previous discussion we implicitly assumed the effect of the *vena contracta* factor  $S_j/S_d$  to be known. As we will see in the next paragraph this implies an additional implicit dependence on the Mach number  $M_j$ .

### 5.3 Vena contracta

An important parameter for the aeroacoustic response of a diaphragm is the ratio of the velocity in the jet and the velocity in the pipe. The jet velocity is determined by the aperture of the diaphragm combined with the so-called *vena contracta* effect. The flow separates at a sharp corner in the direction of the local flow along the wall of the diaphragm. Near the sharp edges of the diaphragm the flow is directed towards the pipe axis. To pass the diaphragm the flow has to bend in the direction of the main pipe. This results in an additional contraction of the flow following the passing of the diaphragm. In figure 5.6 this effect is illustrated. The contraction ratio  $\Upsilon$  is defined as the ratio of the jet height  $h_j$  and the diaphragm height  $h_d$ . For a two-dimensional flow which we consider here this is equal to  $\Upsilon = \frac{S_j}{S_d}$ .

A typical value for the contraction ratio of the flow through a diaphragm was calculated by Kirchhoff for a two-dimensional incompressible flow through a hole in an infinitely extended thin plate (as shown on the left in figure 5.6). He found the value  $\Upsilon_0 = \frac{\pi}{\pi+2} \approx 0.611$  (see Prandtl & Tietjens (1934) for a detailed derivation). There is a number of reasons that the value of the contraction ratio is different from the value found by Kirchhoff. The most important one is the influence of the geometry as determined by the ratio of the area of the

diaphragm opening to the pipe cross-sectional area. Another significant influence is due to the compressibility of the flow. As shown by Blevins (1984) the influence of the Reynolds number becomes important when the Reynolds number is much smaller than  $10^4$ . Based on the expression for cylindrical diaphragms in cylindrical pipes presented by Blevins, the influence of the Reynolds number is expected to be small, however, and is therefore neglected in our experiments. Finally, the sharpness of the edges of the diaphragm is crucial. Blevins presented data that show that rounding the edges by a few percent of height of the opening reduces the *vena contracta* effect considerably. In our experiments considerable attention was given to keeping the rounding of the edges within 1 % of the diaphragm height  $h_d$  and in the further analysis sharp edges are assumed. In this section we focus on the influence of the geometrical parameter  $\frac{S_d}{S_p}$  and the influence of the compressibility, i.e. the Mach number  $M_j$ . We consider  $\Upsilon$  as a function  $\Upsilon(S_d/S_p, M_j)$  of the geometric ratio  $S_d/S_p$  and the jet Mach number  $M_j$ .

By means of a hodograph method Busemann (1937) derived an expression for the contraction ratio  $\Upsilon_0 = \Upsilon(S_d/S_p, 0)$  of a two-dimensional pipe flow through a diaphragm. The hodograph method (Prandtl and Tietjens 1934) consists of constructing a flow solution in the velocity plane which is subsequently transformed to the physical plane by integrating along the streamlines<sup>3</sup>. The geometry that was considered by Busemann is shown on the right in figure 5.6. A diaphragm with an opening of  $S_d$  is placed in a square pipe with a cross-sectional area  $S_p$ . Behind the diaphragm the flow forms a jet with a cross-sectional area  $S_j$ . The contraction ratio  $\Upsilon_0$  derived by Busemann is the solution of the following implicit equation:

$$\Upsilon_0 = \frac{S_j}{S_d} = \frac{\pi}{\pi + 2 \left( \frac{1}{\Upsilon_0} \frac{S_p}{S_d} - \Upsilon_0 \frac{S_d}{S_p} \right) \arctan \left( \Upsilon_0 \frac{S_d}{S_p} \right)}. \quad (5.22)$$

In this equation the asymptotic solution of Kirchoff can be found by taking the limit of  $S_d \ll S_p$ . In figure 5.7 the contraction ratio  $\Upsilon_0$  is shown as a function of the ratio  $\frac{S_d}{S_p}$ . The two limits of the solution are  $\Upsilon_0 = \frac{\pi}{\pi+2}$  for  $\frac{S_d}{S_p} = 0$  and  $\Upsilon_0 = 1$  for  $\frac{S_d}{S_p} = 1$ . It is clear from figure 5.7 that for  $\frac{S_d}{S_p} \leq 0.2$  Kirchoff's results is a very reasonable approximation.

In order to take the compressibility into account Busemann proposed the tangent-gas approximation. The isentropic relation between pressure and density is linearised around the values in the pipe. This is an approach for a slightly compressible flow. Within this approach he finds the following expression for the contraction ratio as function of the jet Mach number for a hole in a thin flat plate of infinite extent:

$$\Upsilon(0, M_j) = \frac{\pi}{\pi + 2 \frac{\rho_j}{\rho_{tot}}}, \quad (5.23)$$

where  $\rho_{tot}$  is the reservoir (total) density. Shapiro (1953) showed that the use of the exact isentropic relation for the density ratio  $\frac{\rho_j}{\rho_{tot}}$  in Busemann's equation (5.23) improved the

<sup>3</sup>In two-dimensional potential-flow theory the complex velocity  $w = u + iv$  is related to the complex stream function  $F$  by:  $\bar{w} = \frac{dF(z)}{dz}$  where  $z = x + iy$ . When it is possible to construct  $F(w)$  the physical coordinates  $z$  can be obtained by integration:  $z = \int \frac{dF}{\bar{w}} + \text{constant}$ .

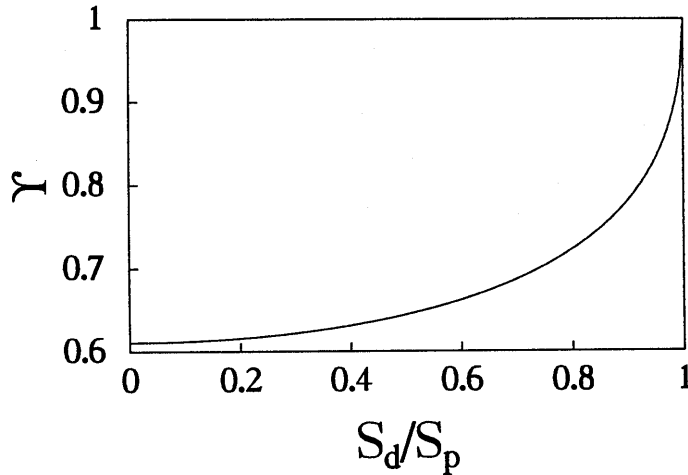


Figure 5.7: Contraction ratio  $\Upsilon(S_d/S_p, 0)$  as a function of the ratio of diaphragm opening and pipe height (Busemann 1937).

agreement between the predicted contraction ratio and experimental measurements of this ratio. This leads to the following expression for  $\Upsilon(0, M_j)$  as a function of the jet Mach number  $M_j$ :

$$\Upsilon(0, M_j) = \frac{\pi}{\pi + 2 \left(1 + \frac{\gamma-1}{2} M_j^2\right)^{\frac{1}{1-\gamma}}}. \quad (5.24)$$

The form of the equation remains only accurate in the tangent-gas approximation. Chaplygin derived an exact solution for a two-dimensional compressible flow through a hole in a plate by means of the hodograph method (Sears 1954). This solution is shown in figure 5.8 together with the result of equation (5.24). At low Mach numbers the results agree very well, at high Mach numbers the two results diverge.

With Busemann's solution  $\Upsilon(S_d/S_p, 0)$  for  $M_j = 0$ , Chaplygin's solution  $\Upsilon(0, M_j)$  for  $S_d/S_p = 0$ , and the obvious result  $\Upsilon(1, M_j) = 1$  for  $S_d/S_p = 1$ , the contraction ratio  $\Upsilon$  is known along three boundaries of the  $(M_j, S_d/S_p)$ -plane. In order to find the general result for  $\Upsilon(S_d/S_p, M_j)$  some interpolation is necessary. In appendix E we show for the so-called Borda mouthpiece that the correction for compressibility is not expected to be sensitive to the factor  $S_d/S_p$ . If we apply a similar reasoning to the diaphragm problem a reasonable interpolation would be:

$$\Upsilon\left(\frac{S_d}{S_p}, M_j\right) = \Upsilon\left(\frac{S_d}{S_p}, 0\right) + \Upsilon(0, M_j) - \Upsilon(0, 0), \quad (5.25)$$

with

$$\Upsilon(0, 0) = \frac{\pi}{\pi + 2},$$



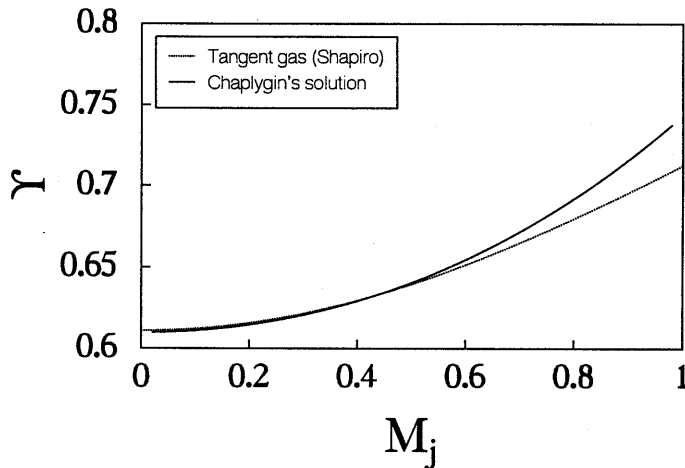


Figure 5.8: Contraction ratio  $\Upsilon(0, M_j)$  as a function of Mach number  $M_j$  in the jet for a hole in a flat plate. Solution obtained by Chaplygin (Sears 1954). Also shown is the modified tangent-gas solution proposed by Shapiro (1953).

while  $\Upsilon(S_d/S_p, 0)$  and  $\Upsilon(0, M_j)$  are given by equation (5.22) and a fit of Chaplygin's result shown in figure 5.8, respectively.

## 5.4 Experimental results for low-frequencies

### 5.4.1 Experimental set-up and procedure

In order to verify the accuracy of the models introduced in the previous sections, low-frequency experiments have been performed on the acoustic behaviour of a diaphragm in a pipe. In figure 5.9 a schematic drawing of the set-up is presented. Dry air at high pressure enters the system at (A). The flow is controlled by the reduction valve and the flow rate is measured at (C). The mean static pressure (accuracy 0.1 %) and temperature (accuracy 0.1 %) are measured in order to characterise the conditions of the experiments. From these data the speed of sound  $c_1$  is determined which together with the flow rate provides the Mach number  $M_1$  of the flow (accuracy 2 %). After passing the settling chamber the flow is led through the sound source: a siren. Here amplitude and frequency of the acoustic perturbations can be adjusted. Via a flexible connection tube and a box of sand for the damping of mechanical vibrations the flow finally enters the test section. This is a 6 m long cylindrical steel pipe with an internal radius of 15.013 mm and a wall thickness of 5 mm. The roughness of the internal walls of the pipe is of the order of 0.1  $\mu\text{m}$ . The diaphragm is positioned at some position in the pipe. At both sides of the diaphragm

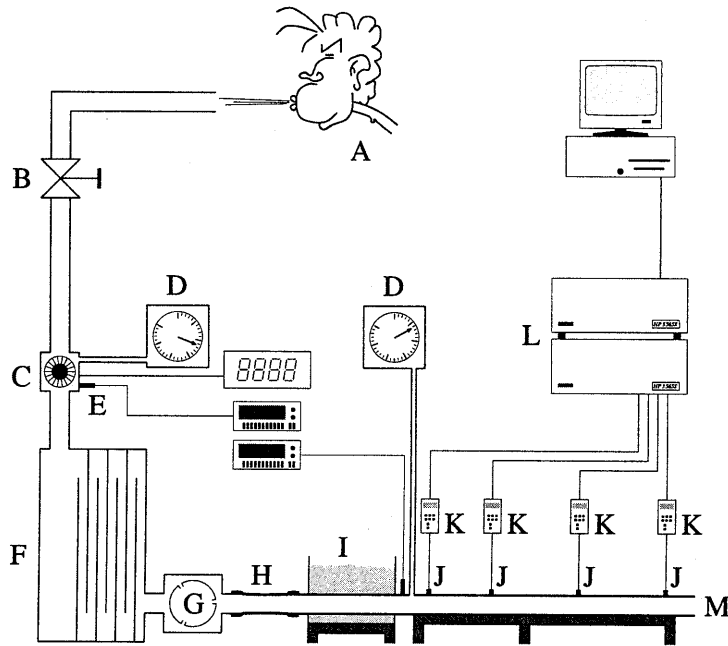


Figure 5.9: Experimental set-up: (A) high pressure supply, (B) pressure reduction valve, (C) flow meter, (D) manometer, (E) thermometer, (F) settling chamber, (G) siren, (H) flexible connection, (I) sand box, (J) piezo-electric pressure transducers, (K) charge amplifiers, (L) data analyser, (M) pipe termination. Courtesy of R. Boot (1995).

piezo-electric pressure transducers (PCB 116A) are present in the pipe wall. The signals of the transducers are led to a set of charge amplifiers (Kistler 5011) which are connected to the data analyser (HP-35650).

The reflection and transmission coefficients are measured by using the so-called two-microphone method described by Åbom and Bodén (1986, 1988). Several pairs of microphones are used to measure the acoustic response of the diaphragm. The microphone positions are chosen for an optimal measurement. Using the data analyser the complex transfer function  $H_{ij}(\omega)$  is measured. This function is the ratio of the complex acoustic pressure amplitudes at positions  $x_i$  and  $x_j$ :

$$H_{ij}(\omega) = \frac{p'(x_i, \omega)}{p'(x_j, \omega)}. \quad (5.26)$$

The reflection and transmission coefficients can then be expressed in terms of transfer functions. The wave number is corrected for convection (Doppler) effects and for visco-

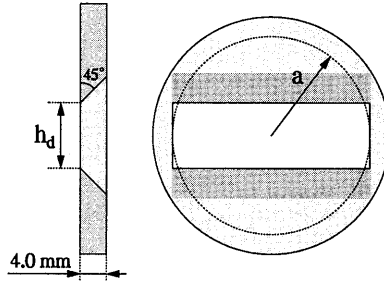


Figure 5.10: Three different slit-like diaphragms that have been used in the experiments: diaphragm I has  $h_d = 10.7$  mm and  $S_d/S_p = 0.45$ ; diaphragm II has  $h_d = 6.4$  mm and  $S_d/S_p = 0.27$ ; diaphragm III has  $h_d = 2.6$  mm and  $S_d/S_p = 0.11$ .

thermal dissipation using Kirchhoff's damping coefficient  $\alpha_0$  (Tijdeman 1975, Pierce 1989):

$$k^\pm = \frac{(k_0 + 1 - i)\alpha_0}{1 \pm M}, \quad (5.27)$$

$$\alpha_0 = \frac{\sqrt{2\omega\nu}}{2ac_0} \left( 1 + \frac{\gamma - 1}{\sqrt{Pr}} \right), \quad (5.28)$$

where  $\nu$  is the kinematic viscosity of air,  $a$  the radius of the pipe, and  $Pr$  is the Prandtl number of air. Peters (1993) presents theoretical and experimental results for the correction of  $\alpha_0$  due to the interaction of the acoustic waves with the turbulent main flow. This correction is used to account for the effects of visco-thermal dissipation on the wave propagation (see appendix F).

The diaphragms being studied are slit-shaped diaphragms in a cylindrical pipe. Although this is a three-dimensional configuration, the response of the configuration is expected to be governed by the two-dimensionality of the slit-shaped diaphragm. This makes a comparison to two-dimensional numerical simulations reasonable. Three diaphragms with different apertures have been used. The aperture can cover 45%, 27% or 11% of the surface area. In figure 5.10 the diaphragm is shown. The edge of the diaphragm is kept sharp

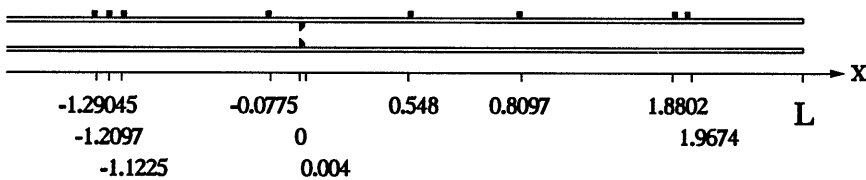


Figure 5.11: Microphone configuration used for the low-frequency measurements at 77 Hz. Positions of the microphones ■ given in metres.

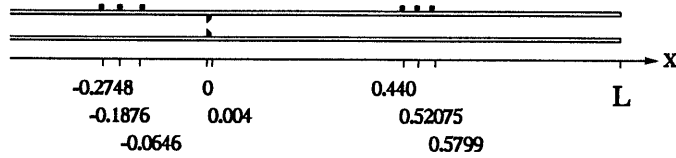


Figure 5.12: Microphone configuration used for the measurements at 793 Hz. Positions of the microphones ■ given in metres.

(radius of curvature less than  $10^{-5}$  m) and at the downstream side the bevel angle is  $45^\circ$ . This ensures a predictable *vena contracta* effect.

Downstream of the diaphragm the pipe has a length  $L$ . The air exits the set-up at the end of the pipe into the surroundings of the laboratory. At both sides of the diaphragm three or four pressure transducers are located. The position of the diaphragm is chosen as the reference point for the coordinate system. In figure 5.11 the microphone positions that are used for the low-frequency experiments (77 Hz) are shown. In order to show the deviations from the quasi-steady model for higher frequencies also experiments have been performed at a higher frequency (793 Hz). In figure 5.12 the microphone positions for these experiments are shown.

## 5.4.2 Results

The results of the theoretical model are compared to experimental measurements of the reflection and transmission of acoustic waves by a diaphragm in a pipe. Because the measurement of the elements of the scattering matrix requires a special experimental technique that had not yet been carried out within our laboratory, the experiments consisted of measuring the following complex quantities:

$$R_1 = \frac{p_1^-}{p_1^+}, \quad T_{21} = \frac{p_2^+}{p_1^+}, \quad R_2 = \frac{p_2^-}{p_2^+}.$$

These measurements do not measure the response of the diaphragm alone but the combined response of the diaphragm and pipe termination (open pipe end). However, all the information of the open pipe end is contained in the reflection coefficient  $R_2$  and a lot of theoretical and experimental work has already been done on open pipe ends. In (Peters 1993) an elaborate discussion on the open pipe end was presented. The experimental data of Peters present us with the possibility to use an experimental fit. These data have been obtained in the range  $0.01 < M < 0.2$  and  $0.01 < Sr < 1$ , which is close to the range of the present experiments. The magnitude of the reflection coefficient of the open pipe end is then described, as proposed by Cargill (1982), by:

$$|R| = (1 + AM) \left( 1 - \frac{(ka)^2}{2} \right),$$

where  $\mathcal{A}$  is approximated by:

$$\mathcal{A}(x) = \begin{cases} \frac{x^2}{3} & 0 \leq x < 1 \\ \frac{2x-1}{3} & 1 \leq x < 1.85 \\ 0.9 & 1.85 \leq x \end{cases}$$

with

$$x = \frac{ka}{M} = \frac{2\pi fa}{u_0} = 2\pi Sr.$$

The phase of the reflection coefficient is presented in terms of an end correction  $\delta_{end}$  which is approximated by:

$$\frac{\delta_{end}}{a} = \begin{cases} 0.2 + 0.4x^2 & 0 \leq x < 1 \\ 0.6 & 1 \leq x. \end{cases}$$

The contraction ratio used in the compressible-flow model of section 5.2.3 is estimated by:

$$\Upsilon = \frac{\Upsilon_0}{\frac{\pi}{\pi+2}} \left( \frac{\pi}{\pi+2} + 0.13M_j^2 \right),$$

where  $\Upsilon_0$  is taken from figure 5.7 at the average value of  $h_d/h_p$  across the width of the diaphragm. The term between brackets is the correction for the compressibility of the flow and it is an accurate fit to the result of Chaplygin (shown in figure 5.8).

In figure 5.13 the prediction obtained from the compressible-flow model is compared to experimentally obtained values of  $R_1$ ,  $T_{21}$ , and  $R_2$  at a frequency of 77 Hz for the diaphragm with the largest aperture (diaphragm I, 45%). On the left the magnitude of the coefficients is shown and on the right the phase of the coefficients is shown. The experimental results are the markers and the lines are the theoretical predictions from the compressible-flow model. As can be expected, the results for  $R_2$  (which are experimental data for the open pipe end) coincide with our fit of the results of Peters (1993). Also the values for  $R_1$  and  $T_{21}$  are in excellent agreement with our quasi-steady model. A similar agreement is evident in figure 5.14. The frequency is again 77 Hz and the diaphragm used in this case has the smallest aperture (diaphragm III, 11%). In both cases the quasi-steady approximation gives very accurate predictions of the acoustic response of the diaphragm. In the next part of this chapter it is shown that the important parameter for the unsteadiness caused by the flow through the diaphragm is the Strouhal number based on the aperture height and velocity:  $Sr = \frac{fh_d}{u_d}$  with  $u_d = \frac{S_d}{S_d} u_1$ . In both experiments series the highest value of the Strouhal number encountered is less than 0.05, which confirms the assumption of quasi-steadiness. When the frequency is raised to 793 Hz the results for diaphragm III are still in reasonable agreement with the experiment (see figure 5.15). The difference between results of theory and experiment is somewhat larger than in the low-frequency case, but this might be due to inaccuracies in the fit for  $R_2$ . These inaccuracies affect the values of  $R_1$  and  $T_{21}$  as well. When diaphragm III is replaced by diaphragm I the inaccuracies in  $R_2$  are no longer the only source of inaccuracies. In figure 5.16 the difference between results

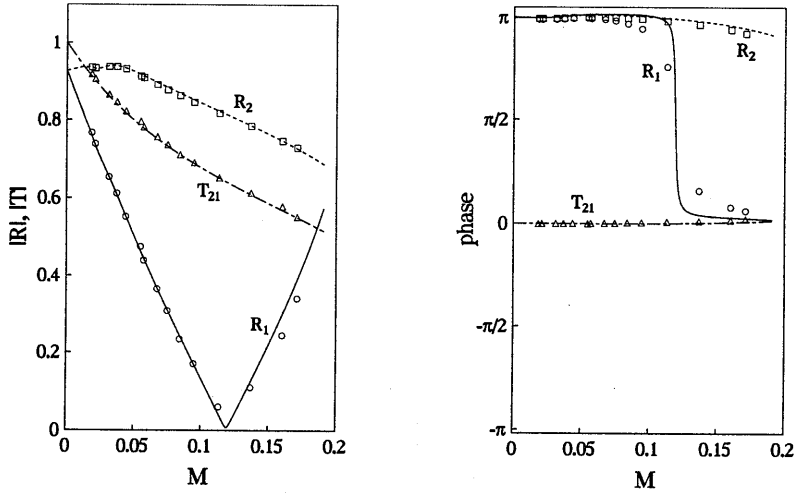


Figure 5.13: Comparison of experimentally measured reflection and transmission coefficients and theoretical predictions based on the compressible-flow model including the vena contracta effect. Diaphragm I,  $f = 77$  Hz,  $L = 2.1959$  m.

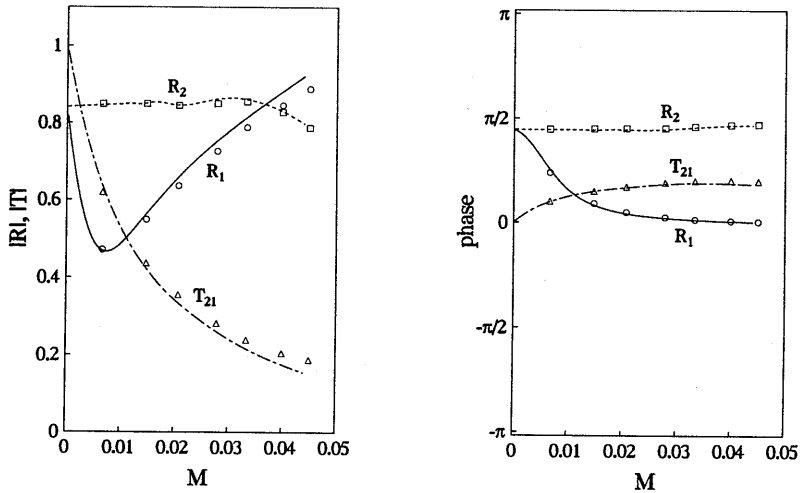


Figure 5.14: As figure 5.13, now with diaphragm III,  $f = 77$  Hz,  $L = 5.0069$  m.

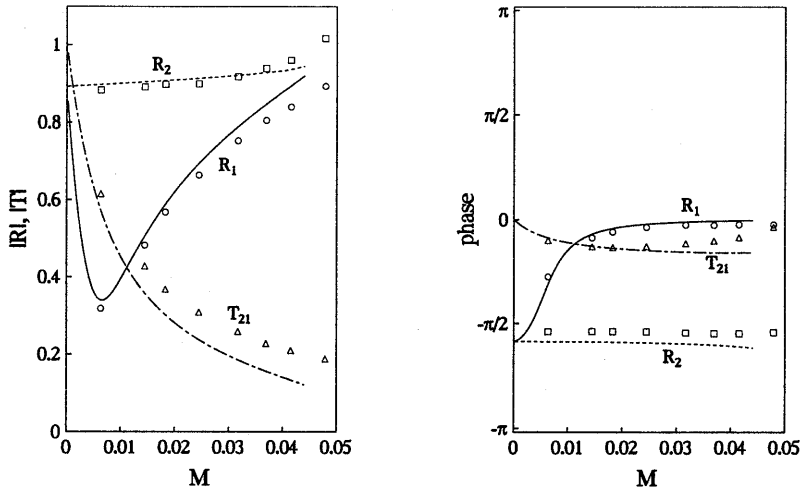


Figure 5.15: As figure 5.13, now with diaphragm III,  $f = 793$  Hz,  $L = 0.8089$  m.

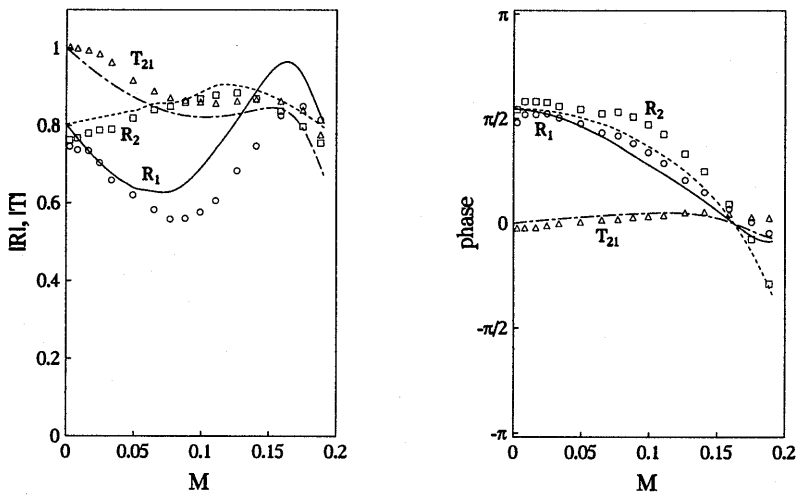


Figure 5.16: As figure 5.13, now with diaphragm I,  $f = 793$  Hz,  $L = 1.7651$  m.

of theory and experiments can be seen to be significant as opposed to differences in the other three cases. In fact at a Mach number of 0.01 the Strouhal number is close to unity which implies that the flow through the diaphragm is essentially unsteady. In the next section results of a two-dimensional incompressible-flow model (the vortex-blob method) will be compared to results of unsteady-flow experiments.

## 5.5 Application of vortex-blob method



Figure 5.17: The two diaphragms that were studied numerically. On the left is the thin diaphragm, which is an approximation of a line diaphragm, and on the right is a two-dimensional representation of the actual diaphragm used in experiments.

To study the unsteady behaviour of the flow through a diaphragm in a pipe we use the vortex-blob method. This two-dimensional flow method assumes the flow to be incompressible and inviscid. That the method is for incompressible flow means that it can only be used to study a source region that can be considered compact and has negligible compressibility effects. That the method is inviscid implies that viscous effects have to be small and occur in to limited areas (high-Reynolds-number flows). However, one important viscous effect is taken into account, namely the flow separation at the edge of the diaphragm. Flow separation is taken into account by means of a Kutta-like condition. At the point at which the Kutta condition is applied (a sharp corner) vorticity is generated. The vorticity is represented by point vortices. These point vortices are convected with the local flow velocity and represent the developing shear layer. In order to have a stable numerical method a desingularisation parameter  $\delta$  is introduced in the expression for the velocity induced by a discrete vortex. Uniform flow conditions are imposed on the in- and outflow boundary. The inflow and outflow velocities consist of a steady flow component and an oscillatory flow that is superimposed:

$$u_1(t^*) = u_2(t^*) = u_1 (1 + u'_1 \sin(2\pi Sr t^*)),$$

where  $t^*$  is the time non-dimensionalised with the reference length  $h_d$  and the reference velocity  $u_d$ . The numerical simulation is started from a steady potential-flow solution.

The diaphragm that has been used in the experiments (diaphragm II shown in figure 5.10) is approximated by one of the two-dimensional forms shown in figure 5.17. The numerical simulations were performed for two different thicknesses of the diaphragm. First a



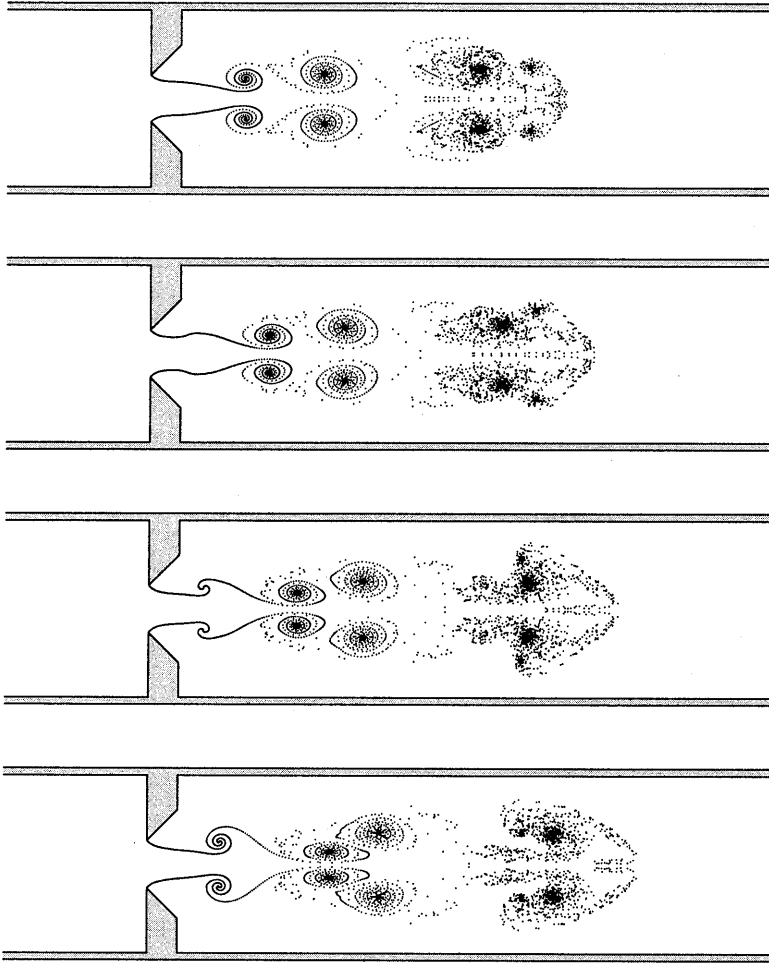


Figure 5.18: Development of the jet flow through the diaphragm. From top to bottom the time is increasing by  $T/4$  between each figure. The markers give the positions of the point vortices. This is a result of the vortex-blob calculations for  $Sr = 0.4$  and  $u_{ac} = 0.1$ .

thin diaphragm was used that is a representation in the vortex-blob method of a diaphragm of infinitesimal thickness. It has a thickness much smaller than the height  $h_d$  of the aperture of the diaphragm: its thickness is  $0.05h_d$ . The second diaphragm has a thickness that is of the same order as the height  $h_d$ . This is the diaphragm that actually is used in the experiments. It has a thickness equal to  $0.63h_d$ . The ratio of pipe cross-sectional area and

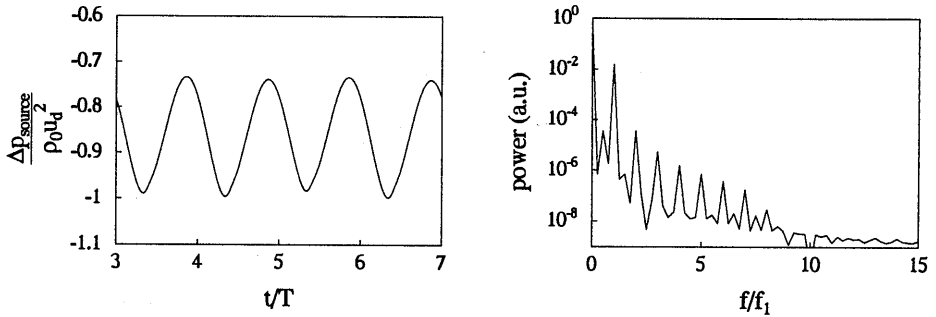


Figure 5.19: Acoustic source pressure (vortex pressure) as a function of time and the associated power spectrum. The simulation was started at  $t = 0$ .  $Sr = 0.4$ ,  $u_{ac} = 0.1$ .

the aperture of the diaphragm is 0.27 and  $h_d = 6.4$  mm in both cases.

In figure 5.18 a typical result of the vortex-blob method is shown. Top to bottom time increases with  $T/4$  between each figure. The simulation exhibits features that are well known for (two-dimensional) jet flows: the *vena contracta* effect and the pairing of vortices. Although the jet flow is still developing and the flow does not look periodic, the resulting acoustic source pressure and therefore also the acoustic source power soon becomes periodic. The acoustic source pressure (vortex pressure) is shown as a function of time on the left in figure 5.19. On the right the associated power spectrum is shown. The fundamental (forcing) frequency  $f_1$  is dominant by three orders of magnitude, but also several higher modes are present. The vortex pairing visible in figure 5.18 produces a period doubling of the fundamental period of forcing. This mode at  $\frac{1}{2}f_1$  is also weakly present in the signal, as can be seen in the power spectrum. Further numerical simulations indicate that for  $Sr \geq 0.5$  the period doubling has a significant influence on the signal.

## 5.6 Acoustic source power

In an unsteady vortical flow the interaction of the acoustic field with the vorticity field can lead to production or dissipation of acoustic energy. Howe (1980, 1984) proposed an energy formulation for the acoustic power generated by a turbulent flow. The amount of acoustic energy that is generated or dissipated in the numerical simulations is obtained by two methods. The first method is a direct implementation of Howe's energy formulation for the time-averaged acoustic source power as used by Kriesels *et al.* (1995):

$$\langle \mathcal{P} \rangle = -\rho_0 \int_V \langle (\vec{\omega} \times \vec{u}) \cdot \vec{u}' \rangle dV, \quad (5.29)$$

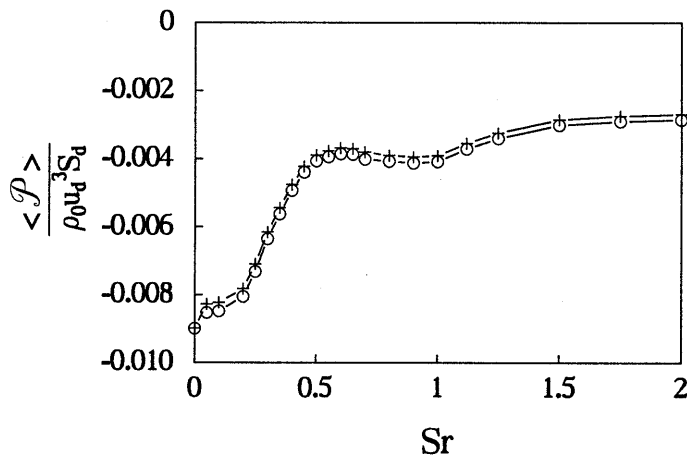


Figure 5.20: Time-averaged acoustic source power as a function of Strouhal number for a slit-like diaphragm in a pipe. The slit area is 27 % of the pipe area and  $u_1'/u_1 = 0.1$ . Results obtained by Howe's formulation are marked by + and results obtained by the pressure formulation are marked by O.

where  $\vec{\omega} = \vec{\nabla} \times \vec{u}$  is the vorticity,  $\vec{u}$  is the convection (total) velocity of the vorticity, and  $\vec{u}'$  is the acoustic velocity defined as the irrotational time-dependent part of the velocity.  $V$  is a volume enclosing the vorticity present in the flow field. The second method is the pressure formulation:

$$\langle \mathcal{P} \rangle = \int_S \langle \vec{I} \cdot \vec{n} \rangle dS, \quad (5.30)$$

where  $\vec{I} = B'(\rho\vec{u})'$ , and  $B'$  is the total-enthalpy perturbation.  $S$  is the surface enclosing the whole computational domain. In the limit of incompressible flow this can be approximated by  $\vec{I} = p'\vec{u}'$ . The pressure formulation involves an integral formulation for the total pressure  $P = p + \frac{1}{2}\rho u^2$  to be considered over the boundaries of the computational domain. The contributions to this surface integral are due to the inflow and outflow boundaries. These boundaries are chosen to be far from the region of vorticity, so that the inflow and outflow velocities can be considered uniform. In that case the integral reduces to the time average of the pressure difference due to the presence of vorticity times the acoustic velocity  $u_1'$  at the boundaries:

$$\langle \mathcal{P} \rangle = S_p \langle \Delta p_{source} u_1' \rangle, \quad (5.31)$$

where  $\Delta p_{source}$  is defined as the difference between the actual pressure  $p$  in the flow containing vorticity and the potential-flow contribution  $p_{pot}$  to the actual pressure:

$$\Delta p_{source} = \Delta p(t) - \Delta p_{pot}(t). \quad (5.32)$$

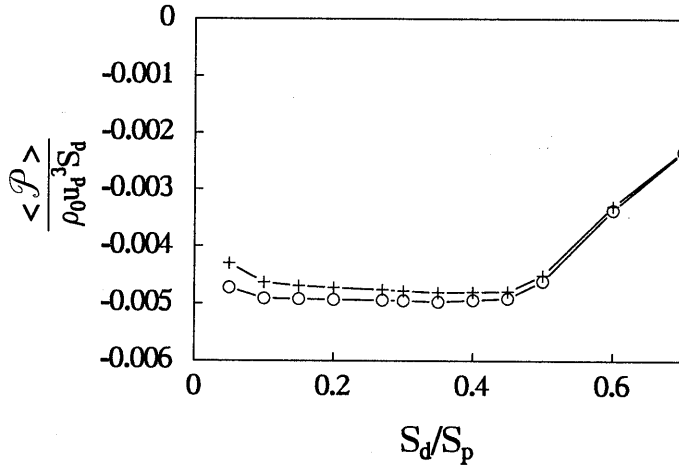


Figure 5.21: Time-averaged acoustic source power as a function of the ratio of the cross-sectional area of the aperture and the cross-sectional area of the pipe. a slit-shaped diaphragm in a pipe:  $Str = 0.4$ ,  $u'_1/u_1 = 0.1$ . Results obtained by Howe's formulation are marked by + and results obtained by the pressure formulation are marked by o.

In figure 5.20 the time-averaged acoustic source power is shown as a function of the Strouhal number ( $Str = \frac{f h_d}{u_d}$ ). The power is non-dimensionalised with the diaphragm velocity  $u_d = S_p/S_d u_1$  and the cross-sectional area of the aperture  $S_d$ . These results have been obtained for the thick ( $0.63h_d$ ) diaphragm. Clearly this diaphragm is only dissipating acoustic energy. In the figure the results of both formulations (5.30) and (5.31) are presented. The two formulations are in fair agreement, which implies an adequate accuracy of the vortex-blob results. At  $Str = 0$  the quasi-steady incompressible-flow model of section 5.2.2 is used. The results of the vortex-blob method show a quasi-steady limit that approaches this result reasonably well. The difference in the calculated power is only 7%. The quasi-steady limit of the numerical simulations differs from the quasi-steady model due to the inability of the vortex-blob method to accurately capture the *vena contracta* effect (within 5%) with the numerical input parameters that have been used. For  $Str$  larger than 0.5 a slight oscillation in the power can be seen (see figure 5.20). A satisfactory explanation has not yet been found for this feature. It will be shown that it has consequences for the agreement between numerical and experimental data presented in section 5.8.

In order to illustrate the influence of the pipe wall on the acoustic behaviour of the diaphragm the time averaged acoustic source power is in figure 5.21 presented as a function of the opening fraction  $S_d/S_p$ . For small values of this ratio the power reaches a constant value. Only when the ratio exceeds 0.45 the power is significantly influenced by the geometry. At very low values ( $< 0.1$ ) the power starts to deviate from the constant value but this is most likely due to inaccuracies in the numerical method for these geometries. This

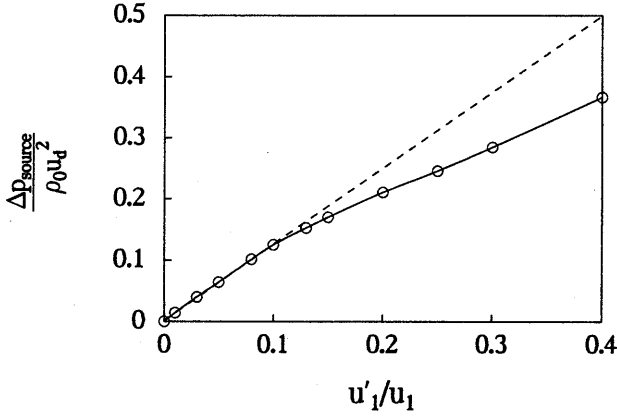


Figure 5.22: Acoustic source pressure as a function of the acoustic amplitude for the thick diaphragm at  $Sr = 0.4$ . Note that for small acoustic amplitudes the source pressure is linearly proportional to the acoustic amplitude.

is also indicated by the diverging results of Howe's energy formulation and the pressure formulation for small values of  $S_d/S_p$ .

## 5.7 Acoustic response

To interpret the numerical results in this section an acoustic description is provided. The first relation is the incompressible form of the equation of mass conservation across the acoustic source region:

$$p_1^+ - p_1^- - (p_2^+ - p_2^-) = 0, \quad (5.33)$$

where region 1 is the region upstream of the diaphragm and region 2 is the region downstream of the diaphragm. The second relation follows from the momentum conservation across the acoustic source region neglecting friction:

$$p_1^+ + p_1^- - (p_2^+ + p_2^-) = \Delta p_{source} + i\rho_0\omega L_{eff}u'_1, \quad (5.34)$$

where  $\Delta p_{source}$  is the acoustic source pressure obtained from numerical simulations and  $i\omega L_{eff}$  is the contribution due to the inertial effects of the potential flow through the diaphragm. This separation of contributions is due to the definition of  $\Delta p_{source}$ , which does not include potential-flow contributions, although of course, also the unsteady potential flow through the diaphragm is a source of acoustic power. In the case of the diaphragm considered here (diaphragm II,  $S_d/S_p = 0.27$ ) the effective length  $L_{eff}$  is  $2.59h_d$  obtained from the potential flow solution of the numerical simulation at  $t = 0$ .

In figure 5.22 the acoustic source pressure is shown as a function of the acoustic amplitude for the thick diaphragm at  $Sr = 0.4$ . For  $u'_1/u_1 < 0.1$  the acoustic source pressure is

linearly proportional to the acoustic velocity  $u'_1$ . If we assume the acoustic source pressure to be proportional to the acoustic velocity  $u'_1$  we obtain the following equation:

$$(p_1^+ + p_1^-) - (p_2^+ + p_2^-) = K u'_1 + i \rho_0 \omega L_{eff} u'_1, \quad (5.35)$$

where  $K$  is a function of  $Sr$  and  $S_d/S_p$ . This can be rewritten as:

$$p_1^+ + p_1^- - (p_2^+ + p_2^-) = (K + i \rho_0 \omega L_{eff}) \frac{p_1^+ - p_1^-}{\rho_0 c_0}. \quad (5.36)$$

We can now write the two equations (5.33) and (5.36) in the form of a scattering matrix defined by (5.8):

$$\begin{pmatrix} p_2^+ \\ p_1^- \end{pmatrix} = \begin{pmatrix} T^+ & R^- \\ R^+ & T^- \end{pmatrix} \begin{pmatrix} p_1^+ \\ p_2^- \end{pmatrix},$$

where

$$T^+ = T^- = \frac{2 \rho_0 c_0}{K + i \rho_0 \omega L_{eff} + 2 \rho_0 c_0} \quad (5.37)$$

and

$$R^+ = R^- = \frac{K + i \rho_0 \omega L_{eff}}{K + i \rho_0 \omega L_{eff} + 2 \rho_0 c_0}. \quad (5.38)$$

These elements have a form similar to that of the elements found for the quasi-steady incompressible-flow model (5.9). Also in the case of an unsteady incompressible description of the source region a symmetric matrix is obtained with elements that satisfy the relations:  $T^+ + R^+ = T^- + R^- = 1$ .

## 5.8 Results for low-Mach-number unsteady flows

The acoustic source pressure  $\Delta p_{source}$  is obtained from numerical simulations using the vortex-blob method. The method yields the acoustic source pressure as a function of two input parameters, i.e. the acoustic amplitude  $u_{ac} = \frac{u'_1}{u_1}$  and the Strouhal number  $Sr$ . Since the method is a method for incompressible flow, compressibility effects are not taken into account. In table 5.1 the numerical results are presented for both diaphragms. Using equations (5.37) and (5.38) we obtain results for the reflection coefficient and transmission coefficient as a function of Strouhal number.

Ajello (1997b) measured the scattering matrix of the diaphragms also used in the present investigation. He used an experimental set-up similar to our set-up described in section 5.4.1. Instead of the siren of our set-up two sets of six loudspeakers positioned upstream and downstream of the diaphragm were used as sources of sound. Both sides of the main pipe (entrance and exit) were manufactured as anechoic as possible and corrections are made for the reflections that do occur.

On both sides of the diaphragm three pressure transducers were mounted. By alternately using the upstream and downstream loudspeaker as a source of sound the four

$Str$	thin		actual	
	$ \Delta p_{source} /\rho U_d^2$	$arg(\Delta p)$	$ \Delta p_{source} /\rho U_d^2$	$arg(\Delta p)$
0.0	0.180	0	0.180	0
0.1	0.169	$-0.032\pi$	0.172	$-0.047\pi$
0.2	0.168	$-0.069\pi$	0.170	$-0.105\pi$
0.3	0.160	$-0.113\pi$	0.149	$-0.177\pi$
0.4	0.145	$-0.140\pi$	0.124	$-0.206\pi$
0.5	0.128	$-0.146\pi$	0.098	$-0.186\pi$
0.6	0.118	$-0.145\pi$	0.086	$-0.147\pi$
0.7	0.110	$-0.141\pi$	0.087	$-0.124\pi$
0.8	0.107	$-0.136\pi$	0.087	$-0.112\pi$
0.9	0.104	$-0.130\pi$	0.087	$-0.106\pi$
1.0	0.100	$-0.138\pi$	0.087	$-0.110\pi$

Table 5.1: Numerical results obtained with the vortex-blob method for the acoustic source pressure and the phase difference relative to the acoustic velocity for the thin diaphragm and the actual experimental geometry. Acoustic amplitude  $u_{ac} = 0.1$ .

elements of the scattering matrix as defined by equation (5.8) were determined. During one experimental run the elements were measured for a range of frequencies (typically 100 frequencies). Since on both sides three microphones were used to measure two acoustic waves ( $p^+$  and  $p^-$ ) a regression technique can be used to determine the elements of the matrix with the temperature as an additional unknown quantity. A complete description of the experimental set-up and procedure used by Ajello can be found in (Ajello 1997a).

The diaphragm used in the experiments presented here is the same as the diaphragm shown in figure 5.10. Diaphragm II with  $S_d/S_p = 0.27$  and  $h_d = 6.4$  mm was used. The experiments were performed at a Mach number  $M_1$  in the main pipe of 0.0092. The frequency range was from 20 Hz to 1620 Hz, with steps of 20 Hz. The value of the Strouhal number corresponding with these measurements ranges from 0.005 to 0.9, and the Helmholtz number ranges from 0.001 to 0.13. With these values of  $M_1$ ,  $Str$ , and  $He$  an incompressible unsteady flow model is expected to be a reasonable approximation. In figures 5.23 to 5.26 a comparison between experimental and numerical results is presented. The solid lines are the experimental results for  $R^+$  and  $R^-$  or  $T^+$  and  $T^-$ . The markers are the results obtained from the vortex-blob method for the two diaphragm of figure 5.17. Since the model used to convert the numerical results for  $\Delta p_{source}$  to reflection and transmission coefficients assumes incompressible flow the scattering matrix is symmetric and only one value is found for  $R^+$  and  $R^-$  as well as for  $T^+$  and  $T^-$ . This is confirmed by the experimental results although the transmission coefficients show a small difference between  $T^+$  and  $T^-$ . This is most clear in figure 5.26 where the phase of the transmission coefficient is shown. Furthermore it is clear that the experimental results show a larger scatter for higher frequencies ( $Str > 0.7$ ) than for lower Strouhal numbers. This is most probably due to the microphone positions that are used since the set-up was designed

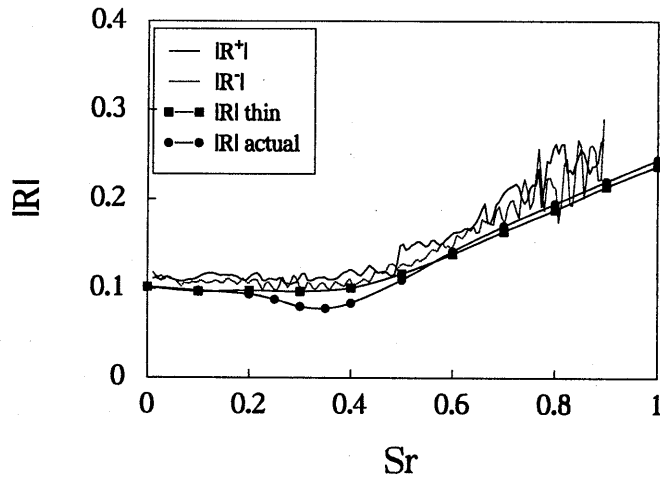


Figure 5.23: Comparison of measured reflection coefficients (Ajello 1997b) and reflection coefficients obtained from the vortex-blob method. Numerical results are obtained for two different diaphragms: one with the actual thickness of 4 mm and one much thinner with a thickness of 0.32 mm.

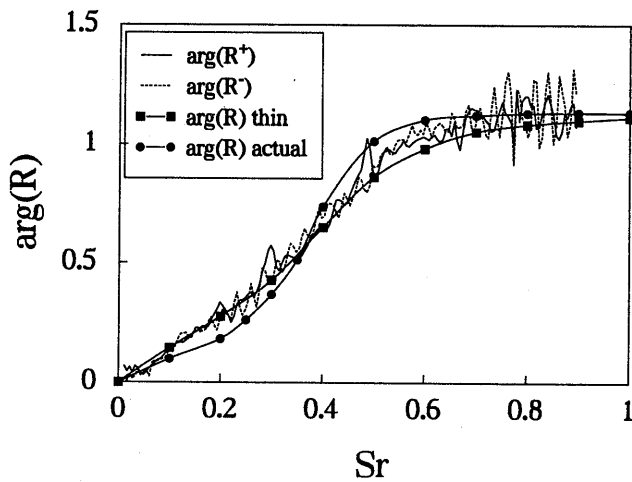


Figure 5.24: Comparison of measured argument of the reflection coefficients (Ajello 1997b) and argument of reflection coefficients obtained from the vortex-blob method as in figure 5.23



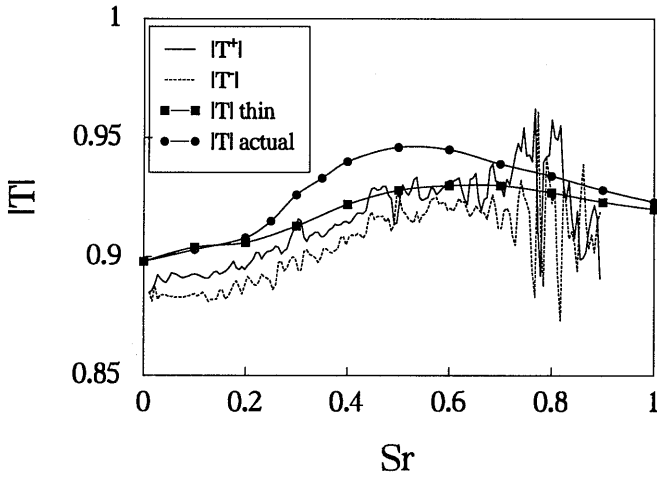


Figure 5.25: Comparison of measured transmission coefficients (Ajello 1997b) and transmission coefficients obtained from the vortex-blob method as in figure 5.23.

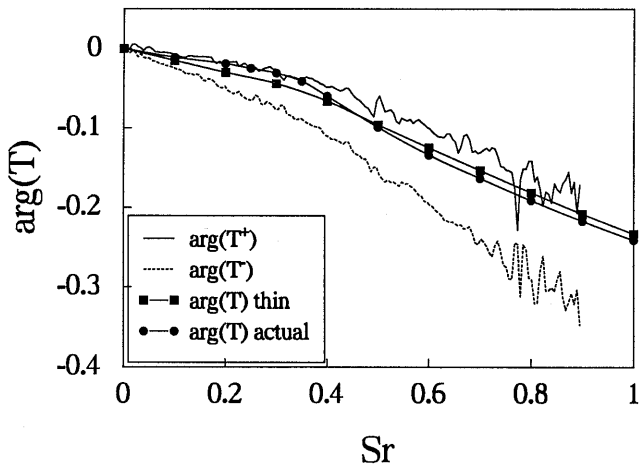


Figure 5.26: Comparison of measured argument of the transmission coefficients (Ajello 1997b) and argument of transmission coefficients obtained from the vortex-blob method as in figure 5.23.

to be used for frequencies up to 800 Hz. It is interesting to observe that the numerical results for the thin diaphragm agree better with the experimental results than the results for the thick diaphragm. Between  $Sr = 0.2$  and  $Sr = 0.6$  a small decrease in  $|R|$  and a small increase in  $|T|$  can be observed. In figure 5.20 we already observed an unexplained feature around  $Sr = 0.5$ . One possible explanation is that the thickness of the diaphragm introduces an additional length scale and a corresponding time scale: the jet velocity is approximately  $u_d/\Upsilon$  and the thickness is  $0.63h_d$  so the value of the Strouhal number based on this velocity and length scale is approximately  $0.38Sr$ . Why this feature is absent in the experimental results is yet unclear but it may be due to the experimental set-up being essentially three-dimensional and the flow being viscous.

## 5.9 Concluding remarks

In this chapter we presented a study of the flow through a slit-shaped diaphragm in a pipe. This study consisted of theoretical modelling, measurements, and numerical simulations. We showed that for small acoustic perturbations the diaphragm can be acoustically characterised by the so-called scattering matrix. This matrix relates the outgoing waves to the incoming waves. In the case of an incompressible flow the matrix is shown to be symmetric. The symmetry of the matrix is destroyed by compressibility effects.

The three models we present in this chapter represent different approximations to the flow through the diaphragm. We focussed on high-Reynolds-number and low-Helmholtz-number flows. Viscous effects can then be neglected in the bulk of the flow, but flow separation at the edges of the diaphragm has to be taken into account. In the case of low Helmholtz number flow the flow can be separated into two regions: a region of wave propagation (far upstream and far downstream of the diaphragm) and a source region (around the diaphragm). The source region can be considered compact and the effect of wave propagation can be neglected inside the source region. The production or dissipation of acoustic energy takes place in the source region. For  $M_j \ll 1$  and  $Sr \ll 1$  the incompressible quasi-steady flow model of paragraph 5.2.2 can be applied. When  $M_j \leq 1$  and still  $Sr \ll 1$  compressibility is important in the source region and the compressible quasi-steady flow model paragraph 5.2.3 can be used. When on the other hand  $M_j \ll 1$  but now  $Sr = \mathcal{O}(1)$  the flow in the source region is essentially unsteady but can still be considered incompressible. In that case the vortex-blob method presented in 5.5 is a useful flow model. Other approximations require more complex flow models such as that of the Euler equations.

Both an incompressible and a compressible quasi-steady model of the flow through a diaphragm in a pipe have been presented. An important parameter in these models is the *vena contracta* factor  $\Upsilon$ . The influence of the diaphragm geometry ( $S_d/S_p$ ) as well as the influence of compressibility on the *vena contracta* factor has been discussed. An interpolation method to obtain  $\Upsilon$  as a function of both  $S_d/S_p$  and  $M_j$  is proposed. The predictions of the compressible-flow model are compared to low-frequency experimental results for reflection and transmission coefficients. The agreement between the model and

the experiments is very good at a frequency of 77 Hz. At a higher frequency of 793 Hz the experimental results diverge from the model predictions. The unsteadiness caused by the flow is expected to be important in that case.

For low-Mach-number flows that are essentially unsteady and two-dimensional the vortex-blob method can be used. Two methods are used to determine the acoustic source power numerically: Howe's energy formulation and our pressure formulation. We show that these methods can lead to equivalent results. The pressure formulation however contains additional information on the non-linearity of the source. Together with an acoustic interpretation of the flow, results of the vortex-blob method are used to predict the elements of the scattering matrix as a function of frequency. These results are compared to results of experiments performed by Ajello (1997b) and are found to be in good agreement. Surprisingly the numerical results for a very thin diaphragm agree better with the experimental results than the numerical results for the geometrically more accurate representation of the actual diaphragm which is quite thick. In the vortex-blob method the thickness introduces a second length scale which might result in a kind of whistling effect. However, this effect is not observed in the experimental results. A satisfactory explanation is still lacking and requires additional work.

We focussed on a rectangular aperture in order to enable a comparison with the results of the vortex-blob method for two-dimensional flow. Boot (1995) presented a comparison between measurements and the results of quasi-steady flow models for round orifices. Measurements of the scattering matrix as a function of frequency for round orifices were presented by Ajello (1997a).

## References

- ÅBOM, M. & BODÉN, H. (1988) Error analysis of two microphone measurements in ducts with flow. *J. Acoust. Soc. Am.* **83**, 2429–2438
- ÅBOM, M. (1991) Measurement of the scattering-matrix of acoustical two-ports. *Mechanical Systems and Signal Processing* **5**, 89–104
- AJELLO, G. (1997a) Mesures acoustiques dans les guides d'ondes en présence d'écoulement: mise au point d'un banc de mesure applications à des discontinuités *PhD thesis Université du Maine*
- AJELLO, G. (1997b) *private communication*
- BECHERT, D.W. (1980) Sound absorption caused by vorticity shedding, demonstrated with a jet flow. *J. Sound & Vibr.* **70**, 389–405
- BLEVINS, R.D. (1984) Applied fluid dynamics handbook. *Van Nostrand Reinhold Company Inc., New York*

- BODÉN, H. & ÅBOM, M. (1986) Influence of errors on the two-microphone method for measuring acoustic properties in ducts. *J. Acoust. Soc. Am.* **79**, 541-549
- BOOT, R.J.J. (1995) Het aeroakoestisch gedrag van diafragma's. *Report R-1370-A, Eindhoven University of Technology*
- BUSEMANN, A. (1937) Hodographmethode der Gasdynamik. *Zeitschrift für angew. Math. und Mech.* **17**, 73-79
- CARGILL, A.M. (1982) Low frequency acoustic radiation from a jet pipe - a second order theory. *J. Sound & Vibr.* **83**, 339-354
- CUMMINGS, A. & EVERSMAN, W. (1983) High amplitude acoustic transmission through duct terminations: theory. *J. Sound & Vibr.* **91**, 503-518
- HOWE, M.S. (1979) Attenuation of sound in a low Mach number nozzle flow. *J. Fluid Mech.* **91**, 209-229
- HOWE, M.S. (1980) The dissipation of sound at an edge. *J. Sound & Vibr.* **70** 407-411
- HOWE, M.S. (1984) On the absorption of sound by turbulence and other hydrodynamic flows. *I.M.A. J. of Appl. Math.* **32**, 187-209
- INGARD, U. (1953) On the theory and design of acoustic resonators. *J. Acoust. Soc. Am.* **25**, 1037-1061
- INGARD, U. & ISING, H. (1967) Acoustic non-linearities of an orifice. *J. Acoust. Soc. Am.* **42**, 6-17
- KRIESEL, P.C., PETERS, M.C.A.M., HIRSCHBERG, A., WIJNANDS, A.P.J., IAFRATI, A., RICCARDI, G., PIVA, R., & BRUGGEMAN, J.C. High amplitude vortex-induced pulsations in a gas transport system. *J. Sound & Vibr.* **184**, 343-368
- PETERS, M.C.A.M. (1993) Aeroacoustical sources in internal flows. *PhD thesis Eindhoven University of Technology*
- PIERCE, A.D. (1989) Acoustics: an introduction to its physical principles and applications. *Acoustical Society of America, New York*
- PRANDTL, L. & TIETJENS, O.G. (1934) Fundamentals of hydro- and aeromechanics. *Dover Publications Inc., New York*
- RAYLEIGH, J. (1896) The theory of sound. *Dover Publications Inc., New York*
- RONNEBERGER, D. (1967) Experimentelle Untersuchungen zum akustischen Reflexionsfaktor von un stetigen Querschnittsänderungen in einem luftdurchströmten Rohr. *Acustica* **19**, 222-235

- 
- SEARS, W.R. (1954) General theory of high speed aerodynamics, volume VI. *Princeton University Press, Princeton*
- SHAPIRO, A.H. (1953) The dynamics and thermodynamics of compressible fluid flow, volume I. *Ronald Press, New York*
- TIJDEMAN, H. (1975) On the propagation of sound waves in cylindrical tubes. *J. Sound & Vibr.* **39**, 1 - 33

# Numerical study of the acoustic interaction in a T-joint

## 6.1 Introduction

In this chapter we study numerically the flow through T-joint configurations in order to acquire knowledge about the acoustic properties of such a geometry. A T-joint is a common element in pipe systems like gas-transport systems. In the T-joint the flow either has to turn around a corner or has to cross the side branch opening. In both situations flow separation occurs at the upstream edge of the T-joint. Flow separation and the resulting shear layer provide a means to transfer energy from the steady main flow to an acoustic (fluctuating) flow. In case a pipe system contains several closed branches it is very well possible that in the system some (high quality) acoustic resonators are present. Consequently, when the flow reaches the resonance condition of such a system, strong acoustic pulsations can occur in the system. Since a T-joint geometry is a common element of complex pipe systems it has been the subject of several experimental and numerical studies (Bruggeman 1987, Jungowski & Bortos 1989, Ziada & Bühlmann 1992, Peters 1993, Kriesels *et al.* 1995a).

We start by presenting a quasi-steady (low-frequency) flow model for the acoustic source pressure in T-joint configurations. Since we are also interested in Strouhal numbers of order unity we also need an unsteady flow model, for which the vortex-blob method was chosen. The vortex-blob method yields a solution of the unsteady incompressible two-dimensional flow equations including flow separation. Flow separation is implemented by using an approximate model for the Kutta condition at the separation points. That the method is incompressible means that we can only apply the results of the model to low-Mach-number flows, and for aeroacoustic purposes only in case the source region can be considered compact. Hence the model itself does not predict pulsation levels; it only provides information on the source strength for given flow conditions. However, it is possible to predict pulsation levels by combining the results of the vortex-blob method with an acoustic model for this. An acoustic energy balance for an acoustic mode of the system will be used. The source power calculated by means of the vortex-blob method is

balanced by losses due to friction, heat transfer and radiation, which provides a predicted pulsation amplitude.

We present numerical results of the aeroacoustic source power for a number of flow configurations in a T-joint. The results consist of two different formulations of the acoustic source power: the integral of the power density as proposed by Howe (1975) and the convolution of the source pressure  $\delta p$  with the acoustic flow. The results of these two formulations are compared. Also the acoustic power as a function of the acoustic amplitude is presented. Finally we compare the numerical results with results of experiments for low to moderate acoustic amplitudes (Bruggeman 1987) as well as for high acoustic amplitudes.

## 6.2 T-joint configurations

In the two-dimensional T-joint configurations that we study the side branch has a width  $S_b$  which in all cases studied is equal to the width of the main pipe  $S_p$ . We distinguish three distinct steady main flow configurations and three distinct acoustic flow configurations. These flow configurations are shown in figure 6.1. Combining the steady main flow configurations and the acoustic flow configurations we obtain a total of nine configurations.

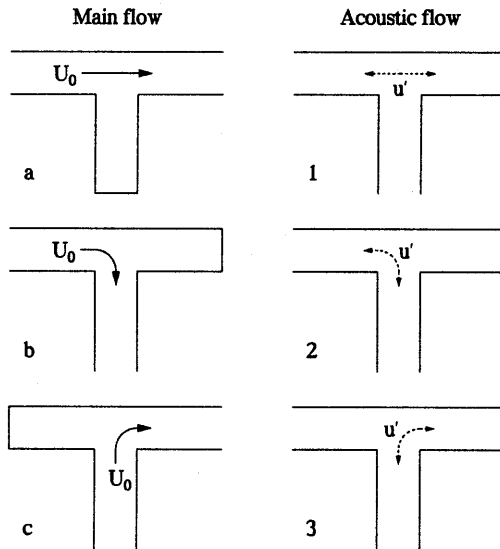


Figure 6.1: Definition of flow configurations in a T-joint.

The a-configuration consists of a main pipe and a closed side branch, so the main flow is through the main pipe. The flow separates at both edges of the side branch. However, in most cases separation at the upstream edge is the most important one. The shear

layer originating from this edge will cover the whole width of the side branch, while the shear layer originating from the downstream edge might form a small separation bubble downstream of this edge. In the vortex-blob method it is assumed that only separation at the upstream edge needs to be taken into account. Calculations with flow separation at both edges have been carried out to check the validity of this approximation.

The b-configuration is very different since in this configuration the downstream segment of the main pipe is closed and the main flow has to turn around the corner into the side branch. In this configuration a large separation bubble is formed in the side branch just below the upstream edge. A jet is formed into the side branch and the main flow is accelerated in this jet. At the downstream edge a similar separation occurs although this is expected to be generating less vorticity. Again in the vortex-blob method only separation at the upstream edge is taken into account. A few simulations including flow separation at the downstream edge show that in the case of the b-configurations this second flow separation can have a strong influence on the acoustic energy production and should be taken into account for an accurate calculation of the acoustic behaviour of the b-configurations. However, from the point of view of production of acoustic energy this second separation is not important, since it only introduces additional absorption. The separation bubble at the upstream edge is very large and almost steady. Turbulent dissipation is expected to be essential in this region. The vortex-blob method yields results for this configuration that are less accurate than for the other two configurations because it does not model turbulence.

The c-configuration is somewhat similar to the a-configuration, but now the upstream segment of the main pipe is closed and the main flow turns from the side branch into the downstream segment of the main pipe. Flow separation at the outer edge (left) of the flow bend is expected to be most important for the generation of sound and in the vortex-blob method only separation at the outer edge is taken into account. Also for these configurations some simulations with separation at both edges have been carried out.

### 6.3 Acoustic-velocity field

The acoustic velocity field is defined as the time-dependent irrotational part of the velocity field and therefore it is a potential flow solution. Consequently the acoustic velocity field in a T-joint with sharp edges contains singularities. The production or absorption of acoustic energy can strongly depend on details of the acoustic velocity field. Therefore a closer look at the flow field is warranted.

Figure 6.2 shows the streamlines of the three acoustic flow configurations in the T-joint. These flow configurations each contain singularities at both sharp edges of the T-joint. The singularity is of the following form:  $Cr^{-\zeta}$ , in which  $C$  is a proportionality constant determined by the local flow configuration,  $r$  is the distance to the sharp edge, and  $\zeta$  is the exponent of the singularity determined by the geometry of the sharp edge. When the acoustic flow is directed along the main pipe, as shown in figure 6.2 (1), the singularities are equally strong due to the symmetry of the velocity field with respect to the centre line



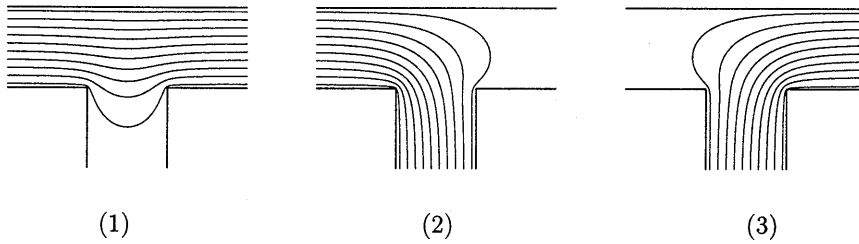


Figure 6.2: Streamlines of the acoustic field. The acoustic flow is directed along the main pipe in (1), between upstream main pipe and side branch in (2), and between downstream main pipe and side branch in (3).

of the side branch. Quite a different situation occurs when the acoustic flow is diverted from the upstream main pipe segment into the side branch, as shown in figure 6.2 (2). In this flow configuration the proportionality constant  $C$  at the upstream (left) edge is about three times as strong as the one at the downstream (right) edge, see Bruggeman (1987). This can result in a stronger interaction near the upstream edge. Just the opposite is true in the third flow configuration shown in figure 6.2 (3), in which the acoustic flow is diverted from the side branch into the downstream main pipe segment.

Furthermore, in the first configuration we recognise that the direction of the flow is changing when crossing the side branch along a line parallel to the main pipe axis: when at a certain instant in time the flow is directed into the side branch near the upstream (left) edge, it is directed out of the side branch near the downstream (right) edge. In the other two configurations the direction of the flow into or out of the side branch is the same across the whole side branch. Finally, another feature of these flow configurations is the strong decrease of the magnitude of the acoustic velocity field in that branch that is neither entrance nor exit for the acoustic flow.

## 6.4 Quasi-steady modelling

### 6.4.1 Introduction

The acoustic source pressure is defined as the difference between the pressure in the actual flow and that in the potential flow at equal inflow and outflow conditions. In fact the acoustic source pressure can only perform work when there is a pressure difference between the acoustic inflow and outflow boundary. In an inviscid flow the quasi-steady acoustic source pressure difference between points 1 and 2 is defined as

$$\Delta p_{source} = (p_1 - p_2)_{source} = p_1 - p_2 + \frac{1}{2}\rho(u_1^2 - u_2^2). \quad (6.1)$$

The time-averaged acoustic source power  $\langle \mathcal{P} \rangle$  associated with this source pressure is defined as:

$$\langle \mathcal{P} \rangle = \int_{out} \langle p'u' \rangle ds - \int_{in} \langle p'u' \rangle ds = S_p \langle \Delta p_{source} u' \rangle, \quad (6.2)$$

where the surface integral is over the cross-section of the pipe with constant area  $S_p$ . The definition of the acoustic source pressure is equal to the definition of the total pressure loss of an equivalent steady flow upon correction for the frictional losses. Which means that a prediction of the total pressure loss in a steady flow is also a prediction of the acoustic source pressure in a quasi-steady description (Ingard & Ising 1967, Ronneberger 1972).

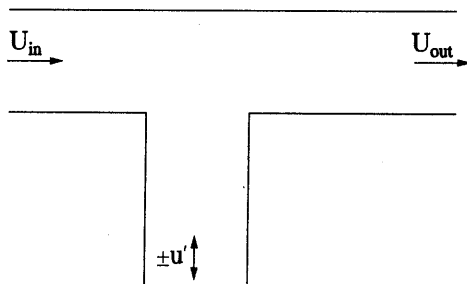


Figure 6.3: Schematic drawing of the flow situation.

Consider the configuration as shown in figure 6.3. The steady main flow is from left to right through the main pipe, while the acoustic flow  $u'$  is assumed to exit or enter through the side branch as in configurations a2 and a3. We only study the situation in which the height of the main pipe is equal to the width of the side branch ( $S_p = S_b$ ). The situation in which the acoustic flow enters through either the upstream or downstream main pipe segment and exits through the side branch is referred to as “acoustic outflow”. The reversed flow situation is referred to as “acoustic inflow”. Since the flow configuration changes significantly for an acoustic outflow with respect to an acoustic inflow we treat both cases separately. We focus on an a-type flow configuration in a T-joint since the results for the b-type and c-type configurations are closely related to the two cases defined above. In fact the results for the b-type configuration are similar to the acoustic outflow results and the results for the c-type configuration can be mapped almost exactly on those for the a-type configurations since in the present simplified quasi-steady flow description the actual T-joint geometry is irrelevant.

In the following subsections we provide a simplified description of the steady flow in order to derive the total pressure loss. It is not our aim to provide an accurate detailed description of the flow, but to predict the total pressure loss in terms of simple analytical expressions. Although most of these relations are based on a physical description of the flow, the closure of the simplified formulations requires additional assumptions. A number

of alternative assumptions are possible and each assumption results in a different prediction of the total pressure loss. Results using alternative assumptions are presented and compared to each other. Also shown are some numerical results obtained by the vortex-blob method in the present study as well as steady-flow experimental results by Ito and Imai (1973).

### 6.4.2 Acoustic outflow

When the acoustic flow is directed from the main pipe into the side branch a flow develops as sketched in figure 6.4. The velocities in the main pipe ( $U_{in}$  and  $U_{out}$ ) consist of a steady contribution  $U_0$  and one or the other also has a contribution due to the time-dependent acoustic flow with an amplitude of  $u'$ : so either  $U_{in} = U_0 + u'$  and  $U_{out} = U_0$  or  $U_{in} = U_0$  and  $U_{out} = U_0 - u'$ . Since the acoustic flow enters the T-joint at 1 or 2 it has to divert from the main pipe into the side branch and exit at 3, i.e. it has to cross the shear layer formed by the main flow and form a jet (width  $S_j$ ) into the side branch at  $j$ . This jet will become turbulent, dissipate and eventually result in a uniform velocity profile somewhere far into the side branch. In addition to a fundamental law like mass conservation, Bernoulli's equation can be applied between points 1, 2 and a point inside the jet flow at  $j$ . The turbulent mixing zone between the jet region  $j$  and the uniform outflow region 3 can be represented by a region in which momentum is conserved. Assuming the fluid in region  $j$  outside the jet to be at rest and the flow in the jet to be uniform, it is possible to apply an integral momentum balance to this dissipation region.

A final assumption is now necessary to complete the set of equations. This requires a further simplification of the description of the flow. We assume the flow in the main pipe to be one-dimensional away from the junction. If we extend this assumption to the edge at which flow separation occurs, the pressure at the upstream separation point is equal to the pressure  $p_1$  at the inflow boundary (1). Because it is impossible to sustain a

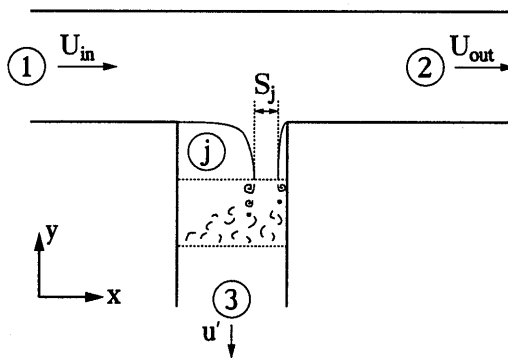


Figure 6.4: Schematic drawing of the flow situation during acoustic outflow.

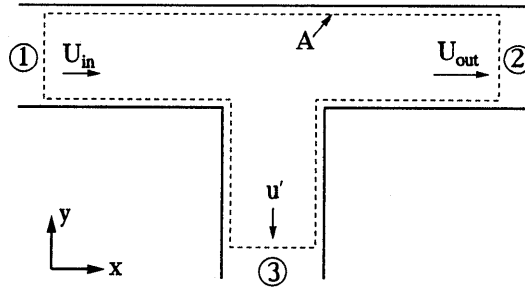


Figure 6.5: Control volume used in the integral balance of  $y$ -momentum over the whole flow domain.

pressure difference across a shear layer the pressure  $p_j$  in the jet region is then also equal to  $p_1$ ; we assume  $p_j$  to be uniform. Although this assumption might be reasonable at low acoustic velocities ( $u'/U_0 \ll 1$ ) it is not correct when the main flow is turning into the side branch:  $u' = U_{in}$  and  $U_{out} = 0$ . Contrary to the experience that a flow bend with sharp edges results in a considerable total pressure loss, this assumption would lead to a predicted total pressure loss that is equal to zero when no assumptions are made about flow separation from the edge.

An alternative method to complete the set of equations is based on the application of the integral balance of  $y$ -momentum:

$$\iint_A \rho(\vec{u} \cdot \vec{e}_y)(\vec{u} \cdot \vec{n})dA = - \iint_A p(\vec{n} \cdot \vec{e}_y)dA. \quad (6.3)$$

The integration is along the boundary of the control volume that is depicted in figure 6.5. The integral on the left-hand side has only a contribution due to the acoustic outflow at 3, i.e.  $-\rho u'^2 S_b$ . The right-hand integral on the right-hand side has contributions due to the pressure distribution on the top wall of the main pipe, the lower wall of the main pipe, and the outflow boundary at 3. Under the assumption that the flow to is uniform in both segments of the main pipe and non-uniform only at the junction, the integral on the right-hand side has only two non-zero contributions: one is the contribution of the outflow boundary ( $S_b p_3$ ) and the other is the contribution due to the part of the top wall opposite to the side branch. The pressure integral is approximated by

$$\iint_A p(\vec{n} \cdot \vec{e}_y)dA = -S_b p_3 + S_b(p_1 + C(p_2 - p_1)), \quad (6.4)$$

where  $C$  is a constant that is equal to  $\frac{1}{2}$  in case a linear pressure variation from  $p_1$  to  $p_2$  is assumed. A different choice  $C \neq \frac{1}{2}$  can account for other contributions to the integral.

Two complete sets of equations have been chosen to represent the quasi-steady total pressure loss (acoustic source pressure) in a T-joint with the acoustic flow exiting through

the side branch. In order to evaluate the validity of each analytical model the results are compared to experimental results from Ito and Imai (1973) and numerical results that are obtained by means of the vortex-blob method. Ito and Imai measured total pressure losses in T-joints in a large number of different flow configurations. Their experiments were performed in geometries consisting of cylindrical pipes with a smooth inner surface. The measured pressure loss was corrected for frictional losses at the walls of the pipes by using measured friction factors.

First the consequences of the assumption  $p_j = p_1$  are investigated. Applying Bernoulli's equation from 1 to  $j$ , we have the following relation in steady flow:

$$p_1 + \frac{1}{2}\rho U_{in}^2 = p_j + \frac{1}{2}\rho u_j^2. \quad (6.5)$$

Since the pressure  $p_j$  is assumed to be equal to  $p_1$  this leads to the condition that the velocity  $u_j$  is equal to the inflow velocity  $U_{in}$ . In order to find the width  $S_j$  of the jet mass conservation is applied between regions  $j$  and 3, which leads to  $S_j u_j = u' S_b$ , or, after rewriting,  $S_j/S_b = u'/U_{in}$ . Applying the integral formulation of the conservation of  $y$ -momentum to the turbulent mixing region between the jet and region 3 results in:

$$p_j S_b + S_j \rho u_j^2 = p_3 S_b + \rho u'^2 S_b. \quad (6.6)$$

Using the previous result for  $S_j/S_b$  and that the pressures  $p_1$  and  $p_j$  are equal, this equation can be rewritten as:

$$p_1 - p_3 = \rho u'^2 - \rho u' U_{in} = \rho u'(u' - U_{in}). \quad (6.7)$$

For the potential flow in this situation the relation between region 1 and 3 is Bernoulli's equation:

$$(p_1 - p_3)_{pot} = \frac{1}{2}\rho u'^2 - \frac{1}{2}\rho U_{in}^2 = \frac{1}{2}\rho(u' - U_{in})(u' + U_{in}). \quad (6.8)$$

It is now possible to calculate the total pressure loss between 1 and 3 by subtracting the potential pressure difference from the actual pressure difference, so:

$$\begin{aligned} (p_1 - p_3)_{source} &= (p_1 - p_3) - (p_1 - p_3)_{pot} \\ &= \frac{1}{2}\rho(U_{in} - u')^2 = \frac{1}{2}\rho U_{in}^2 \left(1 - \frac{u'}{U_{in}}\right)^2. \end{aligned} \quad (6.9)$$

Considering the pressure loss between 1 and 2 we find that the actual flow in the main pipe does differ from the potential flow, so the total pressure loss is equal to zero:

$$(p_1 - p_2)_{source} = 0. \quad (6.10)$$

In figure 6.6 we show the results for the total pressure loss between the upstream main branch and the other two branches. Three results are shown. The dashed lines are the results of the quasi-steady model described above using the condition  $p_j = p_1$ . The solid lines are fits to data from experiments performed in cylindrical pipes by Ito and Imai

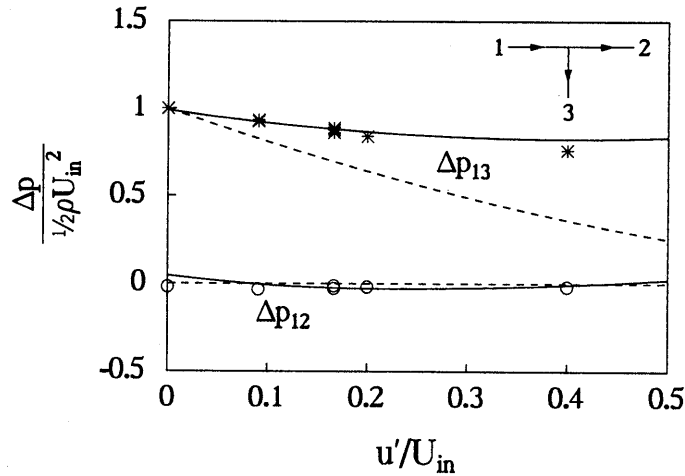


Figure 6.6: Total pressure loss as a function of  $u'/U_{in}$  in a T-joint configuration for an acoustic outflow condition. The dashed lines are the predictions using  $p_j = p_1$ . The solid lines represent the experimental results of Ito and Imai (1973) for cylindrical pipes. The symbols represent results obtained numerically using the vortex-blob method.

(1973). Finally, the symbols are results obtained from numerical simulations with the vortex-blob method assuming flow separation at the upstream (left) edge only. The three results are similar for the pressure loss  $\Delta p_{12}$  between upstream and downstream segment of the main pipe. The numerical results show a systematic small deviation from zero, but this is within the numerical accuracy. The behaviour found by Ito and Imai in cylindrical pipes is not reproduced, but this can be related to the difference between the flow in cylindrical pipes and that in (square) two-dimensional pipes. In fact Ito and Imai found for this configuration a small difference between the results for cylindrical and square pipes.

Our numerical results and the empirical data of Ito and Imai are also in satisfactory agreement for the pressure loss  $\Delta p_{13}$ , i.e. the total pressure loss between the upstream main pipe segment and the side branch. The results for the quasi-steady model, however, differ significantly from the numerical results. This must be a consequence of the assumption that the pressure upstream in the main pipe  $p_1$  and the pressure in the jet  $p_j$  are equal. Although the assumption of zero pressure difference across the shear layer at the separation point is reasonable, the value of the pressure at the separation point might be quite different from either  $p_1$  or  $p_j$  because the flow near the separation point the assumption of a quasi one-dimensional flow is not accurate.

The alternative description is based on the integral balance of  $y$ -momentum over the whole geometry. The  $y$ -momentum in the side branch is due to pressure forces acting on the flow. On the top wall the pressure changes from  $p_1$  at the inflow to  $p_2$  at the outflow. It is assumed that this pressure drop is the source of the  $y$ -momentum in the side branch

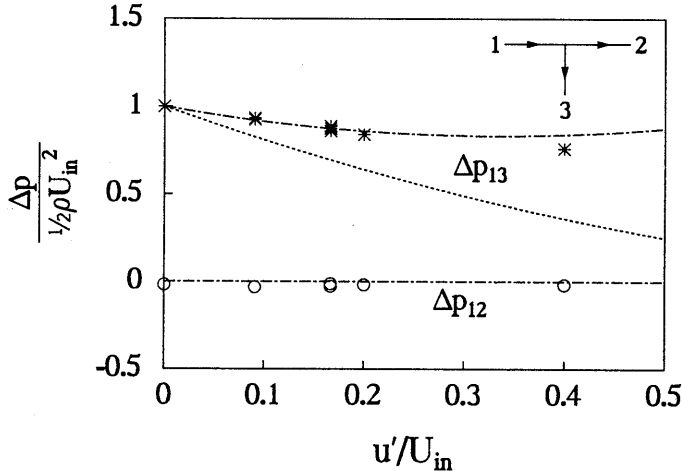


Figure 6.7: Total pressure loss as a function of  $u'/U_{in}$  in a T-joint configuration for an acoustic outflow condition. The dashed line is the original model. The dashed-dotted lines represent the alternative theoretical model using the integral form of the  $y$ -momentum equation with  $C = \frac{1}{2}$ . The symbols represent results obtained numerically using the vortex-blob method.

and the following approximation of the integral form of the  $y$ -momentum equation is used:

$$S_b(p_3 + \rho u'^2) = \int_{\text{upper}} p dS - \int_{\text{lower}} p dS = S_b [p_1 + C(p_2 - p_1)], \quad (6.11)$$

where  $C$  is a constant that represents the net result of the pressure integration along the upper and lower wall of the main pipe. Our first guess is  $C = \frac{1}{2}$ .

Since  $p_2$  is related to  $p_1$  by Bernoulli's equation we find for the pressure between 1 and 3:

$$p_1 - p_3 = \rho u'^2 - \frac{1}{2} \rho C (U_{in}^2 - U_{out}^2), \quad (6.12)$$

which together with the potential pressure difference in equation (6.8) and using mass conservation  $U_{in} = U_{out} + u'$  results in the total pressure loss:

$$\begin{aligned} (p_1 - p_3)_{\text{source}} &= \frac{1}{2} \rho U_{in}^2 - C \rho u' U_{in} + (1 + C) \frac{1}{2} \rho u'^2 \\ &= \frac{1}{2} \rho U_{in}^2 \left[ 1 - 2C \frac{u'}{U_{in}} + (1 + C) \left( \frac{u'}{U_{in}} \right)^2 \right]. \end{aligned} \quad (6.13)$$

The new results are presented in figure 6.7, where the results of both quasi-steady models are shown and compared to the numerical results. It is clear that the alternative

model results in a much improved agreement for the source pressure upstream main pipe segment and side branch.

We have presented two possible descriptions of the quasi-steady flow in the acoustic outflow configuration. In both cases a rather arbitrary assumption was necessary to close the set of equations. These assumptions are based on crude simplifications of the actual flow descriptions and do not reflect the complex flow that actually is present in the T-joint. However, both descriptions lead to analytical expressions for the total pressure loss. One of them agrees reasonably well with experimental and numerical results. The model is therefore a convenient tool for engineering purposes. Furthermore in this model the constant  $C$  can be used as a tuning parameter.

### 6.4.3 Acoustic inflow

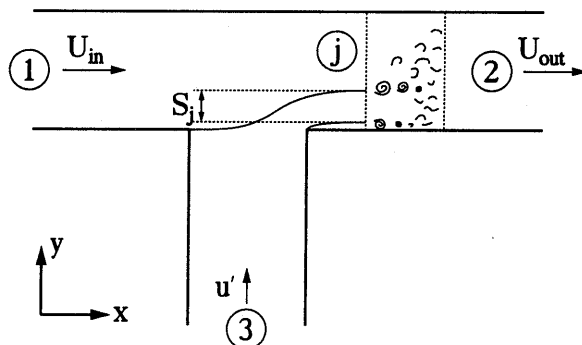


Figure 6.8: Schematic drawing of the flow situation during acoustic inflow.

In the case of an acoustic flow from the side branch into the main pipe a flow develops as sketched in figure 6.8. The jet is now formed in the main pipe along the bottom wall. This jet (height  $S_j$ ) dissipates forming the turbulent mixing region between the jet region  $j$  and region 2. Note that in region  $j$  the flow is fed by the flow of two regions with different velocities separated by a shear layer. The outflow at 2 is assumed uniform. Similar to the description in the acoustic outflow we can apply mass conservation and Bernoulli's equation between a point in the inflow region 1 and a point in the top part of the jet region at  $j$ , as well as between a point in the side branch 3 and a point in the lower part of the jet region  $j$ . Between the jet region  $j$  and the uniform outflow region 2 we apply the integral form of the equation for the conservation of momentum. To close the set of equations for predicting the steady total pressure loss and with that the quasi-steady acoustic source pressure we assume a uniform flow in the main pipe up to the separation point and zero pressure difference across the shear layer. There are two possibilities for the equation that closes our system. The first possibility is to consider the separation point to be a stagnation



point for the acoustic flow that enters through the side branch. This leads to the relation:

$$p_1 - p_3 = \frac{1}{2} \rho u'^2. \quad (6.14)$$

The second possibility is similar to the one considered in the acoustic outflow case, where we assumed the pressure  $p_j$  to be uniform in the jet region. In this case we assume the pressure  $p_3$  to be uniform in the side branch leading to the condition  $p_3 = p_1$ . Unlike in the acoustic outflow configuration an approximation of the integral form of the momentum equation is now much more difficult to apply. In the present case the flow configuration is far away from being symmetric and more assumptions about the pressure distribution on the walls would be necessary. We therefore disregard this option.

Both possibilities are investigated and evaluated by comparing the results to experimental results obtained for the flow in cylindrical pipes by Ito and Imai (1973) and numerical results obtained with the vortex-blob method. Again we do not intend to provide an accurate description of the flow in the T-joint, but rather we try to provide simple analytical expressions that predict the total pressure loss.

Using the assumption that the separation point is a stagnation point for the flow in the side branch, (6.14) together with the potential flow pressure difference obtained by applying Bernoulli's equation between the inflow region 1 and the side branch 3:

$$(p_1 - p_3)_{pot} = \frac{1}{2} \rho u'^2 - \frac{1}{2} \rho U_{in}^2. \quad (6.15)$$

The resulting acoustic source pressure then is:

$$\begin{aligned} (p_1 - p_3)_{source} &= (p_1 - p_3) - (p_1 - p_3)_{pot} \\ &= \frac{1}{2} \rho U_{in}^2. \end{aligned} \quad (6.16)$$

To obtain an expression for the pressure difference between 1 and  $j$  we apply Bernoulli's equation:

$$p_1 - p_j = \frac{1}{2} \rho U_{j1}^2 - \frac{1}{2} \rho U_{in}^2, \quad (6.17)$$

where  $(1 - S_j/S_p)U_{j1} = U_{in}$  due to mass conservation. Here we ignore the small correction on this due to the region of separated flow near the bottom wall of the main pipe in the jet region  $j$ ; this region is assumed to be negligibly small. Next we apply Bernoulli's equation between  $j$  and 3 to find:

$$p_j - p_3 = \frac{1}{2} \rho u'^2 - \frac{1}{2} \rho U_{j3}^2, \quad (6.18)$$

where  $(S_j/S_p)U_{j3} = u'$  due to mass conservation. Using these last two equations we derive a relation for  $S_j$  by adding them:

$$p_1 - p_3 = \frac{1}{2} \rho \left( \frac{U_{in}}{1 - \hat{S}_j} \right)^2 - \frac{1}{2} \rho U_{in}^2 + \frac{1}{2} \rho u'^2 - \frac{1}{2} \rho \left( \frac{u'}{\hat{S}_j} \right)^2, \quad (6.19)$$

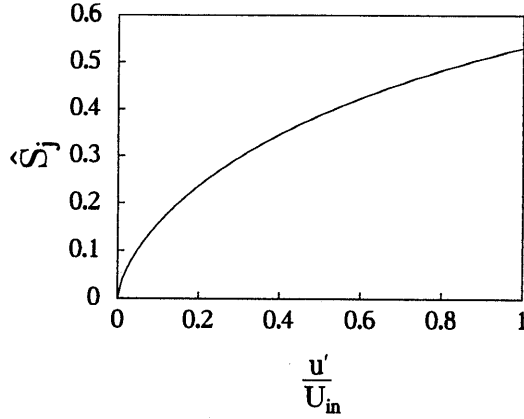


Figure 6.9:  $S_j$  as a function of the ratio  $u'/U_{in}$  as given by equation (6.20).

in which  $\hat{S}_j = S_j/S_p$  is the ratio of surface areas. Substitution of (6.14) yields the following relation between  $\hat{S}_j$  and the ratio of acoustic velocity and inflow velocity:

$$\frac{\hat{S}_j^3(2 - \hat{S}_j)}{(1 - \hat{S}_j)^2} = \left(\frac{u'}{U_{in}}\right)^2. \quad (6.20)$$

In figure 6.9 the solution for  $\hat{S}_j$  is shown as a function of  $u'/U_{in}$ .

Having obtained an expression for  $S_j$  we can now proceed to relate the pressure at 2 to the pressure at  $j$ . Across the turbulent mixing zone we apply the integral form of the conservation momentum in the  $x$ -direction:

$$p_2 + \rho U_{out}^2 = p_j + \rho \frac{U_{in}^2}{1 - \hat{S}_j} + \rho \frac{u'^2}{\hat{S}_j}. \quad (6.21)$$

The relation between 1 and  $j$  is already known so that the resulting pressure difference between 1 and 2 is given by:

$$p_1 - p_2 = \frac{1}{2} \rho U_{in}^2 \left( \frac{1}{(1 - \hat{S}_j)^2} - \frac{2}{1 - \hat{S}_j} - 1 \right) - \rho \frac{u'^2}{\hat{S}_j} + \rho U_{out}^2. \quad (6.22)$$

As we are interested in the acoustic source pressure between 1 and 2 we subtract the potential flow result. The resulting pressure loss is:

$$(p_1 - p_2)_{source} = \frac{1}{2} \rho U_{in}^2 \left( \frac{1}{(1 - \hat{S}_j)^2} - \frac{2}{1 - \hat{S}_j} \right) - \rho \frac{u'^2}{\hat{S}_j} + \frac{1}{2} \rho U_{out}^2, \quad (6.23)$$

where  $U_{out} = U_{in} + u'$  due to mass conservation.

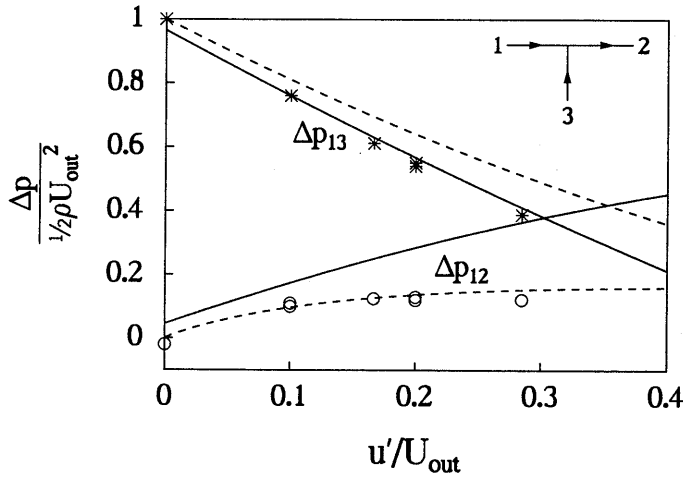


Figure 6.10: Total pressure loss as a function of  $u'/U_{out}$  in a T-joint configuration for an acoustic inflow condition. The dashed lines are the predictions using  $p_1 - p_3 = \frac{1}{2}\rho u'^2$ . The solid lines represent the experimental results of Ito and Imai (1973) for cylindrical pipes. The symbols represent results obtained numerically using the vortex-blob method.

In figure 6.10 the results for the total pressure loss between the upstream branch of the main pipe and the other two branches are shown. Three results are shown. The dashed lines are the results of the quasi-steady theory as described above, while the solid lines are the empirical results of Ito and Imai (1973). Results of the numerical simulation using the vortex-blob method are represented by the symbols.

That the empirical results of Ito and Imai for cylindrical pipes do not agree with the predictions for square pipes concerning the total pressure loss in the main pipe was already explained in the case of acoustic outflow. In this case we clearly see the difference between the data of Ito and Imai and our numerical and theoretical results.

The total pressure loss between the upstream branch of the main pipe and the side branch shows a good agreement between empirical data of Ito and Imai and the numerical results. As in the case of acoustic outflow the present prediction does differ significantly. Again this is due to the assumption that the pressure at the separation point is equal to  $p_1$ . The alternative assumption that is suggested by the numerical results is to take the pressure in the side branch equal to the pressure in the upstream branch of the main pipe. This replaces equation (6.14) by the simple relation  $p_3 = p_1$ , which results in the following total pressure loss:

$$(p_1 - p_3)_{source} = \frac{1}{2}\rho U_{in}^2 - \frac{1}{2}\rho u'^2. \quad (6.24)$$

Equation (6.20) for  $\hat{S}_j$  is also affected by the alternative assumption, resulting in the new

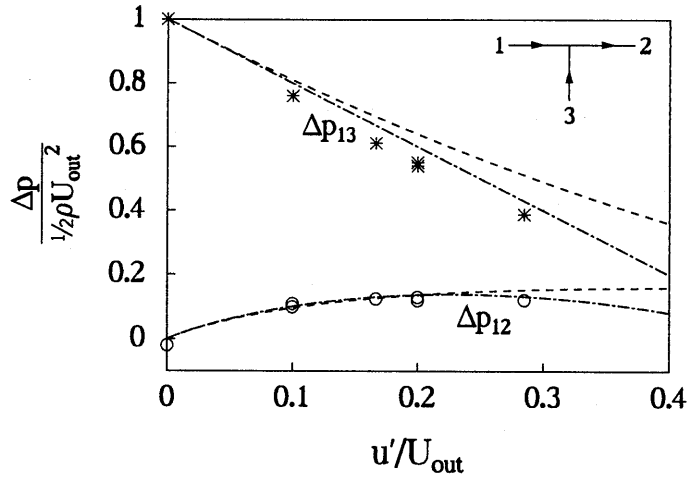


Figure 6.11: Total pressure loss as a function of  $u'/U_{out}$  in a T-joint configuration for an acoustic inflow condition. The dashed line is the original model. The dashed-dotted line represents the alternative theoretical model using  $p_3 = p_1$ . The symbols represent results obtained numerically using the vortex-blob method.

relation:

$$\frac{\hat{S}_j^3(2 - \hat{S}_j)}{(1 - \hat{S}_j^2)(1 - \hat{S}_j)^2} = \left(\frac{u'}{U_{in}}\right)^2. \quad (6.25)$$

The pressure loss in the main pipe is again defined by equation (6.23), but now  $S_j$  as defined by (6.25) is to be used:

$$(p_1 - p_2)_{source} = \frac{1}{2}\rho U_{in}^2 \left( \frac{1}{(1 - \hat{S}_j)^2} - \frac{2}{1 - \hat{S}_j} \right) - \rho \frac{u'^2}{\hat{S}_j} + \frac{1}{2}\rho U_{out}^2.$$

Results of this alternative model are shown in figure 6.11. We see that the prediction of the total pressure loss between upstream main pipe and side branch is improved. Also the total pressure loss in the main pipe is in good agreement with the results of the numerical method assuming only flow separation at the upstream (left) edge. So this is an improvement in comparison with the previous model.

As in the case of the acoustic outflow, we derived for the acoustic inflow configuration simple analytical expressions that describe the steady total pressure loss and thus the quasi-steady acoustic source pressure. Most of the assumptions are based on the physics that describe the flow, but additional simplifications were necessary to obtain the relations that predict the total pressure loss. The equations that have been derived should therefore be considered to be useful engineering tools. Agreement between theory and experiments

probably implies that the errors induced by our final closing assumption compensate other errors in the model.

## 6.5 Acoustic power versus Strouhal number

### 6.5.1 Introduction

In this section we present the results of the numerical simulations with the vortex-blob method for the nine separate flow configurations defined by the three main flow configurations and the three acoustic flow configurations sketched in figure 6.1. In order to show the typical behaviour of the flow in a configuration, the time-averaged acoustic source power is computed for a ratio of the amplitude of the acoustic velocity  $u'$  and the steady main flow velocity  $U_0$  equal to 0.2. This ratio  $\frac{u'}{U_0}$  is called the acoustic amplitude and its value is chosen in accordance with Kriesels *et al.* (1995b). It represents a moderate-amplitude oscillation and is therefore easier to calculate than low-amplitude oscillations, while the results do not yet show the behaviour of a high-amplitude oscillation. To get an impression of the power at a lower acoustic amplitude, a linear interpolation between these data and the condition of zero power at zero acoustic amplitude can be used. However, one should be very careful: the relation between the acoustic amplitude and the time-averaged acoustic source power may be very non-linear, as will be shown in the next section. In fact, the average acoustic source power initially increases with the square of the acoustic amplitude for  $\frac{u'}{U_0} = \mathcal{O}(10^{-2})$ .

Howe's energy formulation (Howe 1984) for the acoustic energy generation due to the presence of vorticity states that when vorticity is present in a flow it is possible for the main flow to interact with the acoustic flow thereby producing or absorbing acoustic energy. The time-averaged acoustic source power  $\langle \mathcal{P} \rangle$  is given by:

$$\langle \mathcal{P} \rangle = -\rho_0 \int_V \langle (\vec{\omega} \times \vec{u}) \cdot \vec{u}' \rangle dV, \quad (6.26)$$

where  $\vec{\omega} = \vec{\nabla} \times \vec{u}$  is the vorticity vector,  $\vec{u}$  is the local velocity,  $\vec{u}'$  the irrotational acoustic velocity and  $V$  is the volume enclosing the region with vorticity. In this formulation of the acoustic source power we recognise that the angle between the vector  $(\vec{\omega} \times \vec{u})$  and the acoustic velocity  $\vec{u}'$  is very important. In the two-dimensional case considered here it is related to the angle between the actual velocity  $\vec{u}$  at which the vorticity is convected and the acoustic velocity  $\vec{u}'$ : when  $\vec{u}$  and  $\vec{u}'$  are parallel, no interaction between the main flow and the acoustic field is possible. On the other hand, when they are perpendicular the interaction is strongest. The acoustic field and the main flow are certainly non-parallel in the junction and here the vorticity field is evolving in a spatially varying acoustic field implying that the flow in this region will give a significant contribution to the acoustic energy production. Interactions between vortex structures present in the branches away from the junction will result in an acoustic source with a quadrupole character and this is a much weaker source of acoustic energy than the source at the junction that has a dipole

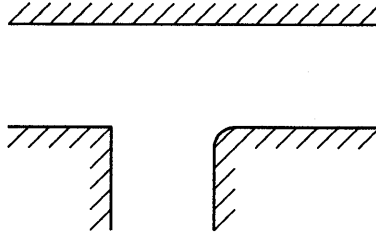


Figure 6.12: Effective T-joint geometry studied by taking only one separation point into account.

character. Therefore only locally at the junction there is a strong production or absorption of acoustic energy.

For all configurations the acoustic source power obtained with Howe's formulation is compared to the acoustic power obtained with the pressure formulation as defined in equation (6.2):

$$\langle \mathcal{P} \rangle = S_p \langle \Delta p_{source} u' \rangle, \quad (6.27)$$

In this formulation  $p_{source}$  is the difference in pressure between the actual unsteady flow (including flow separation) and the unsteady potential flow (without flow separation):

$$\Delta p_{source} = p_1 - p_2 + \frac{1}{2} \rho u_1^2 - \frac{1}{2} \rho u_2^2 + \rho \frac{\partial \Delta \phi_{12}}{\partial t}, \quad (6.28)$$

where  $\Delta \phi_{12}$  is the difference in the velocity potential between point 1 and point 2. The degree of agreement of the results from equations (6.26) and (6.27) is a measure of the accuracy of the simulation. Since both results are obtained from the same vorticity field, they should be identical in a perfect numerical simulation.

For most flow configurations we expected that only the flow separation from one edge was important for the production of sound. For this reason we only considered flow separation from the upstream (left) edge in all configurations. We will show that this approach is not always an accurate description for a T-joint geometry with two sharp edges. So in that case the results can be interpreted as if they are obtained for a geometry with the second edge rounded as shown in figure 6.12.

Information on the input of the vortex-blob calculations is given in appendix C. The influence of the choice of the input parameters can be found there as well

## 6.5.2 Configurations with flow separation at one edge

The flow configurations with a steady main flow through the main pipe are called a-configurations. In the case of an a-configuration we have a situation in which a vortex structure is formed in the side branch due to the roll-up of the shear layer. At the same time it traverses the width of the side branch. For low to moderate Strouhal numbers (of

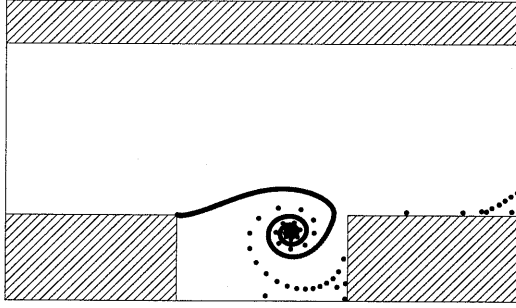


Figure 6.13: Typical result of the vortex-blob method for the flow in a T-joint for a configuration with the steady flow through the horizontal (main) pipe (a-configuration) at  $Sr = 0.4$ .

order unity) the generation of a new vortex structure is triggered by the change of direction of the acoustic field. When the acoustic flow changes direction from out of the side branch to into the side branch, the formation of a new vortex structure is started. This vortex structure is convected across the side branch with the main flow. Typically it travels at convective speeds  $U_c$  slightly less than half the main flow velocity (0.3 to 0.4 times  $U_0$ , depending on the acoustic amplitude). This results in a typical time scale  $T_c = W_b/U_c$  for the acoustic source power, where  $W - B$  is the width of the side branch. The ratio of  $T_c$  and the period of oscillation  $T$  is:

$$\frac{T_c}{T} = \frac{W_b f}{U_c} = \frac{U_0}{U_c} Sr.$$

For the a-configurations we can therefore expect some typical behaviour of the acoustic power as a function of the Strouhal number.

For a Strouhal number in the range of 0.3 – 0.4 the two time scales  $T_c$  and  $T$  are approximately equal. This means that a vortex structure travels across the side branch in one period of oscillation of the acoustic field. This implies that at any time only a single vortex structure is present in the junction as illustrated in figure 6.13. When the acoustic flow is directed into the side branch a new vortex structure starts to develop, while the previous vortex structure is just leaving the junction. This new vortex structure is still small and weak, although it will grow in strength during the period of oscillation. During this period it is crossing the side branch and it experiences a changing acoustic flow due to the geometrical configuration and due to the intrinsic time dependence of the acoustic flow. Because of its growth the interaction of the vortex structure with the acoustic field becomes stronger in time. As explained in section 6.3, depending on the flow configuration, the acoustic field is stronger or weaker in downstream direction, and the direction of the acoustic velocity  $\vec{u}$  also changes. The net result of the interaction is therefore strongly dependent on the configuration that is considered. The qualitative behaviour of the a-configurations was already discussed by Bruggeman (1987), who used a

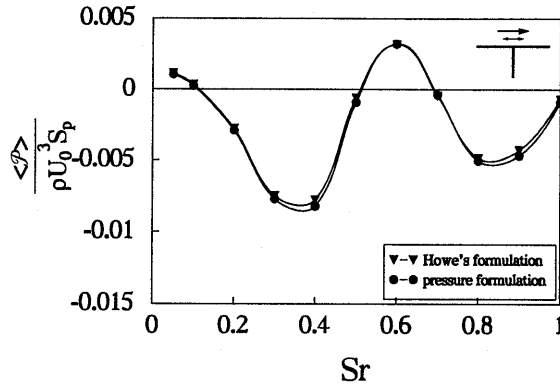


Figure 6.14: Time-averaged acoustic source power  $\langle \mathcal{P} \rangle$  as a function of Strouhal number for the a1-configuration. The acoustic amplitude is 0.2.

simplified single-vortex model proposed by Nelson *et al.* (1983). We will summarise some of Bruggeman's results.

As opposed to the other two a-configurations the a1-configuration is not an essential part of an acoustic resonator. The acoustic field in the a1-configuration is not directed into the closed side branch, but instead along the main pipe. This configuration can only influence an acoustic resonance when the main pipe is part of a resonator formed by two other acoustic reflectors. So, combining this configuration with any other T-joint configuration of equal pipe diameter will not result in an acoustic resonance. However, when it is part of a resonator it might just have enough influence to destroy any resonance that is likely to occur. Figure 6.14 shows that the acoustic power is negative at a Strouhal number of 0.3. This can be understood qualitatively by considering the total strength of the vortex structure and the direction of the acoustic field. As can be observed in figure 6.2 (1) in the case of the a1-configuration, the acoustic field is slightly deviated into the side branch. It is symmetric with respect to the centre line of the side branch so that when the flow is directed into the side branch near the upstream edge it is directed out of the side branch near the downstream edge and vice versa. In the situation that the two time scales are equal ( $Sr \approx 0.38$ ) we have the following time history of the acoustic energy production. When a new vortex starts to develop, the acoustic flow is directed into the side branch. Together with the direction of the convective velocity of the vortex and the strength of the vortex, this will result in an initially negative contribution to the acoustic energy production. While the vortex starts to travel, it grows in strength and the acoustic velocity first increases and then decreases again. All this time the net result is negative. When the vortex reaches the middle of the side branch the acoustic velocity in the main pipe changes sign. Since the direction of the acoustic streamlines also changes when reaching the middle of the side branch, the net result is again an acoustic velocity directed into the side branch. This results in even more negative contributions



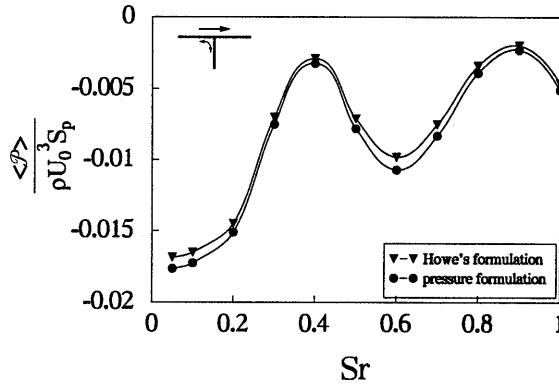


Figure 6.15: Time-averaged acoustic source power  $\langle \mathcal{P} \rangle$  as a function of Strouhal number for the a2-configuration. The acoustic amplitude is 0.2.

to the acoustic energy production. The time-averaged acoustic source power is therefore negative. At twice this Strouhal number, around  $Sr = 0.8$ , the situation is somewhat more complex, but it reduces to a combination of strong negative contributions combined with weak positive contributions. Again the net result is an absorption of acoustic energy by the main flow. In the range between  $Sr = 0.5$  and  $Sr = 0.7$  there is a stronger positive contribution to the power, so that the net result is closer to zero or, as shown in figure 6.14, even slightly positive.

For the a2-configuration the acoustic source power is shown in figure 6.15 as a function of the Strouhal number. In the a2-configuration the acoustic flow oscillates between the

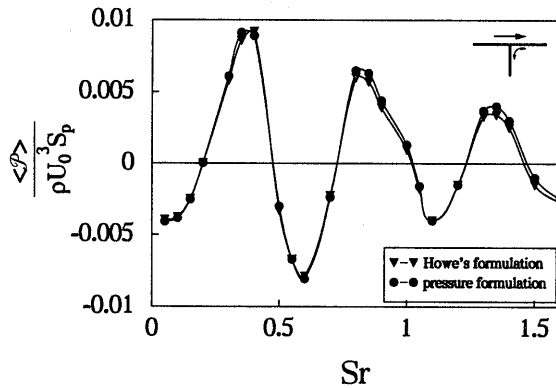


Figure 6.16: Time-averaged acoustic source power  $\langle \mathcal{P} \rangle$  as a function of Strouhal number for the a3-configuration. The acoustic amplitude is 0.2.

upstream main pipe segment and the closed side branch. Although the net result is an absorption of acoustic energy as in the case of the a1-configuration, the dependence on the Strouhal number is quite different. In fact this configuration shows a similar dependence on the Strouhal number as the a3-configuration of which the results are shown in figure 6.16. In the a3-configuration the acoustic flow oscillates between the downstream main pipe segment and the closed side branch. The qualitative explanation for this is analogous to the case of the a1-configuration and this explanation applies to both the a2- and a3-configuration.

A new vortex structure starts to develop when the acoustic flow changes direction into the side branch. When  $T/T_c \approx 1$  the previous vortex structure is just leaving the junction at the same time. This results in an absorption of acoustic energy during the first half period of oscillation. During the second half of the period the vortex structure is much stronger and the direction of the acoustic flow is reversed, which leads to a net production of acoustic energy during one period of oscillation. Figure 6.17(a) shows the acoustic source pressure  $\Delta p_{source}$  as a function of time ( $t = 0$  is the start of the simulation), while figure 6.17(b) presents the time history of the instantaneous acoustic source power. This figure shows that after two periods a stable solution is reached. In the case of the a3-configuration the net result will be a production of acoustic energy for  $0.2 < Sr < 0.45$ . The reason is that the acoustic velocity near the downstream edge, as explained in (Bruggeman 1987), is stronger than the acoustic velocity near the upstream (separation) edge. The acoustic flow is a potential flow and as such has a singularity in the velocity near the two sharp edges of the side branch. Both local velocities depend on a power  $Cr^{-\zeta}$  of the distance to the edge  $r$ . The proportionality constant  $C$  is 3 times higher at the edge around which the acoustic flow is directed, i.e. the upstream edge in the a2-configuration and the downstream edge in the a3-configuration. At the same time the total circulation of the vortex structure is higher. Together these two effects will lead to a larger rate of production of acoustic energy during the second half of an oscillation period than the rate of absorption of acoustic energy during the first half of an oscillation period. In the case of the a2-configuration the net result is a downward shift of the acoustic source power relative to that of the a3-configuration. The fact that the net result is shifted downward as a whole with respect to the a3-configuration is not yet completely understood. An influence of the relatively strong acoustic flow ( $u'/U_0 = 0.2$ ) on the generation of vorticity cannot be excluded. This has, however, not been considered in the qualitative explanation. In figure 6.15 we see that the net result for the a2-configuration is always negative, which would not necessarily be the case based on qualitative arguments.

Bruggeman (Bruggeman 1987) presented a single-vortex model to predict the acoustic source power for the a-configurations. Although the qualitative behaviour of the acoustic source power as a function of Strouhal number is predicted correctly for all three a-configurations, Bruggeman's model does not predict the downward shift for the a2-configuration. The predictions by Bruggeman's model are typically four times too high and the low Strouhal number behaviour is not predicted correctly at all. The vorticity that is generated in the single-model is concentrated into a single point vortex. In the vortex-blob method, as employed to obtain the results presented in figures 6.14 to 6.16,

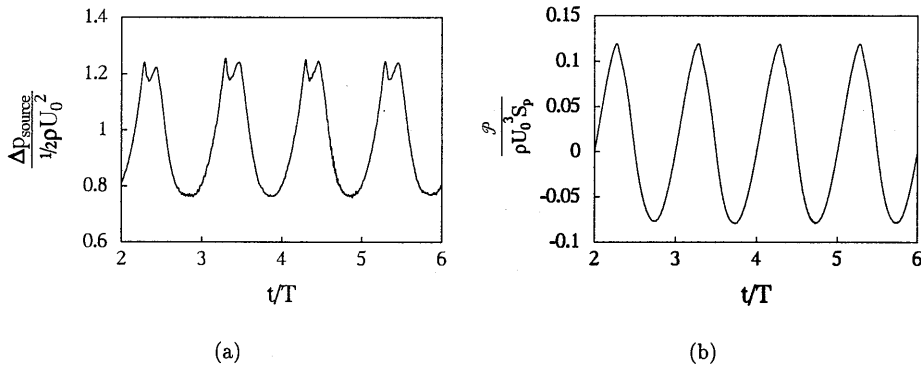


Figure 6.17: Acoustic source pressure (a) and the acoustic source power (b) as a function of time. Results obtained for an a3-configuration for a Strouhal number of 0.4 and an acoustic amplitude of 0.2.

vorticity is distributed over a large area, with a high value in the core region of the vortical structure. This difference leads to a stronger interaction of the vortex with the flow in the single-vortex model than in the vortex-blob method, and thus to a higher predicted acoustic source power. In the simple model of Nelson used by Bruggeman, the vortex path is imposed, and it is a straight line between the two sharp edges of the junction. The point vortex therefore hits the singularity of the flow at the downstream edge, which results in a severe overestimation of the acoustic power. The model does not describe any influence of the acoustic flow on the generation of vorticity and its convection. In this simple model the results for the three configurations are related: the source power in the a1-configuration equals the source power in the a2-configuration minus the source power in the a3-configuration. This relationship is not exactly satisfied by the results of the vortex-blob method. This indicates that for an acoustic amplitude of 0.2 the acoustic flow has a small but significant influence on the generated vorticity. This makes a simple linear scaling of the results for  $\langle \mathcal{P} \rangle$  rather inaccurate.

A comparison between the acoustic source power obtained by Howe's energy formulation (6.26) and that by the pressure formulation (6.2) is presented in figures 6.14 to 6.16. In general the results of these two formulations are in excellent agreement, which is an indication of the reliability of the numerical results. For  $St > 0.6$  all three a-configurations show a behaviour of period doubling. Results for the time-averaged acoustic source power are obtained by averaging over two periods of oscillation in this case. We will discuss this phenomenon in more detail later.

In the b-configurations the interaction of main flow and acoustic flow is very different from that occurring in the a-configurations. The steady flow is deviated into the side branch, thereby producing a jet flow into the side branch and thus a large area of separated flow just downstream of the upstream edge of the branch. The flow also separates at the

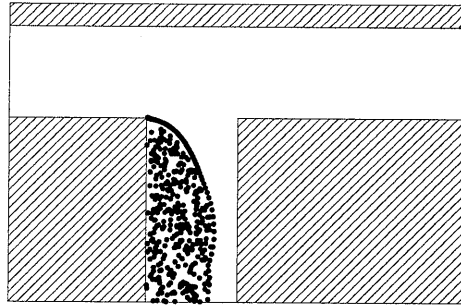


Figure 6.18: Typical result of the vortex-blob method for the flow in a T-joint configuration with the steady flow entering through the upstream branch of the main pipe and exiting through the side branch (b-configuration). The downstream (right) branch of the main pipe is closed.

downstream edge, producing a smaller second region of separated flow. In our vortex-blob simulations of the dependence of  $\langle \mathcal{P} \rangle$  on the Strouhal number only separation at the upstream edge is taken into account. A typical result from the vortex-blob method is presented in figure 6.18. Simulations that did include the separation at the downstream edge show that it can have a significant influence on the acoustic source power. The jet flow into the side branch is followed by a turbulent mixing zone, after which the outflow again is uniform. The interaction of the acoustic field with the turbulent jet flow is an essential feature of the b2 and b3-configurations. Due to this interaction we expect the b-configurations to be mainly dissipative.

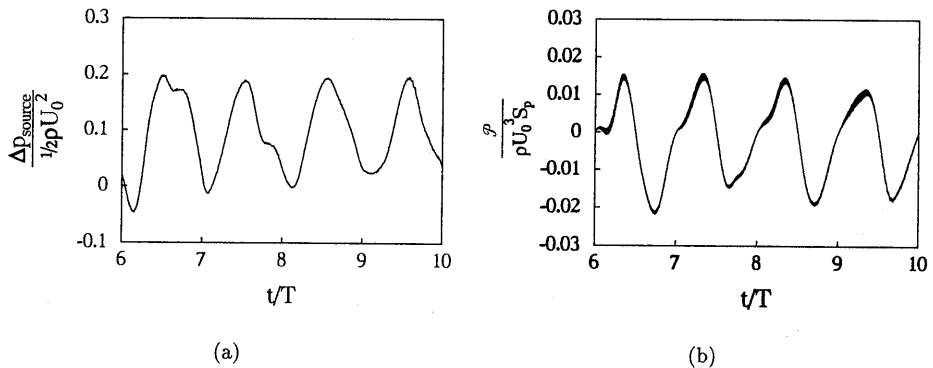


Figure 6.19: Acoustic source pressure (a) and the acoustic source power (b) as a function of time. Results obtained for a b1-configuration with a Strouhal number of 0.4 and an acoustic amplitude of 0.2.

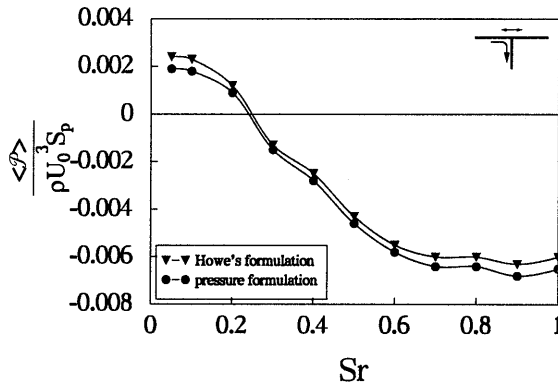


Figure 6.20: Time-averaged acoustic source power  $\langle \mathcal{P} \rangle$  as a function of Strouhal number for the b1-configuration. The acoustic amplitude is 0.2.

The acoustic source pressure and the instantaneous acoustic source power for the b1-configuration are shown in figure 6.19. While in the case of the a-configuration the acoustic source pressure and the instantaneous acoustic source power already after two periods of oscillation showed distinct periodic behaviour, one can see that in this case not even after six periods of oscillation a periodic solution is reached. This is typical for the results obtained with the vortex-blob method for the b-configurations. However, an average periodic behaviour is identifiable, so that results, although with less accuracy, can still be obtained.

In the b1-configuration the interaction of main flow and acoustic flow is restricted to the small region around the separation point. The local description of the separating shear layer is more important than the description of the turbulent mixing zone. The results for this configuration are shown in figure 6.20. As expected, the source power is mainly negative, except in the low-frequency limit although there it is just slightly positive.

In figure 6.21 the results for the b2-configuration are presented. These results show a large discrepancy between the power obtained via Howe's formulation and the power obtained via the pressure formulation. This indicates an inaccuracy in the simulation and the results should be considered only as a reasonable indication of the behaviour in this configuration. This is the result of the complex flow behaviour in the region of separated flow, where the interaction of acoustic flow and turbulent jet is essential. This region is not accurately described by the vortex-blob method, however. The vortex blobs in the simulation exhibit chaotic motion. The contributions to the source power originate from a large area, up to five pipe diameters deep into the side branch. It is clear that this configuration results in a strong absorption of acoustic energy.

The results for the b3-configuration shown in figure 6.22 are surprising, as they show that in this configuration it is possible to produce acoustic energy, although just a small amount. This must be explained by an effect discussed by Howe (Howe 1975) for the flute. The vortex path with respect to the acoustic streamlines is such that a net positive power

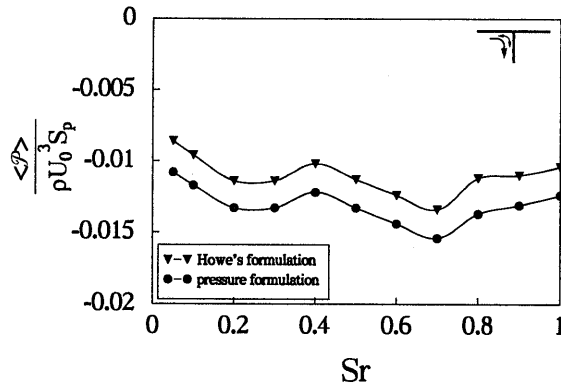


Figure 6.21: Time-averaged acoustic source power  $\langle \mathcal{P} \rangle$  as a function of Strouhal number for the b2-configuration. The acoustic amplitude is 0.2.

results. When the opposite edge of the side branch is also sharp, the separation at this edge will probably compensate this sound production. Due to the acoustic velocity field it is likely that the second separation point is important: the proportionality constant of the singularity in the acoustic velocity at the downstream edge is a factor three stronger than the one at the upstream edge. In fact, the second separation point is essential to describe this b-configuration with two sharp edges.

In the c-configurations the flow is turning from the side branch into the main pipe and one branch of the main pipe is closed. The characteristics of the c-configurations are somewhat similar to the ones of the a-configurations. A vortex structure generated

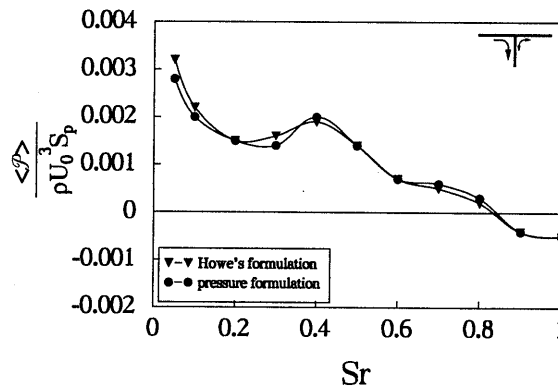


Figure 6.22: Time-averaged acoustic source power  $\langle \mathcal{P} \rangle$  as a function of Strouhal number for the b3-configuration. The acoustic amplitude is 0.2.

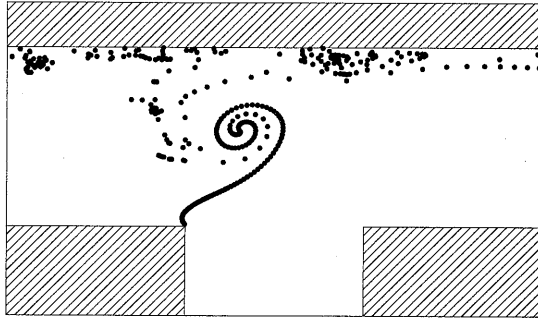


Figure 6.23: Typical result of the vortex-blob method for the flow in a T-joint configuration with the steady flow entering through the side branch and turning into the right branch of the main pipe (c-configuration). The upstream (left) branch of the main pipe is closed.

at the outer corner of the flow bend is travelling across the main pipe as shown in figure 6.23. This leads a convective time scale, but in the c-configurations it does not lead to such typical results as in the case of the a-configurations. One reason for this is that the vortex structure does not encounter the singularity associated with the acoustic flow around the downstream edge in the a-configuration. The strong absorption of acoustic energy near the separation point is not counterbalanced by a strong production near the top wall of the main pipe. This leads to the results that are presented in figure 6.25 to 6.27: all c-configurations show only a negative acoustic source power. Because the main flow is turning from the side branch into the main pipe, the c-configurations also show some

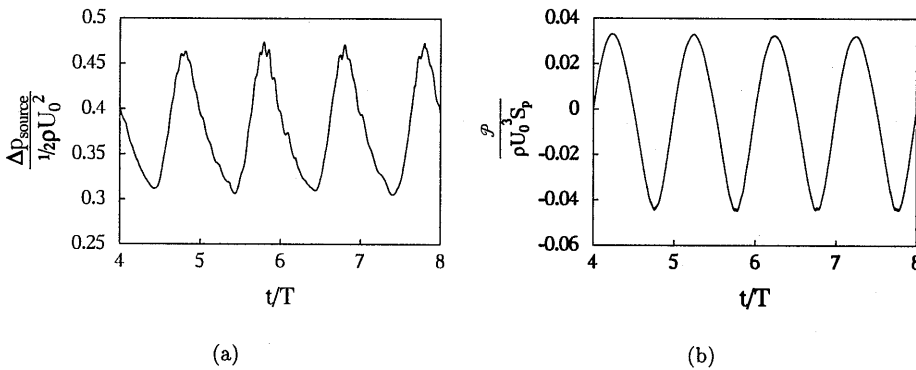


Figure 6.24: Acoustic source pressure (a) and the acoustic source power (b) as a function of time. Results obtained for a c2-configuration with a Strouhal number of 0.4 and an acoustic amplitude of 0.2.

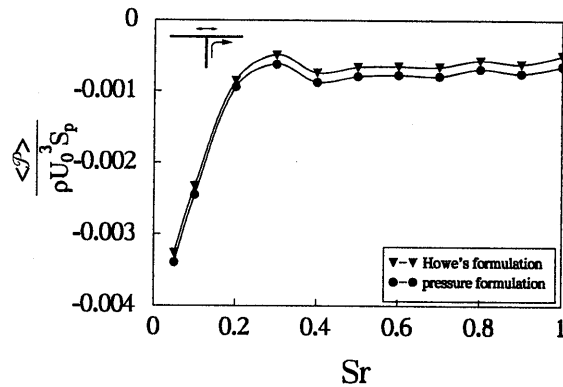


Figure 6.25: Time-averaged acoustic source power  $\langle \mathcal{P} \rangle$  as a function of Strouhal number for the c1-configuration. The acoustic amplitude is 0.2.

behaviour similar to the b-configurations. At the inner (right) corner of the flow bend also separation occurs, leading to jet formation in the downstream part of the main pipe and thus an interaction of the acoustic flow field and the turbulent jet flow is possible. In the following results only flow separation at the outer (left) corner of the flow bend is taken into account, since this separation is expected to result in a production of acoustic energy. Including the second separation point is expected to introduce more dissipation.

In figure 6.24 results for the acoustic source pressure and the instantaneous acoustic source power of a numerical simulation are presented. After four periods of oscillation the numerical solution shows periodic behaviour. Although the periodic behaviour is not

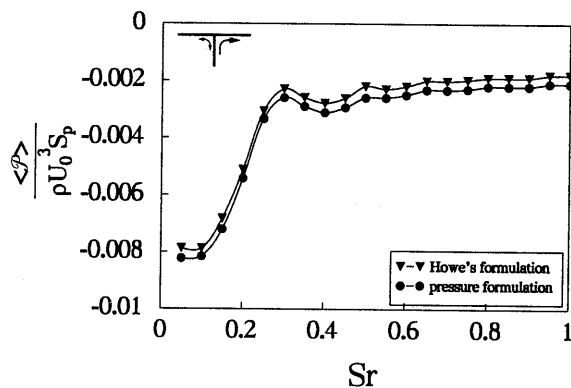


Figure 6.26: Time-averaged acoustic source power  $\langle \mathcal{P} \rangle$  as a function of Strouhal number for the c2-configuration. The acoustic amplitude is 0.2.



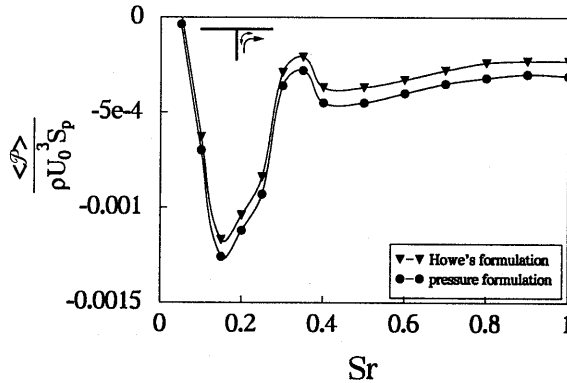


Figure 6.27: Time-averaged acoustic source power  $\langle \mathcal{P} \rangle$  as a function of Strouhal number for the c3-configuration. The acoustic amplitude is 0.2.

as clear-cut as for the a-configurations, it is much better than for the b-configurations. The results for the c-configurations are therefore more reliable than the results for the b-configurations. In general we observe a satisfactory agreement between the results of Howe's energy formulation and those of the pressure formulation.

In figure 6.25 the results are presented for the c1-configuration. The configuration is only dissipating acoustic energy. The behaviour as a function of Strouhal number is very similar to the results obtained for the c2 and c3-configuration shown in figures 6.26 and 6.27. These results are not yet explained but the absence of a singularity, such as that due to the acoustic flow field at the downstream edge in the a-configurations, might be an indication. The initially negative contributions to the acoustic source power are high due to the singularity at the separation point. The production that takes place during the second half of a period is not strong enough to balance this.

### 6.5.3 Influence of second separation

The results presented so far have been obtained by taking into account flow separation at one edge of the side branch only, although both edges are sharp. Effectively the vortex-blob simulations have been carried out for situations where the second edge does not result in a strong vortex layer that influences the acoustic source power. This is achieved by rounding the second edge as shown in figure 6.12. However, in some situations the results are also valid for T-joint configurations with two sharp edges: the second separation does not significantly influence the acoustics.

When the flow is directed along the main pipe (a-configurations) it was found that the separation at the downstream edge does not strongly affect the acoustic source power. Although taking flow separation at the downstream edge into account caused some numerical problems, generally it was found that at an acoustic amplitude of 0.2 the power was less

than 10% lower than for the situation without second separation. The numerical problems arose because in the a-configurations the vortex blobs that are generated at the upstream (left) edge are convected downstream and pass the downstream (right) edge at a close distance. When a vortex blob, generated at the upstream edge some time earlier, passes the downstream edge at the moment that at this edge a new vortex blob is generated, a physically not realistic very strong interaction between two vortex blobs occurs, leading to numerical instabilities in the vortex-blob method.

In the case of the flow turning into the side branch (b-configuration) the interaction is mainly dissipative. It is expected that taking into account flow separation at the other edge will only add to this. The main flow velocity is lower at the downstream(right) edge than at the upstream (left) edge. In the b1-configuration the acoustic velocity field is symmetric with respect to the centre line of the side branch; therefore, the second separation is expected to change the results typically only 30%, a change related to the difference in the singularity of the acoustic velocity field. Similar considerations apply to the b2-configuration. The interaction results from a large vortical flow region deep into the side branch (typically 5 pipe diameters), but the shear layer originating from the downstream edge contains less vorticity and only a fractional increase of the dissipation is expected. The b1 and b3-configurations exhibited the surprising result that sound is produced at low Strouhal numbers. Simulations that did take the second separation into account show a considerable downward shift of the curve for the time-averaged acoustic source power shown in figure 6.22. Results for the b3-configuration for  $Str = 0.4$  and  $Str = 0.8$  are presented in table 6.1. In fact, the small peak around  $Str = 0.4$  is reduced to zero power. At higher Strouhal number the effect is even stronger. This confirms the expected dissipative behaviour of the b-configurations, but it shows also that a rounding of the downstream edge can change the acoustic behaviour of a T-joint configuration.

When the flow is turning into the main branch (c-configurations) we expect the influence of separation at the inner corner (where the flow bends into the main pipe) to depend very

configuration	$Str$	$\frac{\langle \mathcal{P} \rangle}{\rho_0 U_0^3 S_p}$ (no 2 <sup>nd</sup> separation)	$\frac{\langle \mathcal{P} \rangle}{\rho_0 U_0^3 S_p}$ (with 2 <sup>nd</sup> separation)
b3	0.4	$20 \cdot 10^{-4}$	$-1 \cdot 10^{-4}$
b3	0.8	$3 \cdot 10^{-4}$	$-49 \cdot 10^{-4}$
c1	0.4	$-8 \cdot 10^{-4}$	$-67 \cdot 10^{-4}$
c1	0.8	$-6 \cdot 10^{-4}$	$-54 \cdot 10^{-4}$
c2	0.4	$-30 \cdot 10^{-4}$	$-35 \cdot 10^{-4}$
c2	0.8	$-22 \cdot 10^{-4}$	$-44 \cdot 10^{-4}$
c3	0.4	$-4 \cdot 10^{-4}$	$-151 \cdot 10^{-4}$
c3	0.8	$-3 \cdot 10^{-4}$	$-159 \cdot 10^{-4}$

Table 6.1: The influence of including the second separation at the downstream edge in the vortex-blob simulations;  $u'/U_0 = 0.2$ .

strongly on the configuration considered. In the case of the c1 and the c3-configuration the separation at the inner corner is expected to have an effect that is comparable to effect seen in the b2-configuration. The main flow turning from the side branch into the downstream main pipe segment in the c-configurations is similar to the flow turning from the main pipe into the side branch in the b-configuration. The similarity is expected to be strongest near the bottom wall of the main pipe. The flow separation from the inner corner of the flow bend is therefore very similar to the flow separation from the upstream edge in the b-configurations. In the case of the c1- and c3-configuration the acoustic streamlines in the downstream segment of the main pipe are also similar to the acoustic streamlines in the case of the b2-configuration. Numerical simulations including the separation from the inner corner of the flow bend confirm this idea. The flow separation at the inner corner of the flow bend adds dissipation of the order of the dissipation found in the b2-configuration (see figure 6.21). Results for two Strouhal numbers are presented in table 6.1. For the c3-configuration the added amount of dissipation is equivalent to that found in the b2-configuration. For the c1-configuration it is approximately half this amount. On the other hand, the results for the c2-configuration are considerably less influenced by the flow separation at the inner corner of the flow bend. The acoustic field near this corner and in the downstream main pipe segment is relatively weak. Hence the interaction is weak as well. Including the second separation in the simulations increases the dissipation in the c2-configuration by at most a factor two.

#### 6.5.4 Period doubling

Above a Strouhal number of 0.6 all three a-configurations (flow through the main pipe) show a period doubling in the acoustic source power. Figure 6.28 illustrates what is happening. One period the vortex structure leaves the junction through the side branch (figure 6.28(a,c,e)) and the next period the vortex structures leaves through the main pipe (figure 6.28(b,d,f)). It is unlikely that this non-linear effect is due to the value of the acoustic amplitude, since, as found numerically, a reduction of the acoustic amplitude by an order of magnitude does not significantly affect the generation at half the forcing frequency. Data supporting this are presented in table 6.2. By a fast Fourier transform of the acoustic source pressure signal  $\Delta p(t)$  the amplitude at the forcing frequency  $\Delta p_1$  and the amplitude

$u'/U_0$	$\Delta p_{\frac{1}{2}}/\Delta p_1$
0.200	0.73
0.100	1.24
0.050	1.41
0.025	1.33

Table 6.2: Ratio of the acoustic source pressure amplitudes at half the frequency of forcing and at the frequency of forcing as a function of the acoustic amplitude  $u'/U_0$ ;  $Sr = 1$ .

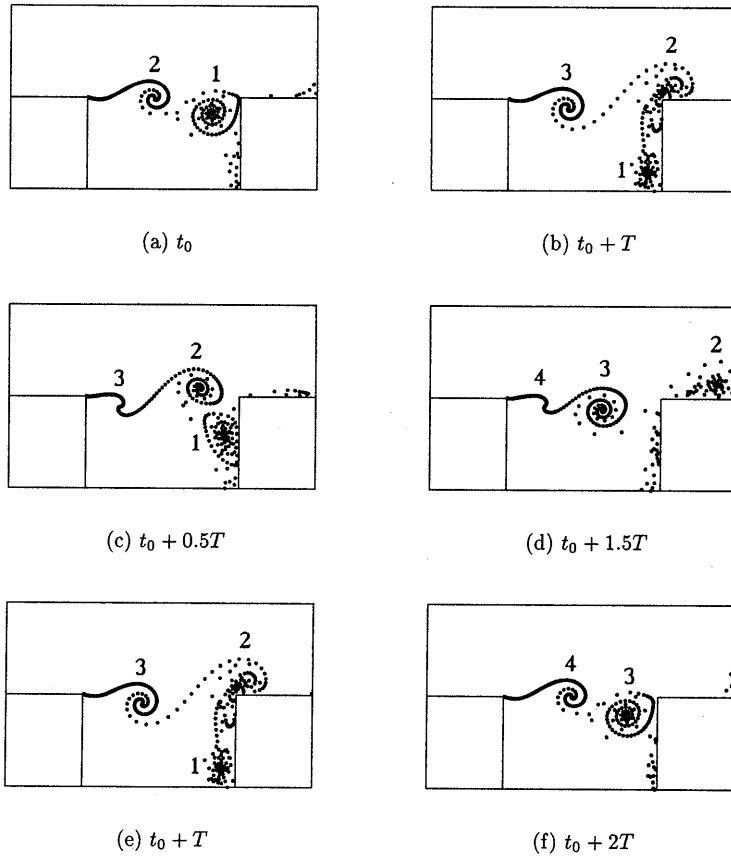


Figure 6.28: Development of flow during period doubling. One vortex structure enters the side branch and the other one enters the main pip. The pictures on the left-hand side show the vortex structures one period of oscillation earlier than the ones on the right-hand side.

at half the forcing frequency  $\Delta p_{\frac{1}{2}}$  are obtained.

We cannot explain why the period doubling is taking place. Apparently a small perturbation is enough to trigger this very persistent phenomenon under certain conditions (a-configurations,  $Sr > 0.6$ ).

### 6.5.5 Remarks on rounding the upstream edge

Three of the nine configurations (a1, b2, and c3-configuration) are not able to cause resonances in pipe systems because the closed branch in these configurations is not a part of the

resonator: the steady main flow and the acoustic flow enter and leave the T-joint through the same branches. All three act mainly as dissipaters of acoustic energy. Considering the other six possible flow configurations in a T-joint with sharp edges, we find that only the a3-configuration can be a strong source of flow-induced vibrations in pipe systems. Although it is the only configuration with sharp edges that can produce a significant amount of acoustic energy, the acoustic energy that it produces is so high that most combinations of the a3-configuration with another T-joint configuration are able to cause and sustain flow-induced vibrations in pipe systems. Although all the results were obtained for sharp edges, a small amount of rounding of the edges does not change the conclusions, as was shown by Kriesels *et al.* (1995b). He also showed that when the radius of curvature of the edges exceeds 0.1 times the pipe diameter some flow configurations, as for example the a2- and c2-configurations, can change from a dissipative behaviour to a productive behaviour. A more complete overview of the effect of rounding the edges on the acoustic behaviour of T-joints will be given in (Peters & Hofmans 1998).

## 6.6 Acoustic power versus acoustic amplitude

In this section the results for the acoustic source power as a function of the acoustic amplitude are presented. The flow configuration that is the strongest source of acoustic resonances consists of a steady main flow through the main pipe and an acoustic flow between the side branch and the downstream segment of the main pipe (a3-configuration). In the previous section numerical results for a given acoustic amplitude were presented. As a rule of thumb it has been suggested to use a linear interpolation of these data and the condition of zero power at zero amplitude. In this section it is shown that this linear interpolation does not accurately describe the relationship between the acoustic source power and the acoustic amplitude. In fact the time-averaged acoustic source power initially increases quadratically with the acoustic amplitude. This means that the linear interpolation will generally result in an over-prediction of the pulsation level for  $u'/U_0 < 0.2$  and in an underestimation for  $u'/U_0 > 0.2$ .

Figure 6.29 presents a contour plot of the time-averaged acoustic source power as function of both Strouhal number and acoustic amplitude. The range of Strouhal numbers is chosen around the first hydrodynamic mode of the configuration. It is immediately clear from this figure that: firstly, the relationship between acoustic amplitude and acoustic source power is generally non-linear; and secondly, the maximum source strength depends on the acoustic amplitude: for  $u'/U_0 = 0.1$  the maximum is found at  $Sr = 0.39$  and for  $u'/U_0 = 0.2$  the maximum is found at  $Sr = 0.36$ . This shift of Strouhal number as a function of acoustic amplitude is also observed in experiments.

Figure 6.30 shows the acoustic source power as a function of the acoustic amplitude for a Strouhal number of 0.3 and 0.4. The initial increase of the source power is quadratic: up to an acoustic amplitude of 0.25 for a Strouhal number of 0.3; up to an acoustic amplitude of 0.02 for a Strouhal number of 0.4. Although the quadratic dependence can be explained qualitatively, a quantitative model is yet lacking. At moderate-amplitude oscillations the

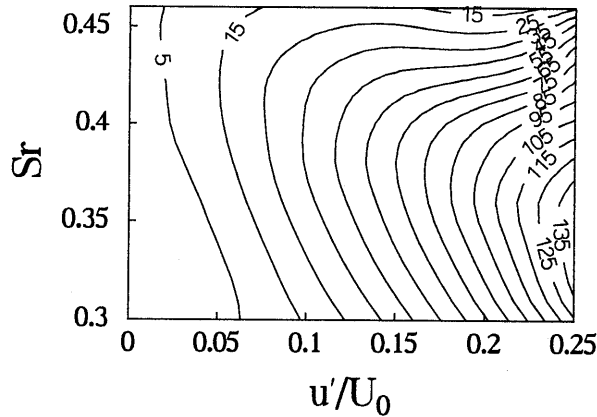


Figure 6.29: Contour plot of 1000 times the time-averaged acoustic source power  $\langle \mathcal{P} \rangle / \rho U_0^3 S_p$  as a function of acoustic amplitude and the Strouhal number for the a3-configuration

vortex shedding was assumed to be independent of the acoustic amplitude as a result of saturation in the shear-layer perturbation by roll-up of the shear layer into coherent structures (Bruggeman 1987, Kriesels *et al.* 1995a). At low acoustic amplitudes the shear layer across the side branch is no longer rolling up into discrete vortex structures. The production or absorption of acoustic energy is then determined by the whole shear layer instead of being dominated by a vortex structure travelling across the side branch. Since a uniform vorticity distribution in a steady shear layer leads to a zero net production of acoustic energy, deviations from the uniform distribution are necessary to produce or absorb acoustic energy. These deviations are caused by the perturbations as a result of the acoustic flow and therefore depend on the acoustic amplitude. Two such perturbations can be recognised: perturbations in the vorticity field that is generated at the sharp edge, and perturbations in the position of the shear layer. For small amplitude both perturbations are linear in the acoustic amplitude. Because obviously the acoustic velocity depends on the acoustic amplitude, the combined result is an acoustic power that depends quadratically on the acoustic amplitude.

In order to have a better look at the low-amplitude behaviour the acoustic source pressure and the relevant part of the acoustic source pressure that performs work on the acoustic field are plotted in figure 6.31 for two Strouhal numbers.  $\Delta p$  is the amplitude of the acoustic source pressure and  $\varphi$  is the phase difference between the acoustic source pressure and the acoustic velocity. Hence  $\Delta p \cos \varphi$  is the part of the acoustic source pressure that performs work on the acoustic field. The average acoustic source power is then equal to:

$$\langle \mathcal{P} \rangle = \frac{1}{2} S_p \cdot \Delta p \cos \varphi \cdot u'. \quad (6.29)$$

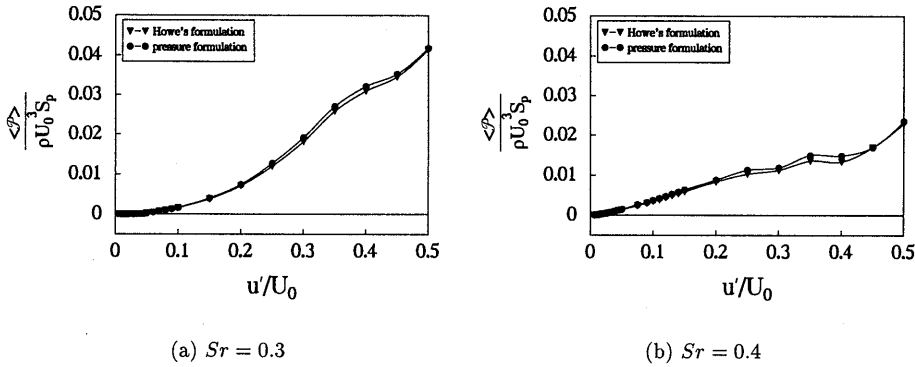


Figure 6.30: Time-averaged acoustic power as a function of acoustic amplitude for the a3-configuration.

The time-averaged acoustic source power shown in figure 6.30 differs considerably for the two Strouhal numbers. The cause of this difference is explained by figures 6.31(a) and 6.31(b), which show the acoustic source pressure as a function of the acoustic amplitude for Strouhal numbers 0.3 and 0.4, respectively. Although the acoustic source pressure for  $Str = 0.3$  is generally lower than for  $Str = 0.4$ , the behaviour is very similar. The relevant part of the acoustic source pressure ( $\Delta p \cos \varphi$ ), however, is very different for these Strouhal numbers, as is clear from figures 6.31(c) and 6.31(d). For a Strouhal number of 0.4, the increase is initially very strong up until an acoustic amplitude of 0.1. At that point  $\Delta p \cos \varphi$  starts to saturate, leading to the linear relationship between the acoustic source power and the acoustic amplitude, as evident from figure 6.30(b). This saturation is mainly due to the phase difference, as can be deduced by comparing figures 6.31(b) and 6.31(d). For a Strouhal number of 0.3 the relationship between  $\Delta p \cos \varphi$  and the acoustic amplitude is almost linear up to an acoustic amplitude of 0.25. This leads to the quadratic relationship between the acoustic source power and the acoustic amplitude shown in figure 6.30(a). Apparently the phase behaviour determines the behaviour of the acoustic source power. At acoustic amplitudes below 0.1 inaccuracies in the phase  $\varphi$  lead to inaccurate results for  $\Delta p \cos \varphi$ , which explains the scatter in figures 6.31(c) and 6.31(d).

The acoustic source pressure has also been measured as a function of the acoustic amplitude in an experimental set-up for the T-joint configuration using cylindrical pipes. The pressure fluctuation at the end of the side branch has been measured. The acoustic source pressure  $\Delta p \cos \varphi$  has been obtained from these data by using an acoustic energy balance or an acoustic model. The results of these experiments are presented in figure 6.32, together with numerical results obtained with the vortex-blob method (also presented in figure 6.31(d)). The Strouhal number in the experiments varied between 0.43 and 0.45. When comparing results for a two-dimensional T-joint to results for a T-joint consisting of cylindrical pipes a conversion of the results is necessary. In this case we use the ratio

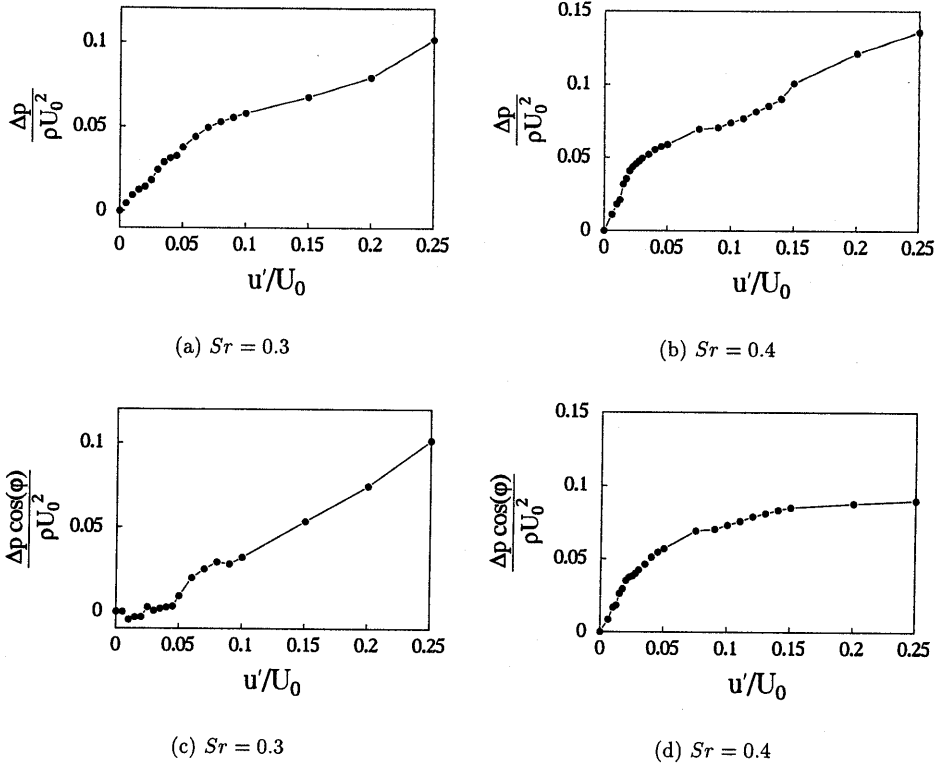


Figure 6.31: Acoustic source pressure as a function of the acoustic amplitude for a Strouhal number of 0.3 (a) and 0.4 (b), respectively. The relevant parts of the acoustic source pressure that is performing work on the acoustic field belonging to (a) and (b) are shown in (c) and (d), respectively. The angle  $\varphi$  is the phase difference between the acoustic source pressure and the acoustic velocity.

of the cross-sectional areas to convert the Strouhal number of the experiment based on the diameter of the pipe, to a Strouhal number for the two-dimensional case based on the height of the channel:

$$Sr_H = \frac{fH}{U_0} = \sqrt{\frac{\pi}{4}} \frac{fD}{U_0} = \sqrt{\frac{\pi}{4}} Sr_D. \quad (6.30)$$

So the results measured at an average Strouhal number of 0.44 in the cylindrical-pipe configuration are compared to numerical results obtained for a Strouhal number of 0.4 for the two-dimensional configuration. Although this is not an exact match, the comparison shows that the numerical results agree very well with the experimental results. A more detailed comparison of experimental and numerical results for pipes with square cross-



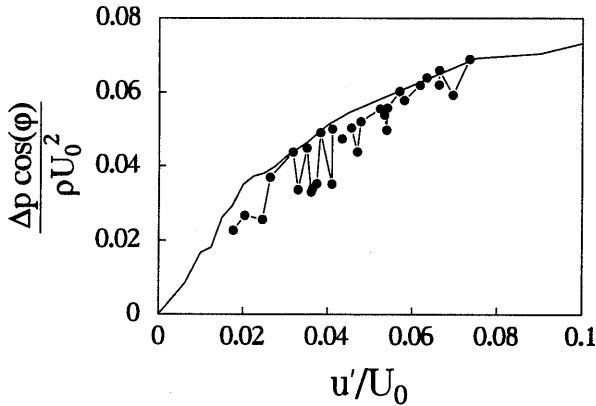


Figure 6.32: Measurement of the acoustic source pressure in a cylindrical pipe set-up at an average Strouhal number of 0.44. The solid line is the results of two-dimensional numerical simulations with the vortex-blob method for a Strouhal number of  $0.4 \approx \sqrt{\pi/4} \cdot 0.44$ .

sections is presented in the next two sections.

## 6.7 Comparison of numerical simulation to experiments

### 6.7.1 Low- to moderate-amplitude oscillations

To gain insight into the robustness and accuracy of the vortex-blob simulations, we compare the numerical results to experimental results by Bruggeman (1987) for a T-joint geometry. This is achieved by applying an energy balance to the system and equate the (known) acoustic losses in the system to the production of acoustic energy by the process of vortex shedding. The configuration considered is a T-joint as shown in figure 6.33. Air accelerates out of the settling chamber on the left into the square pipe (height 6 cm), where it reaches a velocity  $U_0$ . Connected to the main pipe is a side branch (width 6 cm) of length 59 cm. The main pipe length downstream of the side branch is 121 cm. It is terminated by a muffler so that the radiation losses at the pipe end can be varied. This pipe termination acts almost like an open pipe end and it is characterised by the pressure reflection coefficient  $R_p$ . The reflection coefficient was measured by means of a two-microphone method (see (Bruggeman 1987)).

In this configuration it is possible to have an acoustic resonance at certain flow conditions. The vortex shedding at the side branch provides the source for the acoustic resonance. The first resonant mode in this configuration is a standing acoustic wave with an acoustic velocity node at the end of the side branch and an acoustic pressure node at the termination of the main pipe (assuming that this can be considered an open pipe

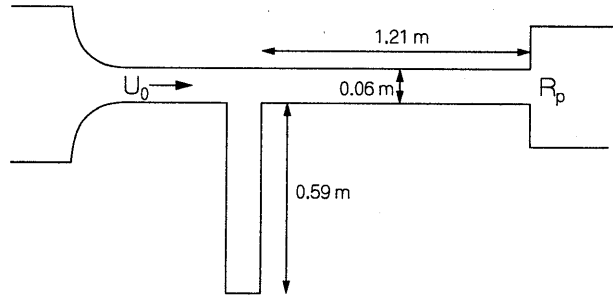


Figure 6.33: Experimental set-up used by Bruggeman (1987) to measure pulsation levels as a function of main flow velocity  $U_0$  and pressure reflection coefficient  $R_p$ .

termination). So the length of the main pipe plus the side branch has to be equal to three quarters of the wavelength  $\lambda$  in order to have the first resonant mode. In this case the resonant frequency is expected to be around 137 Hz.

The steady flow  $U_0$  from left to right is varied in the range of 18 m/s to 26 m/s. The pulsation level is measured as a function of the velocity. In order to run the vortex-blob simulations a flow condition is characterised by two parameters: the Strouhal number  $St = fH/U_0$  and the acoustic amplitude  $u_{ac} = u'/U_0$ . The Strouhal number is based on the measured frequency, velocity and height of the square pipe. The acoustic amplitude is obtained from the experimental pulsation level:  $u'/U_0 = p'/c_0\rho_0U_0$  at the end of the side branch. The simulation then yields an acoustic source power for the given conditions. Using an acoustic energy balance, the pulsation level is predicted from these theoretical source power calculations.

The two main sources for acoustic losses in this system for given conditions are the visco-thermal dissipation in the pipes and the vortex shedding at the main pipe termination. Due to the acoustic configuration of a pressure node at the junction, radiation losses into the upstream main pipe segment are small and can be neglected. The theoretical damping coefficient that we will use is given by (Pierce 1989, Peters 1993):

$$\alpha_0 = \frac{k_0\delta_{ac}}{H} \left( 1 + \frac{\gamma - 1}{\sqrt{Pr}} \right), \quad (6.31)$$

where  $k_0$  is the wave number of the resonance frequency,  $H$  is the height of the pipe,  $\gamma$  and  $Pr$  are Poisson's constant and the Prandtl number, respectively, and  $\delta_{ac}$  is the acoustic-boundary-layer thickness, defined by:

$$\delta_{ac} = \sqrt{\frac{2\nu}{\omega}}. \quad (6.32)$$

Here  $\nu$  is the kinematic viscosity and  $\omega$  is the radial frequency. For air at room temperature and atmospheric pressure  $\gamma = 1.4$ ,  $Pr = 0.71$ , and  $\nu = 1.5 \cdot 10^{-5} \text{ m}^2/\text{s}$ . This leads to a

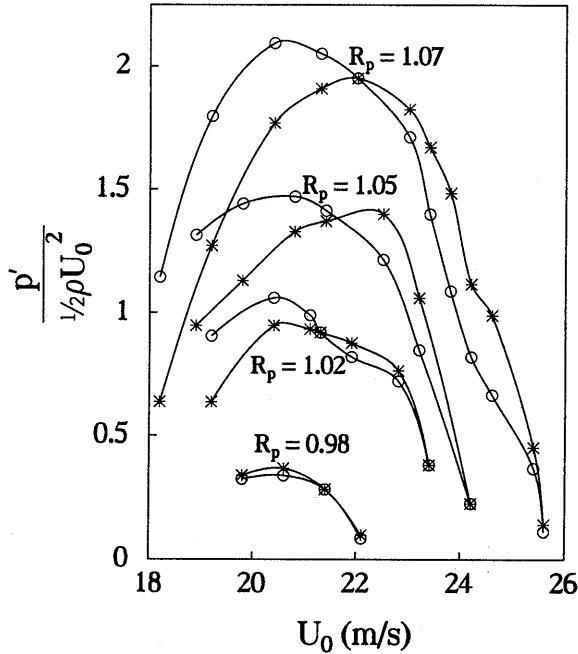


Figure 6.34: Pulsation level at the end of the side branch as a function of the main flow velocity  $U_0$  for four reflection conditions  $R_p$ . Experimental results (\*) by Bruggeman (1987) and numerical results of the vortex-blob method (O) are shown.

value for  $\alpha_0$  of the order of  $10^{-2} \text{ m}^{-1}$ . Peters (1993) compares this theoretical prediction to experiments at conditions close to the experimental conditions of Bruggeman (1987) discussed here. A small correction as a function of the parameter  $\delta_{ac}^+$  is taken into account.  $\delta_{ac}^+$  is the acoustic-boundary-layer thickness scaled with the friction velocity  $v^*$  and the kinematic viscosity:  $\delta_{ac}^+ = \delta_{ac} v^* / \nu$ . The friction velocity  $v^*$  is determined from Prandtl's equation for smooth pipes (Schlichting 1979). The vortex shedding at the main pipe termination is taken into account by a quasi-steady model. Equating the acoustic source power to the acoustic losses we find the following equation:

$$\frac{\langle \mathcal{P} \rangle}{\rho_0 U_0^3 S_p} = \left( \frac{p'}{\frac{1}{2} \rho_0 U_0^2} \right)^2 \frac{M}{32} \left( 4(\alpha_1 L_1 + \alpha_2 L_2) + 1 - R_p^2 \left( \frac{1-M}{1+M} \right)^2 \right), \quad (6.33)$$

in which  $M$  is the Mach number of the main flow, and  $\alpha_1$  and  $\alpha_2$  are the damping coefficients in the main pipe (length  $L_1$ ) and side branch (length  $L_2$ ). The left-hand side contains the non-dimensional time-averaged acoustic source power, which is obtained from the numerical simulations. The right-hand side consists of the product of the non-dimensional

acoustic pressure amplitude times the acoustic loss terms. By changing the outflow condition represented by the pressure reflection coefficient  $R_p$ , the saturation of the system is changed and hence the pressure amplitude. Experimentally the pressure amplitude is measured as a function of the main flow velocity  $U_0$  for four values of the pressure reflection coefficient:  $R_p = 1.07, 1.05, 1.02, \text{ and } 0.98$ .

In figure 6.34 the present numerical results are compared with the experimental results of Bruggeman. The numerical results have been obtained by substituting the numerical results for the acoustic source power  $\langle \mathcal{P} \rangle$  in equation (6.33) and computing  $p'$ .

The vortex-blob method combined with the energy balance is able to predict pulsation levels within 10 %. The velocity at which the maximum pulsation level is attained is predicted typically 1 m/s too low. This could indicate an error in the phase predicted by the vortex-blob method, since the phase is mainly determined by the roll-up behaviour of the shear layer. Numerically the desingularisation parameter  $\delta$  can have a large influence on the roll-up characteristics of the shear layer emanating from the sharp edge of the T-joint. However, reducing the influence of the desingularisation parameter by decreasing its value, thus reducing the influence of the desingularisation parameter, does not significantly change the results shown in figure 6.34.

### 6.7.2 High-amplitude oscillations

The implementation of the pressure formulation (given by equation (6.2)) in the vortex-blob method has the advantage above the energy formulation of Howe (given by equation (6.26)) that the generation of higher-order modes by the fundamental forced mode is a natural result. To study the generation of higher-order modes by the fundamental (forcing) frequency and to evaluate the accuracy of the predictions of the vortex-blob method, numerical simulations have been carried out for cases for which the acoustic amplitude is high (typically  $u'/U_0 > 0.2$ ). Results of high-acoustic-amplitude experiments are compared to the corresponding numerical results.

A schematic drawing of the experimental set-up is shown in figure 6.35. This set-up is very similar to the set-up described in the previous section. A fan at the entrance of the square settling chamber (height 480 mm, length 1850 mm) produces the steady main flow through the set-up. The settling chamber contains several fine gauzes to homogenise the flow. By means of two successive smooth contractions the height of the channel is reduced to the height of the square main pipe (60 mm). The closed side branch of equal width is connected to the main pipe at a short distance downstream of the second contraction. The main pipe is terminated by a horn from which the flow exits into the large open space of the laboratory. In this way an acoustic resonator is obtained consisting of the side branch and the downstream segment of the main pipe. The horn has the property that it can increase the pulsation level in the resonator considerably. The first resonant mode in this set-up is a standing acoustic wave with an acoustic velocity node at the end of the side branch and an acoustic pressure node at the termination of the main pipe (as long as this can be considered an open pipe termination). So the length of main pipe plus the length of the side branch has to be equal to three quarters of the wavelength  $\lambda$ . In this case



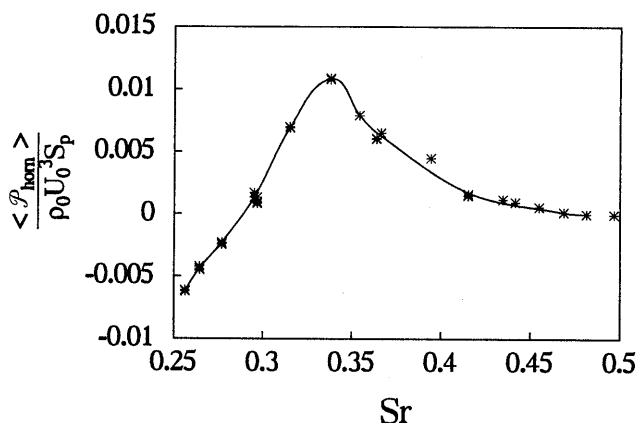


Figure 6.36: Time-averaged acoustic source power of the horn  $\langle \mathcal{P}_{horn} \rangle$  as a function of the Strouhal number  $Sr$ . The symbols represent the measurements, while the solid line represents the fit to the experiments that was used in the energy balance.

the flow through the horn is generating acoustic energy instead of dissipating it. This leads to the high-amplitude oscillations.

The reflection coefficient of the upstream pipe segment is found to be low enough (typically  $R_p < 0.4$  for a frequency of 196 Hz) to ignore energy reflections in this part of the set-up. Furthermore, the resonant modes have a pressure node at the junction, hence radiation of acoustic energy into the upstream branch can be neglected. Therefore the upstream pipe segment is not taken into account in the energy balance.

The numerical results of the vortex-blob method will be combined with an acoustic model in order to facilitate their physical interpretation. We can use two different approaches. The first approach is an energy balance as was described in the previous section. The second approach is a complete acoustic modelling of the whole set-up. However, it was found that the energy balance is much less sensitive to inaccuracies in the measured acoustic properties, and we will use the energy balance for the resonant modes (first and third harmonic) and a simplified acoustic description for the non-resonant modes (second and fourth harmonic).

For the resonant modes an adaptation of equation (6.33) is used:

$$\frac{\langle \mathcal{P} \rangle + \langle \mathcal{P}_{horn} \rangle}{\rho_0 U_0^3 S_p} = \left( \frac{p'}{\frac{1}{2} \rho_0 U_0^2} \right)^2 \frac{M}{8} (\alpha_1 L_1 + \alpha_2 L_2). \quad (6.34)$$

The source power of the horn is moved to the left-hand side with respect to equation (6.33). This is necessary because the dependence on the amplitude of the oscillation is not known for the power of the horn. By moving this power to the left-hand side the measured source power of the horn is inserted, and no assumption is made about the relation between amplitude of the oscillation and the acoustic power of the horn.

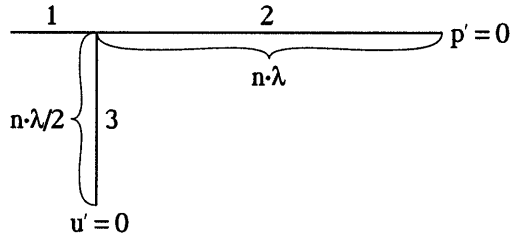


Figure 6.37: Schematic drawing of the non-resonant acoustic waves in the T-joint.

In order to achieve the high-amplitude oscillations the horn was used as an additional source of acoustic energy. For a Strouhal number in the range of 0.3 to 0.4 the power  $\langle \mathcal{P}_{horn} \rangle$  generated by the vortex shedding at the horn, can be as much as 25% of the power  $\langle \mathcal{P} \rangle$  generated by the vortex shedding at the T-joint and it is therefore a significant source. A small error in the determination of  $\langle \mathcal{P}_{horn} \rangle$  can have considerable consequences for the energy balance and thus for the prediction of the pulsation level.

For the non-resonant modes a simplified acoustic model of the experiments is used, The length of the side branch equals  $n/2$  times the wavelength of a non-resonant mode (with  $n$  an integer number). The downstream segment of the main pipe will then have a length  $n$  times the wavelength. In figure 6.37 a sketch of the acoustic situation is presented. The boundary condition at the outflow of the main pipe is  $p' = 0$  and at the end of the side branch  $u' = 0$ . The pressure fluctuations at the junction in each of the three branches are denoted by  $p'_1$ ,  $p'_2$ , and  $p'_3$ , respectively. The acoustic source is located at the junction leading to the following equations (neglecting convective effects):  $p'_1 - p'_2 = \Delta p_{12}$  and  $p'_2 - p'_3 = \Delta p_{23}$ . The condition at the end of the main pipe leads to  $p'_2 = 0$  and therefore we find:

$$p'_3 = -\Delta p_{23} \quad (6.35)$$

and

$$p'_1 = \Delta p_{12}. \quad (6.36)$$

Since the side-branch has a length equal to  $n\lambda/2$ , the pressure at the end of the side branch is equal to the pressure  $p'_3$  at the junction, which is equal to the source pressure between the side branch and the downstream main pipe segment.

It is more difficult to determine the losses for high-amplitude oscillations than for low-amplitude oscillations. For low-amplitude oscillations the important losses are the visco-thermal dissipation and the radiation at the pipe termination. These can be estimated reasonably well, as was shown in the previous section.

Because for the high-amplitude oscillations velocities are higher, the correction for turbulent-boundary-layer effects in the main pipe is essential. This correction can be made by using the data of Peters (1993). Additional losses become important when the amplitude of the oscillation is high.

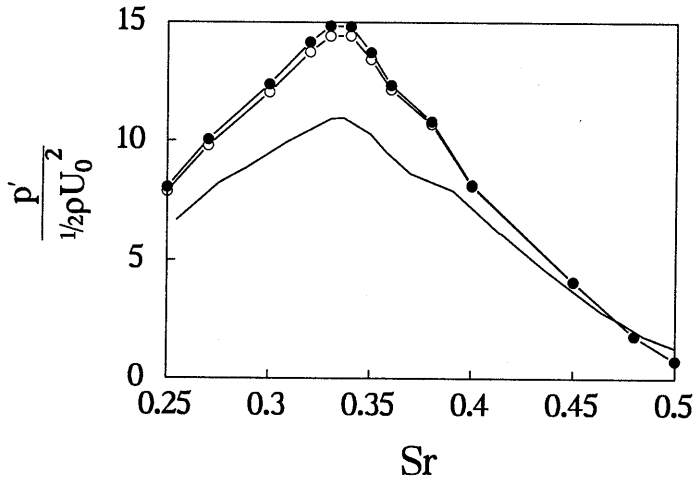


Figure 6.38: Measurement (—) of the pressure amplitude at the end of the side branch and the numerical prediction based on an acoustic energy balance without non-linear losses (•) and with non-linear losses (o), shown as a function of the Strouhal number.

Using equation (6.34) to determine the pressure amplitude at the end of the side branch we find the results that are shown in figure 6.38 marked by the bullets (•). The solid line represents the experimental results. The experimental conditions that correspond to the data points of this line are presented in table 6.3. In figure 6.39 the acoustic source pressure and the power spectrum of the source pressure are shown. These numerical results are obtained for the maximum pulsation level at an acoustic amplitude of 0.532 and a Strouhal number of 0.34. The figure clearly shows that at these conditions the acoustic source is rich in higher harmonics; in the power spectrum shown in figure 6.39(b) at least fifteen harmonics are clearly identifiable. Many of these harmonics are generated at the end of each period when the vortex structure passes near the downstream sharp edge of the side branch (see the high peaks in figure 6.39(a)). This suggests that rounding the downstream edge is going to have a strong influence on the pulsation level.

At the highest acoustic amplitudes the predicted values are approximately 35% too high. Several explanations are possible. Firstly, the power generation by the horn might be over-estimated. The uncertainty in the source power of the horn of 10% leads to an uncertainty of 2% in the pressure amplitude at the highest oscillation level. This could explain approximately 8% of the difference between measurement and prediction. Additional losses could be the result of wall vibrations, transition of the acoustic boundary layer in the side branch from laminar to turbulent, or non-linear wave steepening.

In the experimental set-up the effect of wall vibrations is much reduced by reinforcing the pipes with a layer of lead that is 1 cm thick. The lead is glued on the aluminium pipes which is expected to dampen the vibrations strongly.



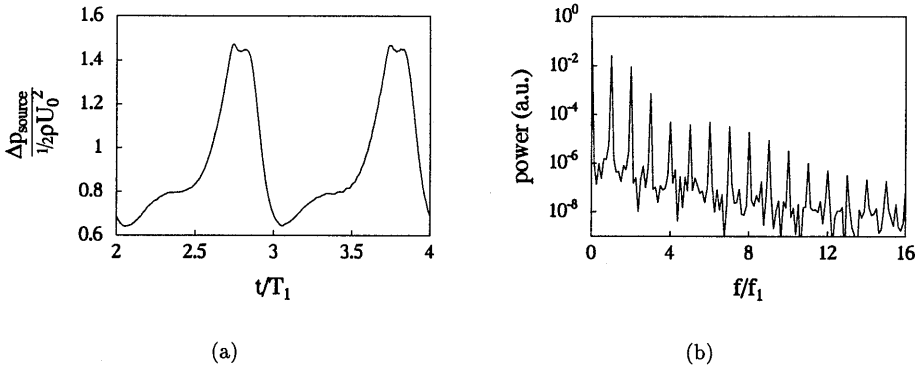


Figure 6.39: The acoustic source pressure as a function of time for the high-amplitude oscillation at  $Sr = 0.34$  and  $u'/U_0 = 0.532$  (a) and the associated power spectrum (b). The time is non-dimensionalised by the period of oscillation of the fundamental mode  $T_1 = 1/f_1$ .

The acoustic boundary layer becomes turbulent when the Reynolds number with respect to the acoustic-boundary-layer thickness exceeds 400 (Hirschberg 1997). This can increase visco-thermal dissipation considerably. The definition of this Reynolds number is:

$$Re_{\delta_{ac}} = \frac{u' \delta_{ac}}{\nu} = u' \sqrt{\frac{2}{\nu \omega}}. \quad (6.37)$$

Using the values from table 6.3 we find a Reynolds number of approximately 200 near the maximum of the pulsation in figure 6.38. This renders the transition not likely in the side branch and Kirchhoff's damping coefficient as given by (6.31) can be used with confidence.

The influence of non-linear wave steepening can be estimated by considering the wave steepening of a simple wave. The effect strongly depends on the ratio  $\sigma = x/x_s$  of the distance  $x$  travelled by the wave and the shock-formation distance  $x_s$ . Pierce (1989) derived the generation of harmonics from a sinusoidal signal  $p(0, t) = \hat{p} \sin(\omega t)$  as a function of the distance travelled by the wave. He derived the following relations for the first four harmonics:

$$\hat{p}_1 = \hat{p} \left( 1 - \frac{\sigma^2}{8} \right), \quad (6.38)$$

$$\hat{p}_2 = \hat{p} \frac{\sigma}{2}, \quad (6.39)$$

$$\hat{p}_3 = \hat{p} \frac{3\sigma^2}{8}, \quad (6.40)$$

$$\hat{p}_4 = \hat{p} \frac{\sigma^3}{3}, \quad (6.41)$$

$Str$	$u'/U_0$	$U_0$ (m/s)	$M$	$f_1$ (Hz)	$T$ (°C)
0.506	0.035	22.63	0.064930	191.00	27.50
0.484	0.062	23.78	0.068199	192.00	27.70
0.473	0.083	24.36	0.069874	192.25	27.70
0.464	0.101	24.90	0.071414	192.50	27.60
0.458	0.116	25.26	0.072454	192.75	27.60
0.456	0.121	25.36	0.072735	192.62	27.60
0.435	0.179	26.63	0.076383	193.00	27.70
0.415	0.245	27.95	0.080204	193.25	27.30
0.413	0.248	28.04	0.080458	193.25	27.50
0.391	0.334	29.66	0.085139	193.50	27.20
0.391	0.337	29.73	0.085299	193.75	27.40
0.369	0.390	31.50	0.090407	194.00	27.35
0.359	0.440	32.49	0.093294	194.25	27.00
0.358	0.442	32.54	0.093440	194.25	26.90
0.350	0.492	33.36	0.095811	194.50	26.90
0.336	0.547	34.78	0.099843	195.00	27.05
0.330	0.556	35.46	0.101866	195.25	26.75
0.309	0.543	38.00	0.109148	195.50	26.80
0.289	0.518	40.64	0.116734	195.75	26.70
0.282	0.512	41.75	0.119952	196.00	26.60
0.275	0.505	42.73	0.122754	196.00	26.70
0.255	0.443	46.26	0.132965	196.25	26.35

Table 6.3: Experimental conditions: Strouhal number  $Str = \frac{fH}{u_0}$ , acoustic amplitude  $u'/U_0$ , main flow velocity  $U_0$ , Mach number  $M = U_0/c_0$ , the fundamental frequency of the oscillation  $f_1$ , and air temperature  $T$ .

(6.42)

where  $\hat{p}$  is the amplitude of the undisturbed simple wave, and  $\sigma$  is given by:

$$\sigma = \frac{x}{x_s} = \frac{\gamma + 1}{2\gamma} kx \frac{\hat{p}}{p_0}. \quad (6.43)$$

Here  $k$  is the wave number of the undisturbed wave and  $p_0$  is the atmospheric pressure ( $\gamma p_0 = \rho_0 c_0^2$ ). It is important to recall that this description is only valid for a simple wave. In the side branch the first harmonic is a standing wave. In order to apply equations (6.38) to (6.41) to our situation, we assume that the source is generating a simple sinusoidal wave that travels up and down the side branch. While the wave propagates, higher harmonics are formed due to non-linearities and the wave is deformed slightly. The most important

effect is generation of the second harmonic. We assume that the second harmonic is formed while the wave propagates up and down the side branch, and that it is radiated away into the main pipe. The amplitude of the second harmonic is then given by equation (6.39) using  $kx = \frac{2\pi}{4L}2L = \pi$  in equation (6.43) and  $\hat{p} = \frac{1}{2}p'$ . The power that is radiated is:

$$\mathcal{P}_2 = \frac{\hat{p}_2^2}{2\rho_0 c_0}. \quad (6.44)$$

This power originates from the fundamental resonant mode. This leads to a correction on the energy balance (6.34), which becomes a quadratic equation for  $(p')^2$ :

$$\begin{aligned} \frac{\langle \mathcal{P} \rangle + \langle \mathcal{P}_{horn} \rangle}{\rho_0 U_0^3 S_p} &= \left( \frac{p'}{\frac{1}{2}\rho_0 U_0^2} \right)^2 \frac{M}{8} (\alpha_1 L_1 + \alpha_2 L_2) \\ &+ \left( \frac{p'}{\frac{1}{2}\rho_0 U_0^2} \right)^4 \left( \frac{M}{32} \right)^2 \frac{\pi^2 (\gamma + 1)^2}{8}. \end{aligned} \quad (6.45)$$

The result for  $p'$  obtained from this equation is included in figure 6.38 by means of the open circles (o). The effect of non-linear wave steepening explains about 10% of the difference between the experimental measurement and the numerical prediction. Although a more elaborate analysis is necessary to determine what the precise effect of non-linear wave steepening is in our experiments, this simple description demonstrates that it is a significant but not dominant loss mechanism for the fundamental mode.

Besides possible errors in the interpretation of the experimental results it should be noted that also the numerical method has limitations. Flow separation at the downstream (right) edge is not taken into account. Since it is expected that the second separation will result in additional dissipation of acoustic power, these limitations could explain some of the differences between the results of experiment and numerical simulation. Preliminary simulations taking into account the second separation showed that even for the high-amplitude oscillations the effect of the second separation is considerable. The second separation results typically in a 20 % reduction of the acoustic source power at these amplitudes. This would explain another 35% of the difference that we try to explain.

A preliminary study of the influence of the downstream corner was carried out by rounding the downstream corner. Experimentally it was found that rounding the downstream corner led to higher pulsation levels in the set-up. Numerically the rounding of the downstream corner has the opposite effect: a lower acoustic source power at equal acoustic amplitude. For a rounding with a radius of curvature that is 0.2 times the height of the channel, the combined effect reduces the over-prediction to 25 %.

Another cause for concern is the time-averaged pressure in the side branch. If in the experiment the pressure in the side branch is higher than the pressure in the numerical simulation, then this will affect the path of the vortex structure by tending to push it out of the side branch. This could result in a weaker interaction of the vortex structure with the downstream edge and thus in less production of acoustic energy. Awaiting experimental measurements of the time-averaged pressure in the side branch, we present numerical results

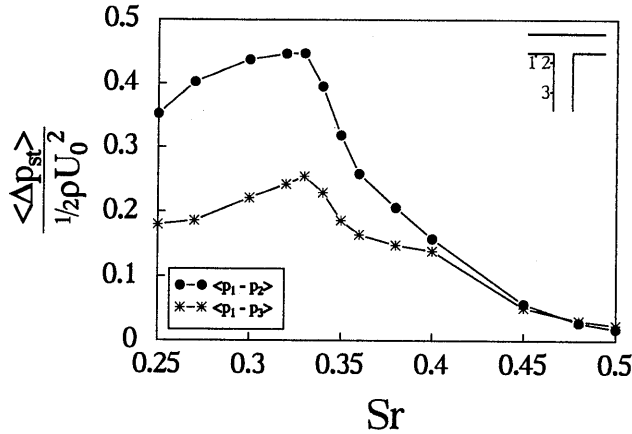


Figure 6.40: Numerical results for the time-averaged pressure in the side branch relative to a point in the upstream main branch. Point 1 is positioned at  $5H$  upstream of the side branch, point 2 at  $0.47H$  deep in the side branch, and point 3 at  $2.03H$  deep in the side branch.

for the pressure at two positions in the side branch, see figure 6.40. The first position is only  $0.47H$  deep in the side branch and here the pressure will be strongly influenced by the proximity of the vortex structure. The second position is deeper into the side branch at  $2.03H$  and here the pressure will only be influenced by the pressure difference as a result of the flow in the side branch. As is clear from figure 6.40, the time-averaged pressure in the side-branch is considerably lower than in the main pipe.

Finally we will compare the numerical results for the first three higher harmonics to the experimental results. The results for the second  $p'_2$ , third  $p'_3$ , and fourth harmonic  $p'_4$  are presented in figure 6.41. The higher harmonics have two important sources. The first one is the non-linearity of the acoustic source pressure, as demonstrated in figures 6.39(a) and 6.39(b). The second one is the non-linear wave steepening, as described by equations (6.38) to (6.41). For the non-resonant modes the resulting pressure at the end of the side branch due to the non-linear source pressure is given by (6.35). In figures 6.41(a) and 6.41(c) these results are indicated by \*. For the second harmonic this explains approximately 50% of the pressure measured at the end of the side branch. For the fourth harmonic it gives an indication for the order of magnitude of the pressure level. For the second harmonic we find that, if only non-linear wave steepening is considered, it also explains approximately 50% of the pressure level. The fourth harmonic cannot be explained by this effect. In figures 6.41(a) and 6.41(c) these results are indicated by o. Assuming that these effects can be added (constructive interference) then the resulting prediction (indicated by ●) agrees within 20% with the measured pulsation level of the second harmonic.

The third harmonic, which is resonant, is treated differently. We use equation (6.33) to estimate the pulsation level. Since for the third harmonic no acoustic source power is

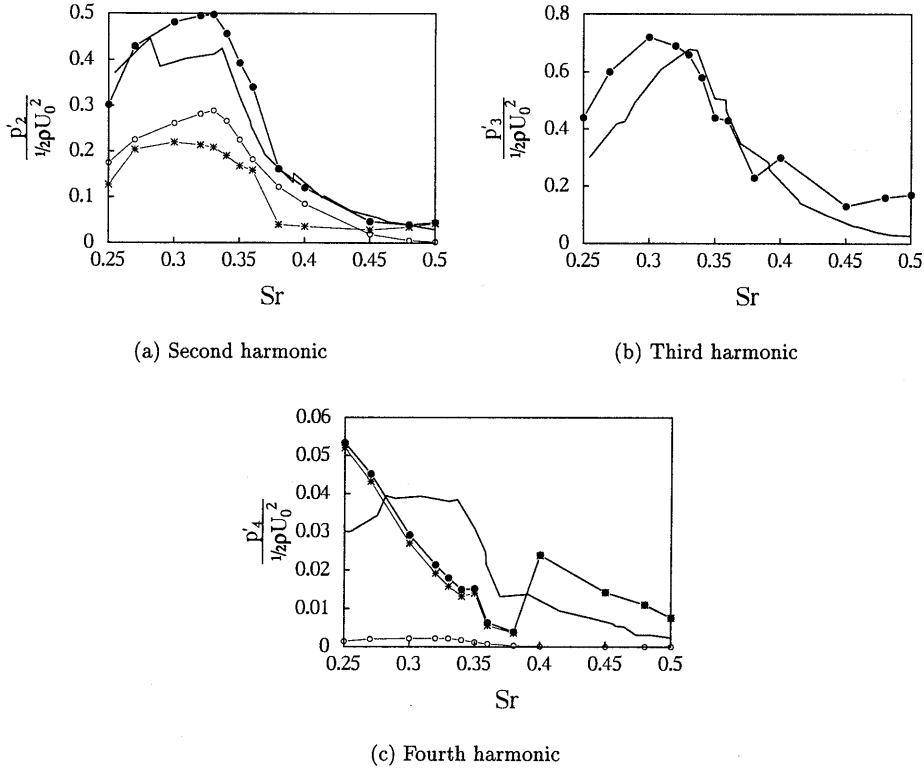


Figure 6.41: Measurements (—) and predictions of the higher harmonics. In (a) the pressure amplitude of the second harmonic is shown together with the numerical prediction (\*), the generation of the second harmonic by non-linear wave steepening (○) and the total predicted amplitude (●) assuming constructive interference. In (b) the pressure amplitude of the third harmonic is shown together with the numerical results (●) based on the energy balance using  $|R_p| = 1$  for the horn. In (c) the pressure amplitude of the fourth harmonic is shown together with the same results as in (a).

available from the numerical simulation we will use the following estimate based on the calculated source pressure for an harmonic acoustic velocity at the fundamental frequency:

$$\langle \mathcal{P}_3 \rangle = \frac{1}{2} \Delta p_{3,source} \frac{p'_3}{\rho_0 c_0}. \quad (6.46)$$

This assumes that the phase difference between the acoustic source pressure and the acoustic velocity is zero and it is therefore an upper limit estimate. The pressure reflection coefficient of the horn is assumed to be equal to 1:  $R_p = 1$ . The resulting prediction

(indicated by • in figure 6.41(b)) agrees quite well with the measurement. In order to have a better comparison additional experiments to measure the reflection coefficient and the phase difference between  $\Delta p_{3,source}$  and  $p'_3$  are necessary.

## 6.8 Concluding remarks

In this chapter we have presented our current state of the understanding of the resonances in pipe systems as caused by flow separation in T-joint configurations. Different aspects of the description of the flow through a T-joint were treated.

The quasi-steady limit was studied by using the fact that in the quasi-steady limit the acoustic source pressure is equal to the steady pressure loss. Analytical expressions have been derived for the steady total pressure loss in different flow configurations as can occur in a T-joint. In order to derive these expressions a simplified flow model was used, together with an additional closure assumption in order to solve the set of equations. Different closure assumptions are possible because they are based on a simplified interpretation of the flow. We showed the influence of different closure assumptions on the prediction of the total pressure loss. The predictions were compared to experimental measurements of Ito and Imai (1973) as well as numerical results obtained by means of the vortex-blob method. In most cases a reasonable agreement between predictions, experimental and numerical results was obtained when a single parameter is used to adjust the fit.

The vortex-blob method was used to study nine flow configurations that may occur in a T-joint with sharp edges. The most important flow configuration causing resonances is the a3-configuration with a grazing flow along a closed side branch and an acoustic flow between the closed side branch and the downstream segment of the main pipe. In our discussion of the Strouhal number dependence of the source, only flow separation at one edge was taken into account. This can be interpreted as having the other edge rounded. We showed that the effect of the second separation depends strongly on the flow configuration and that it can be neglected in some cases. The effect of rounding the upstream edge in the T-joint is discussed in (Peters & Hofmans 1998).

Although for engineering purposes one can assume a linear relationship between acoustic source power and acoustic amplitude, we demonstrated that this is not an accurate approximation. Simulations carried out with the vortex-blob method showed that at low acoustic amplitude ( $u'/U_0 = \mathcal{O}(10^{-2})$ ) the relationship between acoustic source power and acoustic amplitude is to leading order quadratic. This explains the sudden disappearance of self-sustained pulsations upon an increase of damping when this pulsation level is reached.

In order to assess the accuracy of the predictions of the vortex-blob method, numerically obtained results were compared to experimental measurements for low acoustic amplitudes ( $u'/U_0 < 0.1$ ) (Bruggeman 1987) as well as for high acoustic amplitudes ( $u'/U_0 > 0.1$ ). A balance of acoustic energy sources and acoustic energy losses was used to incorporate the numerical results. At moderately-low acoustic amplitudes the agreement between measured pressure amplitude and numerically obtained prediction of the pressure amplitude was typically within 10%. At high acoustic amplitudes the numerical prediction of the pressure

amplitude was generally too high. The over-prediction depends strongly on the acoustic amplitude and reaches a maximum value of 35% at the highest amplitudes. A part of this larger difference can be explained by additional losses due to non-linear wave steepening that need to be considered at high acoustic amplitudes. However, after correction the numerical results are still 30% too high at the highest amplitude. It is expected that this is mainly due to flow separation at the downstream edge, which has been ignored in the numerical simulation. Some questions remain concerning the time-averaged pressure in the side branch and the effect of the second separation for flow cases at high acoustic amplitudes.

## References

- BRUGGEMAN, J.C. (1987) Flow induced pulsations in pipe systems. *PhD thesis Eindhoven University of Technology*
- HIRSCHBERG, A (1997) Selsustained aeroacoustical oscillations in gas transport systems: a prediction method for pulsations induced by closed pipe segments. *Report TUE NT R-1428-D, Eindhoven University of Technology*
- HOWE, M.S. (1975) Contribution to the theory of aerodynamic sound, with application to excess jet noise and the theory of the flute. *J. Fluid Mech.* **71**, 625-673
- HOWE, M.S. (1985) On the absorption of sound by turbulence and other hydrodynamic flows. *IMA, J. Appl. Math.* **32**, 187-209
- INGARD, U. & ISING, H. (1967) Acoustic nonlinearity of an orifice. *J. Acoust. Soc. Am.* **42**, 6-17
- ITO, H. & IMAI, K. (1973) Energy losses at 90° pipe junctions. *ASCE J. Hydraulics Div.* **99**, 1353-1368
- JUNGOWSKI, W.M. & BORTOS, K.K. (1989) Damping pressure pulsations in piping systems. *U.S. Patent No. 486-71-90*
- KRIESELS, P.C, PETERS, M.C.A.M., HIRSCHBERG, A. & WIJNANDS, A.P.J. (1995) High amplitude vortex-induced pulsations in a gas transport system. *J. Sound & Vibr.* **184**, 343-368
- KRIESELS, P.C, HOFMANS, G.C.J., PETERS, M.C.A.M., & HIRSCHBERG, A. (1995) Flow-induced pulsations in pipe systems. Appeared in *Flow-induced vibration*, P.W. Bearman editor *Balkema Rotterdam*, 505-514
- NELSON, P.A., HALLIWELL, N.A. & DOAK, P.E. (1983) Fluid dynamics of flow excited resonance, part 2: theory. *J. Sound & Vibr.* **91**, 375-402

- PETERS, M.C.A.M. (1993) Aeroacoustical sources in internal flows. *PhD thesis Eindhoven University of Technology*
- PETERS, M.C.A.M. & HOFMANS, G.C.J. (1998) Flow-induced pulsations in T-joints, impact of flow-direction and edge rounding. *to be submitted*
- PIERCE, A.D. (1989) Acoustics: an introduction to its physical principles and applications. *Acoustical Society of America, New York.*
- RONNEBERGER, D. (1972) The acoustical impedance of holes in the wall of flow ducts. *J. Sound & Vibr.* **24**, 133–150
- SCHLICHTING, H. (1979) Boundary-layer theory. seventh edition *McGraw-Hill, New York*
- ZIADA, S. & BÜHLMANN, E.T. (1992) Self-excited resonances of two side-branches in close proximity. *J. Fluids & Struct.* **6**, 583–601



# General discussion, conclusions and recommendations

The present research was concerned with the study of sound production by vortices formed due to flow separation. The work was restricted to internal flows at high Reynolds number and low Mach number and focussed on two-dimensional geometries. The combined experimental, numerical, and theoretical effort has resulted in new insights that are useful for modelling of the flows for engineering purposes.

The assumption of laminar boundary layers inside the human glottis is found to be quite reasonable. Measurements of the steady pressure loss that support this assumption are presented in chapters 3 and 4. Also presented in these chapters are two-dimensional numerical simulations based on the unsteady Navier-Stokes equations that further confirm this. Experiments also show that, although the boundary layer may be laminar, turbulence in the jet flow is important.

The nature of the transition from laminar to turbulent flow observed in the experiments presented in chapter 4 is still unclear. Research to clarify this is advisable.

The implementation of a Coanda effect in a model of the flow through the glottis is not recommended for voiced sound production. Experiments show that establishing the Coanda effect takes time (see figure 4.14). A typical vocal-fold oscillation with a frequency of 100 Hz for men and 200 Hz for women does not leave enough time for the Coanda effect to set in. In section 4.2.5 pressure measurements in an asymmetric vocal-fold model are presented that confirm this.

Quasi-steady modelling is a useful engineering tool. In chapter 4 figure 4.34 it is shown that a simplified quasi-steady description of flow separation in a glottis model leads to a reasonable prediction of the pressure forces acting on the vocal folds. It must be noted, however, that in the modelling of the vocal fold oscillation there is always a short period of essentially unsteady flow just before the glottis closes.

Application of quasi-steady modelling to the flow through a diaphragm in a pipe and to the flow in a T-joint has been shown to result in accurate predictions for the low-frequency acoustic properties of these systems. For the flow through the diaphragm a good

agreement between the results obtained from the quasi-steady model and measurements at low-frequencies was found. For the flow through a T-joint results of a simplified quasi-steady model were compared to measurements in cylindrical pipes and numerical results. The agreement found was quite reasonable when a single parameter is used in order to adjust the fit.

Using the desingularisation parameter  $\delta$  in the vortex-blob method to model physical properties of a shear layer may be mathematically incorrect, the results obtained in this way are however convincingly realistic (see chapter 3). This procedure can be used in engineering applications.

Although the flow through the diaphragm and the flow in the T-joint are essentially turbulent ( $Re = 10^5$ ) the effect of turbulence is not important: using a two-dimensional inviscid numerical flow model that does not describe turbulence leads to accurate predictions of the low-frequency aeroacoustic properties of these systems (see chapters 5 and 6). Turbulence modelling is of course essential when considering broad-band noise generation.

The vortex-blob method used in the present study has been shown to be a robust and (mostly) efficient numerical method. Results were obtained for the unsteady flow through a square-edge nozzle, for an oscillatory flow through a diaphragm, and for nine configurations of the flow in a T-joint. In chapters 5 and 6 it was shown that also in the quasi-steady limit reliable results could be obtained. There were, however, also some configurations for which the vortex-blob method did not yield reliable results. The flow in the T-joint was modelled by only taking flow separation at the upstream edge into account. Modelling flow separation at the downstream edge of a T-joint led to numerical instabilities in the configuration with a steady mean flow through the main pipe. In the configurations with the steady mean flow diverted into the side branch less reliable results were obtained than for the other configurations.

In chapter 2 the concept of an acoustic analogy was introduced. In the present study a comparison was made between Howe's analogy concerning vortex sound and a pressure formulation involving an integral formulation for the total pressure distribution along the boundaries of the computational domain. Both methods have been implemented in the vortex-blob method for two-dimensional incompressible flows. Note that without an acoustic analogy it would have been impossible to extract information on the acoustic implications from the incompressible-flow model. The agreement between the two methods for computing the acoustic source power of the numerical flow solution was found to be good. In fact it was found that when these two methods did not agree an inaccurate solution of the flow field had been obtained. This allowed for an independent check on the quality of the solution obtained by the vortex-blob method.

The use of a point-vortex method for solving two-dimensional low-Mach-number, high-Reynolds-number flows is very efficient. By discretising only the vorticity field all computational effort is focussed on those areas of the flow where it is needed. This is comparable to a high degree of local mesh refinement in a grid-based method (like the Euler method). Conservation of total circulation of the flow is automatically satisfied and problems with numerical diffusion or dissipation are avoided. In a point-vortex method it is very easy to enlarge the computational domain in order to avoid spurious sound production by the

interaction of vortex structures with artificial boundaries. Furthermore, viscous effects can also be incorporated in a very natural way (see section 2.4.3) There are, however, some limitations to the use of point-vortex methods. First of all they are restricted to incompressible flows, and secondly they are restricted to two-dimensional flows. So, although the Euler method showed itself to be a slow but accurate alternative for the two point-vortex methods in chapter 3, it is the method to be used for an extension to compressible and/or three-dimensional flows.

Methods to accelerate the computation of vortex-vortex interactions are available in the form of either a multi-pole expansion of the velocity field induced by a cluster of point-vortices or a Taylor expansion of the interaction Kernel. The acceleration method based on the multi-pole expansion has been introduced by Ranucci in the viscous vortex-blob method. Results of this method are presented in chapters 3 and 4. Incorporating such an acceleration method in the inviscid vortex-blob method might result in an efficient method for large computations (number of point vortices  $> 2,000$ ). It is doubtful whether the bulk of the computations presented in the present work would have profited from these acceleration methods. However, an attempt to incorporate such a method is advisable.

As was illustrated by the results presented in chapters 3 and 4, a simplified boundary-layer model can yield quite accurate results. In order to model flow separation from curved walls in high-Reynolds-number flows ( $Re > 10^5$ ) it can therefore be useful to combine a simplified boundary-layer description with either the inviscid vortex-blob method or the Euler method. In such a case one should seek for a reasonable flow model for turbulent boundary-layer separation. In first approximation a quasi-steady flow model might be considered. However, such an approach is difficult because it is essential to solve the main flow model and the boundary-layer model simultaneously. Decoupling the two calculations leads to numerical instabilities. Unfortunately, the viscous vortex-blob method that already incorporates viscous effects is restricted by present-day computer power to Reynolds numbers less than  $10^4$ .



## Appendix A

---

# Lighthill's analogy

Taking the time derivative of the equation of conservation of mass:

$$\frac{\partial}{\partial t} \left\{ \frac{\partial \rho}{\partial t} + \frac{\partial \rho u_i}{\partial x_i} \right\} = 0 \quad (\text{A.1})$$

and the divergence of the momentum equation:

$$\frac{\partial}{\partial x_i} \left\{ \frac{\partial \rho u_i}{\partial t} + \frac{\partial \rho u_i u_j}{\partial x_j} - \frac{\partial P_{ij}}{\partial x_j} \right\}, \quad (\text{A.2})$$

then subtracting these two equations while adding on both sides the term  $-c_0^2 \frac{\partial^2 \rho'}{\partial x_i^2}$ , yields the inhomogeneous wave equation for the time-dependent density perturbation  $\rho'$ :

$$\frac{\partial^2 \rho'}{\partial t^2} - c_0^2 \frac{\partial^2 \rho'}{\partial x_i^2} = \frac{\partial^2 T_{ij}}{\partial x_i \partial x_j}, \quad (\text{A.3})$$

in which  $T_{ij} = \rho u_i u_j + P_{ij} - c_0^2 \rho' \delta_{ij}$ . This is Lighthill's wave equation and  $T_{ij}$  is called the Lighthill stress tensor. A formal solution of this equation can be found by using Green's function  $G(\vec{x}, t | \vec{y}, \tau)$  or in short notation just  $G$ :

$$G \times \left\{ \frac{\partial^2 \rho'}{\partial y_i^2} - \frac{1}{c_0^2} \frac{\partial^2 \rho'}{\partial \tau^2} = -\frac{1}{c_0^2} \frac{\partial^2 T_{ij}}{\partial y_i \partial y_j} \right\}, \quad (\text{A.4a})$$

$$\rho' \times \left\{ \frac{\partial^2 G}{\partial y_i^2} - \frac{1}{c_0^2} \frac{\partial^2 G}{\partial \tau^2} = -\delta(\vec{x} - \vec{y}) \delta(t - \tau) \right\}. \quad (\text{A.4b})$$

This leads to the following equation for  $p' (= c_0^2 \rho')$ <sup>1</sup>:

$$p'(\vec{x}, t) = \int_{-\infty}^t \iiint_V G(\vec{x}, t | \vec{y}, \tau) \frac{\partial^2 T_{ij}}{\partial y_i \partial y_j} dV(\vec{y}) d\tau$$

---

<sup>1</sup>  $d\vec{y} := dV(\vec{y})$  and  $d\vec{s} := dS(\vec{y})$  where the closed volume  $V$  is enclosed by the surface  $S$

$$\begin{aligned}
& + \int_{-\infty}^t \iiint_V \left[ \rho'(\vec{y}, \tau) \frac{\partial^2 G}{\partial \tau^2} - G \frac{\partial^2 \rho'(\vec{y}, \tau)}{\partial \tau^2} \right] dV(\vec{y}) d\tau \quad (\text{A.5}) \\
& + \int_{-\infty}^t \iiint_V \left[ G \frac{\partial^2 c_0^2 \rho'(\vec{y}, \tau)}{\partial y_i^2} - c_0^2 \rho'(\vec{y}, \tau) \frac{\partial^2 G}{\partial y_i^2} \right] dV(\vec{y}) d\tau.
\end{aligned}$$

Due to the initial condition and causality the second integral can be shown to be equal to 0. The first and the third integral will be rewritten using partial integration.

Partial integration of the first integral and integrating with respect to  $y_i$  in the third integral yields:

$$p'(\vec{x}, t) = - \int_{-\infty}^t \iiint_V \frac{\partial T_{ij}}{\partial y_j} \frac{\partial G(\vec{x}, t | \vec{y}, \tau)}{\partial y_i} dV(\vec{y}) d\tau \quad (\text{A})$$

$$+ \int_{-\infty}^t \iint_{\partial V} \frac{\partial T_{ij}}{\partial y_j} n_i G(\vec{x}, t | \vec{y}, \tau) dS(\vec{y}) d\tau \quad (\text{B})$$

$$+ \int_{-\infty}^t \iint_{\partial V} \vec{\nabla} (c_0^2 \rho') G(\vec{x}, t | \vec{y}, \tau) \cdot \vec{n} dS(\vec{y}) d\tau \quad (\text{C})$$

$$- \int_{-\infty}^t \iint_{\partial V} c_0^2 \rho' \vec{\nabla} G(\vec{x}, t | \vec{y}, \tau) \cdot \vec{n} dS(\vec{y}) d\tau. \quad (\text{D})$$

We will now introduce  $T'_{ij} = T_{ij} - \rho_0 u_i u_j$  so that:

$$\frac{\partial T'_{ij}}{\partial y_j} = \frac{\partial T_{ij}}{\partial y_j} + \rho_0 u_i (\vec{\nabla} \cdot \vec{u}) + \rho_0 (\vec{\omega} \times \vec{u})_i + \frac{\partial}{\partial y_i} \left( \frac{1}{2} \rho_0 |\vec{u}|^2 \right).$$

Integral (A) is then rewritten as:

$$(\text{A}) = - \int_{-\infty}^t \iiint_V \rho_0 (\vec{\omega} \times \vec{u}) \cdot \vec{\nabla} G dV(\vec{y}) d\tau \quad (\text{E})$$

$$- \int_{-\infty}^t \iiint_V \rho_0 \vec{u} (\vec{\nabla} \cdot \vec{u}) \cdot \vec{\nabla} G dV(\vec{y}) d\tau \quad (\text{F})$$

$$- \int_{-\infty}^t \iiint_V \frac{\partial T'_{ij}}{\partial y_j} \frac{\partial G(\vec{x}, t | \vec{y}, \tau)}{\partial y_i} dV(\vec{y}) d\tau \quad (\text{G})$$

$$- \int_{-\infty}^t \iiint_V \vec{\nabla} \left( \frac{1}{2} \rho_0 |\vec{u}|^2 \right) \cdot \vec{\nabla} G dV(\vec{y}) d\tau. \quad (\text{H})$$

By partial integration integral (G) is rewritten as:

$$(G) = - \int_{-\infty}^t \iint_{\partial V} T'_{ij} \frac{\partial G(\vec{x}, t|\vec{y}, \tau)}{\partial y_i} n_j dS(\vec{y}) d\tau \quad (I)$$

$$+ \int_{-\infty}^t \iiint_V T'_{ij} \frac{\partial^2 G(\vec{x}, t|\vec{y}, \tau)}{\partial y_i \partial y_j} dV(\vec{y}) d\tau. \quad (J)$$

By partial integration integral (H) is rewritten as:

$$(H) = - \int_{-\infty}^t \iint_{\partial V} \left( \frac{1}{2} \rho_0 |\vec{u}|^2 \right) \vec{\nabla} G(\vec{x}, t|\vec{y}, \tau) \cdot \vec{n} dS(\vec{y}) d\tau \quad (K)$$

$$+ \int_{-\infty}^t \iiint_V \frac{1}{2} \rho_0 |\vec{u}|^2 \nabla^2 G(\vec{x}, t|\vec{y}, \tau) dV(\vec{y}) d\tau. \quad (L)$$

Using the defining equation (A.4b) for  $G(\vec{x}, t|\vec{y}, \tau)$  integral (L) can be written as:

$$(L) = \int_{-\infty}^t \iiint_V \frac{1}{2} \rho_0 |\vec{u}|^2 \left[ -\delta(\vec{x} - \vec{y}) \delta(t - \tau) + \frac{1}{c_0^2} \frac{\partial^2 G}{\partial \tau^2} \right] dV(\vec{y}) d\tau$$

$$= -\frac{1}{2} \rho_0 |\vec{u}|^2 + \int_{-\infty}^t \iiint_V \frac{1}{2} \rho_0 |\vec{u}|^2 \frac{1}{c_0^2} \frac{\partial^2 G}{\partial \tau^2} dV(\vec{y}) d\tau.$$

Now we take similar terms together: integrals (E) + (F) + (J) + (L) yield a volume integral, integrals (B) + (C) yield a surface integral containing  $G(\vec{x}, t|\vec{y}, \tau)$  and (D) + (I) + (K) yield a surface integral containing  $\frac{\partial G}{\partial y_i}$ . Together with the momentum equation we then obtain the following expression for the acoustic pressure:

$$p'(\vec{x}, t) + \frac{1}{2} \rho_0 |\vec{u}|^2 = \int_{-\infty}^t \iiint_V \left[ -\rho_0 (\vec{\omega} \times \vec{u}) \cdot \vec{\nabla} G + \right. \\ \left. - \rho_0 \vec{u} (\vec{\nabla} \cdot \vec{u}) \cdot \vec{\nabla} G + T'_{ij} \frac{\partial^2 G}{\partial y_i \partial y_j} + \frac{1}{2} \rho_0 |\vec{u}|^2 \frac{1}{c_0^2} \frac{\partial^2 G}{\partial \tau^2} \right] dV(\vec{y}) d\tau \\ - \int_{-\infty}^t \iint_{\partial V} \frac{\partial \rho \vec{u}}{\partial \tau} \cdot \vec{n} G(\vec{x}, t|\vec{y}, \tau) dS(\vec{y}) d\tau \\ - \int_{-\infty}^t \iint_{\partial V} \left[ P_{ij} + \frac{1}{2} \rho_0 |\vec{u}|^2 \delta_{ij} + (\rho - \rho_0) u_i u_j \right] \frac{\partial G}{\partial y_i} n_j dS(\vec{y}) d\tau. \quad (A.6)$$

## Appendix B

---

### Pressure measurements

In order to check the present pressure measurements against boundary-layer calculations we used the square-edge-nozzle model for a comparison. This model is a constriction followed by a short straight channel (length 10 mm) that is terminated by a square edge so that the separation point is fixed (see figure B.1 for a drawing). The pressure was measured at two positions: one 8 mm upstream of the start of the constriction ( $p_1$ ) in the cylindrical pipe, and one 5 mm upstream of the square edge ( $p_2$ ) inside the nozzle channel. Note that the pressure is measured relative to a reference pressure. In our case the reference pressure is taken to be the pressure in the experiment room. The first transducer (PCB 116A) is mounted flush in the side wall of the cylindrical pipe, while the second transducer (PCB 116A) is mounted inside one of the blocks forming the constriction. This transducer (PCB 116A) measured the pressure inside the nozzle channel by means of a slit-like pressure tap (0.3 mm  $\times$  25 mm) across the channel. But once we found out that the steady pressure measurements were affected by the slit-like pressure tap, we switched to a much smaller

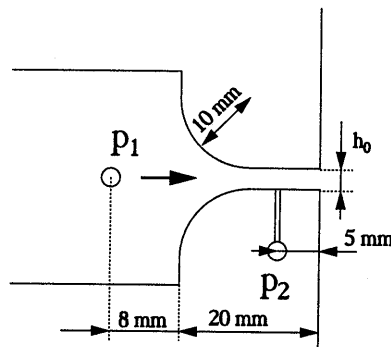


Figure B.1: Schematic of the square-edge nozzle geometry. The air flow is from left to right.



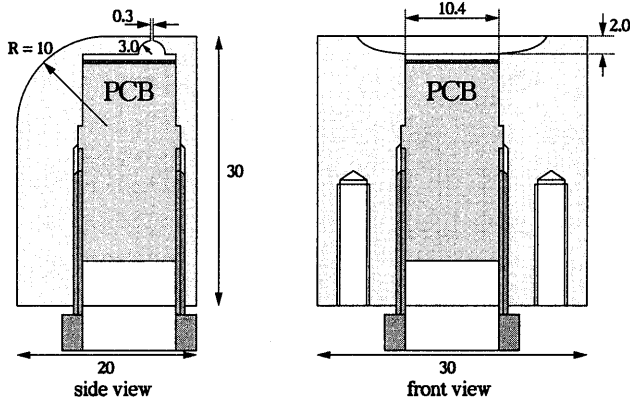


Figure B.2: Mounting of the PCB pressure transducer inside on of the blocks that form the constriction.

pressure transducer that measured the pressure inside the nozzle channel by means of a small round pressure tap (diameter 0.4 mm).

In figure B.2 the mounting of the PCB pressure transducer is shown. Because of the large size of this transducer (diameter 10.4 mm) a large pressure tap is necessary to ensure a fast response. This was achieved by making a slit-shaped tap across the width of the channel. The tap is 0.3 mm wide in stream-wise direction and approximately 25 mm long in the direction across the channel. In figure B.3 the mounting of the much smaller Kulite

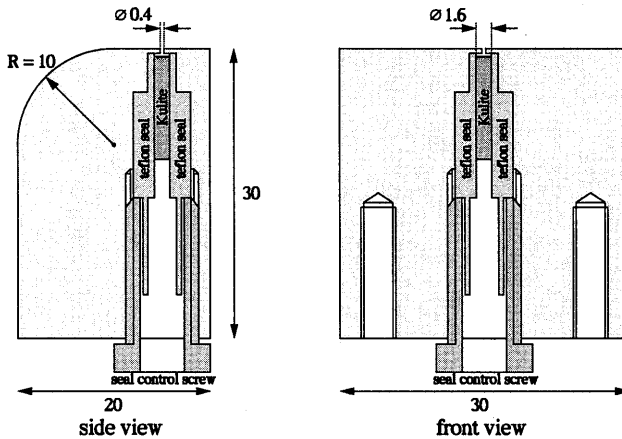


Figure B.3: Mounting of the Kulite pressure transducer inside on of the blocks that form the constriction.

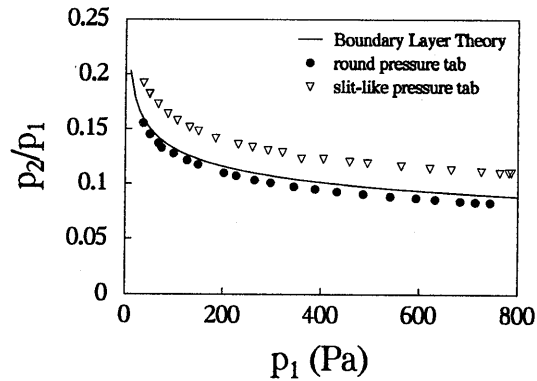


Figure B.4: Results of steady-flow pressure measurements for  $h_0 = 0.985$  mm, comparing two kinds of pressure tap: a small round tap ( $\varnothing 0.4$  mm) and a slit ( $0.3$  mm  $\times$  25 mm).

pressure transducer (diameter 1.6 mm) is shown. In this case the pressure tap is round with a diameter of 0.4 mm.

In the steady-flow measurements the PCB transducer and the Kulite transducer were replaced by “dummy” models that allowed a Betz micro manometer (accuracy 0.5 Pa) to be connected to the pressure taps so that accurate pressure measurements would be possible. The measured pressure ratio  $p_2/p_1$  as a function of the applied pressure  $p_1$  is compared to a simplified boundary-layer calculation. The boundary-layer calculation is based on a simplified Pohlhausen model using a linear velocity profile in the boundary layer and assuming a one-dimensional main-flow description (Van Zon 1989). This model is only

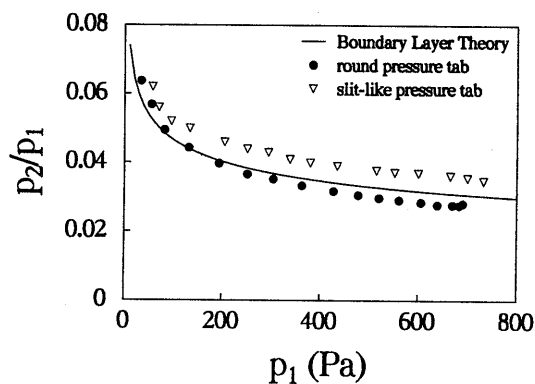


Figure B.5: Results of steady-flow pressure measurements for  $h_0 = 3.35$  mm, comparing two kinds of pressure tap: a small round tap ( $\varnothing 0.4$  mm) and a slit ( $0.3$  mm  $\times$  25 mm).

applicable to a non-separating boundary layer. Although crude it yields very reasonable results in the case of a high-Reynolds-number channel flow.

In figures B.4 and B.5 results are shown for two values of the nozzle height  $h_0$ . It is clear from these figures that the measurements with the round tap agree much better with the boundary-layer theory. The measured ratio is about 20% too high in case the slit-shaped pressure tap is used.

Although literature is available on the influence of round pressure taps on the accuracy of steady-flow pressure measurements (Shaw 1960, Franklin & Wallace 1970, Ower & Pankhurst 1977, Cummings 1996), nothing was found on the influence of slit-shaped pressure taps. Considering the information available on round pressure taps and the agreement between results of the boundary-layer calculation and results of the measurements using the round tap, we do not expect a large influence of the round tap used in the experiments on the pressure measurement.

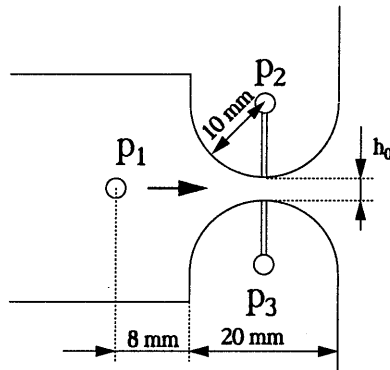


Figure B.6: Schematic of the round lip-like geometry. The air flow is from left to right.

After finding the large discrepancy for the square-edge nozzle geometry we also performed similar experiments using semi-cylindrical models as a constriction (see figure B.6). Again the pressure  $p_1$  is measured 8 mm upstream of the constriction, and pressures  $p_2$  and  $p_3$  are measured at the constriction in the upper part and the lower part of the geometry, respectively.

Measuring pressures  $p_2$  and  $p_3$  using both a slit-like pressure tap and a round pressure tap, we obtained the results as shown in figures B.7, B.8, and B.9 for three values of the throat height  $h_0$ . Note that in these cases the pressures measured using a slit-like tap are approximately 20% lower than the pressures measured using a round tap. So the sign of the difference between slit-like tap and round tap has changed with respect to the square-edge geometry.

In an attempt to solve these problems a new pressure tap was positioned in the side wall of the channel to be used with a PCB transducer. Under the assumption that a small hole (diameter 1 mm) in the side would be much less of a problem than a slit across the

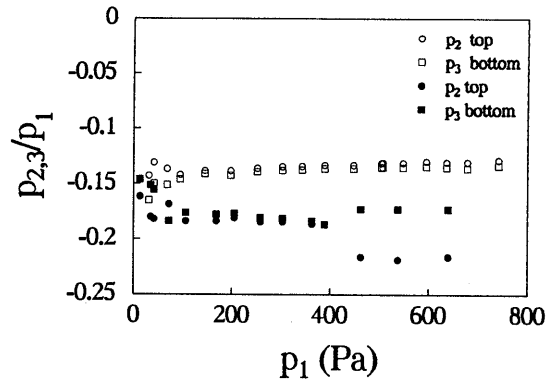


Figure B.7: Pressure ratio in the straight channel as a function of the pressure difference applied across the round geometry for different pressure taps. The channel height  $h_0 = 0.98$  mm, round tap:  $\circ$ ,  $\square$ ; slit-like tap:  $\bullet$ ,  $\blacksquare$ . Note the asymmetric result for  $p_1 > 400$  Pa in the case of the slit-like pressure tap.

whole width of the channel (cross-stream width is 30 mm) new experiments were carried out. Pressure measurement in the side wall of the channel turned out to be impossible; the values measured were always (close to) zero. The only possible explanation we found is that the connection of the upstream cylindrical pipe to the rectangular channel results in a small area of separated flow along the side walls of the channel. This was confirmed by a measurement of the cross-stream velocity profile just outside the square-edge nozzle

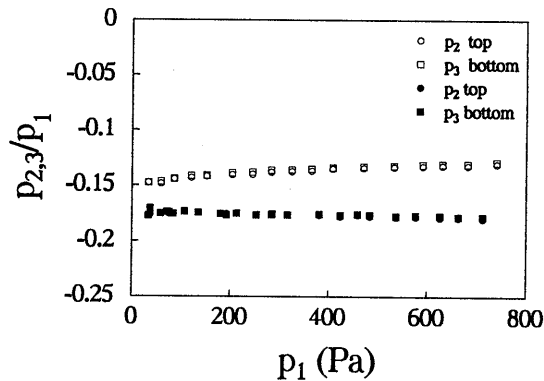


Figure B.8: Pressure ratio in the straight channel as a function of the pressure difference applied across the round geometry for different pressure taps. The channel height  $h_0 = 2.16$  mm, round tap:  $\circ$ ,  $\square$ ; slit-like tap:  $\bullet$ ,  $\blacksquare$ .

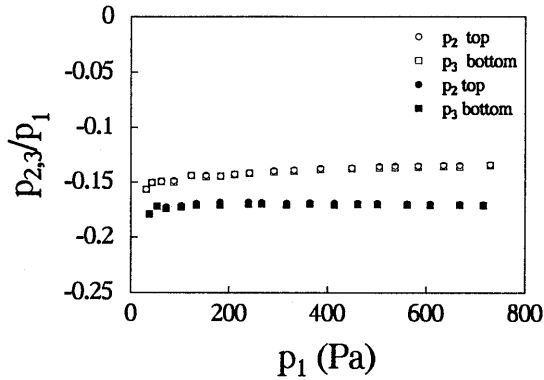


Figure B.9: Pressure ratio in the straight channel as a function of the pressure difference applied across the round geometry for different pressure taps. The channel height  $h_0 = 3.35$  mm, round tap:  $\circ, \square$ ; slit-like tap:  $\bullet, \blacksquare$ .

channel as presented in figure B.10.

The solution to the problem was to switch from the PCB transducer to the Kulite transducer. Using such a small transducer it is very important to have a good seal of the cavity in which the transducer actually measures the pressure: considering the surface area of the tap ( $0.126 \text{ mm}^2$ ) and the diameter of the transducer ( $1.6 \text{ mm}$ ) one can derive that a leak of  $0.025 \text{ mm}$  wide around the transducer creates a leak with a surface area that is equal to that of the pressure tap. A good seal was achieved by forcing a deformable Teflon

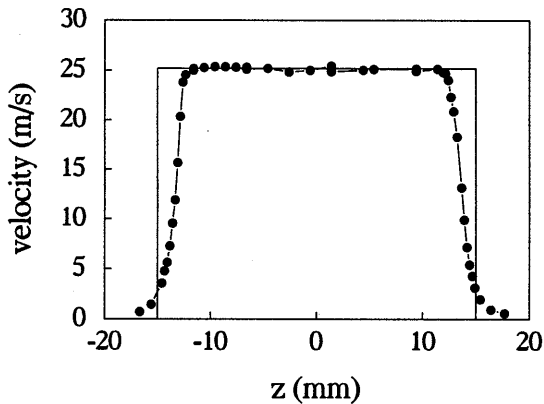


Figure B.10: Velocity profile measured across the width of the channel. Note the (relatively) large areas of low velocity near the side walls.

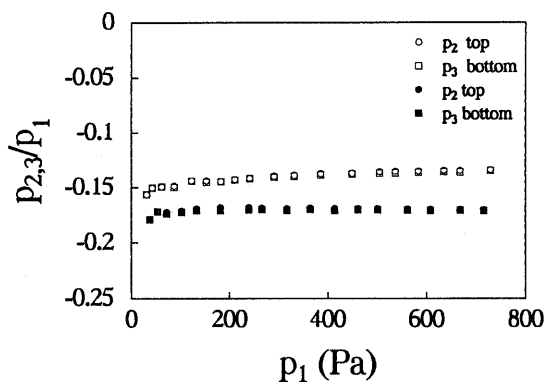


Figure B.9: Pressure ratio in the straight channel as a function of the pressure difference applied across the round geometry for different pressure taps. The channel height  $h_0 = 3.35$  mm, round tap:  $\circ$ ,  $\square$ ; slit-like tap:  $\bullet$ ,  $\blacksquare$ .

channel as presented in figure B.10.

The solution to the problem was to switch from the PCB transducer to the Kulite transducer. Using such a small transducer it is very important to have a good seal of the cavity in which the transducer actually measures the pressure: considering the surface area of the tap ( $0.126$  mm<sup>2</sup>) and the diameter of the transducer ( $1.6$  mm) one can derive that a leak of  $0.025$  mm wide around the transducer creates a leak with a surface area that is equal to that of the pressure tap. A good seal was achieved by forcing a deformable Teflon

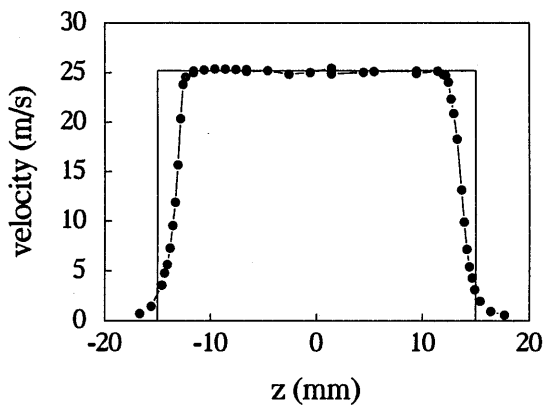


Figure B.10: Velocity profile measured across the width of the channel. Note the (relatively) large areas of low velocity near the side walls.

## Appendix C

---

# Aspects of the inviscid vortex-blob method

Typical values of the parameters used in the numerical simulations with the inviscid vortex-blob method are presented for the three types of flow that have been studied in this thesis. The parameters given below are the desingularisation parameter  $\delta$ , the time step  $\Delta t$ , as well as the smallest panel size  $L_{min}$  and the largest panel size  $L_{max}$  specified. The values are given in non-dimensional form based on a reference length scale and a reference velocity.

For the desingularisation to act efficiently, it is necessary that within a distance from a vortex-blob position equal to  $\delta$ , there should be at least a few other blobs present. This means that the value of  $\delta$  has to be related to the value of  $\Delta t$ . Furthermore, also the sizes of the panels cannot be chosen completely independently since the generation of vorticity is determined by the representation of the flow near the separation point. The minimum panel length  $L_{min}$  given below represents the size of the panels at the sharp corner at which flow separation is specified. The maximum panel length  $L_{max}$  is usually equal to the typical panel size used for the representation of those parts of the geometry where the solution of the flow does not change rapidly, such as the straight pipes of the T-joint configuration. The values given below indicate the relationship between the different numerical input parameters for each geometry considered. A useful guideline should be that when one parameter is changed by an order of magnitude than all other parameters should be changed a similar way.

Because of the coupling of the numerical parameters it was not feasible to perform an extensive study of the convergence of the solution for each parameter. The typical accuracy that was found in the comparison between the numerical results and the experimental results was 10 %. This agrees with the accuracy which we set to achieve with our numerical results. It was found that in most cases halving the value of the parameters presented below resulted in a change of only a few percent in the acoustic properties such as acoustic source power and acoustic source pressure. Doubling of the value of the parameters, on the other hand, led to changes in the acoustic properties of the order of 40 %. This indicates a reasonable convergence of the numerical solution.

## Appendix C

---

# Aspects of the inviscid vortex-blob method

Typical values of the parameters used in the numerical simulations with the inviscid vortex-blob method are presented for the three types of flow that have been studied in this thesis. The parameters given below are the desingularisation parameter  $\delta$ , the time step  $\Delta t$ , as well as the smallest panel size  $L_{min}$  and the largest panel size  $L_{max}$  specified. The values are given in non-dimensional form based on a reference length scale and a reference velocity.

For the desingularisation to act efficiently, it is necessary that within a distance from a vortex-blob position equal to  $\delta$ , there should be at least a few other blobs present. This means that the value of  $\delta$  has to be related to the value of  $\Delta t$ . Furthermore, also the sizes of the panels cannot be chosen completely independently since the generation of vorticity is determined by the representation of the flow near the separation point. The minimum panel length  $L_{min}$  given below represents the size of the panels at the sharp corner at which flow separation is specified. The maximum panel length  $L_{max}$  is usually equal to the typical panel size used for the representation of those parts of the geometry where the solution of the flow does not change rapidly, such as the straight pipes of the T-joint configuration. The values given below indicate the relationship between the different numerical input parameters for each geometry considered. A useful guideline should be that when one parameter is changed by an order of magnitude than all other parameters should be changed a similar way.

Because of the coupling of the numerical parameters it was not feasible to perform an extensive study of the convergence of the solution for each parameter. The typical accuracy that was found in the comparison between the numerical results and the experimental results was 10 %. This agrees with the accuracy which we set to achieve with our numerical results. It was found that in most cases halving the value of the parameters presented below resulted in a change of only a few percent in the acoustic properties such as acoustic source power and acoustic source pressure. Doubling of the value of the parameters, on the other hand, led to changes in the acoustic properties of the order of 40 %. This indicates a reasonable convergence of the numerical solution.



## Flow in the T-joint

The reference length scale is determined by the height of the main pipe, while the reference velocity is determined by the mean flow velocity through the system.

parameter	typical value
$\delta$	0.1
$\Delta t$	0.01
$L_{min}$	0.002
$L_{max}$	0.1

## Appendix D

---

# Scattering matrix for the compressible-flow model

The set of equations (5.12) to (5.17) can be written in linearised form. After elimination of  $u'_j$  the first order terms left are:

$$\rho'_1 u_1 + \rho_1 u'_1 = \rho'_2 u_2 + \rho_2 u'_2,$$

$$u_1 u'_1 + \frac{\gamma}{\gamma-1} \frac{p_1}{\rho_1} \left( \frac{p'_1}{p_1} - \frac{\rho'_1}{\rho_1} \right) = \frac{\mathcal{S}^2 \rho_1^2 u_1^2}{\rho_j^2} \left( \frac{\rho'_1}{\rho_1} + \frac{u'_1}{u_1} - \frac{\rho'_j}{\rho_j} \right) + \frac{\gamma}{\gamma-1} \frac{p_j}{\rho_j} \left( \frac{p'_j}{p_j} - \frac{\rho'_j}{\rho_j} \right),$$

$$u_1 u'_1 + \frac{\gamma}{\gamma-1} \frac{p_1}{\rho_1} \left( \frac{p'_1}{p_1} - \frac{\rho'_1}{\rho_1} \right) = u_2 u'_2 + \frac{\gamma}{\gamma-1} \frac{p_2}{\rho_2} \left( \frac{p'_2}{p_2} - \frac{\rho'_2}{\rho_2} \right),$$

$$p'_j + \rho'_j \frac{\mathcal{S} \rho_1^2 u_1^2}{\rho_j^2} + 2 \rho_j \frac{\mathcal{S} \rho_1^2 u_1^2}{\rho_j^2} \left( \frac{\rho'_1}{\rho_1} + \frac{u'_1}{u_1} - \frac{\rho'_j}{\rho_j} \right) = p'_2 + \rho'_2 u_2^2 + 2 \rho_2 u_2 u'_2,$$

$$\frac{p_1}{p_j} \left( \frac{p'_1}{p_1} - \frac{p'_j}{p_j} \right) = \left( \frac{\rho_1}{\rho_j} \right)^\gamma \left( \gamma \frac{\rho'_1}{\rho_1} - \gamma \frac{\rho'_j}{\rho_j} \right).$$

In these equations we substitute:

$$\begin{aligned} p'_1 &= p_1^+ + p_1^-, & u'_1 &= \frac{p_1^+ - p_1^-}{\rho_1 c_1}, & \rho'_1 &= \frac{p_1^+ + p_1^- + \sigma_1}{c_1^2}, \\ p'_2 &= p_2^+ + p_2^-, & u'_2 &= \frac{p_2^+ - p_2^-}{\rho_2 c_2}, & \rho'_2 &= \frac{p_2^+ + p_2^- + \sigma_2}{c_2^2}, \\ & & & & \rho'_j &= \frac{p'_j + \sigma_j}{c_j^2}. \end{aligned}$$

which results in 5 equations for 8 unknowns:  $p_1^+$ ,  $p_1^-$ ,  $p_j'$ ,  $p_2^+$ ,  $p_2^-$ ,  $\sigma_1$ ,  $\sigma_j$ , and  $\sigma_2$ . This leads to the following matrix representation.

$$\begin{bmatrix} 1 & -1 & M_1 & 0 & 0 \\ 1-S^2\wp_{1j}^2M_1 & 1+S^2\wp_{1j}^2M_1 & -\frac{1}{\gamma-1}-S^2\wp_{1j}^2M_1^2 & -\wp_{1j}+S^2\wp_{1j}^{\gamma+2}M_1^2 & \frac{\gamma}{\gamma-1}\wp_{1j} \\ 1 & 1 & -\frac{1}{\gamma-1} & 0 & 0 \\ 2S\wp_{1j}M_1 & -2S\wp_{1j}M_1 & 2S\wp_{1j}M_1^2 & 1-S\wp_{1j}^{\gamma+1}M_1^2 & -1 \\ 0 & 0 & \wp_{1j}^{-\gamma} & 0 & -1 \end{bmatrix} \begin{bmatrix} (1+M_1)p_1^+ \\ (1-M_1)p_1^- \\ \sigma_1 \\ p_j'+\sigma_j \\ \sigma_j \end{bmatrix} \\ = \begin{bmatrix} \frac{\gamma-1}{\wp_{12}^{\frac{\gamma-1}{2}}} & -\frac{\gamma-1}{\wp_{12}^{\frac{\gamma-1}{2}}} & \frac{\gamma-1}{\wp_{12}^{\frac{\gamma-1}{2}}}M_2 \\ 0 & 0 & 0 \\ \wp_{12} & \wp_{12} & -\frac{1}{\gamma-1}\wp_{12} \\ 1+M_2 & 1-M_2 & M_2^2 \\ 0 & 0 & 0 \end{bmatrix} \begin{bmatrix} (1+M_2)p_2^+ \\ (1-M_2)p_2^- \\ \sigma_2 \end{bmatrix}.$$

This can be reduced to:

$$\begin{bmatrix} 1 & -1 & M_1 \\ 1 & 1 & -\frac{1}{\gamma-1} \\ C_1 & C_2 & C_3 \end{bmatrix} \begin{bmatrix} (1+M_1)p_1^+ \\ (1-M_1)p_1^- \\ \sigma_1 \end{bmatrix} = \begin{bmatrix} \frac{\gamma-1}{\wp_{12}^{\frac{\gamma-1}{2}}} & -\frac{\gamma-1}{\wp_{12}^{\frac{\gamma-1}{2}}} & \frac{\gamma-1}{\wp_{12}^{\frac{\gamma-1}{2}}}M_2 \\ \wp_{12} & \wp_{12} & -\frac{1}{\gamma-1}\wp_{12} \\ 1+M_2 & 1-M_2 & M_2^2 \end{bmatrix} \begin{bmatrix} (1+M_2)p_2^+ \\ (1-M_2)p_2^- \\ \sigma_2 \end{bmatrix}.$$

The new constants that are introduced are defined by:

$$\begin{aligned} A_1 &= S^2\wp_{1j}^2M_1, \\ A_2 &= -\frac{1}{\gamma-1} - S^2\wp_{1j}^2M_1^2 + \frac{\gamma}{\gamma-1}\wp_{1j}^{1-\gamma}, \\ A_3 &= -\wp_{1j} + S^2\wp_{1j}^{\gamma+2}M_1^2, \\ B_1 &= 2S\wp_{1j}M_1, \\ B_2 &= 2S\wp_{1j}M_1^2 - \wp_{1j}^{-\gamma}, \\ B_3 &= 1 - S\wp_{1j}^{\gamma+1}M_1^2, \\ C_1 &= B_1 - (1-A_1)\frac{B_3}{A_3}, \\ C_2 &= -B_1 - (1+A_1)\frac{B_3}{A_3}, \\ C_3 &= B_2 - A_2\frac{B_3}{A_3}. \end{aligned}$$

These equations can be rearranged so that the outgoing waves are on the left and the incoming waves are on the right:

$$\begin{bmatrix} \frac{\gamma-1}{\wp_{12}^{\frac{\gamma-1}{2}}} & 1 & \frac{\gamma-1}{\wp_{12}^{\frac{\gamma-1}{2}}}M_2 \\ \wp_{12} & -1 & -\frac{1}{\gamma-1}\wp_{12} \\ 1+M_2 & -C_2 & M_2^2 \end{bmatrix} \begin{bmatrix} (1+M_2)p_2^+ \\ (1-M_2)p_2^- \\ \sigma_2 \end{bmatrix} = \begin{bmatrix} 1 & \frac{\gamma-1}{\wp_{12}^{\frac{\gamma-1}{2}}} & M_1 \\ 1 & -\wp_{12} & -\frac{1}{\gamma-1} \\ C_1 & -1+M_2 & C_3 \end{bmatrix} \begin{bmatrix} (1+M_1)p_1^+ \\ (1-M_2)p_2^- \\ \sigma_1 \end{bmatrix}.$$

which results in 5 equations for 8 unknowns:  $p_1^+$ ,  $p_1^-$ ,  $p_j'$ ,  $p_2^+$ ,  $p_2^-$ ,  $\sigma_1$ ,  $\sigma_j$ , and  $\sigma_2$ . This leads to the following matrix representation.

$$\begin{aligned} & \begin{bmatrix} 1 & -1 & M_1 & 0 & 0 \\ 1-S^2\varphi_{1j}^2M_1 & 1+S^2\varphi_{1j}^2M_1 & -\frac{1}{\gamma-1}S^2\varphi_{1j}^2M_1^2 & -\varphi_{1j}+S^2\varphi_{1j}^{\gamma+2}M_1^2 & \frac{\gamma}{\gamma-1}\varphi_{1j} \\ 1 & 1 & -\frac{1}{\gamma-1} & 0 & 0 \\ 2S\varphi_{1j}M_1 & -2S\varphi_{1j}M_1 & 2S\varphi_{1j}M_1^2 & 1-S\varphi_{1j}^{\gamma+1}M_1^2 & -1 \\ 0 & 0 & \varphi_{1j}^{-\gamma} & 0 & -1 \end{bmatrix} \begin{bmatrix} (1+M_1)p_1^+ \\ (1-M_1)p_1^- \\ \sigma_1 \\ p_j'+\sigma_j \\ \sigma_j \end{bmatrix} \\ & = \begin{bmatrix} \frac{\gamma-1}{\varphi_{12}^2} & -\frac{\gamma-1}{\varphi_{12}^2} & \frac{\gamma-1}{\varphi_{12}^2}M_2 \\ 0 & 0 & 0 \\ \varphi_{12} & \varphi_{12} & -\frac{1}{\gamma-1}\varphi_{12} \\ 1+M_2 & 1-M_2 & M_2^2 \\ 0 & 0 & 0 \end{bmatrix} \begin{bmatrix} (1+M_2)p_2^+ \\ (1-M_2)p_2^- \\ \sigma_2 \end{bmatrix}. \end{aligned}$$

This can be reduced to:

$$\begin{bmatrix} 1 & -1 & M_1 \\ 1 & 1 & -\frac{1}{\gamma-1} \\ C_1 & C_2 & C_3 \end{bmatrix} \begin{bmatrix} (1+M_1)p_1^+ \\ (1-M_1)p_1^- \\ \sigma_1 \end{bmatrix} = \begin{bmatrix} \frac{\gamma-1}{\varphi_{12}^2} & -\frac{\gamma-1}{\varphi_{12}^2} & \frac{\gamma-1}{\varphi_{12}^2}M_2 \\ \varphi_{12} & \varphi_{12} & -\frac{1}{\gamma-1}\varphi_{12} \\ 1+M_2 & 1-M_2 & M_2^2 \end{bmatrix} \begin{bmatrix} (1+M_2)p_2^+ \\ (1-M_2)p_2^- \\ \sigma_2 \end{bmatrix}.$$

The new constants that are introduced are defined by:

$$\begin{aligned} A_1 &= S^2\varphi_{1j}^2M_1, \\ A_2 &= -\frac{1}{\gamma-1} - S^2\varphi_{1j}^2M_1^2 + \frac{\gamma}{\gamma-1}\varphi_{1j}^{1-\gamma}, \\ A_3 &= -\varphi_{1j} + S^2\varphi_{1j}^{\gamma+2}M_1^2, \\ B_1 &= 2S\varphi_{1j}M_1, \\ B_2 &= 2S\varphi_{1j}M_1^2 - \varphi_{1j}^{-\gamma}, \\ B_3 &= 1 - S\varphi_{1j}^{\gamma+1}M_1^2, \\ C_1 &= B_1 - (1 - A_1)\frac{B_3}{A_3}, \\ C_2 &= -B_1 - (1 + A_1)\frac{B_3}{A_3}, \\ C_3 &= B_2 - A_2\frac{B_3}{A_3}. \end{aligned}$$

These equations can be rearranged so that the outgoing waves are on the left and the incoming waves are on the right:

$$\begin{bmatrix} \frac{\gamma-1}{\varphi_{12}^2} & 1 & \frac{\gamma-1}{\varphi_{12}^2}M_2 \\ \varphi_{12} & -1 & -\frac{1}{\gamma-1}\varphi_{12} \\ 1+M_2 & -C_2 & M_2^2 \end{bmatrix} \begin{bmatrix} (1+M_2)p_2^+ \\ (1-M_2)p_2^- \\ \sigma_2 \end{bmatrix} = \begin{bmatrix} 1 & \frac{\gamma-1}{\varphi_{12}^2} & M_1 \\ 1 & -\varphi_{12} & -\frac{1}{\gamma-1} \\ C_1 & -1+M_2 & C_3 \end{bmatrix} \begin{bmatrix} (1+M_1)p_1^+ \\ (1-M_2)p_2^- \\ \sigma_1 \end{bmatrix}.$$

## Appendix E

---

# The vena contracta in the Borda mouthpiece

The Borda mouthpiece is a configuration for which simple analytical expressions can be found for the contraction ratio  $\Upsilon$  as a function of Mach number or surface area ratio. The Borda mouthpiece is a long narrow tube that extends into a large vessel as shown in figure E.1 (Prandtl and Tietjens 1934). For the two configurations shown it is assumed that the length of the tube is much larger than the diameter of the tube. In that case it is possible to apply a momentum balance in the  $x$ -direction along the boundary shown in figure E.1 (Sears 1954).

In the configuration on the left in figure E.1 the flow is exiting through the tube. Because the flow is separating at the sharp corners of the tube, a jet is formed in the tube with a cross-sectional area  $S_j$  smaller than the tube cross-sectional area  $S_d$ . Outside of the tube, in the reservoir the flow is approximately radially towards the tube entrance. At a distance larger than the tube diameter the velocity drops off rapidly to zero. Assuming a steady flow, a reservoir pressure  $p_0$  in the far field away from the tube, and a pressure  $p_j$  in the jet region, then the integral balance of the  $x$ -component of the momentum in the

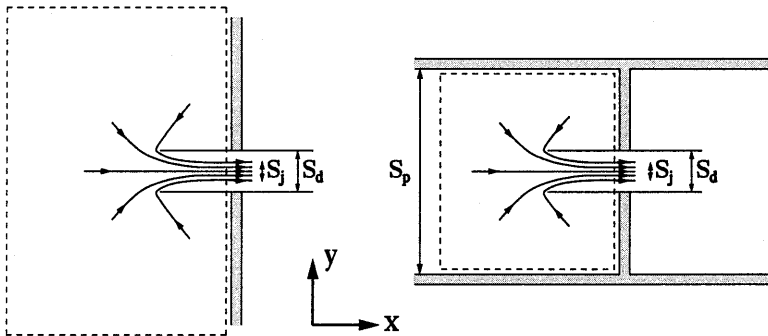


Figure E.1: Borda mouthpiece (left) and Borda mouthpiece in a vessel (right).

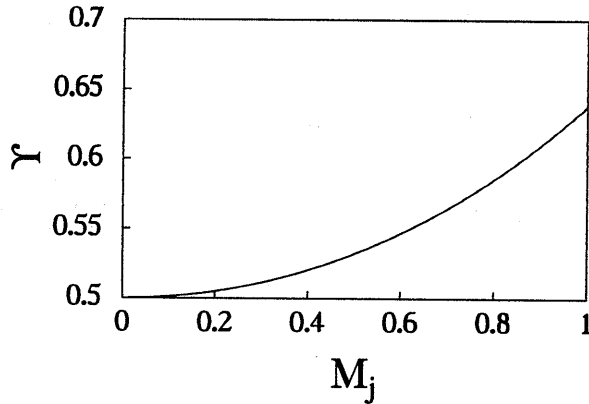


Figure E.2: Contraction ratio  $\Upsilon = \frac{S_i}{S_d}$  as a function of jet Mach number  $M_j$  for the Borda mouthpiece shown on the left in figure E.1. The solution is given by equation (E.4).

control volume yields:

$$S_d p_0 = S_d p_j + S_j \rho_j u_j^2. \quad (\text{E.1})$$

The contributions to the integral on the left boundary are balanced by the contributions on the right boundary except for the small region in the tube and an equal region on the left boundary. Using  $\Upsilon = \frac{S_i}{S_d}$  equation (E.1) is rewritten as:

$$\frac{p_0}{p_j} = 1 + \Upsilon \frac{\rho_j}{p_j} u_j^2. \quad (\text{E.2})$$

When the acceleration of the flow from the reservoir into the jet is isentropic the pressure in the jet is related to the far-field pressure by the compressible form of Bernoulli's equation:

$$\frac{p_0}{p_j} = \left(1 + \frac{\gamma - 1}{2} M_j^2\right)^{\frac{\gamma}{\gamma - 1}}. \quad (\text{E.3})$$

By substituting  $\frac{p_i}{\rho_j} = \frac{c_i^2}{\gamma}$  into equation (E.2) and combining the last two equations,  $\Upsilon$  is found as a function of Mach number  $M_j$ :

$$\Upsilon = \frac{\left(1 + \frac{\gamma - 1}{2} M_j^2\right)^{\frac{\gamma}{\gamma - 1}} - 1}{\gamma M_j^2}. \quad (\text{E.4})$$

In figure E.2  $\Upsilon$  is shown as a function of  $M_j$ . The behaviour is very similar to the behaviour shown in figure 5.8 for an orifice in a thin plate of infinite extent. This supports the assumption that the correction for the compressibility of the flow is not sensitive to details of the geometry of the orifice.

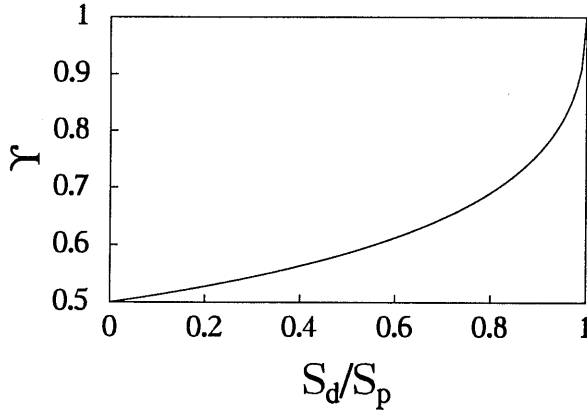


Figure E.3: Contraction ratio  $\Upsilon = \frac{S_j}{S_d}$  as a function of surface area ratio  $\frac{S_d}{S_p}$  for the Borda mouthpiece shown on the right in figure E.1. The incompressible-flow solution is given by equation (E.7).

When the Borda mouthpiece is put into a large vessel or pipe, as shown on the right in figure E.1, the relationship between the contraction ratio and the surface area ratio  $\frac{S_d}{S_p}$  can be derived analytically in the limit of incompressible flow. When the right wall is far from the tube entrance it is reasonable to assume a stagnation condition on the right wall and then the pressure is equal to  $p_0$ . In that case the pressure on the left inflow boundary is  $p_1 = p_0 - \frac{1}{2}\rho u_1^2$  (the velocity here is equal to  $u_1$ ). The pressure in the jet is equal to  $p_j$ , which is related to  $p_0$  by the incompressible form of Bernoulli's equation:  $p_0 = p_j + \frac{1}{2}\rho u_j^2$ . The integral balance of momentum in the  $x$ -direction then yields the following equation:

$$S_p \left( (p_0 - \frac{1}{2}\rho u_1^2) + \rho u_1^2 \right) = (S_p - S_d) p_0 + S_d p_j + S_j \rho u_j^2. \quad (\text{E.5})$$

Together with Bernoulli's equation and mass conservation ( $S_p u_1 = S_j u_j$ ) this leads to the following relation between the surface areas:

$$S_p (S_d - 2S_j) + S_j^2 = 0. \quad (\text{E.6})$$

This quadratic equation for  $\Upsilon$  has the relevant solution:

$$\Upsilon = \frac{1}{1 + \sqrt{1 - \frac{S_d}{S_p}}}. \quad (\text{E.7})$$

Figure E.3 shows  $\Upsilon$  as a function of the surface area ratio  $\frac{S_d}{S_p}$ . The limit solution  $\Upsilon = \frac{1}{2}$  for  $\frac{S_d}{S_p} = 0$  (Borda mouthpiece in an infinite vessel) is in agreement with the limit solution of equation (E.4) for  $M_j \downarrow 0$ . Also the simple result for an unrestricted pipe flow is satisfied:  $\Upsilon = 1$  for  $\frac{S_d}{S_p} = 1$ .

Given the previous results (E.4) and (E.7) and the method by which they were obtained, it is to be expected that also the complete solution of  $\Upsilon$  as a function of both Mach number and surface area ratio can be found. This is indeed the case. Mass conservation yields:

$$S_p \rho_1 u_1 = S_j \rho_j u_j. \quad (\text{E.8})$$

Using the isentropic relation  $\frac{p_1}{p_j} = \left(\frac{\rho_1}{\rho_j}\right)^\gamma$  and  $c^2 = \gamma p/\rho$  this can be rewritten as

$$\Upsilon \frac{S_d}{S_p} = \frac{M_1}{M_j} \left(\frac{\rho_1}{\rho_j}\right)^{\frac{\gamma+1}{2}}. \quad (\text{E.9})$$

The second equation is the compressible equivalent of equation (E.5):

$$S_p (p_1 + \rho_1 u_1^2) = (S_p - S_d) p_0 + S_d p_j + S_j \rho_j u_j^2$$

or:

$$1 + \gamma M_1^2 = \left(1 - \frac{S_d}{S_p}\right) \frac{p_0}{p_1} + \frac{S_d}{S_p} (1 + \Upsilon \gamma M_j^2) \frac{p_j}{p_1}. \quad (\text{E.10})$$

The second line is obtained by dividing the first line by  $S_p p_1$ . The pressure ratios that are still in this equation can be expressed in terms of Mach numbers by using the compressible form of Bernoulli's equation:

$$\frac{p_0}{p_1} = \left(\frac{1}{2}(\gamma - 1)M_1^2 + 1\right)^{\frac{\gamma}{\gamma-1}}, \quad (\text{E.11})$$

$$\frac{p_j}{p_1} = \left(\frac{\rho_j}{\rho_1}\right)^\gamma = \left(\frac{\frac{1}{2}(\gamma - 1)M_1^2 + 1}{\frac{1}{2}(\gamma - 1)M_j^2 + 1}\right)^{\frac{\gamma}{\gamma-1}}. \quad (\text{E.12})$$

When  $\frac{S_d}{S_p}$  and  $M_j$  are used as input parameters, then substitution of equation (E.9) in equation (E.10) results in an equation for  $M_1$ :

$$\begin{aligned} 1 + \gamma M_1^2 &= \left(1 - \frac{S_d}{S_p}\right) \left(\frac{1}{2}(\gamma - 1)M_1^2 + 1\right)^{\frac{\gamma}{\gamma-1}} + \frac{S_d}{S_p} \left(\frac{\frac{1}{2}(\gamma - 1)M_1^2 + 1}{\frac{1}{2}(\gamma - 1)M_j^2 + 1}\right)^{\frac{\gamma}{\gamma-1}} \\ &+ \gamma M_j M_1 \left(\frac{\frac{1}{2}(\gamma - 1)M_1^2 + 1}{\frac{1}{2}(\gamma - 1)M_j^2 + 1}\right)^{\frac{1}{2}}. \end{aligned} \quad (\text{E.13})$$

To summarise the procedure: the surface ratio  $\frac{S_d}{S_p}$  and the jet Mach number  $M_j$  are chosen;  $M_1$  is obtained by iteratively solving the implicit equation (E.13), and the corresponding  $\Upsilon$  is obtained from equation (E.9).

Figure E.4 shows  $\Upsilon$  as a function of the jet Mach number for five different values of  $\frac{S_d}{S_p}$ . By comparing the different curves we find that the effect of compressibility is not sensitive to the geometric parameter  $S_d/S_p$ . For  $\frac{S_d}{S_p}$  less than 0.6 the different curves can be very



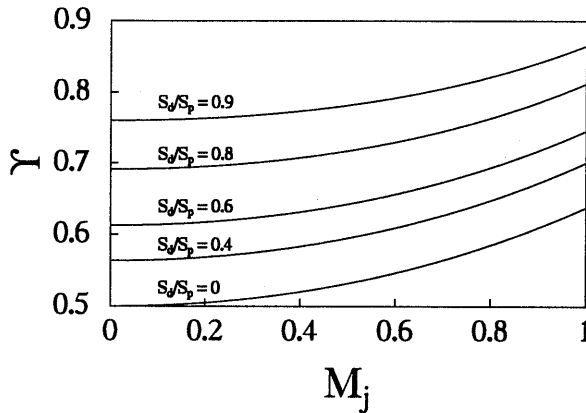


Figure E.4: Contraction ratio  $\Upsilon = \frac{S_i}{S_d}$  as a function of jet Mach number  $M_j$  for five different ratios of  $\frac{S_d}{S_p}$ . The compressible-flow solution is given by equation (E.9) after obtaining  $M_1$  from equation (E.13).

accurately approximated by just shifting the curve for  $\frac{S_d}{S_p} = 0$  upward (equation (E.2)). The approximate expression for  $\Upsilon$  then is:

$$\Upsilon \left( M_j, \frac{S_d}{S_p} \right) \approx \frac{1}{1 + \sqrt{1 - \frac{S_d}{S_p}}} + \frac{\left( 1 + \frac{\gamma-1}{2} M_j^2 \right)^{\frac{\gamma}{\gamma-1}} - 1}{\gamma M_j^2} - \frac{1}{2}. \quad (\text{E.14})$$

For  $\frac{S_d}{S_p} < 0.6$  this expression results in an approximate value for  $\Upsilon$  that is within 0.5% of the exact solution. So the most important influence of the geometric parameter is that it determines the offset of  $\Upsilon$  for  $M_j = 0$ . The effect of the compressibility is then almost independent of the geometry. Since this geometry bears a strong resemblance to the diaphragm in a pipe we expect that a similar behaviour applies to that case. This justifies the interpolation procedure proposed in section 5.3.

## References

- PRANDTL, L. & TIETJENS, O.G. (1934) Fundamentals of hydro- and aeromechanics. *Dover Publications Inc., New York.*
- SEARS, W.R. (1954) General theory of high speed aerodynamics, volume VI. *Princeton University Press, Princeton.*

## Appendix F

---

# Correction for visco-thermal dissipation in a turbulent main flow

In a turbulent main flow the visco-thermal dissipation depends on the ratio of the acoustic boundary-layer thickness  $\delta_{ac} = \sqrt{2\nu/\omega}$  and the thickness of the viscous sublayer  $\delta_l \approx 10\nu/v^*$ . Here  $\nu$  is the kinematic viscosity,  $\omega$  is the radial frequency, and  $v^*$  is the friction velocity. The effect of turbulence on acoustic damping was extensively discussed by Tijdeman (1975) and Pierce (1989). Tijdeman elaborates on the various approximations to the effect of visco-thermal dissipation on acoustic wave propagation. When the acoustic boundary-layer thickness is much smaller than the thickness of the viscous sublayer the average damping coefficient  $\bar{\alpha}$  can be approximated by Kirchhoff's damping coefficient  $\alpha_0$  in a quiescent medium:

$$\alpha_0 = \frac{k_0 \delta_{ac}}{H} \left( 1 + \frac{\gamma - 1}{\sqrt{Pr}} \right), \quad (\text{F.1})$$

where  $k_0$  is the wave number of the resonance frequency,  $H$  is the height of the channel, and  $\gamma$  and  $Pr$  are Poisson's constant and the Prandtl number, respectively. For air at room temperature and atmospheric pressure the following values are used:  $\nu = 1.5 \cdot 10^{-5} \text{ m}^2/\text{s}$ ,  $\gamma = 1.4$ , and  $Pr = 0.71$ .

On the other hand, when the acoustic boundary-layer thickness is much larger than the thickness of the viscous sublayer, the average damping coefficient is strongly affected by the turbulent dissipation. Peters (1993) measured the average wave number  $\bar{k} = \frac{1}{2}(k^+ + k^-)$  using a multi-microphone method and derived the average damping coefficient as a function of the Mach number and the frequency of the wave. He also showed that for low Mach numbers the data of the average wall impedance  $Z$  all collapsed onto a single curve when plotted as a function of the non-dimensional acoustic boundary-layer thickness  $\delta_{ac}^+ = \delta_{ac} v^* / \nu$ . His results are reproduced in figures F.1(a) and F.1(b). Using these data the visco-thermal dissipation was corrected for the influence of a turbulent main flow. For an accurate application of the energy balance this is a very important correction. At the highest experimental velocities the average damping coefficient  $\bar{\alpha}$  is as much as  $1.75 \alpha_0$ , which means an increase of 50% in the visco-thermal dissipation.

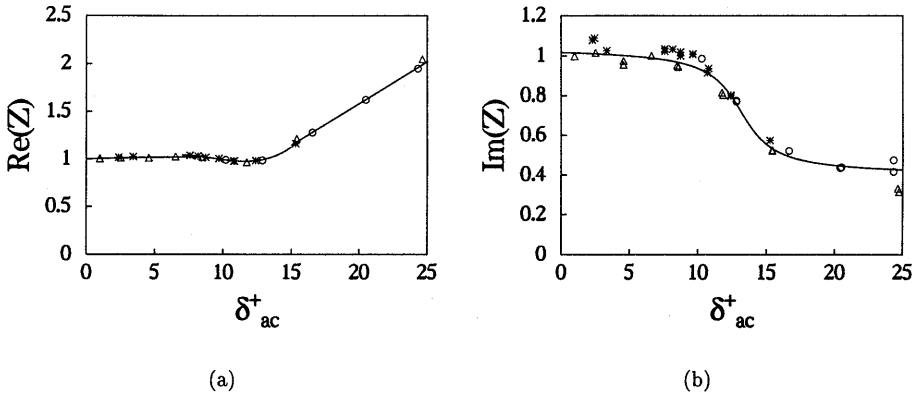


Figure F.1: Average wall impedance  $Z$ , obtained from the average wave number measurements, as a function of the non-dimensional acoustic boundary-layer thickness  $\delta_{ac}^+ = \delta_{ac} v^* / \nu$ . These results have been reproduced from Peters (1993).

In figures F.1(a) and F.1(b) the real part and the imaginary part of the average wall impedance  $Z$  are shown. It is defined as:

$$Z = \frac{\bar{k} - \frac{\omega/c_0}{1-M^2}}{-i\alpha_0} \quad (\text{F.2})$$

for small values of the Mach number  $M$  of the main flow,  $c_0$  is the speed of sound, and  $\frac{\omega/c_0}{1-M^2}$  represents the average wave number for the situation without visco-thermal dissipation. The correction on the average wave number is then:

$$\bar{k} = \frac{\omega/c_0}{1-M^2} + \alpha_0 \text{Im}(Z) - i\alpha_0 \text{Re}(Z). \quad (\text{F.3})$$

The visco-thermal dissipation affects both the wave propagation and the wave strength. In an energy balance only the dissipative term ( $-i\alpha_0 \text{Re}(Z)$ ) is important.

In order to apply the correction for the dissipation of the acoustic wave the non-dimensional acoustic boundary-layer thickness has to be found. The procedure that we used is as follows. Given the relative humidity of air  $RH$ , and the temperature  $T$  (K), the speed of sound is computed by:

$$c_0 = (343.45 + 1.23 RH) \sqrt{\frac{T}{293.16}}. \quad (\text{F.4})$$

Then the Mach number ( $M = \frac{U_0}{c_0}$ ) and the Reynolds number ( $Re = \frac{U_0 H}{\nu}$ ) are obtained using the main flow velocity  $U_0$ , the height of the channel ( $H = 0.06$  m), and the kinematic

$Re$	$\sqrt{c_f}$
$10^4$	0.17575
$10^5$	0.13414
$10^6$	0.10792

Table F.1: The friction coefficient as a function of Reynolds number for a turbulent flow; results from Prandtl's friction law (F.5).

viscosity of air ( $\nu = 1.5 \cdot 10^{-5} \text{ m}^2/\text{s}$ ). Using an iterative procedure the friction coefficient  $c_f$  is calculated from Prandtl's friction law for smooth pipes:

$$\frac{1}{\sqrt{c_f}} = 2.3 \log(Re\sqrt{c_f}) - 0.8, \quad (\text{F.5})$$

valid for  $4 \cdot 10^3 < Re < 3.4 \cdot 10^6$ . With the value of the friction coefficient the friction velocity  $v^*$  is computed:  $v^* = \sqrt{\frac{\tau_w}{\rho_0}} = \sqrt{\frac{1}{8}c_f U_0^2}$ , where  $\tau_w$  is the wall shear stress and  $\rho_0$  is the density of air. Finally the non-dimensional acoustic boundary-layer thickness is obtained  $\delta_{ac}^+ = \delta_{ac} v^* / \nu$ . In figures F.1(a) and F.1(b) the correction is then available.

## References

- PETERS, M.C.A.M. (1993) Aeroacoustical sources in internal flows. *PhD thesis Eindhoven University of Technology*
- PIERCE, A.D. (1989) Acoustics: an introduction to its physical principles and applications. *Acoustical Society of America, New York.*
- TJEDMAN, H. (1975) On the propagation of sound waves in cylindrical tubes. *J. Sound & Vibr.* **39**, 1 – 33.

## Summary

Vortex shedding in pipes and pipe systems is an important source of sound. Depending on the conditions at which vortex shedding takes place, the result is either a desired source of sound (such as speech), a damping of sound (which occurs in car mufflers), or a source of strong unwanted pulsations in gas-transport systems.

The interaction of vortex structures with the acoustic velocity field is prerequisite for the production or absorption of acoustic energy in all cases mentioned above. When the source region in which this interaction occurs is much smaller than the wavelength of the acoustic wave, it is possible to neglect wave propagation in the source region itself. Such a source region is called "compact" and it results in a simplified description of the acoustic source. We have restricted ourselves to compact source regions.

While investigating these sources of sound, we used several methods of investigation. Combination of simple theoretical models with both experimental and numerical methods should provide us with insight in the applicability of such models. Three relevant applications have been studied in this way: speech modelling, damping of acoustic waves by means of diaphragms, and the prediction of flow-induced resonances in bifurcated pipe systems with T-shaped junctions.

During speech the vocal folds are tightened and thus form a strong constriction in the vocal tract, i.e. the glottis. The time-dependent behaviour of flow separation in the glottis is important for the aeroacoustic properties of this system. Experimental as well as numerical work has been carried out for rigid *in vitro* models of the vocal folds. The results of different numerical methods have been compared with each other and with the results of experiments. It was found that it is possible to use a simplified quasi-steady model, which describes the boundary-layer flow in the glottis, to reasonably predict the separation point during a part of one cycle of the vocal-fold movement. This results in a reasonable prediction of the source of sound in voiced speech. Furthermore, it was found that the instability of the jet, that is formed downstream of the glottis, can be a significant source of broad-band sound.

A diaphragm used as a constriction in a pipe is a common element in mufflers. This configuration is investigated theoretically, numerically, and experimentally. For this purpose, a simplified quasi-steady model has been developed, and a numerical method has been applied to essentially unsteady conditions. The different descriptions are related to different approximations that lead to a compact source region. An important feature of the flow through a diaphragm with sharp edges is the so-called *vena contracta*. It appears that this *vena contracta* depends to a large extent on the Mach number of the flow. Results of the quasi-steady flow model and of the numerical calculations are in good agreement with results of experiments. Theory also correctly describes the limit of high frequencies. For the intermediate frequencies we found some deviation between theory and experiments, which is not yet fully understood.

The flow through T-joints, with sharp edges, has been numerically investigated as a function of the acoustic amplitude, the Strouhal number, and the flow configuration. In the limit of low frequencies the acoustic source in a T-joint can be described by means

of a simple quasi-steady theoretical model. At higher frequencies the acoustic source is calculated as a function of the Strouhal number for nine flow configurations in a T-joint. We have restricted ourselves to configurations that have one side branch closed. These results can be used in a qualitative way as a basis for establishing design rules for complex pipe systems. By combining a simple flow model (as, for instance, a single-vortex model) with a low-frequency representation of the acoustics of the pipe system, these results can also be used to make quantitative predictions of pulsation levels in complex pipe manifolds. For the simple case of a single-side-branch system the numerical results have been used to set up an energy balance of the system in order to predict pulsation levels. These results have been compared with the results of experiments. It was found that for low-amplitude pulsations the results agree within 10 %, while for high-amplitude pulsations the predictions appeared to be 35 % too high. These deviations can partially be explained by our model considering only vortex shedding at the upstream edge of the T-joint.

The present study indicates that quantitative predictions of vortex-sound interaction in internal flows is possible with relatively simple numerical tools as long as the flow is approximately two-dimensional and flow separation occurs at sharp edges. In our study of the flow through the glottis also a first step has been taken towards the use of simplified boundary-layer models in the prediction of flow separation from curved walls.

## Samenvatting

Wervelafschudding in buizen en pijpsystemen is een belangrijke bron van geluid. Afhankelijk van de omstandigheden waaronder wervelafschudding plaatsvindt, is het resultaat een gewenste geluidsbron (bijvoorbeeld in spraak), een demping van geluid (bijvoorbeeld in uitlaten van auto's), of een bron van sterke ongewenste pulsaties in bijvoorbeeld gas-transportssystemen.

De interactie van wervelstructuren met het akoestische snelheidsveld is een essentiële voorwaarde voor de productie dan wel absorptie van akoestische energie in elk van de bovengenoemde gevallen. Wanneer het brongebied waarin deze interactie plaatsvindt veel kleiner is dan de golflengte van de akoestische golf, dan mag golfvoortplanting in het brongebied verwaarloosd worden. Zo'n brongebied wordt „compact” genoemd en leidt tot een vereenvoudigde beschrijving van de akoestische bron. Wij hebben ons beperkt tot dergelijke compacte brongebieden.

In de studie van dergelijke geluidsbronnen is er gebruik gemaakt van diverse onderzoeksmethoden. De combinatie van eenvoudige theoretische modellen met experimentele en numerieke methoden heeft als doel om meer inzicht te verschaffen in de geldigheid van dergelijke modellen. Op deze manier zijn drie relevante toepassingen onderzocht: spraakmodellering, demping van akoestische golven met behulp van diafragma's en voorspelling van stromingsgeïnduceerde resonanties in vertakte pijpsystemen met T-vormige verbindingstukken.

Tijdens spraak worden de stembanden aangespannen en vormen zo een sterke vernauwing van het stemkanaal; deze vernauwing is de glottis. Het gedrag van de tijdafhankelijke stromingsloslating in de glottis is in belangrijke mate bepalend voor de aero-akoestische eigenschappen van het systeem. Voor een star *in vitro* model van de stembanden is zowel experimenteel als numeriek werk verricht. Resultaten van verschillende numerieke methoden zijn met elkaar en met resultaten van experimenten vergeleken. Het is mogelijk gebleken om met behulp van een eenvoudige quasi-stationair model voor de grenslaagstroming in de glottis een redelijke voorspelling te geven van het loslaatpunt van de stroming gedurende een bepaald deel van een stembandcyclus. Dit leidt tot een redelijke voorspelling van de geluidsbron voor de door de stembanden geproduceerde spraak. Daarnaast blijkt ook de instabiliteit van de straalstroming, die stroomafwaarts van de glottis ontstaat, een belangrijke bron van breedbandig geluid te kunnen zijn.

Een diafragma als een vernauwing in een pijp wordt veel toegepast in geluiddempers. Deze configuratie is theoretisch, experimenteel en numeriek onderzocht. Hiervoor is zowel een eenvoudig quasi-stationair model ontwikkeld als ook een numerieke methode gebruikt voor essentieel instationaire condities. De verschillende beschrijvingen kunnen worden gerelateerd aan verschillende benaderingen die leiden tot een compact brongebied. Een belangrijke factor voor de akoestische responsie van een diafragma met scherpe randen is de zogenaamde *vena contracta*. Het blijkt dat de *vena contracta* in belangrijke mate afhankelijk is van het Machgetal van de stroming. Resultaten van het quasi-stationaire model en de numerieke methode komen goed overeen met resultaten van experimenten. De theorie voorspelt ook de limiet voor hoge frequenties goed. Voor de tussenliggende

frequenties hebben we enkele afwijkingen van theorie en experiment geconstateerd, welke nog niet helemaal begrepen worden.

De stroming in T-verbindingstukken met scherpe hoeken in pijpsystemen is numeriek bestudeerd als functie van akoestische amplitude, Strouhal getal en stromingsconfiguratie. In de lage frequentie limiet kan de akoestische bron in een T-verbindingstuk beschreven worden met behulp van een eenvoudig quasi-stationair theoretisch model. Bij hoge frequenties is voor negen stromingsconfiguraties in een T-stuk de akoestische bron bepaald als functie van het Strouhal getal. We hebben ons beperkt to configuraties waarvan één zijtak is afgesloten. Deze informatie kan gebruikt worden in kwalitatieve zin als basis voor ontwerpregels voor complexe pijpsystemen. Door het combineren van een eenvoudig model (bijvoorbeeld een één-wervel model) en een lage frequentie beschrijving van de akoestiek van het pijpsysteem kan deze informatie gebruikt worden om kwantitatieve voorspellingen te doen van pulsationiveau's in complexe pijpsystemen. Voor het eenvoudige systeem met slechts één zijtak zijn de numerieke resultaten geïmplementeerd in een energiebalans om op die manier pulsationiveau's te voorspellen. De op deze manier verkregen drukpulsaties zijn vergeleken met resultaten van experimenten. Voor lage amplitude pulsaties komen de resultaten binnen 10 % met elkaar overeen. Voor hoge amplitude pulsaties blijken de voorspellingen ongeveer 35 % hoger te zijn dan de gemeten waarden. Deze afwijkingen zijn voor een deel te wijten aan het beschouwen van alleen wervelafschudding aan de stroomopwaartse hoek van een T-stuk in de numerieke berekeningen.

De studie geeft aan dat kwantitatieve voorspellingen van wervel-geluid interactie mogelijk zijn met behulp van relatief eenvoudige numerieke hulpmiddelen wanneer de stroming ongeveer tweedimensionaal is en stromingsloslating plaatsvindt bij scherpe hoeken. In het kader van onze studie naar de stroming door de glottis is er tevens een eerste stap gezet in de richting van de toepassing van een eenvoudig grenslaagmodel voor de voorspelling van stromingsloslating van gekromde wanden.



## Dankwoord

Het beëindigen van een stuk werk als een promotieonderzoek leidt natuurlijk tot een overpeinzing van de jaren die zijn doorgebracht op deze ene werkplek. Van de 11 jaren die ik verbonden was aan de faculteit Technische Natuurkunde van de TUE, heb ik er ongeveer  $6\frac{1}{2}$  doorgebracht binnen de sectie Gasdynamica/Aeroakoestiek van de vakgroep Transportfysica, eerst als afstudeerder en vervolgens als promovendus. In die jaren heb ik me altijd thuis gevoeld bij de mensen verbonden aan de sectie.

Allereerst wil ik Mico Hirschberg en Harry Hoeijmakers bedanken. Zij hadden de taak om mij tijdens mijn promotieonderzoek te begeleiden. Mico was een constante bron van nieuwe ideeën en toonde op een enthousiaste manier veel belangstelling voor mijn resultaten wat heeft geleid tot de grote hoeveelheid resultaten gepresenteerd in dit proefschrift. Harry keek met name met een kritische blik naar de resultaten verkregen met de vortexblob methode. Het is jammer dat ik deze „driewieler” niet meer „supersoos” heb kunnen maken. Maar ik denk dat de resultaten in dit proefschrift aantonen dat je ook met een „driewieler” kunt komen waar je moet zijn.

Bram Wijnands ontwierp en vervaardigde de experimentele opstellingen met veel zorg en aandacht. Dankzij zijn precisiewerk was het voor mij mogelijk om juist die extra nauwkeurigheid te bereiken die het mogelijk maakte om tot gefundeerde uitspraken te komen over de onderzochte stromingen.

Na  $3\frac{1}{2}$  jaar werd er ontdekt dat alle metingen aan de de stembandmodellen afwijkingen vertonen ten gevolge van de vorm van het drukgat. Dit vereiste snelle actie van verschillende mensen. Hiervoor wil ik in het bijzonder Eep van Voorthuisen en Gerald Oerlemans bedanken. Hun bijdragen aan het vervaardigen van de nieuwe onderdelen voor de opstelling maakte het mogelijk dat alle experimenten alsnog konden worden overgedaan.

Working together on a problem is a much more pleasant way to do physics than working alone. The seven months of collaboration with Massimo Ranucci was a very enjoyable experience. Furthermore, I thank him for the use of the numerical code that he developed together with Giorgio Graziani. But, most of all, I wish to express my gratitude to Massimo and his wife Shoko for taking me into their home during my stay in Rome, and making my stay such a pleasant experience. Moreover, Shoko also acted as my guide to the city of Rome and she pointed out the most beautiful places to visit.

Special thanks I also give to the other people of the university “La Sapienza” in Rome. Particularly I mention prof. R. Piva for receiving me in his group at the university, and also Alessandro Iafrati and Giorgio Riccardi who developed the original inviscid vortexblob method, which I used to obtain the numerical results in chapters 5 and 6 in an adapted form.

Without the experiments performed by Yves Auregan and Grégoire Ajello, of the LAUM in Le Mans, chapter 5 would be incomplete. I am grateful to them for doing the experiments with an accuracy that we could not achieve here in Eindhoven, as well as for the discussion on the basic acoustic variable. My current understanding is that neither total enthalpy nor exergy qualify.

De Eulerberekeningen die gepresenteerd worden in dit proefschrift zijn uitgevoerd door Steve Hulshoff. Hiervoor spreek ik mijn dank uit. Bovendien heeft Steve als vraagbaak gediend wat betreft mijn vragen met betrekking tot de spelling en de grammatica van de Engelse taal.

De volgende afstudeerders hebben allen een belangrijke bijdrage geleverd aan de totstandkoming van het werk dat gepresenteerd is in dit proefschrift: Ronald Boot, Roel Bosch, Jaap den Doelder, Richard van Doren en René ter Riet. Ronald wil ik apart nog bedanken voor de creatie van figuur 5.9, maar nog belangrijker voor zijn bijdrage aan het werk aan het diafragma dat gepresenteerd is in hoofdstuk 5.

Stagiairs leveren ieder op hun eigen manier een bijdrage aan het onderzoek en aan de werkomgeving. Hiervoor ben ik dank verschuldigd aan Rob van Beek, Thor Groeneweg, Gemmeke Groot, Ruud Heijmans, Riekle Kuipers en Michel Pollen. In het bijzonder Gemmeke ben ik veel dank verschuldigd voor het zeer zorgvuldig overdoen van de experimenten aan de stembandmodellen binnen een kort tijdsbestek. Het merendeel van de experimentele resultaten die in hoofdstukken 3 en 4 gepresenteerd worden heb ik aan haar te danken.

Met de volgende mensen heb ik het genoeg gehad een tijdje samen te werken: Seydou Fadoulourahmane, Pierre Kriesels, Gaston Smeets, Hamid Ualit en Edgar van de Ven. Zij waren allen tijdelijk verbonden aan de groep aeroakoestiek in het kader van een TWAIO-opleiding dan wel een Europees project.

For his help on understanding interacting boundary-layer theory and the possibilities of triple-deck theory I wish to thank Pierre-Yves Lagré of the "Université Paris VI".

Van de faculteit Wiskunde ben ik René van Hassel dankbaar voor zijn bijdrage aan de studie van asymptotische expansies en grenslaagtheorie.

Ik dank prof. A. Veldman en Jan-Willem Phylipsen van de Universiteit Groningen voor het numerieke werk uitgevoerd door hun.

René Peters ben ik dankbaar voor de getoonde interesse in mijn werk. Het geeft bovendien veel voldoening om te zien dat de resultaten van hoofdstuk 6 daadwerkelijk kunnen worden toegepast voor praktische problemen.

Ten slotte bedank ik de rest van de collega's van de sectie Gasdynamica/Aeroakoestiek voor hun hulp en hun bijdrage aan het veraangenamen van de tijd die ik binnen de sectie heb doorgebracht.

---

## Curriculum vitae

- 13 februari 1969 : geboren te Horst
- juni 1987 : diploma Gymnasium- $\beta$ ,  
Boschveldcollege, Venray
- augustus 1993 : diploma Technische Natuurkunde (met lof),  
Technische Universiteit Eindhoven
- sept. 1993 - sept. 1997 : Onderzoeker in Opleiding in dienst van NWO,  
Technische Universiteit Eindhoven  
faculteit der Technische Natuurkunde  
vakgroep Transportfysica
- juni & augustus 1996 : verblijf aan de universiteit „La Sapienza”, te Rome
- 1 augustus 1998 : medewerker afdeling Metrologie,  
ASM Lithography, Veldhoven